SKB

TECHNICAL REPORT 95-20

Modelling of the physical behaviour of water saturated clay barriers. Laboratory tests, material models and finite element application

Lennart Börgesson[1], Lars-Erik Johannesson[1], Torbjörn Sandén[1], Jan Hernelind[2]

1 Clay Technology AB, Lund, Sweden
2 FEM-Tech AB, Västerås, Sweden

September 1995

SVENSK KÄRNBRÄNSLEHANTERING AB
SWEDISH NUCLEAR FUEL AND WASTE MANAGEMENT CO
P.O.BOX 5864 S-102 40 STOCKHOLM SWEDEN
PHONE +46 8 665 28 00 TELEX 13108 SKB
FAX +46 8 661 57 19

MODELLING OF THE PHYSICAL BEHAVIOUR OF WATER SATURATED CLAY BARRIERS

LABORATORY TESTS, MATERIAL MODELS AND FINITE ELEMENT APPLICATION

Lennart Börgesson[1], Lars-Erik Johannesson[1], Torbjörn Sandén[1], Jan Hernelind[2]

1 Clay Technology AB, Lund, Sweden
2 FEM-Tech AB, Västerås, Sweden

September 1995

MODELLING OF THE PHYSICAL BEHAVIOUR OF WATER SATURATED CLAY BARRIERS

LABORATORY TESTS, MATERIAL MODELS AND FINITE ELEMENT APPLICATION

Lennart Börgesson
Lars-Erik Johannesson
Torbjörn Sandén

Clay Technology AB, Lund, Sweden

Jan Hernelind

FEM-Tech AB, Västerås, Sweden

September 1995

Keywords: Bentonite, Clay, Clay barrier, FEM, Laboratory test, Material model, Modelling, THM

ABSTRACT

This report deals with laboratory testing and modelling of the thermo-hydro-mechanical (THM) properties of water saturated bentonite based buffer materials. A number of different laboratory tests have been performed and the results are accounted for. These test results have lead to a tentative material model, consisting of several sub-models, which is described in the report. The tentative model has partly been adapted to the material models available in the finite element code ABAQUS and partly been implemented and incorporated in the code. The model that can be used for ABAQUS calculations agrees with the tentative model with a few exceptions.

The model has been used in a number of verification calculations, simulating different laboratory tests, and the results have been compared with actual measurements. These calculations show that the model generally can be used for THM calculations of the behaviour of water saturated buffer materials, but also that there is still a lack of some understanding. It is concluded that the available model is relevant for the required predictions of the THM behaviour but that a further improvement of the model is desirable.

SAMMANFATTNING

Denna rapport beskriver laboratorieförsök på vattenmättat bentonitbaserat buffertmaterial och modellering av dess termo-hydro-mekaniska (THM) egenskaper. Ett stort antal laboratorieförsök av olika slag har utförts och resultaten är redovisade. Dessa försöksresultat har lett till en tentativ materialmodell, som är beskriven i rapporten. Den tentativa modellen har delvis anpassats till de befintliga modellerna i finita-element-programmet ABAQUS och delvis blivit kodade och infogade i programmet. Den modell som kan användas i ABAQUS överensstämmer i stort med den tentativa modellen med ett par undantag.

Modellen har använts i ett antal beräkningar som simulerar olika laboratorieförsök och resultaten har jämförts med utförda mätningar. Beräkningarna visar att modellen generellt kan användas vid THM-beräkningar av funktionen hos vattenmättat buffertmaterial, men de visar också att det fortfarande saknas viss förståelse. Slutsatsen är att den tillgängliga modellen är relevant för att göra erforderliga prognoser av THM processer men att ytterligare förbättringar är önskvärda.

CONTENTS

SUMMARY

The report describes a thermo-hydro-mechanical model of water saturated buffer material and how it can be used for calculation of THM processes with the finite element code ABAQUS. It mainly contains the following five parts:

1. Description of laboratory tests and results which are the basis for the model
2. A tentative material model, which consists of the present knowledge of the THM behaviour
3. A model that can be used with the finite element program ABAQUS to make calculations of the THM behaviour of buffer material in a repository
4. Examples of verification calculations, which shows ABAQUS calculations of some laboratory tests and compares the results with actual measurements
5. Implementation of the plastic part of the mechanical model for the code ABAQUS

The laboratory tests have been performed on samples with different bentonite composition, at different void ratio and temperature, and with different pore water composition. The following tests are accounted for in the report:

- Triaxial tests
- Swelling/compression tests
- Swelling pressure tests
- Hydraulic conductivity tests
- Creep tests

These tests and several other test types shown in other reports, as shear tests, thermal conductivity tests, and thermal expansion tests, have all been used for the material model. E.g. the triaxial tests have been used for evaluating the stress-strain-strength behaviour at a change in deviatoric stress and the swelling/compression tests have been used for evaluating the volume change caused by a change in average stress.

The material model, which consists of many submodels, can be considered to exist in two stages. The first stage is a so called tentative model which describes a defined process in a preliminary way with e.g. a formula. The tentative model is called the CLAYTECH/S/T model where S stands for saturated and T stands for tentative. The second stage is a model completed and adjusted to or implemented for the finite element code ABAQUS. This model is called the CLAYTECH/S/A where A stands for ABAQUS. The report describes both these models. They are very similar for the saturated stage with a few exceptions like the volumetric creep.

The hydraulic and thermal submodels are available in the standard version of ABAQUS, while a new mechanical model have been developed and implemented for the code. The mechanical model consists of the following main components:

- A curved critical state line (CSL)
- A curved failure envelope
- A cap that defines the limit between elastic and plastic volumetric strain
- A porous elastic region with a variable Poisson's ratio
- A plastic region with contractancy on the cap and dilatancy outside the CSL

The model is based on the effective stress theory and Darcy's law with a variable hydraulic conductivity. The heat flow is modelled as resulting from thermal conduction with a variable heat conductivity. The thermo-mechanical response is linked to the thermal expansion of the water and particles. The implementation of the mechanical model is described in Appendix 1.

The mechanical model have been checked with some calculations, which simulate laboratory tests that have been carried out. Two different types of swelling/compression tests and two types of triaxial tests have been simulated and compared to measured results. These calculations show that the model generally can be used for mechanical calculations of the behaviour of water saturated buffer materials, but also that there is still a lack of some understanding. It is concluded that the available model is relevant for the required predictions of the THM behaviour but that a further improvement of the model is desirable.

SYMBOLS

a = creep parameter
a = parameter (Eqn 3-11)
b = parameter (Eqn 3-11)
c = parameter (Eqn 3-12)
c = cohesion
c = creep constant
C_{ae} = secondary compression
D_r = degree of mobilised strength
k = hydraulic conductivity
n = creep parameter
p = average effective stress ($=(\sigma_1+\sigma_2+\sigma_3)/3$)
q = Mises' stress or deviator stress
R = parameter defining cap plasticity
t = time
u = pore pressure
V = volume
w = water ratio

β = parameter (Eqn 3-5)
β = friction angle in q-p plane
γ = parameter defining cap plasticity
ε = strain
$\dot{\varepsilon}$ = rate of strain
ϕ = friction angle
η = parameter (Eqn 3-10)
κ = porous elastic bulk modulus
λ = thermal conductivity
ν = Poisson's ratio
ρ = bulk density
ρ_d = dry density
ρ_m = bulk density at water saturation
ρ_s = density of solids
ρ_w = density of water
σ_1 = major principal effective stress
σ_2 = intermediate principal effective stress
σ_3 = minor principal effective stress

1 INTRODUCTION

The buffer material, which embeds the waste canisters in a nuclear waste repository, passes through the following three phases, yielding different material properties:

- The first phase lasts from the emplacement of the buffer material until enough water has been taken up from the rock by the buffer to make it completely water saturated. The required time depends primarily on the far-field supply of water, the hydraulic conductivity of the rock, the piezometric conditions, and the initial degree of saturation of the buffer. Also, the suction potential and hydraulic conductivity of the buffer and the temperature gradient in the buffer are important factors. This period will last for at least 5 years.

- The second phase is subsequent to the saturation phase and ends when the temperature conditions are back to normal.

- The third phase represents the period when the ambient rock temperature prevails.

The properties and behaviour of water saturated buffer materials have been investigated for several years. Derived material models have been adapted to the finite element program ABAQUS. Several different scenarios of the interaction between rock, buffer and canister have been calculated by use of the derived material models. In these calculations the buffer material has been assumed to be completely water saturated from start and the wetting process has been considered in separate calculations. This report will only treat the behaviour and modelling of water saturated buffer material.

According to the Swedish KBS3 concept the buffer is planned to consist of Na-bentonite MX-80 which will be compacted to blocks under high pressure (about 100 MPa) prior to emplacement. The blocks will be piled around the canister and lowered into the deposition hole either separately or as a complete package. The blocks will be compacted either with the natural water content of the bentonite or with additional water added before compaction. The latter procedure will yield a degree of saturation of 80-90% in the blocks. The slots between the blocks and between blocks and canister or rock, respectively, will either be filled with water after emplacement or left open to be filled with the natural ground water in the rock. The concept with blocks implies that the bentonite swells and establishes a tight contact with the rock and the canister.

This report will describe the laboratory tests that are the basis for the material models and it will describe the models as well as their application to ABAQUS. The two earlier models (Total Stress Model and Effective Stress

Drucker-Prager Model) and the earlier laboratory tests have been described in previous reports (Börgesson, 1988, Börgesson et al, 1988, and Börgesson, 1990). These models and tests will only be briefly described. The latest model (CLAYTECH) and the latest laboratory tests will be described in detail.

The report will also show some calculations, compare them with laboratory measurements, and explain why the improved model (CLAYTECH) is desired.

2 LABORATORY TESTS

2.1 GENERAL

A general material model that describes the Thermo-Hydro-Mechanical (THM) properties of water saturated buffer materials requires knowledge of a large number of properties, which must be determined with many different types of laboratory tests. The following properties need to be investigated:

1. The volume change at increased and decreased average stress.
2. The strain and volume change at increased and decreased deviatoric stress
3. The shear strength or maximum deviatoric stress at different average stress
4. The relation between the plastic non-recoverable strain and the elastic recoverable strain
5. The hydraulic conductivity
6. The thermal conductivity
7. The compressibility of the pore water and the particles
8. The thermal expansion of the pore water and the particles
9. The volumetric and deviatoric creep properties

The dependency of a number of factors also needs to be investigated:

- Temperature
- Average effective stress
- Pore water composition
- Initial void ratio

The properties are different for different types of buffer materials. Especially the smectite content and the exchangeable cations are important for the behaviour. It is also important to test the properties of the possible material changes that may appear during the lifetime of the repository.

There are thus a large number of tests that need to be made in order to have a complete model of the physical behaviour of buffers. This chapter will describe the results of a large number of tests which have been made for developing and validating the latest material model. Tests reported in earlier reports will be included in overview diagrams but not described in detail.

The following tests have been made on the water saturated reference buffer material MX-80:

- Triaxial tests
- Swelling pressure tests
- Hydraulic conductivity tests

- Swelling/compression tests
- Creep tests
- Shear tests
- Thermal conductivity tests
- Thermal expansion tests

These tests are sufficient for deriving a complete THM model. They are also used for determining the necessary parameters of the models and for preliminary validation of the model. A large number of triaxial tests have been made because they can be used for many purposes and are well fitted for material modelling.

2.2 TRIAXIAL TESTS

2.2.1 General

The stress-strain-strength properties are preferably evaluated from triaxial tests. A large number of triaxial tests have been made on different bentonit types under different conditions. The measured results of some of these tests are accounted for in Appendix 2. Figure 2-1 is a schematic drawing of a triaxial cell. The sample is mounted in the cell and confined by a rubber membrane. A cell pressure is applied on the sample and the pore pressure system kept closed. When the pore pressure, which is continuously measured, tends to become constant, the sample has reached equilibrium. After reaching equilibrium the cell is placed in a press and the shear stress in the sample increased by running the press at a constant rate of strain (the vertical stress is increased). Tests have been performed both under drained and undrained conditions. During the test the cell pressure (σ_3), the vertical strain (ε), the vertical stress (σ_1) and the pore pressure (u) or the volume change ($\Delta V/V$) are measured continuously.

So called passive triaxial tests were also performed. In this type of test the vertical stress is decreased until failure is reached. The reduction of the vertical stress was carried out by fixing the piston and the base pedestal to the load frame. By pulling the piston at a constant rate of strain the vertical stress was decreased until failure was reached.

The rate of strain needs to be very low due to the low hydraulic conductivity, especially for the drained tests. Normally, an undrained test took 20-30 days and a drained test 50-70 days.

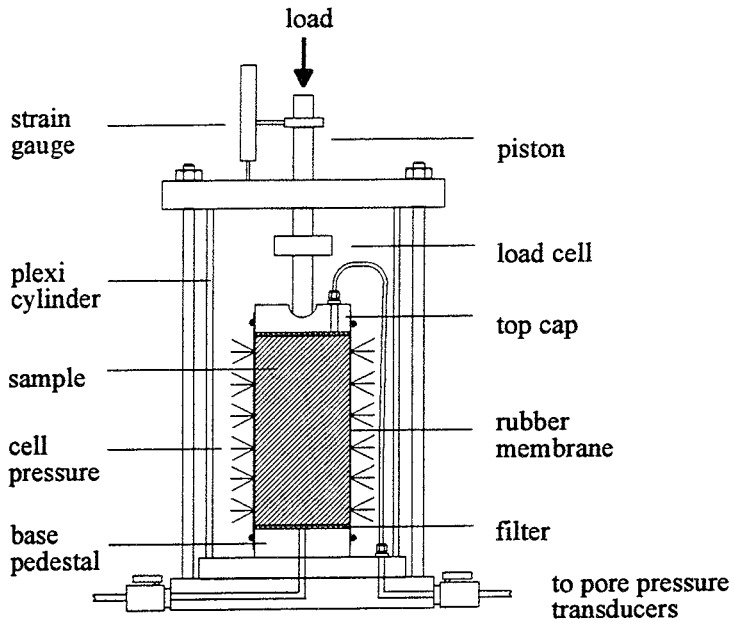

Figure 2-1. *Schematic drawing of the triaxial cell.*

The effective stresses in a triaxial test can be calculated as:

$$\sigma_{1_{tot}} = \sigma_{1_{tot}} - u \tag{2-1}$$

$$\sigma_2 = \sigma_{3_{tot}} = \sigma_{3_{tot}} - u \tag{2-2}$$

The deviator stress (q) and the average effective stress (p) can be calculated as follows:

$$q = \sigma_1 - \sigma_3 \tag{2-3}$$

$$p = \frac{\sigma_1 + \sigma_2 + \sigma_3}{3} = \frac{\sigma_1 + 2\sigma_3}{3} = \frac{\sigma_{1_{tot}} + 2\sigma_{3_{tot}} - 3u}{3} \tag{2-4}$$

According to Mohr -Coulomb failure envelope the shear strength can be described as :

$$\tau_f = c + \sigma_N \tan\phi \tag{2-5}$$

where c′ is called the cohesion intercept and ϕ is the friction angle. If the tests are plotted with the deviator stress (q) as a function of the effective average stress at failure (p) and the material is assumed to be a Mohr-Coulomb material the failure envelope will look like the curve shown in Figure 2-2. From this curve, the friction angle and the cohesion can be calculated:

$$\tan(\beta) = \frac{6\sin(\phi)}{3 - \sin(\phi)} \tag{2-6}$$

$$\sigma_c = 2c\frac{cos(\phi)}{1-sin(\phi)} \tag{2-7}$$

The definitions of β and σ_c are shown in Figure 2-2

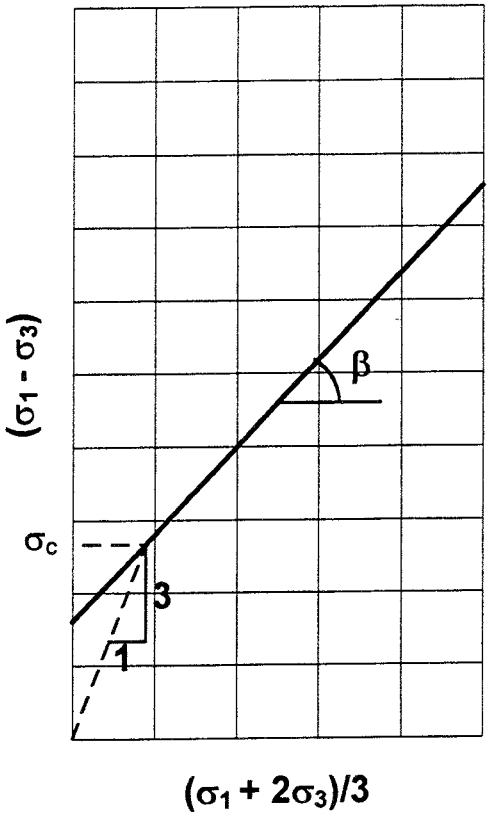

Figure 2-2. *Failure envelop for triaxial test were* $\sigma_2 = \sigma_3$.

2.2.2 Triaxial tests on natural Na-bentonites

Most of the tests were carried out as standard triaxial tests, e.g. the vertical stress was increased until failure of the sample was reached. Two natural bentonites with Na as dominating exchangeable cation were tested, i.e. MX-80 and SPV200 from Wyoming USA. The difference between the two bentonites are the granule size distribution. SPV200 is a powder bentonite while MX-80 is coarser. Four of the samples were saturated in an odometer before they were mounted in the triaxial cell (T12;T13, T17 and T22). The sample T27 was compacted in a special device to almost saturated conditions and mounted in the triaxial cell. Two of the samples were tested under drained conditions (see Table 2-1).

In Table 2-1 some results from the tests on MX-80 and SPV200 are summarised.

- Column 1 shows the test number
- Column 2 shows the bentonite type
- Column 3 shows the type of test
- Column 4 shows the water ratio of the sample after the test
- Column 5 shows the bulk density of the sample after the test
- Column 6 shows the calculated degree of saturation of the sample after the test (using $\rho_s = 2.78$ g/cm^3 and $\rho_w = 1.00$ g/cm^3)
- Column 7 shows the cell pressure at the start of the tests
- Column 8 shows the pore pressure at the start of he tests
- Column 9 shows the deviator stress at failure of the samples
- Column 10 shows the vertical strain at failure of the samples

Table 2-1. Results from standard triaxial test on MX-80 and SPV200

1 Test	2 Bent type	3 Test type	4 w (%)	5 ρ (g/cm^3)	6 S_r (%)	7 σ_3 (kPa)	8 u (kPa)	9 $(\sigma_1 - \sigma_3)_f$ (kPa)	10 ε_f (%)
T12	MX-80	Drained	43.9	1.79[1)]	99	800	305	311	6.5
T13	MX-80	Undrained	31.5	1.94	99	8870	7135	906	8
T17	MX-80	Drained	27.6	1.99	98	4190	432	1664	7
T22	MX-80	Drained	72.5	1.58	99	502	308	158	17
T27	SPV200	Undrained	48.5	1.75	99	972	414	326	7

[1)] Compacted to ρ_m=2.1 g/cm^3 and then allowed to swell

The tests are plotted in Figure 2.3. A straight line is fitted through the failure stresses according to the least square method. From the straight line the friction angle and the cohesion can be calculated with Eq. 2-6 and Eq. 2-7. The evaluated friction angle and cohesion were 9.9° and 56 kPa, respectively.

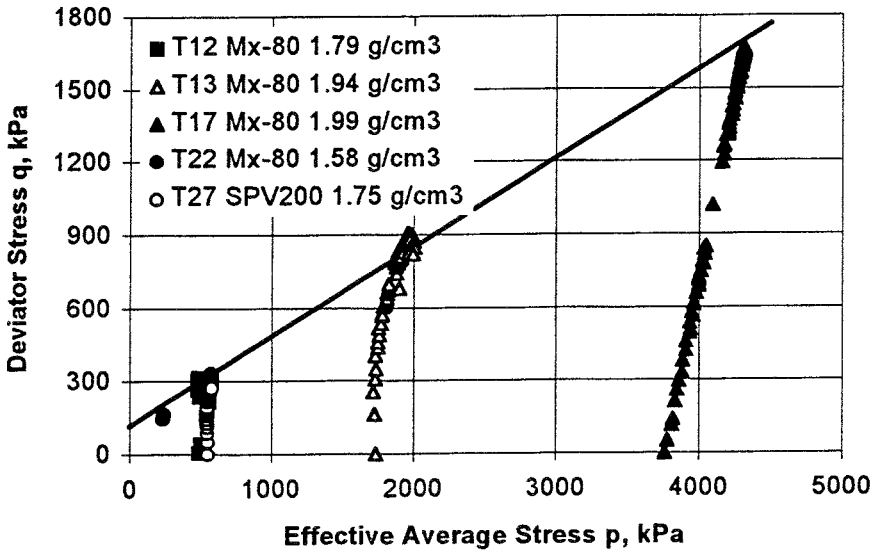

Figure 2-3. Results from standard triaxial test on MX-80 and SPV200

Also two passive triaxial tests have been performed on MX-80. The samples were consolidated with the deviator stress larger than zero. The results from the tests are shown in Table 2-2 and Figure 2-4. The evaluated friction angle and cohesion for these tests are 8.7° and 87 kPa respectively.

Table 2-2. Results from passive triaxial tests on MX-80.

1 Test	2 Bent type	3 Test type	4 w (%)	5 ρ (g/cm³)	6 S_r (%)	7 σ_3 (kPa)	8 u (kPa)	9 $(\sigma_1 - \sigma_3)_f$ (kPa)	10 ε_f (%)
T30	MX-80	Undrained	48.5	1.74	98	1310	512	420	8
T32	MX-80	Undrained	43.4	1.79	98	1807	456	572	8

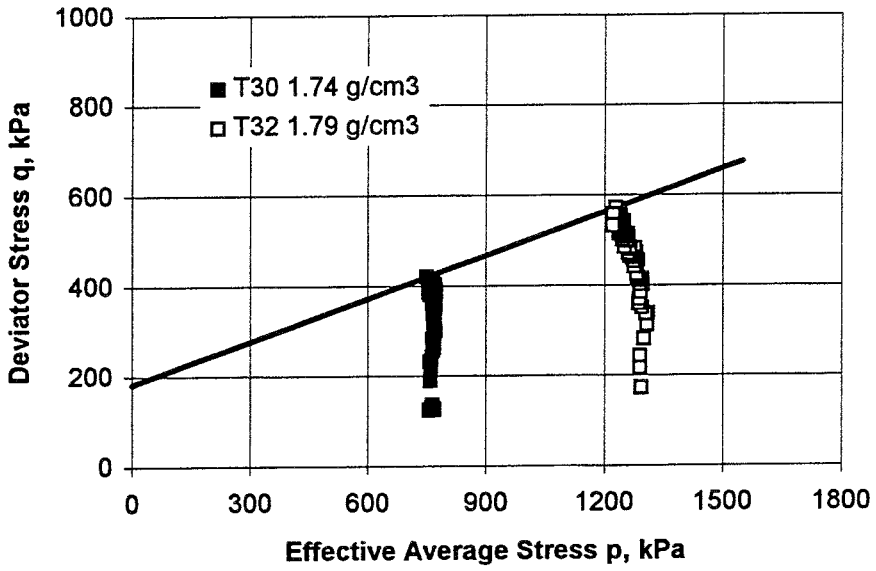

Figure 2-4. Results from passive triaxial tests on MX-80.

2.2.3 Triaxial tests on MX-80 with 3.5% NaCl in the pore water

The behaviour of bentonite may be affected by the content of salt in the pore water. In order to investigate the effect, four standard triaxial tests were performed with 3.5% NaCl in the pore water. The results from the tests are shown in Table 2-3 and Figure 2-5. The evaluated friction angle and cohesion was 12.9° and 106 kPa, respectively. Note that test T18II is disregarded at the evaluation of the friction angle and the cohesion.

Table 2-3. Results from standard triaxial tests on MX-80 with 3.5% NaCl in the pore water.

1 Test	2 Bent type	3 Test type	4 w (%)	5 ρ (g/cm³)	6 S_r (%)	7 σ_3 (kPa)	8 u (kPa)	9 $(\sigma_1 - \sigma_3)_f$ (kPa)	10 ε_f (%)
T18	MX-80	Undrained	32.6	1.91	98	1980	620	957	7
T18II	MX-80	Undrained	34.1	1.92	100	2010	-	873	11
T19	MX-80	Undrained	35.9	1.87[1)]	98	1004	541	515	9
T20	MX-80	Drained	38.4	1.85[2)]	99	1991	728	996	9
T21	MX-80	Drained	34.5	1.91	100	1038	286	669	

[1)] Compacted to ρ_m=2.05 g/cm³ and then allowed to swell
[2)] Compacted to ρ_m = 2.00 g/cm³ and then allowed to swell

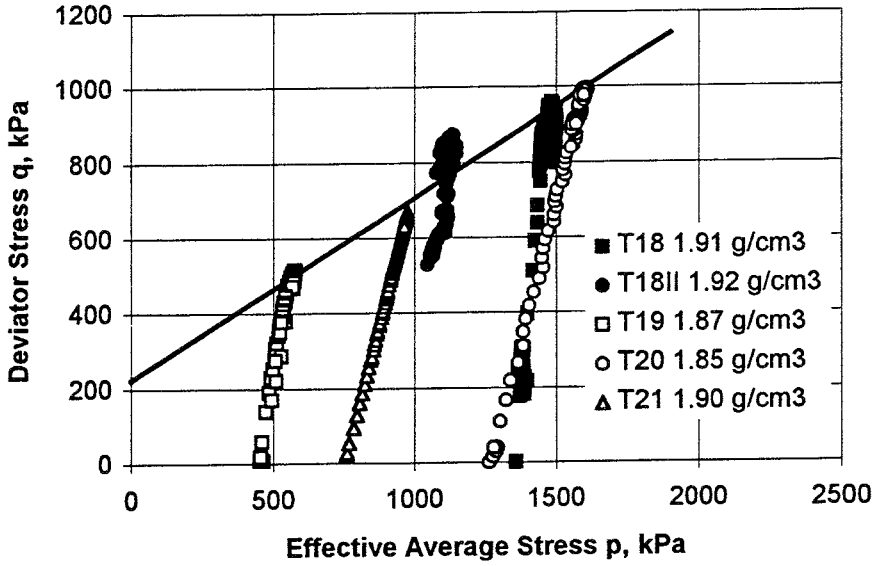

Figure 2-5. Results from standard triaxial tests on MX-80 with 3.5% NaCl in the pore water.

2.2.4 Triaxial tests on a sodium converted Ca-bentonite

Two undrained triaxial tests have been performed on a sodium converted Ca-bentonite from Greece (IBECO). The results from the tests are shown in Table 2-4 and Figure 2-6. The evaluated friction angle and cohesion were 9.1° and 104 kPa, respectively.

Table 2-4. Results from standard triaxial tests on a sodium converted bentonite (IBECO).

1 Test	2 Bent type	3 Test type	4 w (%)	5 ρ (g/cm³)	6 S_r (%)	7 σ_3 (kPa)	8 u (kPa)	9 $(\sigma_1 - \sigma_3)_f$ (kPa)	10 ε_f (%)
T25	IBECO	Undrained	33.1	1.90	97	11997	4837	2636	6
T28	IBECO	Undrained	49.8	1.73	98	993	299	460	5.5

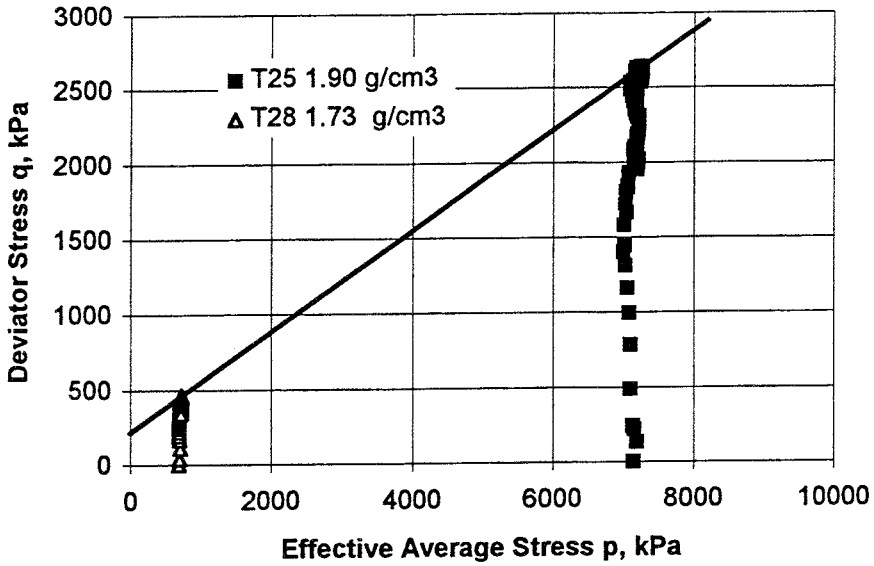

Figure 2-6. Results from standard triaxial tests on a sodium converted bentonite (IBECO).

2.2.5 Triaxial tests on a Ca-bentonite

Four drained triaxial tests have been performed on a Ca-bentonite (Moosburg). The results from the tests are shown in Table 2-5 and Figure 2-7. The evaluated friction angle and cohesion were 13.5° and 124 kPa, respectively.

Table 2-5. Results from standard triaxial tests on a Ca-bentonite (Moosburg).

1 Test	2 Bent type	3 Test type	4 w (%)	5 ρ (g/cm³)	6 Sr (%)	7 σ_3 (kPa)	8 u (kPa)	9 $(\sigma_1 - \sigma_3)_f$ (kPa)	10 ε_f (%)
T14	Moosb.	Drained	29.2	1.95	96	4200	1001	2270	8
T15	Moosb.	Drained	33.9	1.89[1)]	97	1057	92	940	7
T16	Moosb.	Drained	40.0	1.79	95	803	307	525	6
T23	Moosb.	Drained	47.2	1.74	97	702	425	446	11

[1)] Compacted to ρ_m=2.1 and then allowed to swell

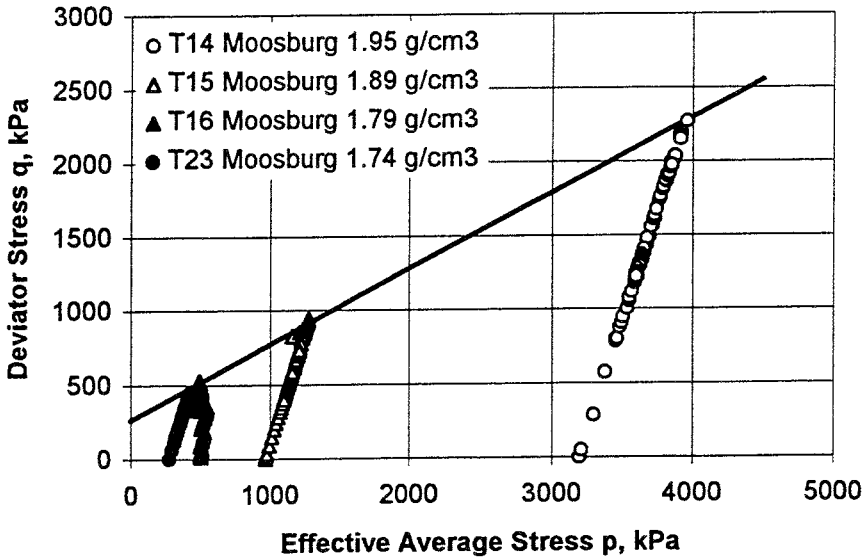

Figure 2-7. Results from standard triaxial tests on a Ca-bentonite (Moosburg).

2.2.6 Comparison of the different triaxial tests

In Table 2-6 the results from the evaluated shear strength parameters are summarised. Although the tests are few, the following preliminary conclusions can bee drawn:

- The test on the converted Ca-bentonite (IBECO) gave a similar friction angle as the tests performed on natural occurring Na-bentonite (MX-80)
- The tests on Ca-bentonite (Moosburg) gave a higher friction angle than the tests on the Na-bentonites.
- The tests on MX-80 with 3.5% NaCl in the pore water gave a higher friction angle than the tests on MX-80 with distilled pore water.

Another conclusion is that the effect of overconsolidation or temperature on the shear strength is very small.

Table 2-6. Results from performed triaxial tests.

Bentonite	Test type	Water	ϕ (°)	c (kPa)
MX-80 - Nat. Na-bentonite	Standard	Distilled	9.9	56
MX-80 - Nat. Na-bentonite	Passive	Distilled	8.7	87
MX-80 - Nat. Na-bentonite	Standard	3.5 % NaCl	12.9	106
IBECO - Conv. Ca-bentonite	Standard	Distilled	9.1	104
Moosburg - Ca-bentonite	Standard	Distilled	13.5	124

In Figure 2-8 the maximum deviator stress is plotted as a function of the effective average stress for all the tests described plus some earlier performed tests (Börgesson et al, 1988; Börgesson, 1990). Modified failure envelops are plotted for the different bentonites in the figure. The plot indicates that the modified failure envelops for the different bentonites are not straight lines.

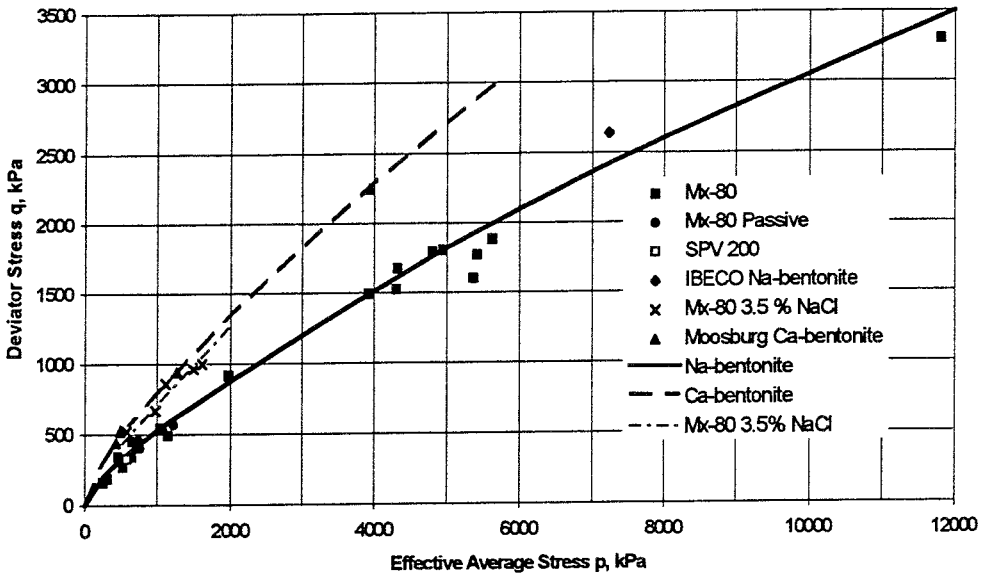

Figure 2-8. Maximum deviator stress plotted as function of effective average stress for different types of bentonite.

2.3 SWELLING PRESSURE AND HYDRAULIC CONDUCTIVITY TESTS

The swelling pressure and hydraulic conductivity are usually measured in a so-called swelling pressure oedometer (Fig 2-9). The clay material is compacted to a cylindrical sample with 5 cm diameter and 2 cm height. After compaction the sample is placed in the oedometer with the piston braced between the sample and the force transducer. The filter stones and the sample are deaired by vacuum suction and water let into the filters. The apparatus is very stiff and the swelling pressure measured with a total displacement of less than 100 μm during the entire water saturation phase. After saturation a hydraulic gradient is applied between the filter stones and the in- and out-flow of water are measured.

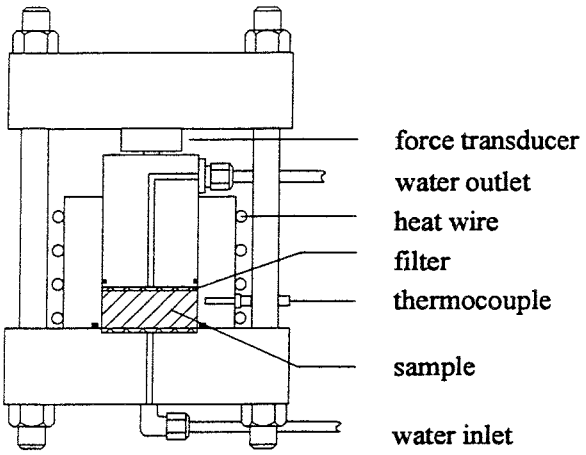

Figure 2-9. Swelling pressure oedometer equipped with heat wires and a force transducer

Several series of hydraulic conductivity and swelling pressure measurements have been made by use of this technique. See e.g. Pusch (1980) and Börgesson et al (1988). Results reported by Karnland et al (1994) are shown in Figs 2-10 and 2-11. The samples were heated and cooled in several steps. Four types of swelling clays with different dominating clay minerals were investigated. The Na-montmorillonite has been industrially converted from Ca-montmorillonite.

2.4 SWELLING/COMPRESSION TESTS

2.4.1 General

Earlier performed tests have shown that the swelling pressure from odometer tests after swelling and compression is different and deviates from the swelling pressure measured at constant volume. In order to investigate how the swelling pressure deviates after swelling and compression the equipment shown in Figure 2-12 has been constructed. The devise consists of a ring and two axial pistons. In the ring there is also a small radial piston which makes it possible to measure the radial pressure during the test. Water can be supplied to the sample through the axial pistons.

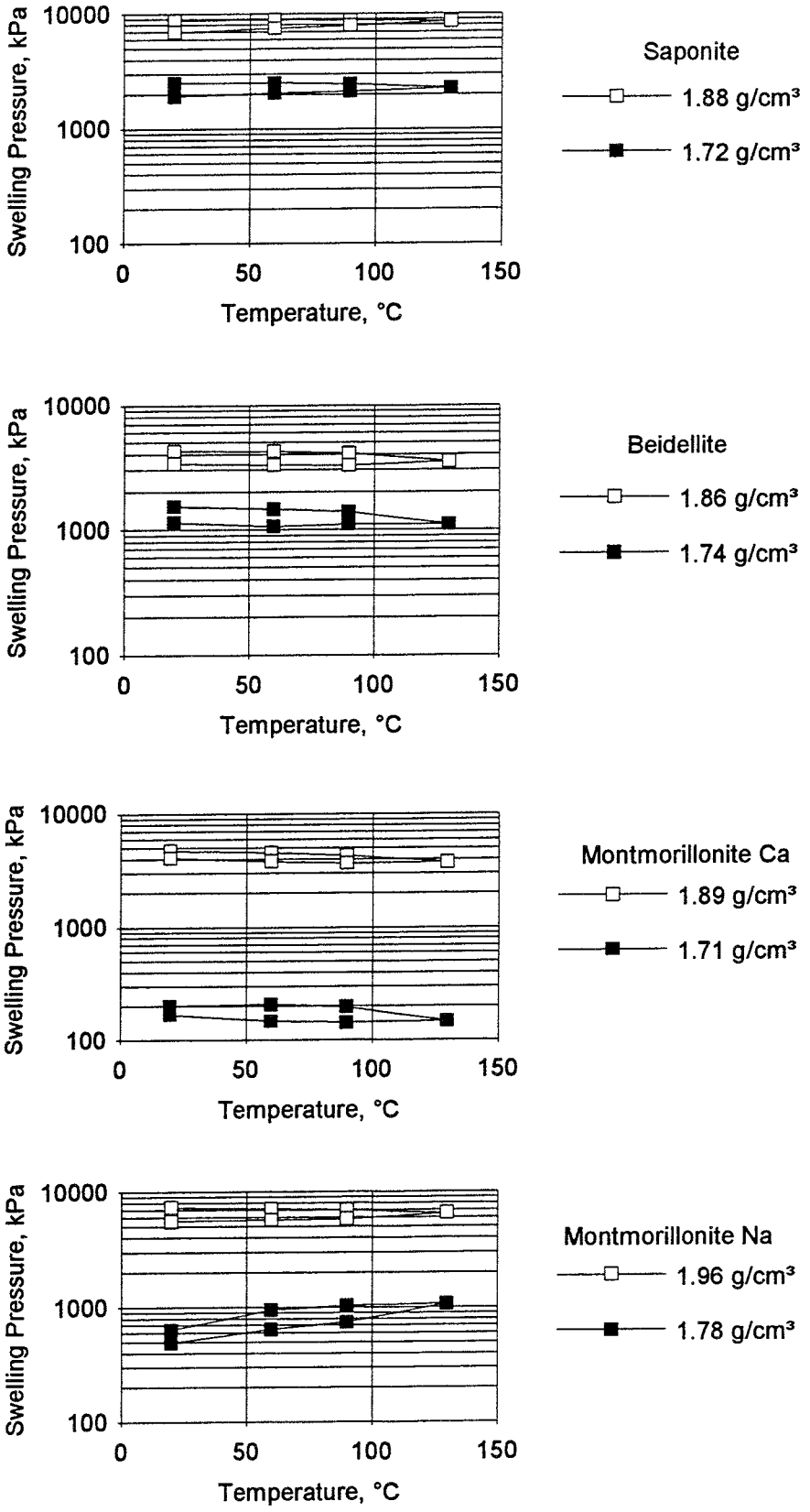

Figure 2-10. *Measured swelling pressure at different temperatures and bulk densities. From Karnland et al (1994)*

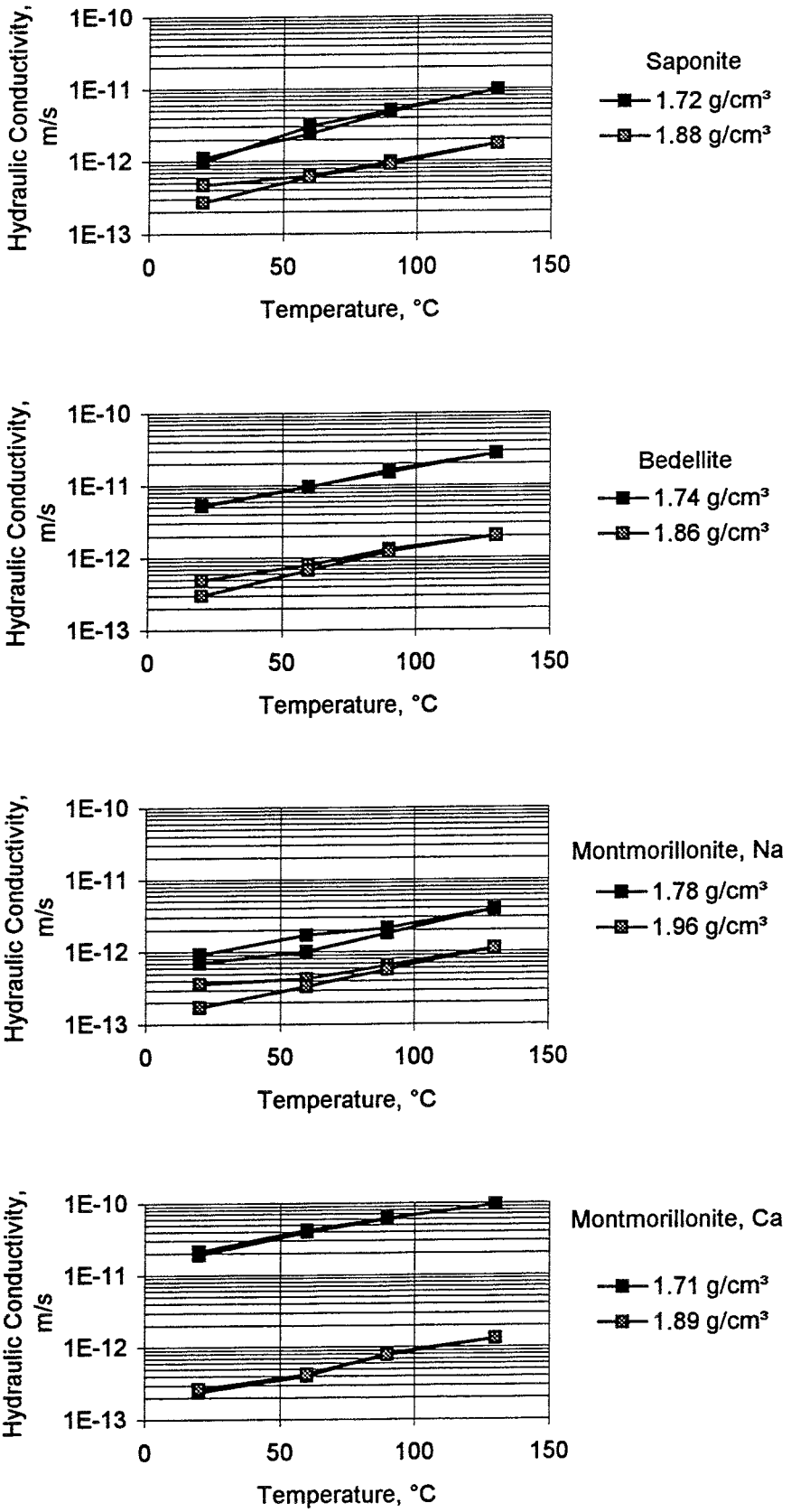

Figure 2-11. *Measured hydraulic conductivity at different temperatures and bulk densities. From Karnland et al (1994)*

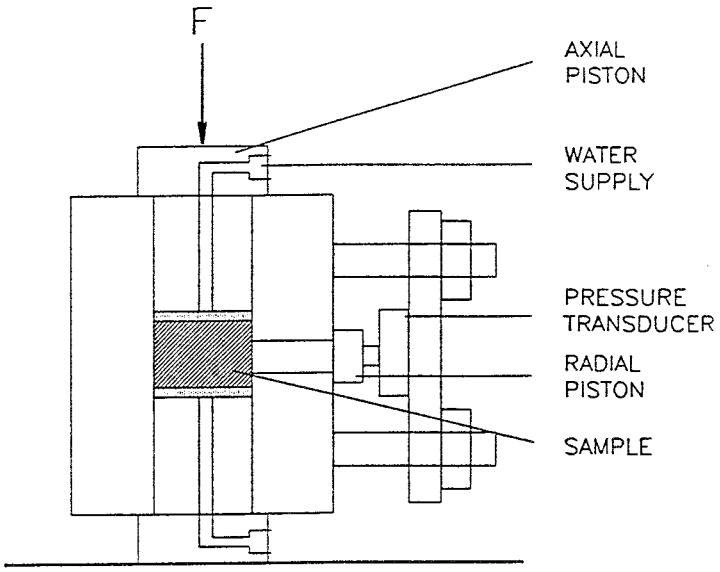

Figure 2-12. Schematic drawing of the oedometer with measurement of radial stress (Börgesson, 1990).

The samples are compacted at the natural water ratio to a certain void ratio and placed in the oedometer ring between the two axial pistons. A constant axial load corresponding to the swelling pressure is applied to the sample and water is supplied after vacuum suction of the filter stones. During the test the vertical displacement and load are measured. The load is changed stepwise. When equilibrium is reached and the sample has not deformed any more, another load step is applied.

2.4.2 Results

A series of 8 tests have been performed in the swelling/compression device. The test program is shown in Table 2-7. Seven of the test were performed with MX-80 (Na-bentonite) and one tests was made on Moosburg (Ca-bentonite). One of the tests with MX-80 was performed with 3.5% NaCl in the pore water. As shown in the table two of the tests started at an initial high void ratio (low axial pressure) and the rest of the tests at an initial low void ratio. In test KMXAR7 the device was heated to 90 °C during the test. The void ratio-pressure relations from the tests are plotted in Figure 2-13 to 2-20. The deformation-time relation of all load steps are accounted for in Appendix 3.

Table 2-7. The test program for the swelling/compression tests.

Test No.	Bentonite	Type	Water	Void ratio at start	Axial pressure at start (kPa)
KONSOL1	MX-80	Na-bent.	Distilled	4.44	28
KMXAR2	MX-80	Na-bent.	Distilled	0.66	13000
KMXAR3	MX-80	Na-bent.	Distilled	0.66	10000
KMXAR4	MX-80	Na-bent.	3.5% NaCl	2.56	40
KMXAR5	MX-80	Na-bent.	Distilled	0.66	10108
KMXAR6	MX-80	Na-bent.	Distilled	0.66	10119
KMXAR7*)	MX-80	Na-bent.	Distilled	0.65	9829
KMoos1	Moosburg	Ca-bent.	Distilled	0.63	10000

*) Performed with the sample heated to 90 °C.

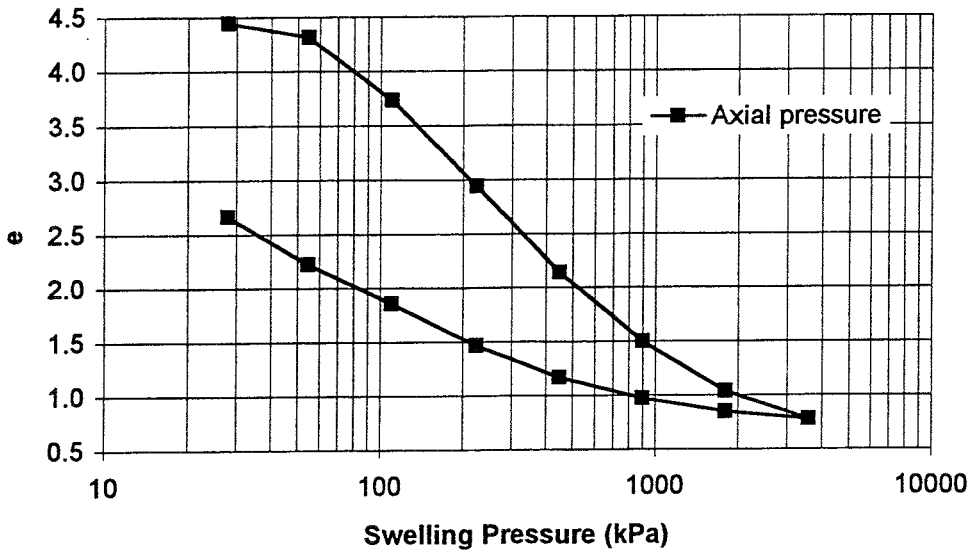

Figure 2-13. The void ratio as function of the measured axial pressure at stepwise loading and unloading of MX-80 (KONSOL1). Initial void ratio 4.44. Initial axial load 28 kPa.

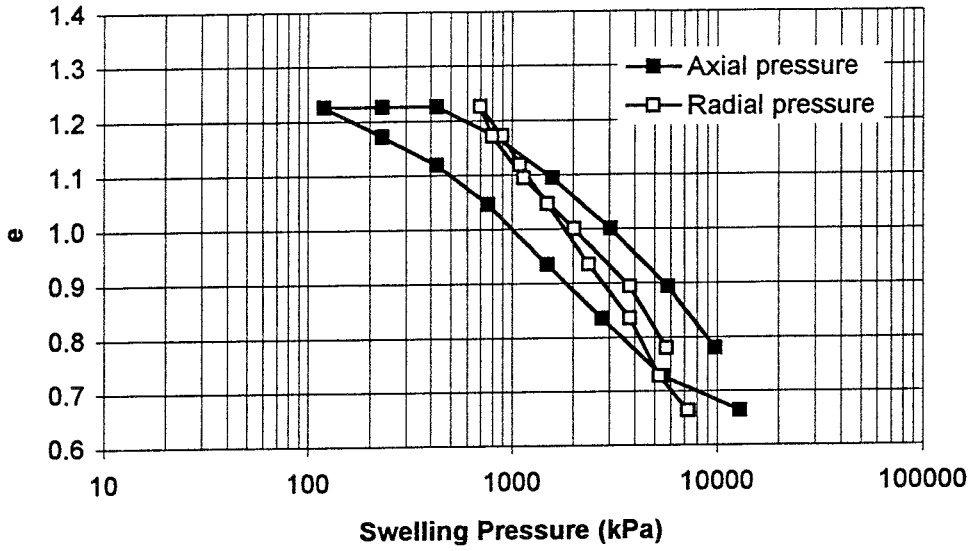

Figure 2-14. The void ratio as function of the measured axial and radial pressure at stepwise unloading and loading of MX-80 (KMXAR2). Initial void ratio 0.66. Initial axial load 13000 kPa.

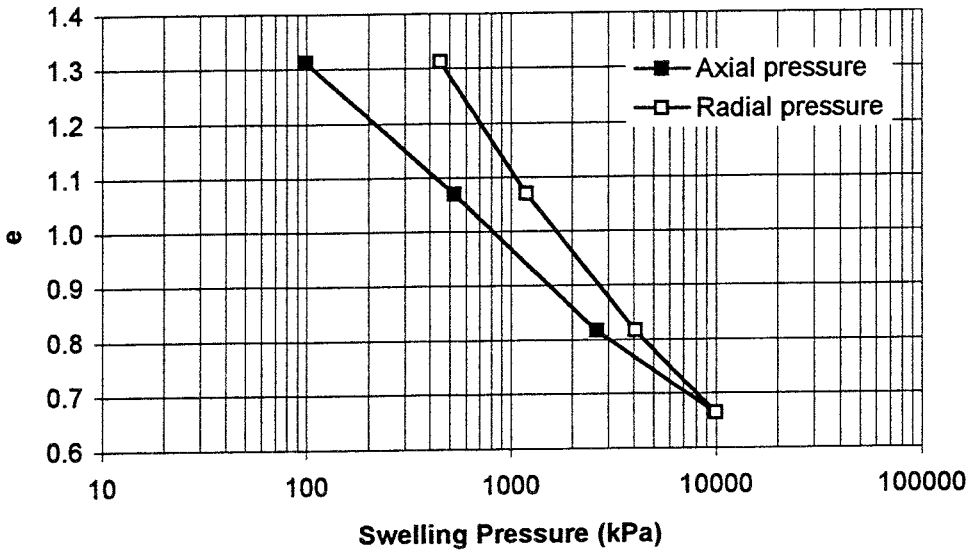

Figure 2-15. The void ratio as function of the measured axial and radial pressure at stepwise unloading of MX-80 (KMXAR3). Initial void ratio 0.66. Initial axial load 10000 kPa.

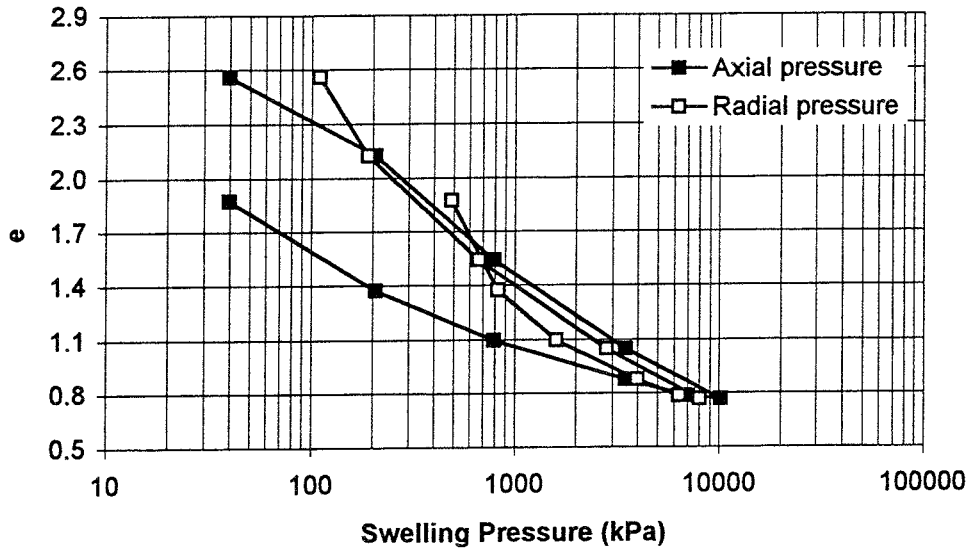

Figure 2-16. The void ratio as function of the measured axial and radial pressure at stepwise loading and unloading of MX-80 (KMXAR4). Initial void ratio 2.56. Initial axial load 40 kPa.

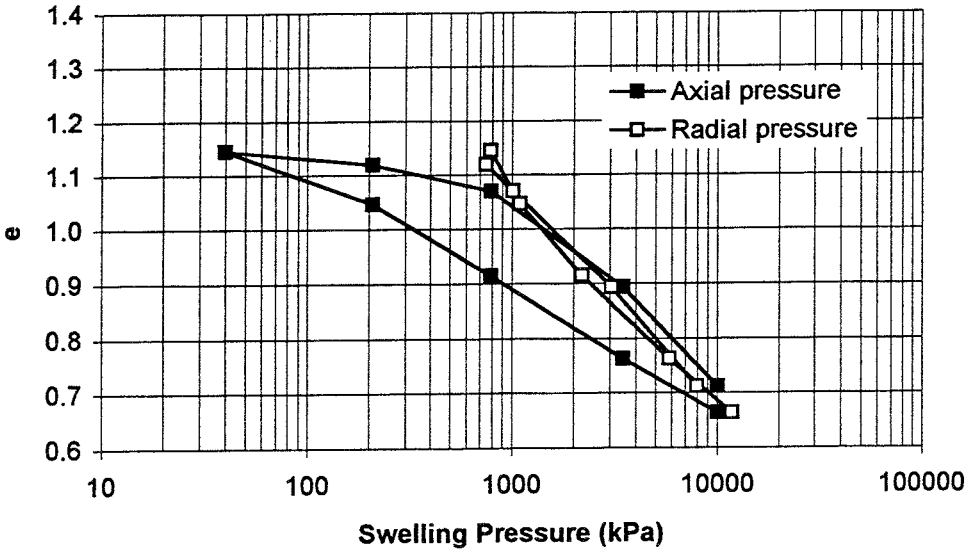

Figure 2-17. The void ratio as function of the measured axial and radial pressure at stepwise unloading and loading of MX-80 (KMXAR5). Initial void ratio 0.66. Initial axial load 10108 kPa.

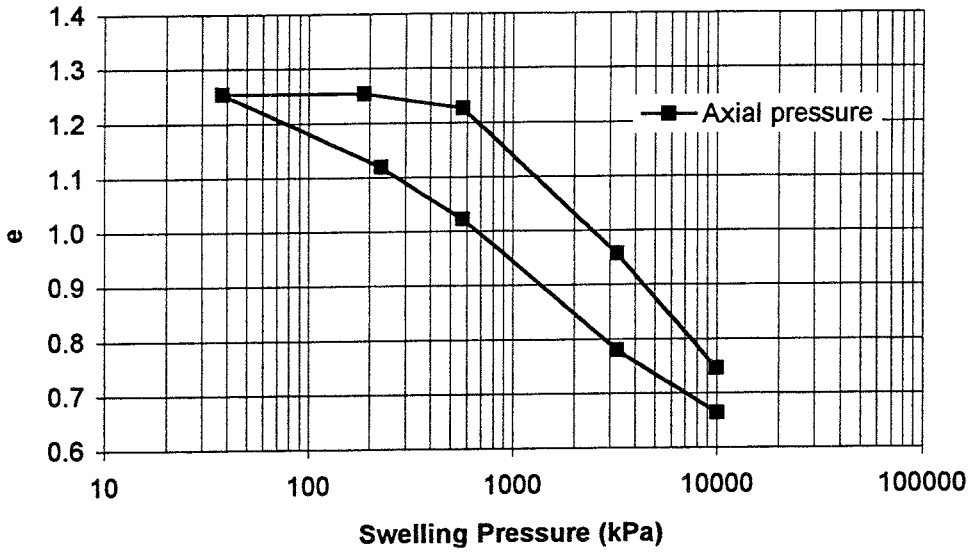

Figure 2-18. The void ratio as function of the measured axial pressure at stepwise unloading and loading of MX-80 (KMXAR6). Initial void ratio 0.66. Inital axial load 10119 kPa.

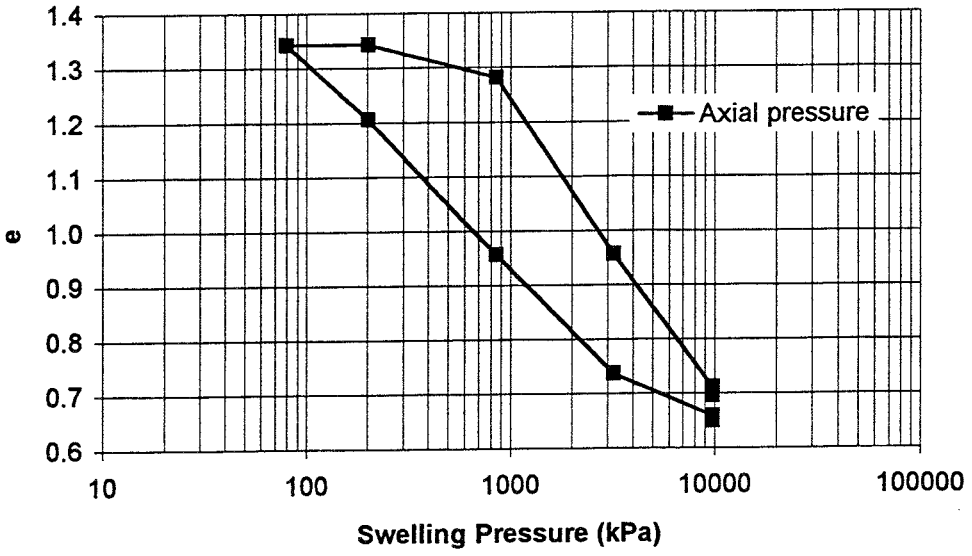

Figure 2-19. The void ratio as function of the measured axial pressure at stepwise unloading and loading of MX-80 (KMXAR7). The device was warmed up to 90 ℃ during the test. Initial void ratio 0.65. Inital axial load 9829 kPa.

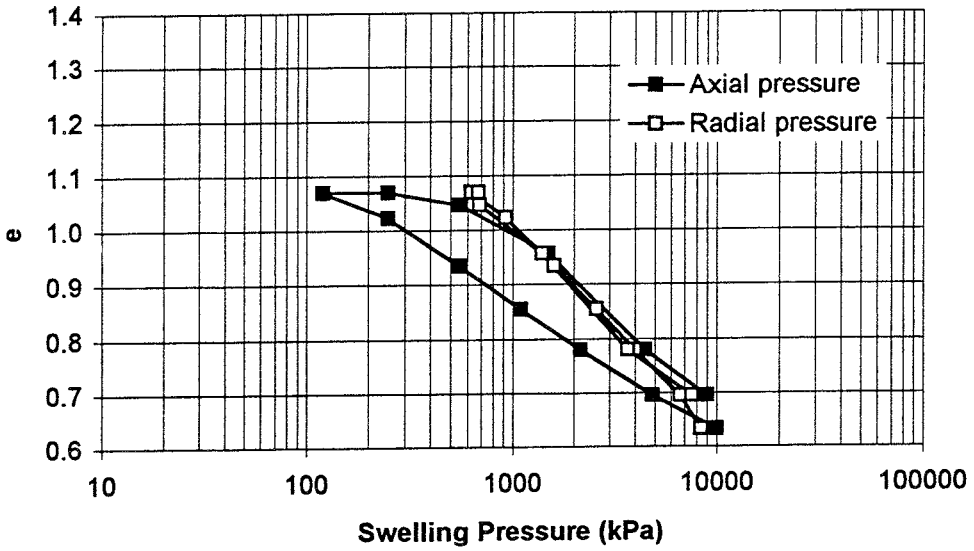

Figure 2-20. The void ratio as function of the measured axial and radial pressure at stepwise unloading and loading of Moosburg (KMoos1). Initial void ratio 0.63. Inital axial load 10000 kPa.

2.5 CREEP TESTS

The definition of creep is according to normal soil mechanics terminology a strain that will increase with time at a constant load and constant pore water pressure. The latter requirement is necessary in order to distinguish creep from consolidation. The rate of creep is thus controlled by viscosity-related deformations in the structure while consolidation is determined by the rate of the pore water flux out from a limited volume of soil.

Creep can be divided into two main processes, namely the volumetric creep and the deviatoric creep with the following symbols:

Volumetric creep strain: ε_{cv}
Volumetric creep rate: $d\varepsilon_{cv}/dt$
Deviatoric creep strain: ε_{cd}
Deviatoric creep rate: $d\varepsilon_{cd}/dt$

The deviatoric creep rate is caused by a change in deviatoric stress at constant average stress, while the volumetric creep rate is caused by a change only in average stress. They are thus evaluated from different tests.

The deviatoric creep rate has been investigated and reported (Börgesson, 1988; Börgesson et al, 1988), while the volumetric creep rate is still being investigated.

Deviatoric creep

The deviatoric behaviour is evaluated according to Singh and Mitchell (1968). The creep rate caused by a deviatoric stress decreases with time when the soil is not close to failure. Plotting the creep rate as a function of the time from start of an applied deviatoric stress shows that the creep rate versus time relation is a straight line in a double logarithmic diagram as shown in an example in Fig 2-21. The curve is defined by the following two parameters:

The inclination of the line $n=\Delta(\log t)/\Delta(d\varepsilon_{cd}/dt)$
The level of the line defined as the creep rate $d\varepsilon_{cd}/dt$ after t=10 000 sec.

The level of the line depends on the magnitude of the deviator stress which can be expressed as the ratio of the applied deviatoric stress and the deviatoric stress at failure (the degree of mobilised strength) D_r:

$$D_r=(\sigma_1-\sigma_3)/(\sigma_1-\sigma_3)_f \qquad (2\text{-}8)$$

where $(\sigma_1-\sigma_3)$ = applied deviatoric stress
$(\sigma_1-\sigma_3)_f$ = deviatoric stress at failure

D_r can thus vary between 0 and 1.0, the latter meaning failure.

Results from several creep tests in the triaxial apparatus have been reported by Börgesson et al (1988). The tests were made by applying a constant deviatoric stress on the sample in a triaxial cell with a dead load under undrained conditions. Since the sample was undrained the increase in total average stress that was achieved by the axial load was balanced by an increase in pore pressure, which resulted in that the effective average stress remained almost constant.

The original creep tests were made at $D_r>0.1$. In addition to those tests two creep tests with very low deviator stress have been made in order to evaluate the behaviour at $D_r<0.1$. The main data from the latter tests are shown in Table 2-7.

Table 2-7 Undrained triaxial creep tests at low deviatoric stress

ρ_m = density at water saturation
σ_3 = applied cell pressure (minor total principal stress)
u_i = initial pore pressure

ρ_m t/m³	σ_3 kPa	u_i kPa	$(\sigma_1-\sigma_3)$ kPa	D_r	$d\varepsilon_{cd}/dt$ (t=10^4 s) 1/s	n
1.80	1000	425	5.0	0.015	$4.5\cdot10^{-9}$	0.80
1.70	800	487	12.5	0.066	$3.3\cdot10^{-9}$	0.88

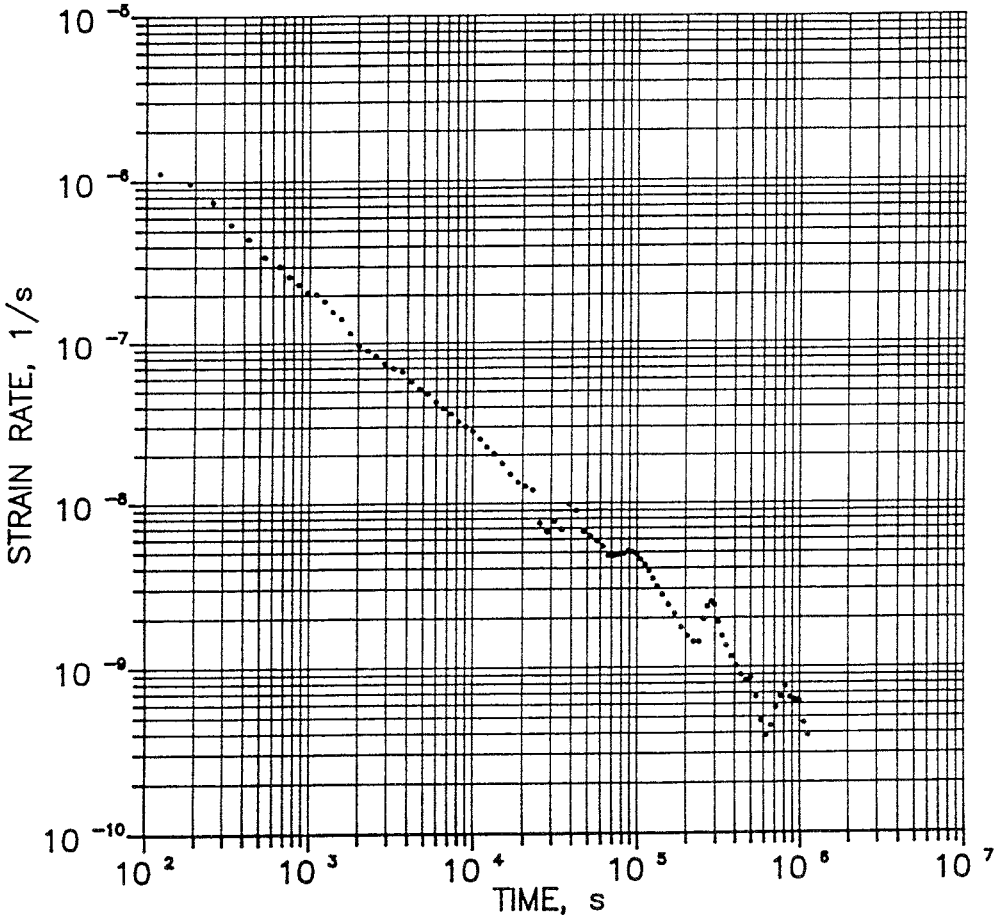

Figure 2-21. *Example of creep test on bentonite. The strain rate is plotted as a function of the time from start loading.* ρ_m*=1.99 t/m*^{3}*,* σ_3*=4.83 MPa,* u_i*=0.75 MPa,* D_f*=0.40*

Figs 2-22 and 2-23 show the creep rate versus time relations. The scatter between the measuring values (or actually calculated rate values since the creep rate is calculated from the strain-time relation) is much larger than in the previous results represented by Fig 2-21, since the load and the creep rate are much smaller.

The relation between D_r and the creep rate after 10 000 s. $d\varepsilon_{cd}/dt$ is plotted in Fig 2-24. The two new values from Table 2-7 are plotted together with older values. The figure indicates that the relation is a straight line in the semi-logarithmic diagram for values not too close to D_r=0 and D_r=1.0.

The results can be used for formulating a creep law for deviatoric creep as will be shown in chapter 3.

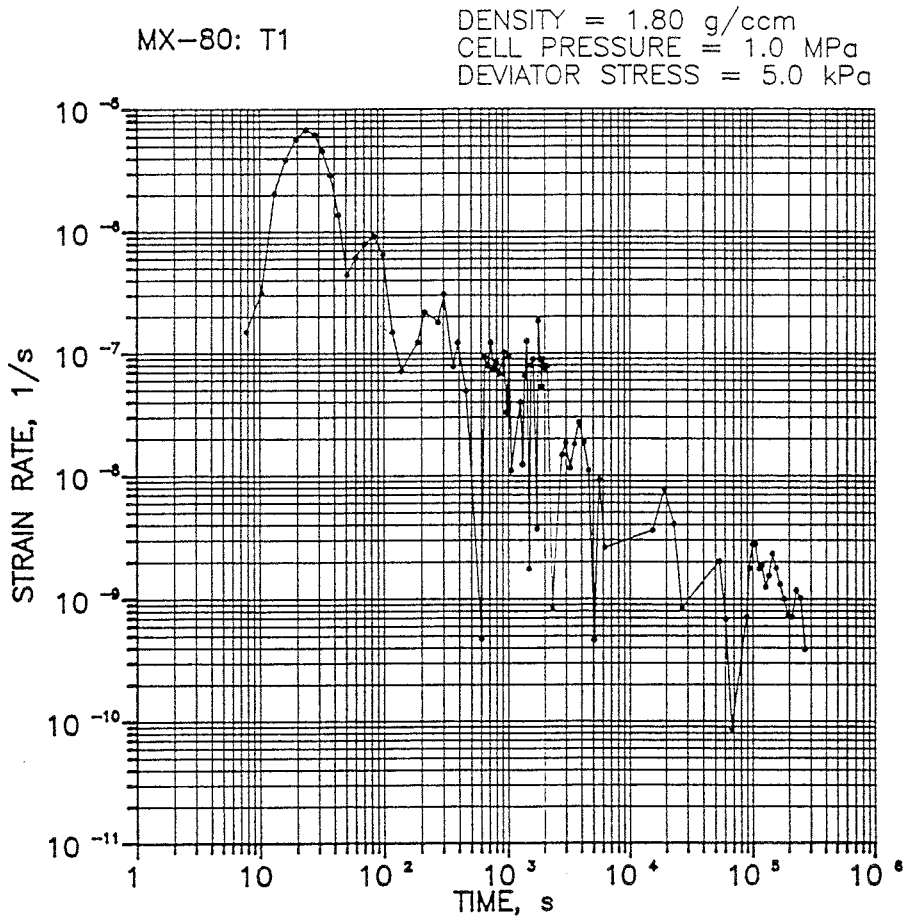

Figure 2-22. Creep test on bentonite with very low deviator stress. The strain rate is plotted as a function of the time from loading. ρ_m*=1.80t/m*^{3}

Volumetric creep

Theoretically, the volumetric creep is best evaluated from triaxial tests with increased isotropic effective stress and measured volume change with time. However, there are two difficulties in making such tests. One problem is that the tests require large samples which means that the time for consolidation until the pore pressure has dissipated is very long. The other problem is that the volume change is very difficult to measure with sufficient accuracy, partly due to the very small volume change and partly due to the risk of water leaching through the rubber membrane that separates the liquid in the cell from the sample.

For avoiding these problems the volumetric creep has instead been measured in oedometers by applying a constant vertical load on the axial piston and measure the displacement of the piston. Since the radius of the sample will be constant the displacement can be recalculated to volume change.

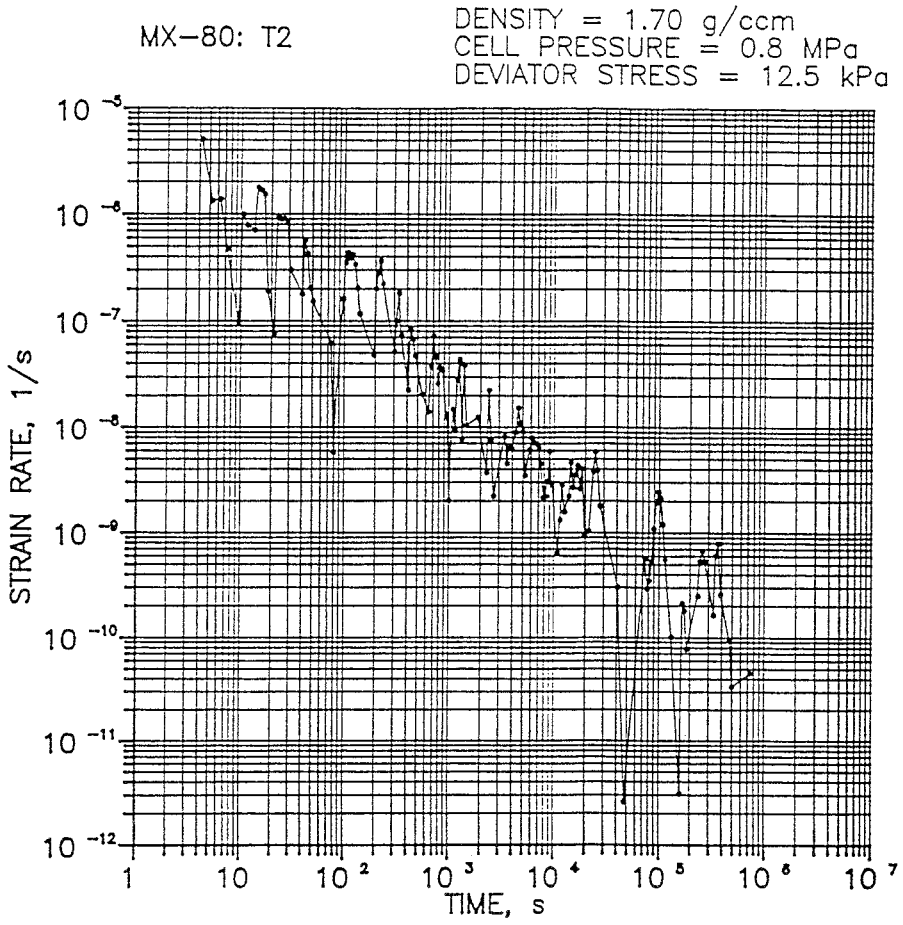

Figure 2-23. *Creep test on bentonite with very low deviator stress. The strain rate is plotted as a function of the time from loading.* ρ_m*=1.70 t/m*^{3}

The disadvantage with these tests is that the stress increase is not isotropic, which means that there is a deviatoric stress increase as well, that needs to be taken into account. The influence of the anisotropy is not known. However, only the change in average stress is affecting the change in volume according to most soil material models. This means that there will be no influence of anisotropy if the change in average stress (instead of the change in axial stress) is considered at the evaluation of the tests. This is also in agreement with the proposed models in chapters 3 and 4.

The volumetric creep tests can be made by letting the constant load at the swelling/compression tests operate for a long time after the end of the consolidation. Such tests are still running and only examples will be shown in this report. The tests accounted for in chapter 2.4 can be used for a preliminary model (see chapter 3.2.7), but the creep time is too short for doing any reliable evaluation.

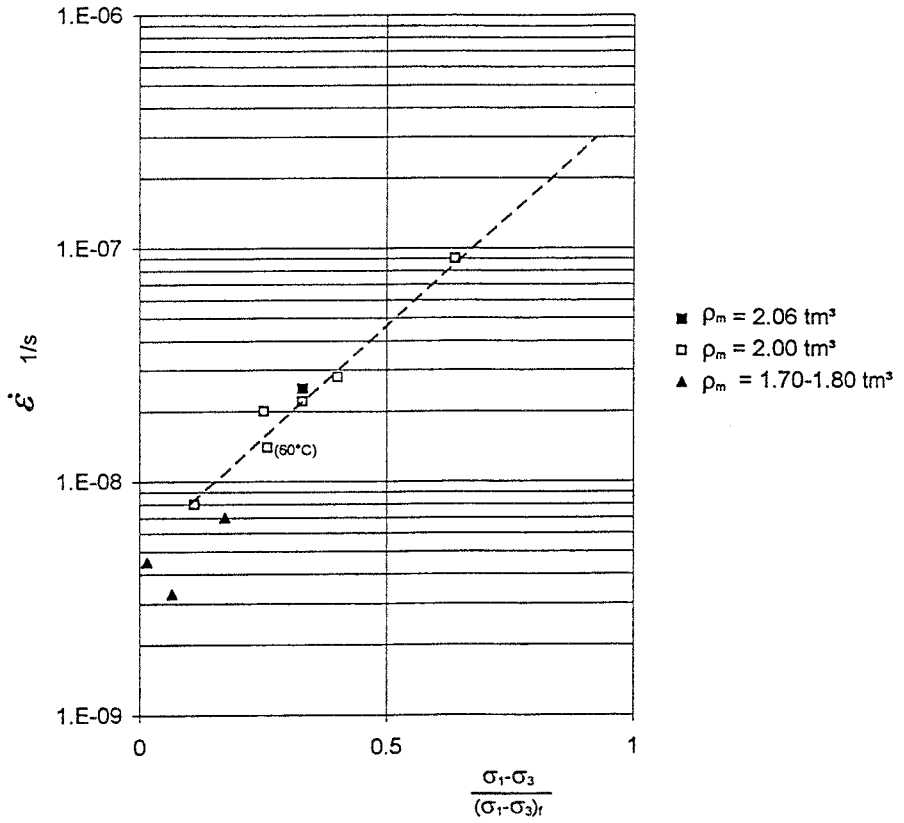

Figure 2-24. *Creep rate after 10^4 seconds ($\dot{\varepsilon}_{cdo}$ in Eqn 3-18) plotted as a function of the degree of mobilized strength D_f for all creep tests on MX-80 in the triaxial cell*

2.6 OTHER TESTS

The other tests required for determining the material model have been accounted for in other reports and will only be briefly touched upon.

Shear tests

The shear resistance, i.e. wall friction between the buffer material and adjacent materials such as the copper canister and the wall in the deposition hole are important parameters for modelling the boundary of the buffer. The tests, which are accounted for by Börgesson (1990), showed that the shear resistance was about 60% of the shear strength of the bentonite itself for tested contacts between bentonite and very smooth surfaces of the following materials:

- *Copper*
- *Stainless steel*
- *Granite rock*

The tests on the contact between bentonite and *cement* showed that the shear strength was the same as for the bentonite itself. The main reason for this

was that the there had been a chemical reaction between the clay and the cement which made the shearing take place in the unaffected bentonite.

Thermal expansion tests

These tests have also been reported by Börgesson (1990). The tests confirmed that the dominating thermo-mechanical effect is the thermal expansion of the pore water, which strongly increases the pore pressure at the same rate as the increase in temperature. The decrease in pore pressure with time after establishing constant temperature was much faster than after an increase in external load. The reason is that the volume of pore water that must leave the clay in order to make the water pressure disappear, is controlled by the compressibility of the water and not by the compressibility of the clay structure. The conclusion was that the behaviour is determined mainly by the following factors:

- The thermal expansion of the pore water α_w
- The compressibility of the pore water B_w
- The degree of saturation S_r

The degree of saturation must be exactly 100% if standard values of α_w and B_w are used since even very little air will strongly affect the compressibility.

Thermal conductivity tests

Measurements of the thermal conductivity of saturated and unsaturated buffer materials have been reported by Börgesson et al (1994). Most of the tests were made on unsaturated bentonite samples at different densities. Back-calculation of some field tests were made as well.

The results from measurements of the thermal conductivity at a degree of saturation higher than 90% are plotted as a function of the void ratio in Fig 2-25. The figure shows that there is some influence of the void ratio but it is smaller than expected (Börgesson, 1994). The average thermal conductivity for the void ratio e=0.7, representing the conditions after water saturation, is λ=1.25 W/m,K.

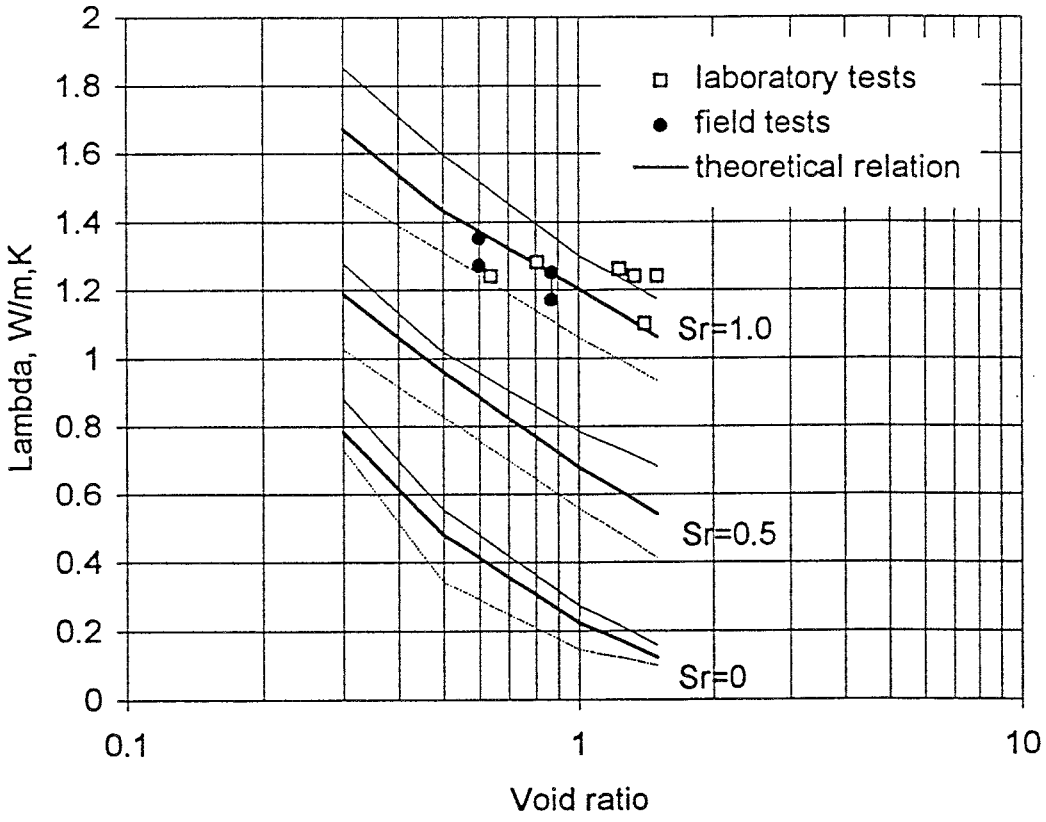

Figure 2-25. *Measured thermal conductivity of bentonite MX-80 with a degree of saturation higher than 90% as a function of the void ratio.*

3 TENTATIVE MATERIAL MODEL

3.1 GENERAL

A general material model for water saturated buffer materials should cover a large range of pressures, void ratios, temperatures, and materials. The model presented in this chapter is very general and it is called tentative because it represents the best knowledge of today and has not yet been coded in all details for use in finite element calculations. A material model should also be tested and verified in different calculations that can be compared with measurements. Only the coded parts can of course be tested and this has been made as will be shown in chapter 5.

Some parts of the model are still somewhat unclear due to test problems and a complex behaviour. This concerns mainly the difference between the elastic and plastic displacements, volumetric as well as deviatoric. The problems are also related to the fact that the model (as all existing models) is simplified with a a too distinct limit between the elastic and plastic parts and a too large elastic zone. In spite of this, the model is considered to be good enough for describing the buffer mass behaviour in a KBS3-repository.

3.2 CLAY-TECH MODEL

3.2.1 General

The model has been successively developed starting with a Total Stress Model that does not take the pore pressure into account. After receiving evidence that the effective stress theory is valid also for dense smectite clay (Graham et al, 1992; Börgesson et al, 1990), a much more general model based on Effective Stress Porous Elasticity and Drucker Prager Plasticity was established. The main concept of the latest model, called the Claytech Model, is based on the earlier models but some important changes and additions have been made.

The model applies the effective stress theory and all stresses mentioned refer to effective stresses. The model is an elastic-plastic model and differs very distinctly between elastic, completely recoverable strains and plastic non-recoverable strains. Another important distinction is the difference between volumetric strain and deviatoric strain

- elastic volumetric strain ε_{el}^{v} determines the volumetric behaviour which is related to the average stress $p = (\sigma_1 + \sigma_2 + \sigma_3)/3$

- elastic deviatoric strain ε_{el}^{d} or the strain that occurs without any volume change determines the deviatoric behaviour which is related to the deviatoric stress $D = \sigma_1 - \sigma_3$

The deviatoric stress is more generally expressed with von Mises' stress that takes the middle principal stress σ_2 into account:

$$\sigma_j = (((\sigma_1 - \sigma_3)^2 + (\sigma_1 - \sigma_2)^2 + (\sigma_2 - \sigma_3)^2)/2)^{1/2} \quad (3\text{-}1)$$

If $\sigma_2 = \sigma_3$ Mises stress is equal to the deviatoric stress ($\sigma_j = D$)

The model, which covers the thermo-hydro-mechanical behaviour of water saturated buffer materials, is built by a number of submodels. They are the following:

Mechanical models of the clay structure

- Elastic Volumetric Model which determines the elastic volume strain at a change in average stress.
- Elastic Deviatoric Model which determines the elastic deviatoric strain at a change in deviatoric stress.
- Plastic Model which determines the plastic volumetric and deviatoric stress-strain behaviour (including the strength)

Modelling of water flux

- Darcy's law with the hydraulic conductivity as the main property

Modelling of thermal flux

- Fourier's law with the thermal conductivity as the main property

Properties of the water and particle phases

- Elastic properties of the pore water and the clay particles
- Thermal expansion properties of the pore water and the clay particles

Hydro-mechanical coupling between the two phases and the structure

- Effective stress model

Creep

- Deviatoric creep
- Volumetric creep

Contact properties

Properties of the contact zone between the buffer and surrounding materials.

Influencing factors

The model also includes the effect of different factors on the parameters in the submodels. These factors are:

- rate of strain
- temperature
- pore water composition
- clay mineral composition

Reference model

The model presented in this chapter is the reference model which means that it concerns the reference material under the following "reference" conditions:

- temperature: 20 °C
- pore water composition: distilled water added to the natural water in the bentonite
- bentonite type: Na-bentonite MX-80

3.2.2 Mechanical models of the clay structure

General

It is important to distinguish between the elastic and plastic behaviour, both regarding the volumetric strain and the deviatoric strain. In an elastic-plastic model the plastic strain superimposes the elastic strain in the following way (considering the so called engineering strain):

$$\varepsilon^{v}_{tot}=\varepsilon^{v}_{el}+\varepsilon^{v}_{pl} \quad (3\text{-}2)$$

$$\varepsilon^{d}_{tot}=\varepsilon^{d}_{el}+\varepsilon^{d}_{pl} \quad (3\text{-}3)$$

where
ε^{v}_{tot} = total volumetric strain
ε^{v}_{el} = elastic volumetric strain
ε^{v}_{pl} = plastic volumetric strain
ε^{d}_{tot} = total deviatoric strain
ε^{d}_{el} = elastic deviatoric strain
ε^{d}_{pl} = plastic deviatoric strain

At unloading and reloading $\varepsilon^{v}_{pl}= \varepsilon^{d}_{pl}=0$

Elastic Volumetric Model

It is difficult to distinguish between the elastic and plastic behaviour of swelling clays like bentonites, since at deloading the swelling ability makes the clay recover most of the compression. The plastic part of the volumetric strain is thus quite small, which was the reason for using Drucker-Prager for the earlier model, since it has no share of plastic compression at isotropic compression (no cap).

The relation between the measured swelling pressure and the void ratio can be used as a measure of the swelling/compression properties. Fig 3-1 shows a collection of measured swelling pressure data plotted as a function of the void ratio. The swelling pressure has been measured by use of the swelling pressure oedometer but also the results from the equilibrium state in the triaxial cell before start of the test have been used.

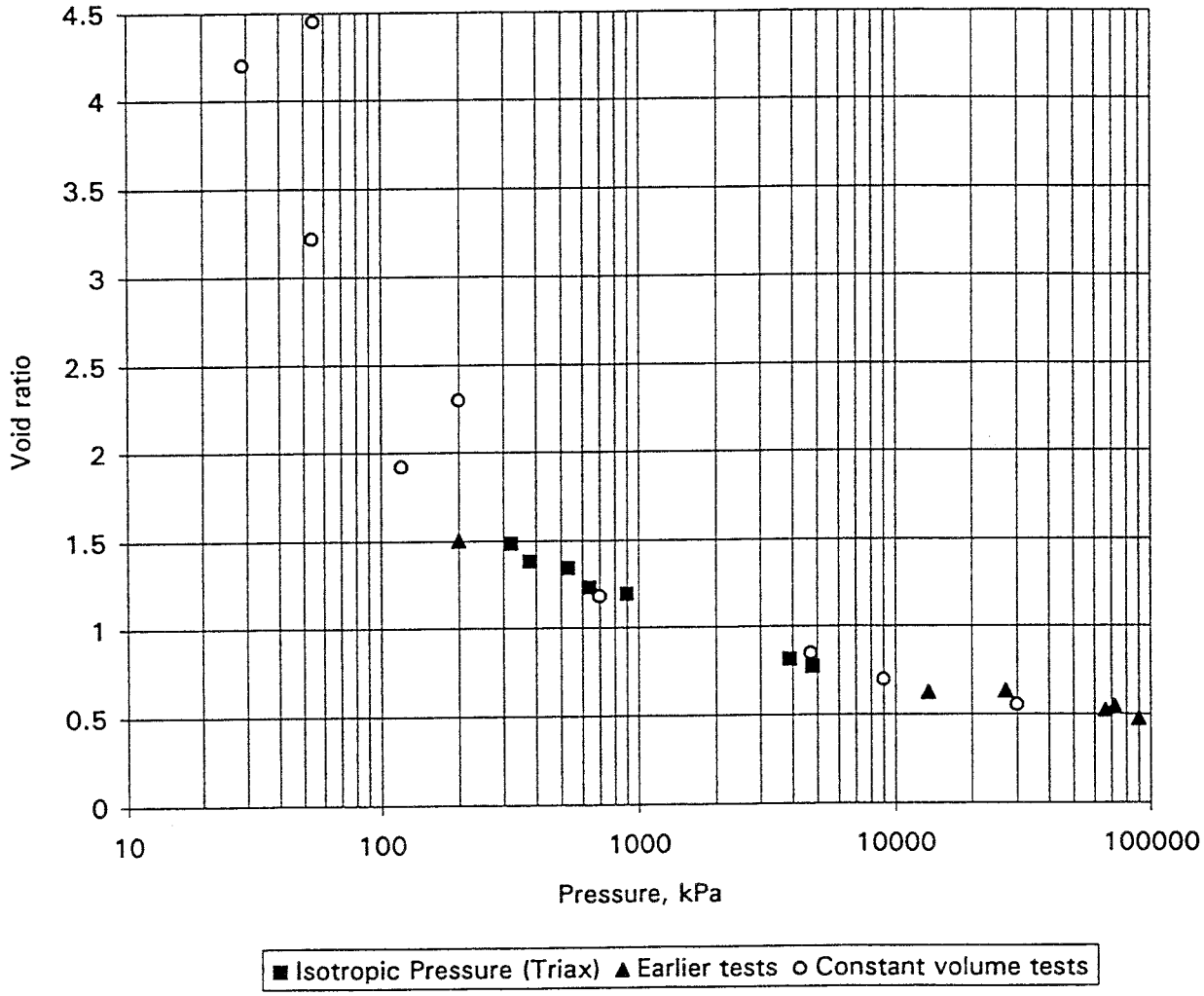

Figure 3-1. Measured relation between swelling pressure and void ratio for MX-80

The compression and expansion of an elastic-plastic soil can be described as in Fig 3-2, which shows the change in void ratio as a function of the average stress. The consolidation follows the "virgin line" A-B at isotropic compression. At deloading from B to C pure elastic expansion takes place followed by the same elastic compression at reloading from C to D. The decrease in void ratio e_A-e_B at an increase in stress from p_A to p_B is thus composed by a plastic void ratio decrease e_A-e_C and an elastic decrease e_C-e_B.

The elastic part of the model includes thus the deformation at un- and reloading B-C-D, while the plastic part is the remaining volumetric strain from the virgin line. The question is thus whether the relation shown in Fig 3-1 represents the virgin line or the pure elastic path at unloading. The samples used for the swelling pressure measurements have usually been compacted under dry conditions at different loads, and then unloaded before being water saturated. Some of them have been compacted directly in the swelling pressure oedometer, while some were compacted in a cylinder and then emplaced in the oedometer. The elastic swelling that takes place after compaction when the samples are released varied between 4% and 10% (Johannesson, et al). The swelling to fill up the swelling pressure oedometer at water saturation varied between 0% and 10%. This means that the samples swelled between 4% and up to 20% before tested. The values in Fig 3-1 should thus be located below the virgin line.

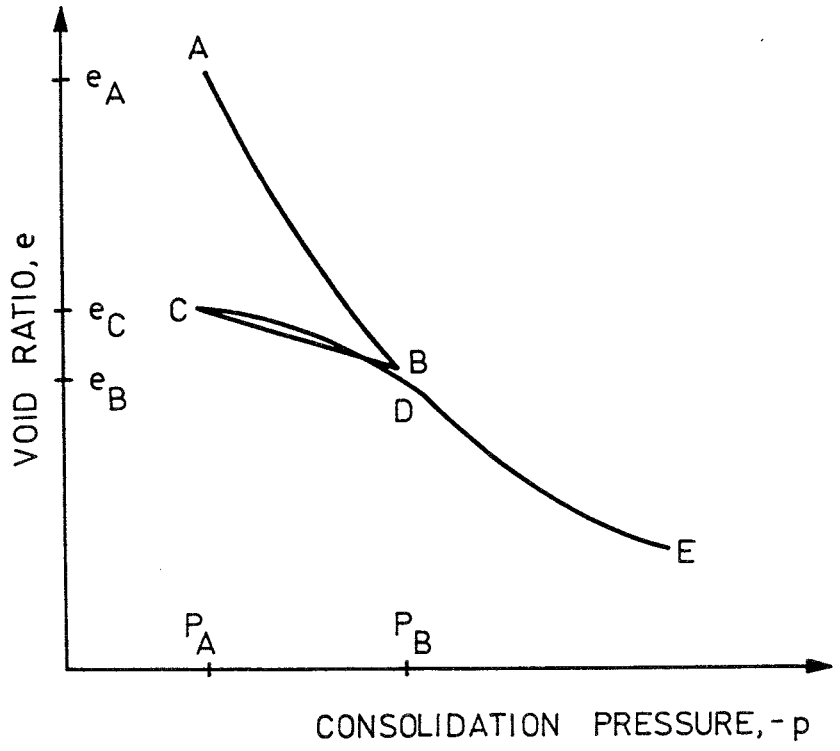

Figure 3-2. Illustration of the volumetric/elastic plastic behaviour of soils.

The results from the swelling/compression tests accounted for in chapter 2-4 can be used for evaluating the difference between the plastic and elastic compression. Fig 3-3 shows the average stress (calculated as $p=(\sigma_a+2\sigma_r)/3$) at three swelling/compression tests and one compression/swelling test. The relation in Fig 3-1 is also indicated in this figure. The virgin compression path represented by the loading curve from the compression/swelling test is as expected situated above the swelling pressure relation from Fig 3-1. However the unloading and reloading paths are very close to the relation in Fig 3-1, which indicates that this relation represents the elastic volumetric behaviour of the clay.

There are several uncertainties related to this relation. The main ones are the following:

- The tests were not made under isotropic conditions
- The measurements of the radial pressure in the oedometers were made at one spot in the centre of the sample surface, which means that it may differ from the average value
- There may be some friction between the sample and the oedometer ring which has not been considered

These uncertainties are probably part of the reason for the scatter in some results.

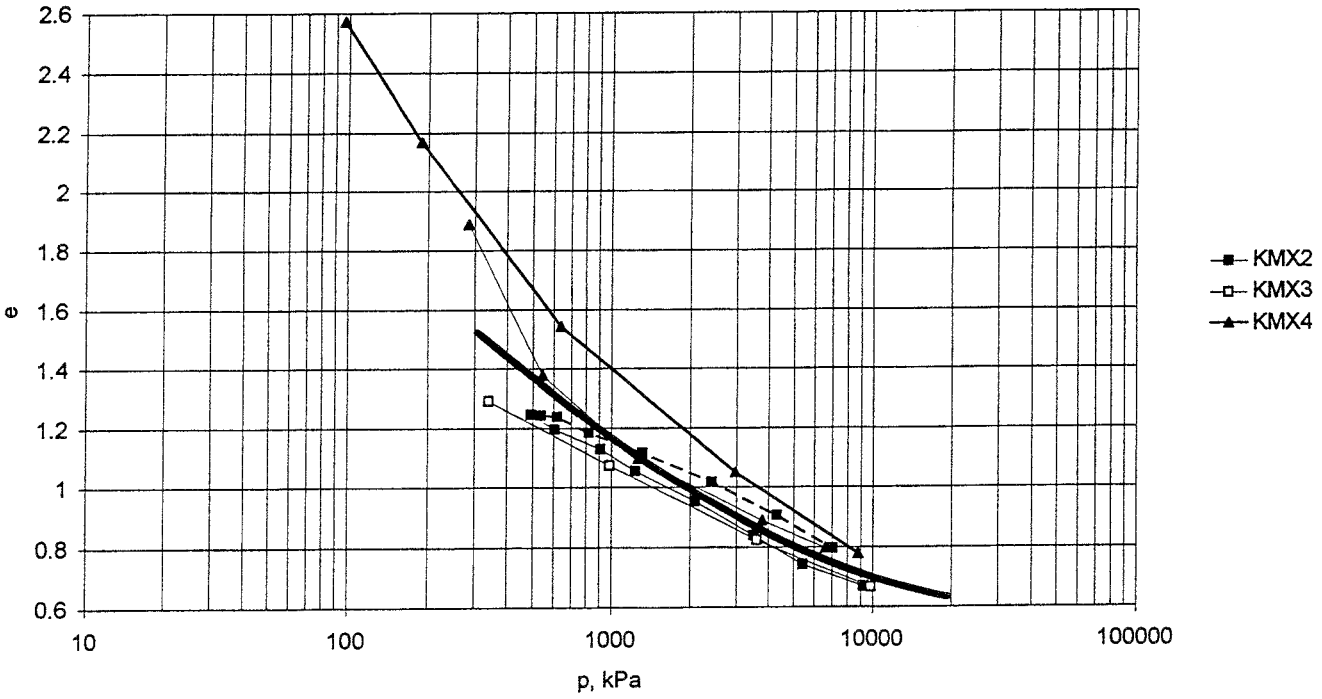

Figure 3-3. *The average stress as a function of the void ratio at expansion/ compression tests (KMX2, KMX3) and one compression/expansion test (KMX4) The thick line represents the measured swelling pressures (Fig 3-1)*

The p-e relation is not a straight line in a e-log$p$ diagram over the large range of pressure shown in Fig 3-1. In Fig 3-4 the relation is plotted in a double logarithmic diagram which yields almost a straight line although it deviates at very high void ratios. A fairly good representation is achieved with Eqn 3-4.

$$e = e_0 \cdot \left(\frac{p}{p_0}\right)^{\beta} \tag{3-4}$$

where

$$\beta = \Delta(\ln e) / \Delta(\ln p) \tag{3-5}$$

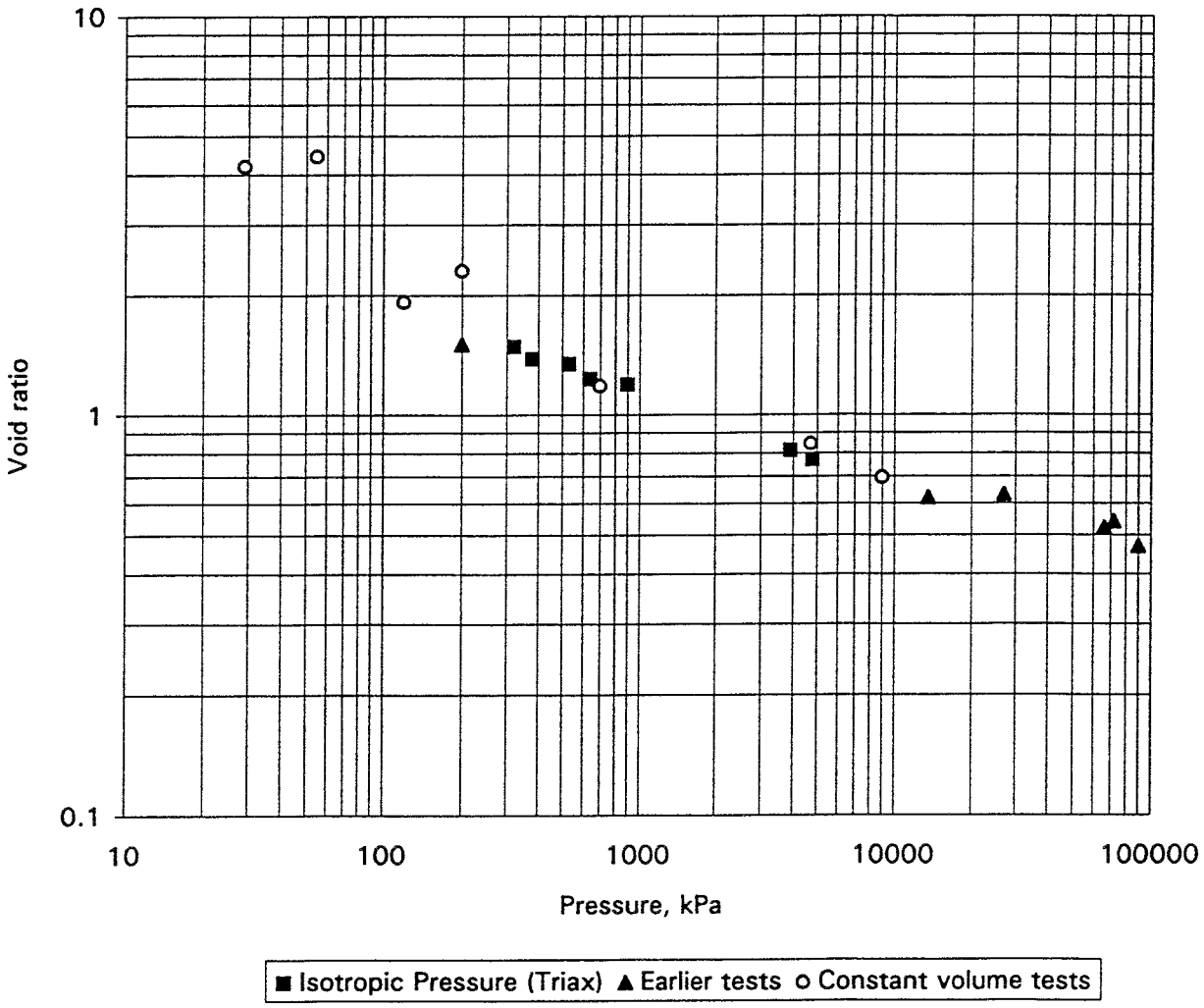

Figure 3-4. Measured relation between swelling pressure and void ratio for MX-80 plotted in a double-logarithmic diagram.

$1/\beta$ corresponds thus to the bulk modulus in a double logarithmic scale with the change in void ratio instead of volumetric strain.

Eqn 3-4 is valid for $0.5<e<1.5$ with the following parameter values:

$\beta = 0.187$
$e_0 = 1.0$
$p_0 = 2000$ kPa

The volumetric elastic behaviour of MX-80 can thus be modelled with Eqn 3-4 and the given parameter values for $0.5<e<1.5$.

Elastic Deviatoric Model

The elastic strain caused by a deviatoric stress change under constant volume can be studied by performing undrained triaxial tests. Fig 3-5 shows two examples with IBECO Na-bentonite, which has mechanical properties that are very similar to those of MX-80. The figure shows two major facts:

1. A positive pore pressure is generated at the same rate as the increase in applied major stress σ_1, which makes the average effective stress about constant during the tests.

2. The shape of the stress-strain curve (deviatoric stress versus axial strain) is almost the same if the deviator stress is normalised (divided by the deviator stress at failure).

This behaviour is common to all studied bentonite types (see chapter 2.2). The following generalised stress strain behaviour can thus be defined:

$$\varepsilon^d_{el} = f(D/D_f) \qquad (3\text{-}7)$$

where

D = deviatoric stress
D_f = deviatoric stress at failure
f = generalised function

or if Mises stresses are used

$$\varepsilon^d_{el} = f(q/q_f) \qquad (3\text{-}8)$$

where

q = Mises' stress
q_f = Mises' stress at failure

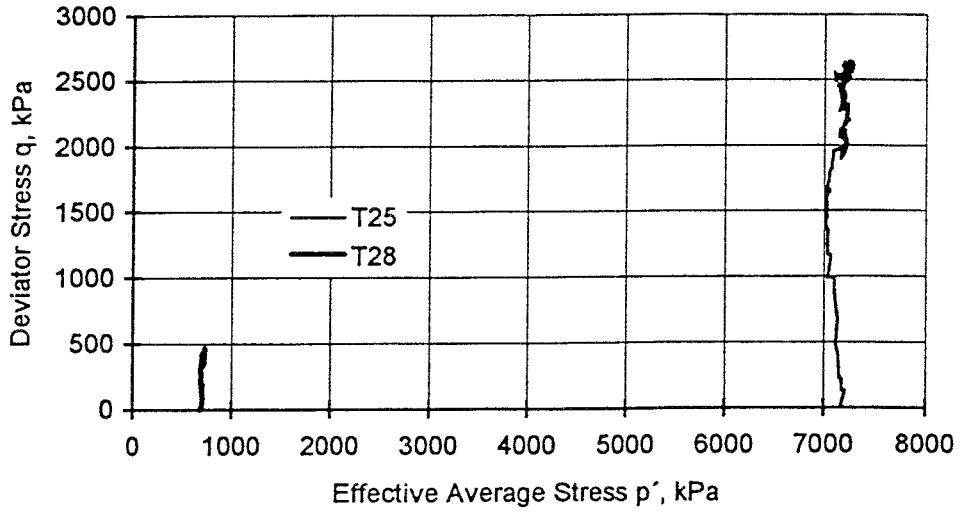

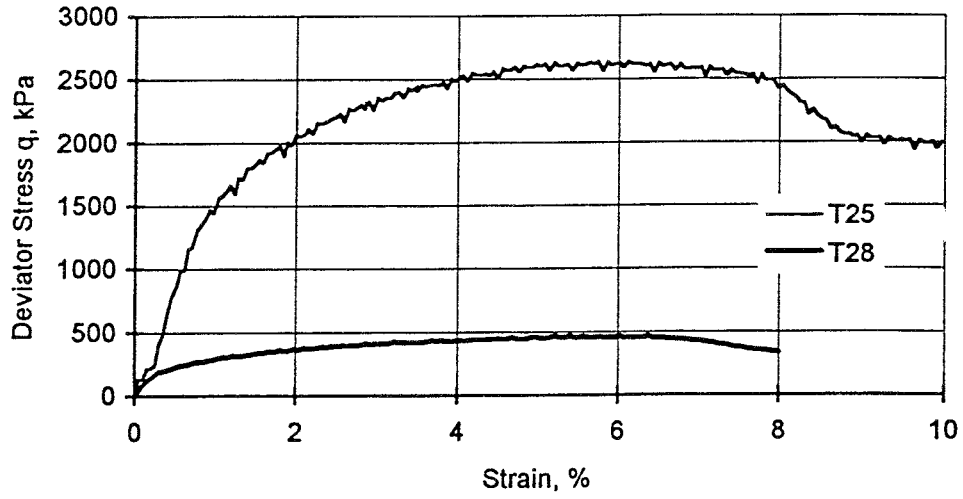

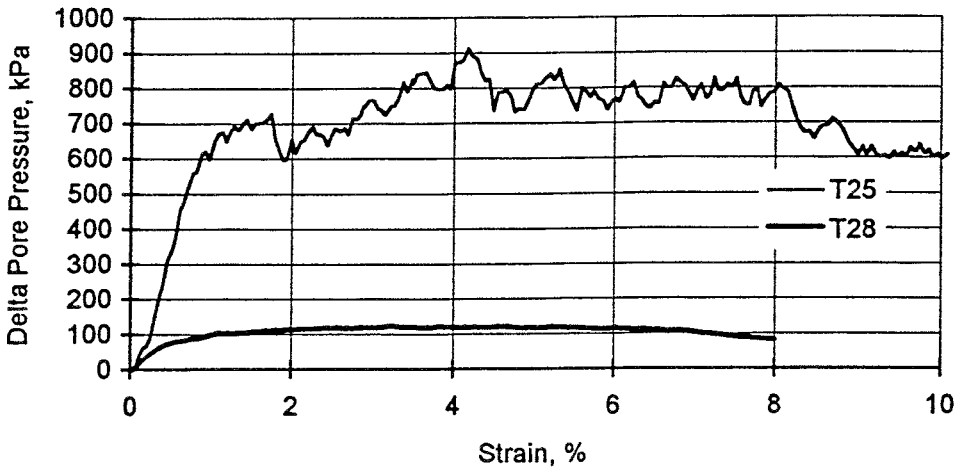

Figure 3-5. *Results from two undrained triaxial tests on Ibeco Na-bentonite*

The function f is usually determined by Poisson's ratio ν. The shape of the function (Fig 3-5) indicates that ν is constant until half the failure stress and then changes with increasing stress. The non-linearity is received by letting Poisson's ratio ν vary with the degree of mobilised friction, which can be expressed by the relation between the applied Mises' stress q and the Mises' stress at failure $q_f(p)$ at the same average stress p. The relation is suggested to be according to Eqns 3-9 and 3-10.

$$\nu = \nu_0 \qquad \text{at} \quad q/q_f \leq \eta \qquad (3\text{-}9)$$

$$\nu = \nu_0 + \frac{q/q_f - \eta}{1-\eta} \cdot (\nu_{max} - \nu_0) \qquad \text{at} \quad q/q_f > \eta \qquad (3\text{-}10)$$

where ν_0 = basic value of Poisson's ratio
ν_{max} = maximum value of Poisson's' ratio
η = ratio of q/q_f below which ν is constant ($=\nu_0$)

Poisson's' ratio is thus constant at $q/q_f \leq \eta$ and varies between ν_0 and ν_{max} in proportion to the excess degree of mobilised friction at $q/q_f > \eta$. The ultimate case

$\nu_0 = 0$
$\nu_{max} = 0.5$
$\eta = 0$

is a nice approximation of Poisson's ratio at the first loading (see chapter 5) but not at unloading or reloading. The choice of parameters in Eqns 3-9 and 3-10 must thus be made with reference to the loading conditions. $\nu_{max}=0.5$ gives a very smooth transition to plastic behaviour at the ultimate Mises' stress.

Since different stress-strain curves represent loading and unloading there must be some plastization much earlier (deviatoric plastic strain) than predicted by this model or any other common soil model. This effect can be modelled by applying different values of the constants in Eqn 3-10.

Plastic model

The plastic model must define

- the boundaries of the elastic zone in the stress space (the yield surface)
- the boundaries of the plastic zone (the failure surface)
- the volumetric behaviour of the plastic zone (the flow surface (plastic potential) and the flow rules)

The following special requirements for the plastic model is desirable:

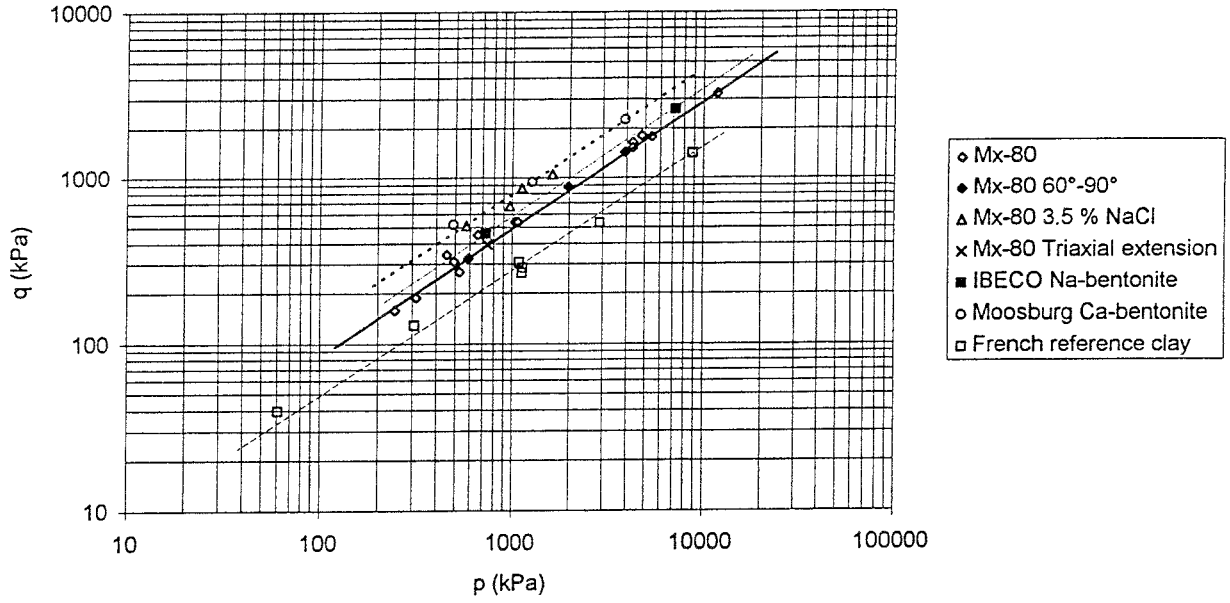

Figure 3-6. *Compilation of a large number of failure stress states determined in triaxial tests with different techniques, bentonite types, temperatures, and pore water composition.*

- The failure surface should be shaped so that no cohesion intercept is required. Fig 3-6 shows that the failure envelope may be drawn as a straight line in a log-log diagram over a large range of stresses for several types of bentonites and conditions. A model of the failure envelope of the following form will thus yield the desired relation between the average effective stress p and the Mises' stress q:

$$q=ap^b$$

- There should be a cap that limits the elastic part in the p-direction in order to make the model more general and to consider the hysteresis at compression and swelling
- A post-failure reduction in strength (strain-softening) is also desired.
- There should be a small dilation at failure in accordance with the measurements

Yield, failure, and flow surfaces

The laboratory testing and the modelling have formed the basis of a general material model. The model is described in Figs 3-7 and 3-8. It is based on the theory of plasticity (see e.g. Chen & Mizuno, 1990 and Schofield and Wroth, 1968). Fig 3-7 shows the yield and failure surfaces in the q-p plane as well as the flow surface. The behaviour in the q-p plane is controlled by two lines that limit the allowable Mises' stress q:

$$q=ap^b \quad (3\text{-}11)$$
$$q=cp^b \quad (3\text{-}12)$$

where $a>c$

The upper line (Eqn 3-11) is a combined yield and failure surface (1) in the over-consolidated state (dry side) while the lower line (Eqn 3-12) is the failure surface (4) on the normally consolidated side (wet side) corresponding to the critical state line of the Cam Clay model (Schofield and Wroth, 1968). The lower line is also the top point of the yield surface at all states. The other parts of the yield surface are the elliptic cap (3) which intersects the p-axis at p_b and an elliptic transition surface between the other two parts (2).

The plastic volumetric behaviour at the yield surface is controlled by the flow surface (plastic potential), which is also shown in Fig 3-7. The flow surface consists of two ellipses. One ellipse for parts 1 and 2, where the flow is not associated since the tangent of the flow surface does not coincide with the tangent of the yield surface, and one for the cap (3), which coincides with the cap and where the flow is thus associated. By letting the ellipse at 1 and 2 be large, the inclination of the flow surface and thus the dilatancy can be made small.

The behaviour of a material modelled in this way resembles the Cam-Clay model but differs in some vital parts. The behaviour is illustrated in Fig 3-8, where the stress strain behaviour (q-ε) and the change in location of the yield and failure surfaces are shown for two stress paths. The upper stress path from A to B shows the behaviour on the wet side. The stress path at first goes in the elastic region. When the stress path intersects the cap, the material starts to plasticize, decrease in volume, and move the cap upwards with the top following the lower failure line. The other stress path from C to D shows the behaviour in the over-consolidated dry part. The stress path is located entirely in the elastic domain and remains so until it intersects the combined failure and yield surface, where the material starts to yield and increase in volume. The volume increase makes the cap of the yield surface shrink at constant q until the transition surface has reached the point D. At this point we have a new yield surface, which is illustrated by broken lines in the figure. If the strain is further increased, q will decrease and the cap will be further reduced until the top part hits point E on the "critical state line", where no further change in q or volume will take place.

The following three additional parameters are required for the definition of the cap plasticity.

p_b = intersection of the cap with the p-axis
p_f = intersection of the elliptic non-associated flow surface on the dry side with the p-axis (flow surface 1 and 2)
γ = ratio of the two axis in the elliptic transition surface (yield surface 2)
R = ratio of the two axis in the elliptic cap (yield surface 3)

Yield surface

1 Shear failure surface
$q = ap^b$
2 Transition surface (elliptic)
3 Cap (elliptic)

Failure surface

1 Shear failure surface
$q = ap^b$
2 Transition surface (elliptic)
4 Shear failure surface
(Critical state line)
$q = cp^b$
$a > c$

Yield and failure surfaces

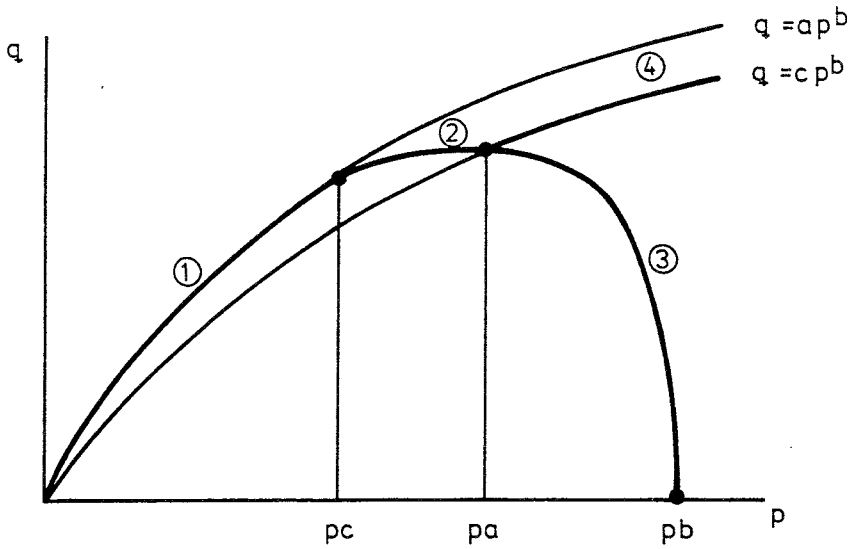

Flow surface

1, 2 elliptic non associated
3 elliptic associated

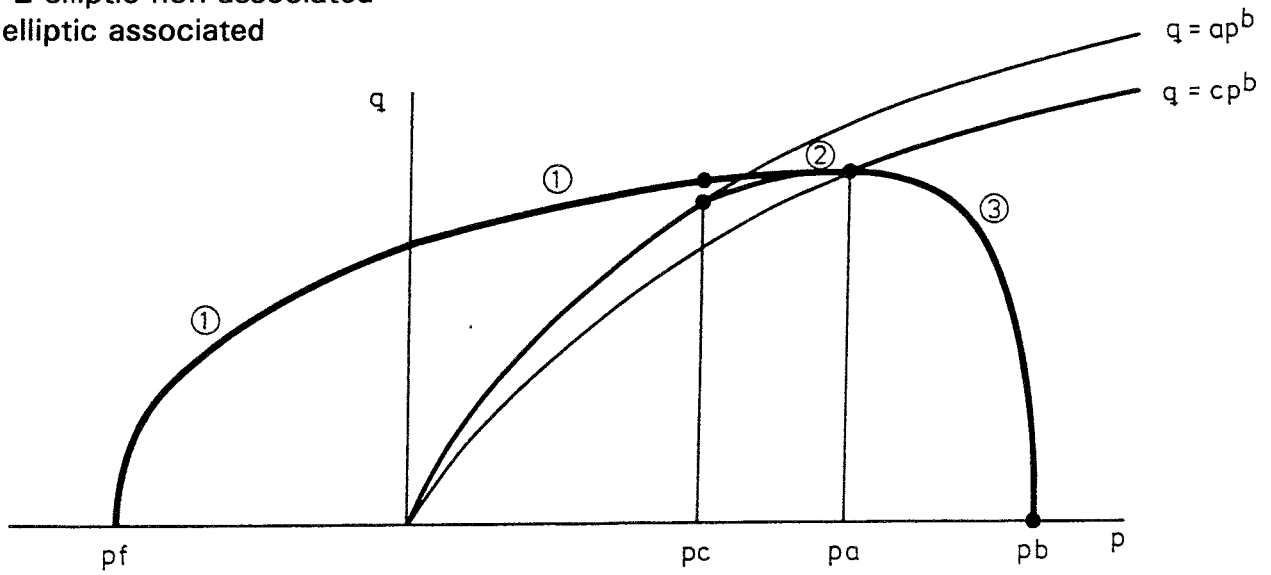

Figure 3-7. Plasticity model of bentonite (Claytech model). The yield surface, failure surface, and plastic flow surface are shown in the p-q stress space.

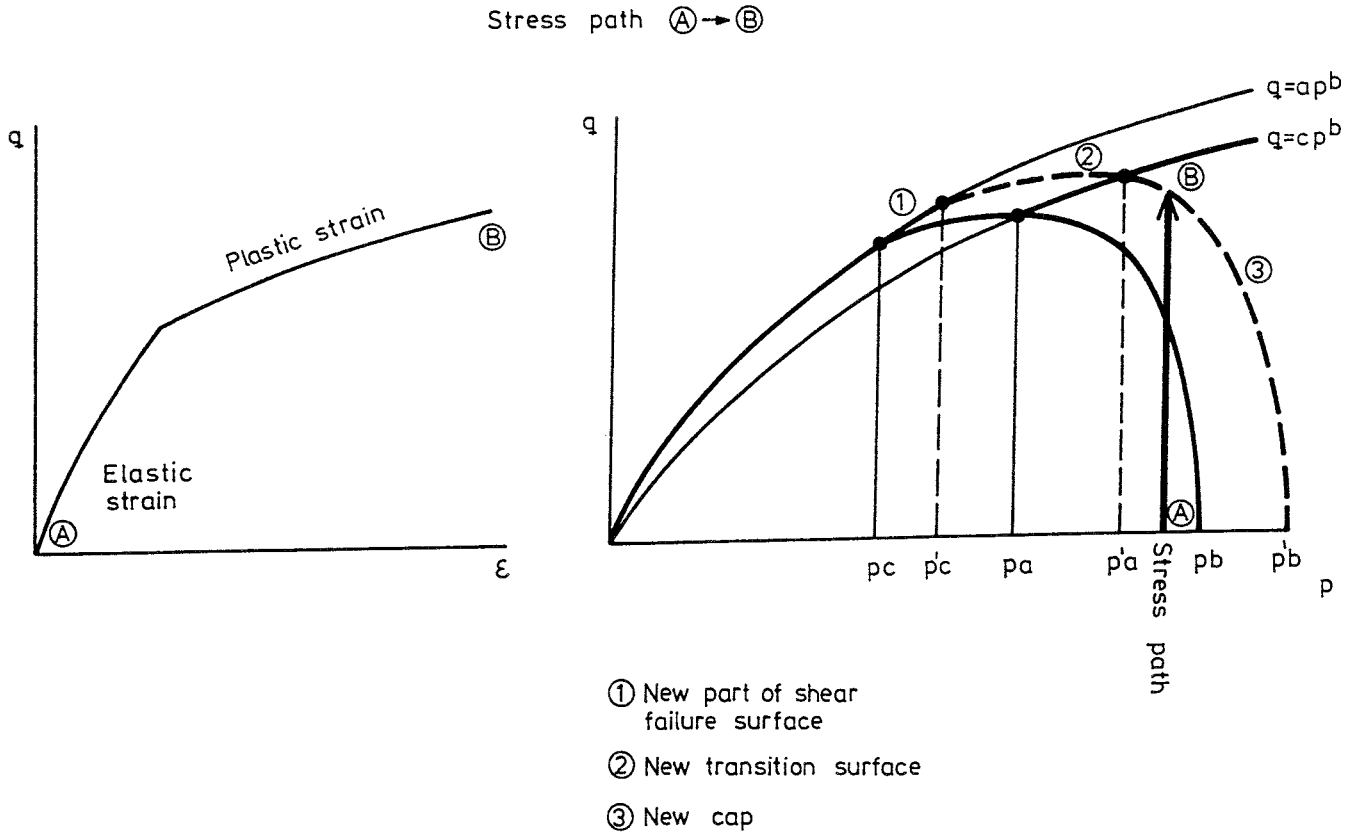

Figure 3-8. *Illustration of the behaviour of the Claytech model at two stress paths.*

The location of the cap is defined by the intercept p_b between the cap and the p axis. The location of the flow surface is defined by the intercept p_f between the flow surface and the p axis (usually a large negative value). The shape of the elliptic transition surface needs to be defined. This is made by the ratio γ of the minor and major axes of this ellipse.

Cap hardening

When the average stress p exceeds the "preconsolidation pressure" p_b the result will be a non-recoverable plastic volume decrease and the cap will expand. The total volume decrease is the sum of the reduction of the elastic and plastic volumes. The plastic volume change is thus the difference between the total volume change and the elastic volume change. It can be described either as a relation between the average stress and the plastic volume change according to Eqn 3-13, or as a modulus according to Eqn 3-14.

$$\varepsilon^{v}_{pl}=f(p_b) \tag{3-13}$$

$$\Delta(\ln e_{pl}) = \beta_{pl} \cdot \Delta(\ln p_b) \tag{3-14}$$

The expansion of the cap at the plastic volume decrease has a corresponding shrinkage of the cap when the material expands the volume plastically due to dilation close to the failure envelope. The magnitude of the cap shrinkage is given by the relation in Eqn 3-13 or 3-14.

3.2.3 Modelling of water flux

The water flux in the bentonite is modelled using Darcy's law. The hydraulic conductivity is the main parameter. The hydraulic conductivity k is mainly a function of the void ratio e but depends also on the temperature, the pore water composition, and the clay mineral composition. Fig 3-9 shows a compilation of some hydraulic conductivity tests. The figure shows that k is strongly dependant on e. The relation can be described according to Eqn 3-15 within certain void ratio limits.

$$k = k_0 \cdot \left(\frac{e}{e_0}\right)^{\eta} \tag{3-15}$$

where

$$\eta = \Delta(\ln k) / \Delta(\ln e) \tag{3-16}$$

Using the diagram in figure 3.9, the parameter data in Eqn 3-15 will be the following for the interval $0.5<e<2.0$ provided that Na-bentonite MX-80 and distilled water are used and that room temperature prevails.

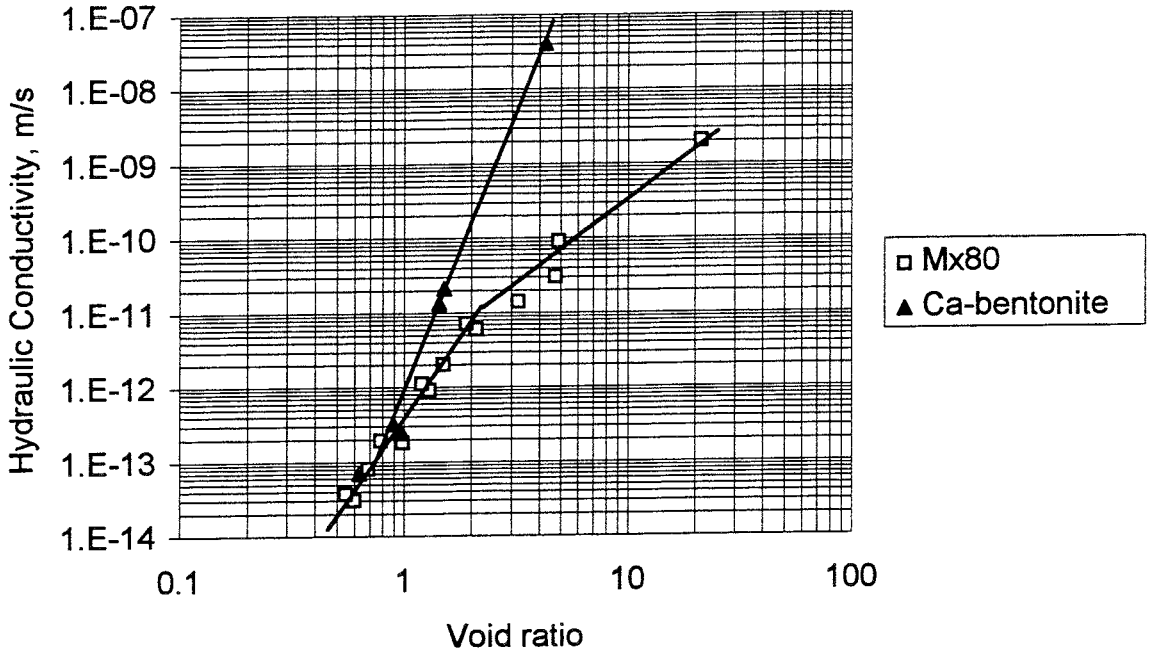

Figure 3-9. *Hydraulic conductivity of distilled water in Na-bentonite MX-80 and Ca-bentonite Moosburg at 20°C.*

k_0 $=3 \cdot 10^{-13}$ m/s
e_0 $=1.0$
η $=4.64$

The hydraulic conductivity is a little higher for Ca-bentonite at void ratio higher than about 1.0 as shown in Fig 3-9. The influence of temperature and pore water composition are shown in Fig 3-10 (from Karnland et al, 1992). Increased temperature and increased electrolyte content in the pore water enhance the hydraulic conductivity.

3.2.4 Modelling of thermal flux

The thermal flux of water saturated buffer material is modelled by using Fourier's law with the thermal conductivity λ and the specific heat c as main parameters. The influence of the density is not very strong and for thermal calculations of the water saturated stage the following average values can be used for the buffer material in the deposition holes under normal conditions and a void ratio e=0.7-0.8:

λ =1.25 W/m,K
c =1500 Ws/kg,K

The measurements indicate that λ decreases with increasing e to about λ=1.15 W/m,K at e=1.5 (see Fig 2-25).

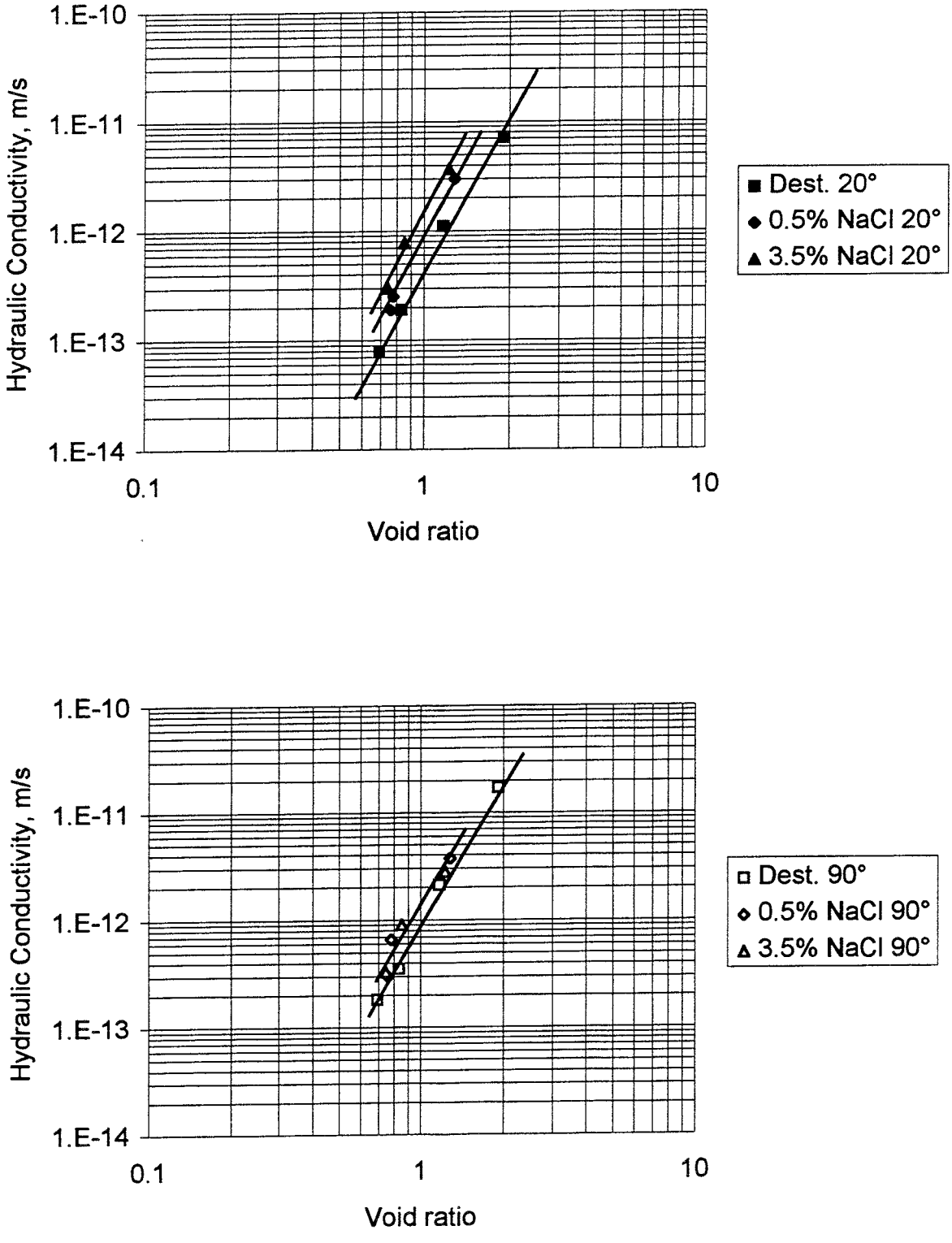

Figure 3-10. *Hydraulic conductivity of MX-80 as a function of the void ratio at different temperatures and different salt concentration in the pore water.*

3.2.5 Properties of the water and particle phases

While the suggested elastic-plastic models describes the behaviour of the clay structure, the mechanical properties of the individual water and particle phases also need to be defined. These phases are modelled as linear elastic with a linear thermal expansion coefficient. The following values are used for the temperature 20 °C:

Pore water

ρ_w =1000 kg/m^3 (density of water)
B_w =2.1·10^6 kPa (bulk modulus of water)
α_w =3.8·10^{-4} 1/K (coeff. of thermal expansion of water)

Particles

ρ_s =2079 t/m^3 (density of solids)
B_s =2.1·10^8 kPa (bulk modulus of solids)
α_s =3.4·10^{-6} 1/K (coeff. of thermal expansion of solids)

α_s can be neglected. α_w and ρ_w are functions of the temperature. The change in ρ_w with temperature is given by α_w while the change in a α_w with temperature can be tabled from standard tables.

3.2.6 Hydro-mechanical coupling of the two phases and the structure

The behaviour of the pore water is coupled to the behaviour of the structure with the effective stress concept. This implies that the mechanical behaviour of the structure is only controlled by the effective stress according to Eqn 3-17

$$\sigma=\sigma_{tot}-u \qquad (3\text{-}17)$$

where

σ = effective stress
σ_{tot} = total stress
u = pore water pressure

All structural stresses in this model refer to effective stresses and are usually represented by an apostrophe. However, for simplicity and for the reason that all stresses in the model pressure are effective, the apostrophe has been excluded in the text and in the equations. The total stress on a structure in contact with the buffer material is thus the sum of the pore pressure and the effective stress.

3.2.7 Creep

Deviatoric creep

The creep tests made with a low degree of mobilised strength D_r, shown in chapter 2.7, verify the creep model proposed by Börgesson (1988) and Börgesson et al (1988). The model states that the creep rate can be simulated according to Eqn 3-18 which is derived from an expression suggested by Singh and Mitchell (1968).

$$\dot{\varepsilon}_{cdt} = \dot{\varepsilon}_{cdo} \cdot e^{\alpha D_r} \cdot e^{-\alpha D_{ro}} \cdot \left[\frac{t}{t_o}\right]^{-n} \qquad (3\text{-}18)$$

where

$\dot{\varepsilon}_{cdt}$ = deviatoric creep rate ($d\varepsilon_{cd}/dt$) at any time
$\dot{\varepsilon}_{cdo}$ = deviatoric creep rate ($d\varepsilon_{cd}/dt$) at $t=t_o$
t = time
t_o = reference time
e = 2.7183
D_r = degree of mobilised strength $(\sigma_1-\sigma_3)/(\sigma_1-\sigma_3)_f$ (see Eqn 2-8)
D_{ro} = reference degree of mobilised strength $(\sigma_1-\sigma_3)_o/(\sigma_1-\sigma_3)_f$
α = inclination of the relation between $\dot{\varepsilon}_{cdo}$ and D_r plotted in a semi-logarithmic diagram as shown in Fig 2-24
n = inclination of the relation between $\dot{\varepsilon}_{cdt}$ and t plotted in a double-logarithmic diagram as shown in Fig 2-21

The reference parameters are

t_r = 10 000 s
D_{ro} = 0.5

The validity of Eqn 3-18 rests on two assumptions. The first assumption is that the relation between $\dot{\varepsilon}_{cdo}$ and D_r must be a straight line in a semi-logarithmic diagram. As indicated in Fig 2-24 this does not seem to be true for $D_r<0.1$. It is neither true for high values of D_r. Instead the relation shown in Fig 3-11 is used, which is partly verified by Fig 2-24. The second assumption is that the relation between $\dot{\varepsilon}_{cdt}$ and t is a straight line in a double-logarithmic diagram. This seems to be true for all values of D_r as indicated in Figs 2-21 to 2-23.

Eqn 3-18 is thus only valid for $0.1< D_r<0.9$ and another relation is required outside this range.

- At $0.1< D_r<0.9$:

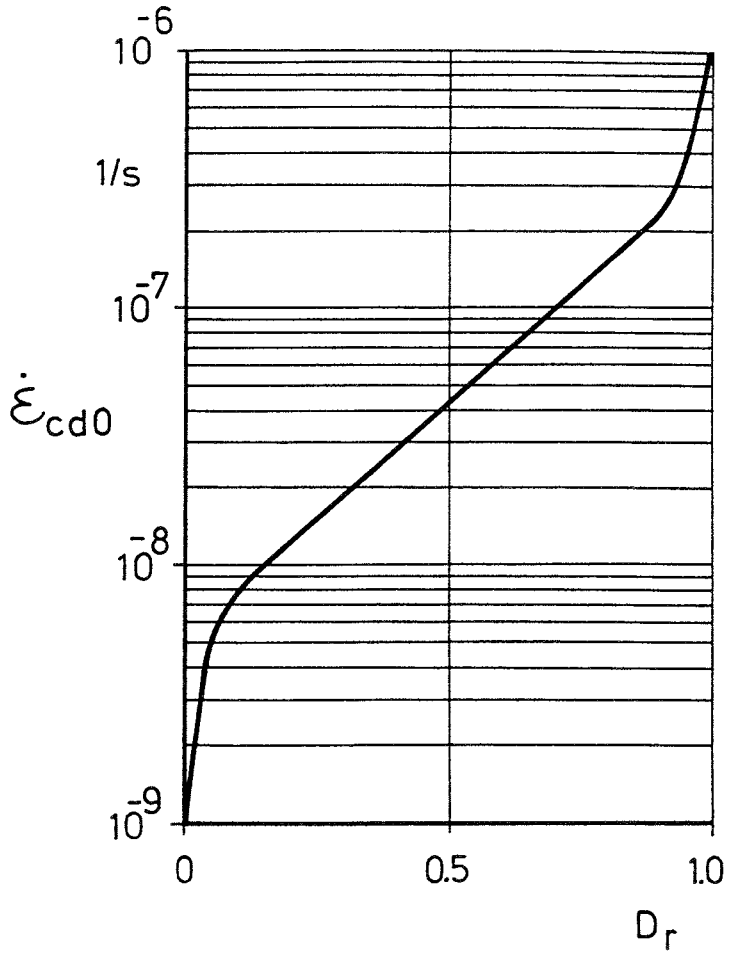

Figure 3-11. *Applied function for the deviatoric creep rate $\dot{\varepsilon}_{cdo}$ vs the degree of mobilized strength D_r at the reference time $t_0=10^4$ s.*

The following values are applied for Eqn 3-18 and the reference parameters:

$\dot{\varepsilon}_{cdo}$ $= 4.4 \cdot 10^{-8}$ 1/s
α $= 4.15$
n $= 0.91$

- At $D_r<0.1$:

The following Eqn based on Fig 3-11 and Eqn 3-18 is applicable:

$$\dot{\varepsilon}_{cdt} = A \cdot D_r{}^{a} \cdot \left[\frac{t}{t_o}\right]^{-n} \qquad (3\text{-}19)$$

with the following parameters

t_o $= 10\,000$ s
n $= 0.91$

as for Eqn 3-18 and with

A $= 8.0 \cdot 10^{-8}$ 1/s
a $= 1.0$

- At $D_r > 0.9$:

The following Eqn based on Fig 3-11 and Eqn 3-18 is applicable:

$$\dot{\varepsilon}_{cdt} = B \cdot \left[1 - D_r\right]^{-b} \cdot \left[\frac{t}{t_o}\right]^{-n} \tag{3-20}$$

with the following parameters

t_o $= 10\,000$ s
n $= 0.91$

as for Eqn 3-18 and with

B $= 2.3 \cdot 10^{-8}$ 1/s
b $= 1.0$

Volumetric creep

The oedometer tests in chapter 2-4 can be used for formulating a preliminary model of the volumetric creep. The secondary consolidation curve in a displacement-time diagram is considered to be a consequence of only volumetric creep, while the S-shaped part, which corresponds to primary consolidation, is mainly the consequence of the delay in outflow of water caused by the hydraulic conductivity of the clay. It has been shown by many investigations that this creep is close to linear in the semi-logarithmic diagram like those in chapter 2-4. The creep relation can be formulated according to Eqn 3-21 (see e.g. Feda, 1992).

$$\varepsilon_{vt} = \varepsilon_{vt_o} + C_{\alpha\varepsilon} \log \frac{t}{t_o} \tag{3-21}$$

where

ε_{vt} = volumetric creep at any time t caused by an increased average stress Δp
ε_{vt_o} = volumetric creep at the time t_o caused by the same increased average stress Δp
t = time
t_o = reference time
$C_{\alpha\varepsilon}$ = secondary compression index

$C_{\alpha\varepsilon}$ is evaluated as the inclination of the creep curve as shown in Fig 3-12.

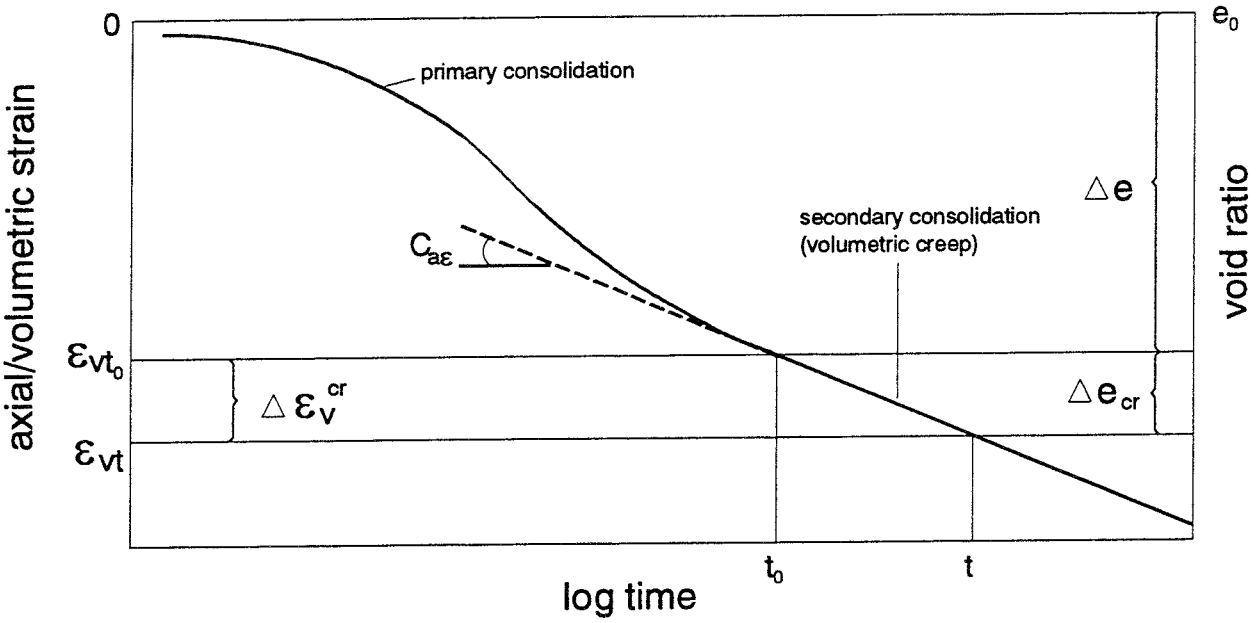

Figure 3-12. *Symbols used for the volumetric creep equations and the technique for evaluation of the secondary compression index $D_{a\varepsilon}$ from a load increase in an oedometer test.*

t_o is chosen to be a time well beyond completion of the primary consolidation period, and suitable for finishing a load step in an oedometer test. The volumetric creep from the time t_o to the time t

$$\Delta\varepsilon_v^{cr}$$

can be written as Eqn 3-22.

$$\Delta\varepsilon_v^{cr} = \varepsilon_{vt} - \varepsilon_{vt_o} = C_{\alpha\varepsilon} \log\frac{t}{t_o} \qquad (3\text{-}22)$$

$C_{\alpha\varepsilon}$ is a function not only of the creep properties of the clay but also of the magnitude of the load increase and average stress. Since the volume change during the primary consolidation is a direct function of the two latter factors $C_{\alpha\varepsilon}$ can be written as in Eqn 3-23. The effect of temperature is probably also important but is neglected here.

$$C_{\alpha\varepsilon} = f(\varepsilon_{vt_o}) \qquad (3\text{-}23)$$

The relation defined by Eqn 3-23 is not known but it is logical to approximate it to imply direct proportionality:

$$C_{\alpha\varepsilon} = c_1 \cdot \varepsilon_{vt_o} \qquad (3\text{-}24)$$

Since the volume change is related to the change in void ratio according to Eqn 3-25, we have

$$\varepsilon=\Delta e/(e+1) \tag{3-25}$$

Eqn 3-22 can be approximately written as Eqn 3-26

$$\Delta e_{cr} = \Delta e \cdot c \cdot \log\frac{t}{t_o} \tag{3-26}$$

where

Δe_{cr} = change in void ratio between the time t and t_0 due to creep caused by a change in average stress p
Δe = change in void ratio due to primary consolidation caused by a change in average stress p
c = creep constant
t = time
t_o = reference time after end of the primary consolidation

Eqn 3-26 can thus be used to calculate the volumetric creep effects if c is known, since Δe can be calculated from the elastic model in Eqn 3-5. At stepwise loading, the remaining effect of the previous load steps can be taken into account by superimposing their respective contributions.

The value of c for MX-80 at conditions corresponding to the reference KBS-3 concept can be determined from the results of oedometer test KMXA6 where a sample compacted to the same density as intended for the blocks was reconsolidated after swelling. The consolidation steps are shown in Fig 3-13. The evaluation of c must be made for a load step that contains no or very little rest creep from preceding steps. As seen in the figure the step from 576 kPa to 3272 kPa is suitable since the consolidation and hence also the creep during the two earlier steps were very small.

By extending the creep phase of $1.0\cdot10^6$ s -$2.0\cdot10^6$ s, back to $\cdot10^3$ s c can be calculated from Eqn 3-26 with the following data taken from Fig 3-13:

Δe_{cr} = 0.0223
Δe = 0.2446
c = creep constant
t = 10^6 s
t_o = 10^3 s

This yields c=0.030.

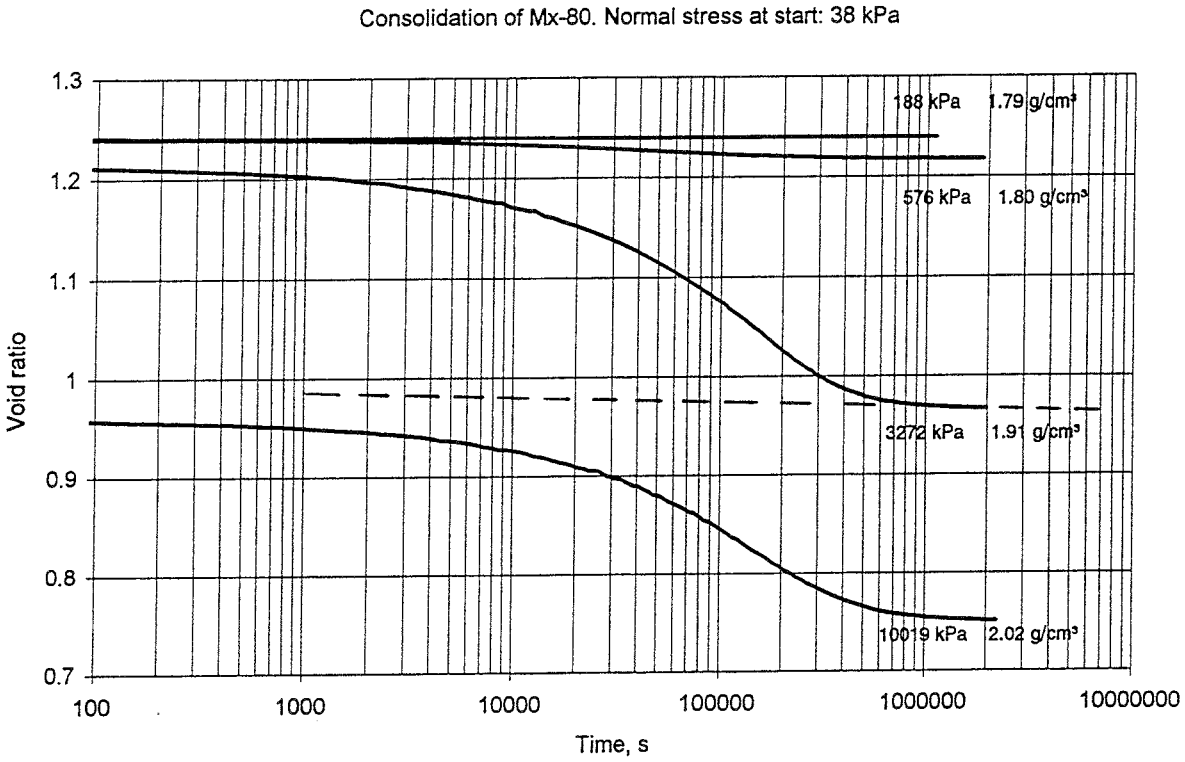

Figure 3-13. *Test example of KMXA6 for illustrating the creep theory.*

If the theory is correct it should be possible to calculate the effect of the subsequent load step. According to the measurements the void ratio decreased from

e=0.7529 at t=1.206·10^6 s to
e=0.7502 at t=2.252·10^6 s or
Δe=0.0027

The creep is the sum of the new creep from the latest step $\Delta e_{cr}^{\ 1}$ and the rest creep from the previous step $\Delta e_{cr}^{\ 2}$ which has been applied for 2.0·10^6 s longer. Eqn 3-26 yields:

$\Delta e_{cr}^{\ 1} = 0.2124 \cdot 0.03 \cdot \log(2.252 \cdot 10^6 / 1.206 \cdot 10^6) = 0.0017$
$\Delta e_{cr}^{\ 2} = 0.2446 \cdot 0.03 \cdot \log(4.252 \cdot 10^6 / 3.206 \cdot 10^6) = 0.0009$

$\Sigma \Delta e_{cr} \quad = 0.0028$

The calculated creep thus agrees very well with the measured one. However, the time function needs to be verified for much longer times, which may imply correction. The proportionality to the volume change at primary consolidation (Eqn 3-24) and the assumption of super imposement need to be checked by performing more tests.

3.2.8 Contact properties

The contact between e.g. the buffer material and the canister or the rock need to be modelled as well. Thermally and hydraulically there is no influence due to the extremely good contact caused by the swelling pressure. However, mechanically there is a change in shear resistance if the material surface in contact with the buffer is smooth. Shear tests on bentonite in contact with different materials have been performed (Börgesson et al, 1990) leading to the conclusion that the contact can be modelled to represent a shear strength that is a function of the shear strength of the bentonite according to the following relations:

τ_{fc}= shear strength of the contact surface and
τ_{fb}= shear strength of bentonite.

Cement/bentonite interaction: $\tau_{fc}= \tau_{fb}$ (no slip)
Stainless steel/bentonite interaction: $\tau_{fc}=0.6\ \tau_{fb}$
Copper/bentonite interaction: $\tau_{fc}=0.6\ \tau_{fb}$
Granite rock/bentonite interaction: $\tau_{fc}=0.6\ \tau_{fb}$

3.2.9 Influencing factors

Rate of strain

The rate of a deformation will influence the values of some parameters. This influence is especially important in the rock shear case when the displacement of the rock can be very fast if it emanates from an earthquake type of disturbance or very slow if it stems from rock creep.

The influence of rate of strain is related to the creep phenomena but it is only important for deviatoric strain since the volumetric strain rate is very low and controlled by the hydraulic conductivity. The influence is thus primarily interesting for the shear strength and can be investigated by performing undrained shear tests. This has been made on MX-80 by Börgesson et al (1988). Fig 3-14 shows the influence on the shear strength in three tests on samples with different void ratios which have been sheared at different shear rates. The figure shows that the shear strength increases with increasing shear rate according to Eqn 3-27.

$$\tau_f = \tau_{fo}\left[\frac{\dot{\gamma}}{\dot{\gamma}_o}\right]^n \qquad (3\text{-}27)$$

where τ_f = shear strength
$\dot{\gamma}$ = rate of shear strain (1/s)
$\dot{\gamma}_o$ = reference rate of shear strain = 1.0 (1/s)
τ_{fo} = shear strength at the reference rate of shear strain
n = rate factor

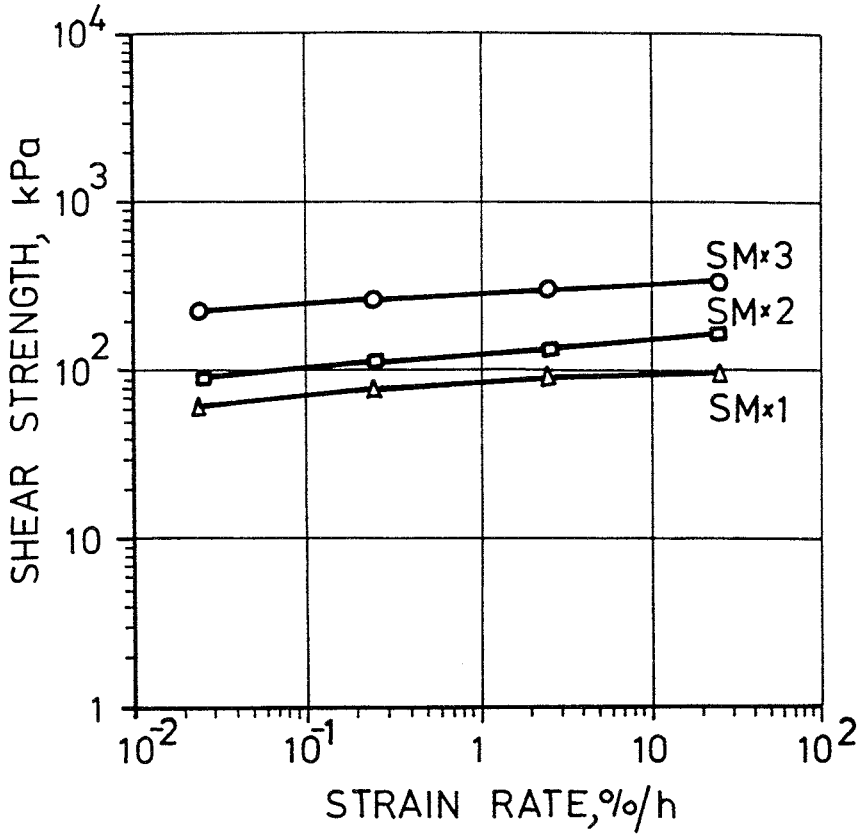

Figure 3-14. The shear strength at different strain rates measured in three shear tests on samples of MX-80 bentonite with different void ratios.

According to these investigations the rate dependency factor n is about

n=0.065

This means that the shear strength will increase by 16% at an increase in rate by 10 times.

Temperature

The influence of temperature on the parameter values in the different submodels seems to be important only for porewater-related properties at temperatures between 10°C and 90°C. No large influence has been found on the mechanical models of the clay structure (with the possible exception of Na-bentonite at low density) and the thermal model. The hydraulic conductivity increases with temperature (see Fig 3-10) mainly due to the decreased viscosity of water, which means that the permeability is constant and that the hydraulic conductivity k can be expressed according to Eqn 3-28.

$$k = k_o \frac{\mu}{\mu_o} \frac{\rho_{wo}}{\rho_w} \qquad (3\text{-}28)$$

where

k_o = hydraulic conductivity at a reference temperature
μ_o = viscosity at a reference temperature
ρ_{wo} = density of water at a reference temperature
ρ_w = density of water

Influence of pore water composition and clay type

The *pore water* composition influences several models. Most tests have been made with distilled water added to the natural water in the bentonite to which the respective models refer. However, if the added water has a significant salt content several of the properties are changed.

The *clay type* is strongly affecting the parameters in the material models. The effect of conversion to illite etcetera is not considered in this report but the difference between Na- and Ca-bentonites will be demonstrated.

Influence of pore water composition and clay type on the elastic behaviour

The influence of the electrolyte content is shown in Fig 3-15, where some results from measurements of the swelling pressure with 3.5% NaCl was added to the pore water of MX-80, are plotted in the same diagram as the other results. The figure shows that the swelling pressure and thus the parameters β and p_o in Eqn 3-4 of the elastic model are slightly changed

$$e = e_0 \cdot \left(\frac{p}{p_0}\right)^{\beta} \qquad (3\text{-}4)$$

The difference between the reference Na-bentonite MX-80 and certain Ca-bentonites is also shown in Fig 3-15. Although there is some scatter among the different Ca-bentonite types, a lower pressure at high void ratios and higher at low void ratios are quite obvious. On an average the parameters β and p_o will be according to Table 3-1 if the reference pressure is set at p_o=1000 kPa.

Table 3-1 Influence of bentonite type and pore water composition on the values of the parameters in the equation for the elastic model (Eqn 3-4).

Bentonite type etc.	β	e_o (kPa)	*Limit* $<e<$
MX-80, Na-bent, dist. water	-0.19	1.1	$0.5<e<1.5$
MX-80, Na-bent, 3.5% salt water	-0.15	1.0	not known
Ca-bent, dist. water	-0.15	1.2	not known

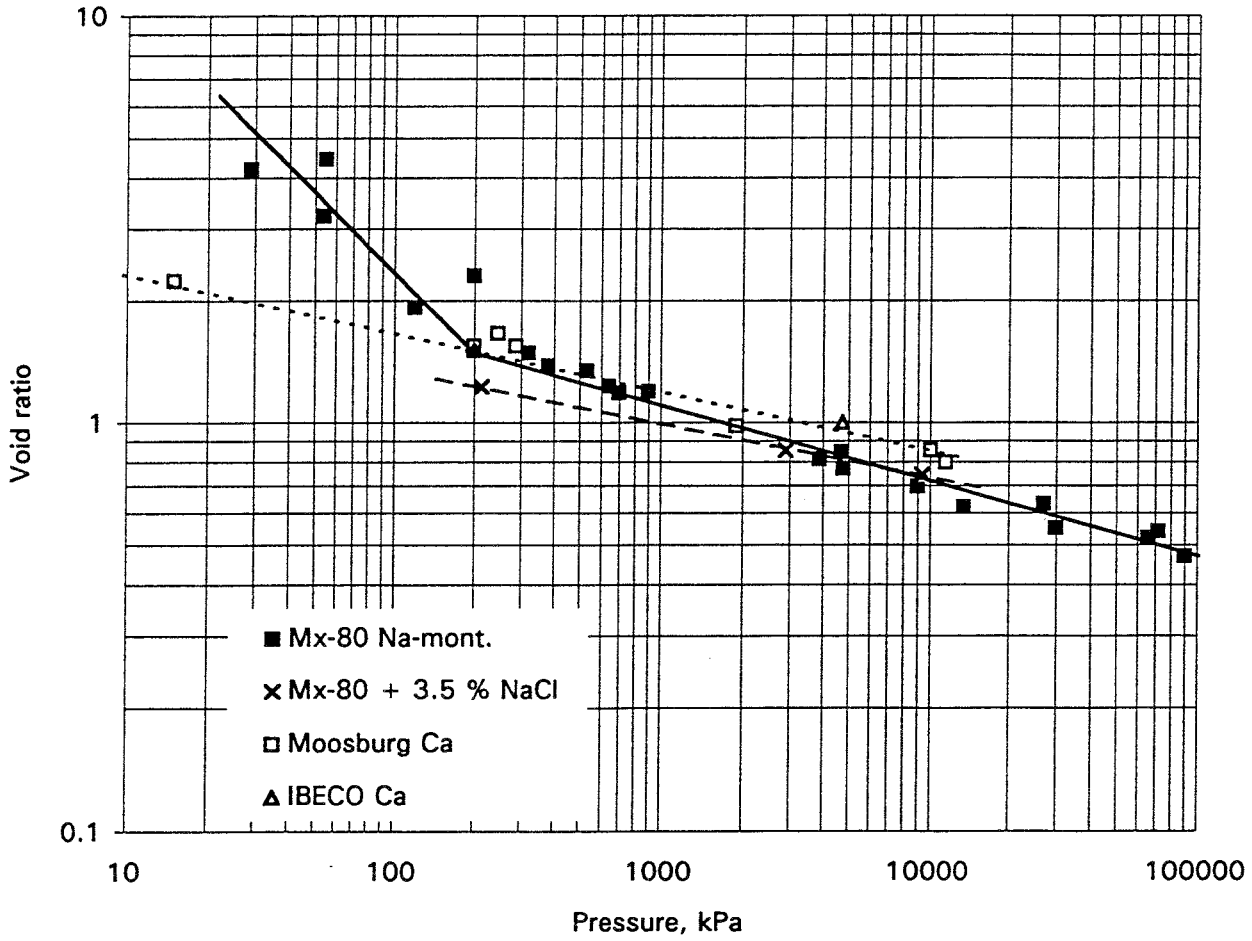

Figure 3-15. *Compilation of measured swelling pressure for Na-bentonite and Ca-bentonite as a function of the void ratio. The solid and hatched lines are used for modelling the elastic behaviour.*

Influence of pore water composition and clay type on the plastic behaviour (failure surface)

The location of the failure surface is influenced by both the electrolyte content and the clay type as shown in Fig 3-6. The parameters in the equation for the failure surface as defined by Eqn 3-11:

$$q=ap^b \tag{3-11}$$

are better understood with the following reformulation

$$q=q_o(p/p_o)^b \tag{3-29}$$

where

q_o = Mises' stress at failure at p_o

p_o = reference average stress =1000 kPa

The parameter b describes the inclination of the straight line in the double logarithmic diagram, while q_o describes the level of the line. Fig 3-6 yields the values in Table 3-2:

Table 3-2 Influence of bentonite type and pore water composition on the values of the parameters in the equation for the failure surface (Eqn. 3-29).

Bentonite type etc.	b	q_o (kPa)
MX-80, Na-bent, dist. water	0.77	500
MX-80, Na-bent, 3.5% salt water	0.77	700
IBECO, Na.bent, dist. water	0.77	580
Moosburg, Ca-bent, dist. water	0.77	750

3.3 CONCLUSIONS

There is sufficient understanding and access to data for formulating a complete model of the thermo-hydro-mechanical behaviour of water saturated MS-80-type buffer materials. Such a model, called the Claytech Model here, has been described in this chapter. However, the model can be improved by making more tests to increase the base for choice of parameter values and for verification of the following features:

- the plastic volumetric behaviour
- the volumetric creep behaviour

The least accurate part of the model is probably the stress-strain behaviour at deviatoric loading and unloading since there is no good model for this behaviour (see Elastic Deviatoric Model in chapter 3.2.2). The reason is not the lack of data but more generally a lack of model, which is the case also for ordinary soils in soil mechanics.

4 MATERIAL MODELS ADAPTED TO ABAQUS

4.1 GENERAL

The tentative material model represents the best approximation of the real behaviour of buffers. The model can only be used for calculations if it is transformed to a numerical tool which needs to be either implemented from scratch or adapted to an existing code. The latter technique has been chosen for the buffer material, using the finite element code ABAQUS.

The development of models and the adaptation of them to ABAQUS have been made in several steps. The earlier models and the latest version (CLAYTECH/S/A where S stands for saturated and A stands for ABAQUS) will be described in this chapter. The latest version is akin to the tentative model (CLAYTECH/S/T where T stands for tentative), which has required coding of some parts of the model, but there are still some parts of the tentative model that have not been included in the finite element program. This chapter will describe the models, adapted to ABAQUS and thus available for calculation. It will also describe the coding made for the latest version (CLAYTECH/S/A).

4.2 FINITE ELEMENT CODE ABAQUS

ABAQUS is a general purpose finite element program designed specially for advanced structural and heat transfer analyses. It is designed both for linear and non-linear stress analyses of very large structures. The element library provides a complete geometric modelling capability. Solids in one, two, and three dimensions as well as specific structures like shells can be modelled using first, second or third order interpolation. Multilevel substructuring capability is another useful facility. ABAQUS is a modular code: any combination of elements, each with any appropriate material model, can be used in the same analysis. Different elements are available for coupled processes like temperature/stress problems and effective stress/groundwater flow problems.

The material library contains several different constitutive models, e.g. non-linear elasticity, rubber, plasticity, concrete, soils, etc.

ABAQUS is a commercially available code that is written, supported and steadily upgraded by HKS (Hibbitt, Karlsson, and Sorensen) with headquarters in Pawntucket, Rhode Island, USA with Scandinavian representation at FEM-Tech AB in Västerås.

The calculations and coding have been made in cooperation between Clay Technology AB and FEM-Tech AB.

4.3 OLDER MODELS

4.3.1 Total stress model

The first scenario calculations concerned the effect of rapid rock displacement across a deposition hole. Since such a displacement is fast and the strain merely deviatoric no net volume change takes place and the process can be considered undrained. This made it possible to use a total stress concept without considering the pore pressure development.

The total stress model of a buffer material is quite simple since it only includes the stress-strain relation describing deviatoric strain as a function of the deviatoric stress until failure is reached. This relation differs at different density and must thus be specified for the actual density of the buffer. The relation between the deviator stress and the strain of the type shown in Fig 3-5, can be used.

A table with the strain listed as a function of Mises' stress is thus required. The relation can be taken from Fig 3-5 corrected for the actual strength according to Eqn 3-8 and corrected for the actual rate of strain according to Eqn 3-27.

4.3.2 Effective stress Drucker-Prager model

General

The plasticity model Drucker-Prager in combination with the effective stress theory is available in the library of ABAQUS. The Drucker-Prager model differs from the new CLAYTECH/S/A model in two parts, namely

- the plastic model
- the elastic deviatoric model

but the other parts of the model (the elastic volumetric model, the hydraulic model etc.) are the same.

Mechanical model

The *plastic model* is illustrated in Fig 4-1 in a *q-p* diagram where q is Mises' equivalent stress and p is the average effective stress. The diagram shows that the stress dependence of the failure stress is controlled by the "friction" angle β and a "cohesion" intercept. The plastic behaviour is limited to a zone between the yield surface and the failure surface. The plastic flow is non-

associated and determined by the dilatancy angle ψ. Since Drucker-Prager's theory takes the intermediate principal stress into account in contrast to Mohr-Coulomb's theory, the influence of this stress on the location of the failure surface can be considered by the parameter K which is the relation of the failure stress in triaxial tension to the failure stress in triaxial compression. The values of these parameters can be derived from the results of the triaxial tests. The parameters evaluated for Na-bentonite MX-80 are the following:

β	=17°
d	=100 kPa
ψ	=2°
K	=1.0

K = 1.0 is justified by fig 3-6 showing that the shear strength at triaxial extension is equal to the shear strength at triaxial compression. The "friction angle" β and "cohesion" d vary with average stress since the failure envelope is not a straight line as shown in chapter 3. The values used in this model are thus either rough approximations that are valid for a large range of pressures or good approximations that are valid for a very narrow range. The values β=17° and d=100 kPa represent rough approximations for the stress interval $200<p<10000$ kPa.

The yield function, which corresponds to the relation between stress and plastic strain in the plastic zone, is defined as the plastic strain ε_{pl} for a stress path that corresponds to uniaxial compression test with no confining pressure. The yield function that has been used for the reference material is shown in Table 4-1.

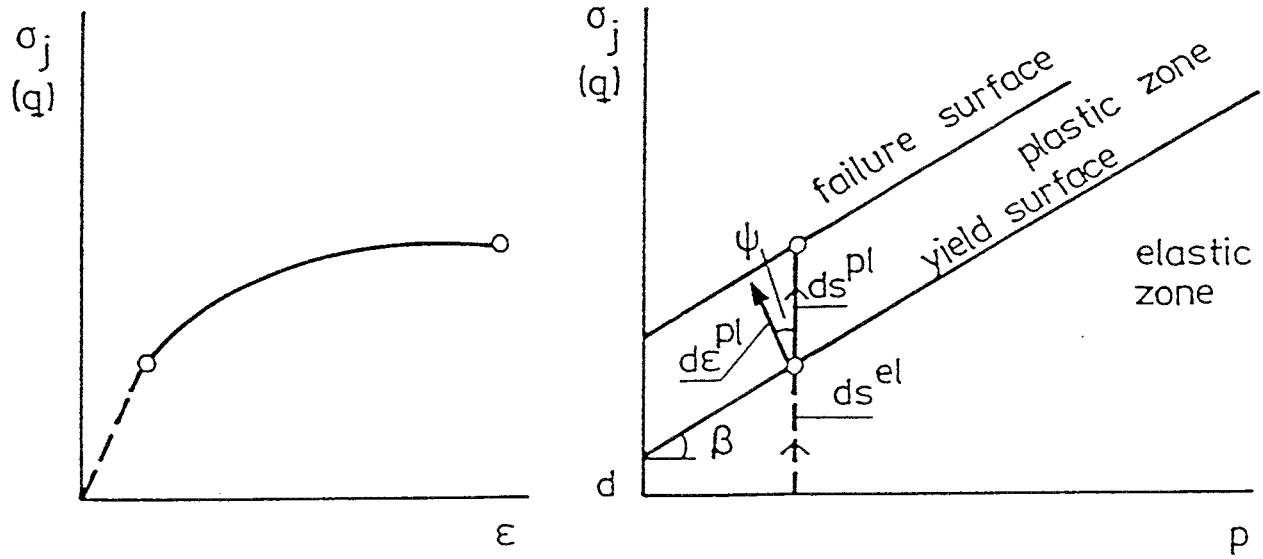

Figure 4-1. The plasticity model of Drucker-Prager.

Table 4-1 Yield function:

q (kPa)	ε_{pl}
113	0
138	0.005
163	0.02
188	0.04
213	0.1

The *elastic model* concerns the zone below the yield surface in the *p-q* diagram. No cap limiting the elastic part in the p direction is used in this model, which means that there is no difference between normally consolidated buffer material and overconsolidated buffer material as in non-swelling clays. This is justified by the swelling properties of the bentonite with the high quality that is considered for buffer material. The model of the elastic properties are called "Porous Elasticity" and is defined by the logarithmic bulk modules κ and Poisson's ratio ν, the values for MX-80 being:

κ =0.21 ($0.7<e<1.5$)
ν =0.4

The logarithmic bulk modulus can be determined from Fig 3-1 and is defined in the following way:

$$\kappa=\frac{\Delta e}{\Delta \ln p} \qquad (4\text{-}1)$$

This relation hence implies that the void ratio is a linear function of the average stress in a semi-logarithmic diagram. Fig 3-1 shows that this is not valid over a large spectrum in void ratio, but for a limited range one can make reasonable approximations. The value κ=0.21 is hence valid for the interval $0.7<e<1.5$.

Modelling of water flux

The water flow resistance in the clay is modelled by Darcy's law with the hydraulic conductivity k being a function of the void ratio e (interpolation between the values). The data in Table 4-2 are based on Fig 3-9 and can be used for Na-bentonite MX-80 percolated by distilled or low-electrolyte water:

Table 4-2 Input for hydraulic conductivity as a function of the void ratio

e	k (m/s)
0.45	$1.0 \cdot 10^{-14}$
0.70	$6.0 \cdot 10^{-14}$
1.00	$3.0 \cdot 10^{-13}$
2.00	$7.0 \cdot 10^{-12}$

Properties of the water and particle phases

The effective stress concept, which states that the effective stress (the total stress minus the pore pressure) determines all the mechanical properties, is modelled by separating the function of the pore water and that of the particles. The density ρ_w and bulk modulus B_w of the pore water as well as the density ρ_s and the bulk modulus of the solid particles B_s are required parameters. The following data can be used for Na-bentonite:

Pore water

ρ_w =1000 kg/m^3 (density of water)
B_w =$2.1 \cdot 10^6$ kPa (bulk modulus of water)
α_w =$3.8 \cdot 10^{-4}$ 1/K (coeff. of thermal expansion of water)

Particles

ρ_s = 2790 kg/m^3 (density of solids)
B_s = ∞ (bulk modulus of solids)
α_s = 0 (coeff. of thermal expansion of solids)

The particles are thus not modelled since the properties of water dominate the behaviour of the separate phases.

Contact properties

The contact between the buffer material and the surrounding is modelled by use of contact elements with no thickness and undergoing only tangential strain. The elements are modelled according to Mohr-Coloumbs theory with the failure parameters:

c_c = $0.6c_b$ (cohesion)
ϕ_c = $0.6\phi_b$ (friction angle)

where ϕ_b = friction angle of bentonite
c_b = cohesion of bentonite

Initial conditions

3 parameters describing the initial situation in the buffer are needed. They are: 1) the initial void ratio e_0, 2) the initial average effective stress p_0 (corresponding to the swelling pressure) and 3) the initial pore water pressure u_0. For the Swedish KBS3 reference concept the following values are assumed to be valid after completed water saturation and pore pressure build-up:

e_0 =0.75
p_0 =8000 kPa
u_0 =5000 kPa

Other properties and the influence of different factors

The other models that are required for the general THM modelling viz. the heat flux and creep models will be described together with the CLAYTECH/S/A model. The influence of temperature, pore water composition, and bentonite type can be evaluated from the information given in chapter 3.

4.4 CLAYTECH/S/A MODEL

4.4.1 General

The CLAYTECH/S/A model is the ABAQUS adapted version of the tentative model described in chapter 3 (CLAYTECH/S/T). It is not the same model altogether since all parts have not been implemented. The latest version will be shown here.

4.4.2 Model description and required input parameters

Mechanical model of the clay structure

The mechanical model can be divided into an elastic part and a plastic part as shown in the description of the tentative model.

Plastic part

The new plastic submodel was shown in Figs 3-7 and 3-8. It has been implemented, coded, and included in ABAQUS. The new model is based on the existing ones in ABAQUS form including a newly developed so-called CAP-model. These models are described in detail in the ABAQUS Theory Manual and the ABAQUS User's Manual and will not be reported here. The new plastic model includes the following new parts:

- A curved failure surface: $q=ap^b$
- A curved critical state line: $q=cp^b$
- An elliptic yield transition surface
- A non-associated elliptic plastic potential function (called flow surface in Fig 3-7)

Yield surface, failure surface, and critical state line

Enclosed as Appendix 1 is a description of the implementation of the new plastic model with the mathematical functions of the yield and failure surfaces as well as the differential coefficients required for the modelling. Code verification calculations have been made using swelling/compression tests. These calculations were not made for certifying the validity of the model but only for checking the code.

The input parameters required for these parts of the new model are the following:

a
c } = Parameters for defining the failure and critical state surfaces in
b

Eqns 5-1 and 5-2.

K = influence of the intermediate principal stress on q_f

γ = Relation between the two axes of the elliptic yield transition surface. Vertical axis divided by the horizontal axis. See Appendix 1. $0<\gamma\leq 1$.

R = Relation between the two axes of the elliptic cap. Horizontal axis divided by the vertical axis. $0<R\leq 1$.

p_b = Intersection of the cap and the p-axis

Flow surface and cap hardening

The volumetric plastic behaviour is controlled by the flow surface (flow potential) and the cap hardening law. The flow surface is a new part of the model. It is described and implemented in Appendix 1. See also Fig 3-7.

The input parameters required for these parts of the new model are the following:

p *vs.* $^e\log(1+\varepsilon^v_{pl})$ = cap hardening relation

p_f = intersection between the elliptic flow surface and the p-axis at $p<0$

The expansion of the cap or "cap hardening" is defined as the relation between the average stress p and the logarithmic plastic volumetric strain $^e\log(1+\varepsilon^v_{pl})$ where $\varepsilon^v_{pl}=\Delta V_{pl}/V$ is the "engineering strain".

ABAQUS operates with logarithmic strain which differs from the engineering strain definition. The strains are added according to Eqn 4-2.

$$^{e}\log(1+\varepsilon^{v}_{tot}) = {}^{e}\log(1+\varepsilon^{v}_{el}) + {}^{e}\log(1+\varepsilon^{v}_{pl}) \qquad (4\text{-}2)$$

where ε^{v}_{tot} = total volumetric strain ($=\Delta V/V$)
ε^{v}_{el} = elastic volumetric strain ($=\Delta V_{el}/V$)
ε^{v}_{pl} = plastic volumetric strain ($=\Delta V_{pl}/V$)

The cap hardening concept thus defines how the logarithmic plastic volumetric strain increases with increasing average stress.

Elastic part

Elastic volumetric model

The elastic volumetric behaviour should according to the tentative model have a *e-p* relation according to Fig 3-15. This is not possible in the present version of ABAQUS. The same porous elastic model as described in chapter 4.3.2 will instead be used. It requires the following parameter:

κ = porous elasticity (see Eqn 4-1)

Elastic deviatoric model

The variable Poisson's ratio has not been included in the subroutine described in the Appendix. It has instead been included as a special subroutine in the Porous Elastic Model with the input parameters

$\left.\begin{matrix} \nu_0 \\ \nu_{max} \\ \eta \end{matrix}\right\}$ as described in Eqns 3-9 and 3-10

Modelling of water flux

The water flux is modelled according to the tentative model in chapter 3.2.3 with the hydraulic conductivity k defined as a function of the void ratio e.

k = f(e)

Modelling of thermal flux

The thermal flux is also modelled according to the tentative model in chapter 3.2.4. with the following parameters

λ = thermal conductivity = f(e)
c = specific heat

Properties of the water and particle phases

Only the pore water phase can be modelled in the present version of ABAQUS since the particle phase is considered to be infinitely stiff with no thermal expansion, which is an acceptable approximation.

Pore water

ρ_w = density of water
B_w = bulk modulus of water
α_w = coeff. of thermal expansion of water

Particles

ρ_s = density of solids

Hydro-mechanical coupling between the two phases and the structure

The effective stress theory according to Eqn 3-17 is used. No additional parameters are required for this part.

Creep

Only deviatoric creep can be modelled in the present version of ABAQUS. Volumetric creep is not yet implemented. The deviatoric creep cannot be coupled to the other parts of the CLAYTECH/S/A model and is hence treated separately. The creep model according to Eqn 3-18 is implemented, coded, and included in ABAQUS and the parameter values shown in chapter 3.2.7 can be used for creep calculation.

Contact properties

The contact between the buffer material and the surrounding is modelled with contact elements with no thickness and undergoing only tangential strain. The elements are modelled according to Mohr-Coloumb theory with the following parameters:

c =0 (cohesion)
ϕ =0.6ϕ_b (friction angle)

where

ϕ_b = the friction angle of the bentonite (= f(p))

Initial conditions

The same initial conditions are required as for the Drucker-Prager model viz. the following:

e_0 = the initial void ratio
p_0 = the initial average effective stress
u_0 = the initial pore pressure

4.4.3 Parameter values

The input values of the required parameters for the CLAYTECH/S model of the reference material depend on the stress history and the initial conditions. With the following reference conditions and stress history a "reference model" can be defined:

- The bentonite blocks have been compacted to the void ratio e=0.6 and then allowed to swell in the deposition hole to e=0.75 without any yielding during swelling.
- Bentonite type: MX-80
- Temperature: 20 °C
- Water taken up by the bentonite: Water with low electrolyte content.
- The exposed canister surface is copper and both this surface and the surface of the granite rock wall of the deposition hole are smooth.
- The deposition holes are situated 500 m below the ground water table.

This reference CLAYTECH/S/A model will have the following input data:

Plastic part of the mechanical model

a =2.45
c =2.20
b =0.77
K =1.0
γ =0.1
R =0.1
p_b =17 000 kPa
p_f =-25 000 kPa
Cap hardening = see Table 4-3

Table 4-3 Cap hardening relation for the reference model

p kPa	${}^{e}\log(1+\varepsilon^{v}_{pl})$
100	0
200	0.103
400	0.192
750	0.264
1200	0.299
2000	0.323
3500	0.379
5500	0.396
8500	0.415
17000	0.444
30000	0.490

The difference between the elastic and plastic parts is very small as discussed in chapter 3. The values of the parameters implying this difference are thus difficult to evaluate and the difference between a and c is therefore postulated. The shapes of the ellipses given by γ and R are also postulated. p_b is the swelling pressure at the initial void ratio of the blocks e=0.6 while p_f is taken as a very high negative value in order to make the dilatancy very small.

Elastic part of the mechanical model

κ=0.22 (0.7<e<1.5)
ν= variable with
ν_0 =0
ν_{max} =0.49
η =0

The value of κ is only valid over a limited range of void ratios, since the present version of the model is not capable of describing the exact relation as shown in Fig 3-15. The parameter values for Eqn 3-10, defining the variable

Poisson's ratio, are chosen to yield good agreement between the measured and calculated stress-strain relation at triaxial testing (see chapter 5).

Water flux

The hydraulic conductivity data, extended to a wide range of void ratios, are shown in Table 4-4.

Table 4-4 Input for hydraulic conductivity as a function of the void ratio

e	k (m/s)
0.45	$1.0 \cdot 10^{-14}$
0.70	$8.0 \cdot 10^{-14}$
1.00	$3.0 \cdot 10^{-13}$
1.5	$2.0 \cdot 10^{-12}$
2.00	$7.0 \cdot 10^{-12}$
3.00	$2.0 \cdot 10^{-11}$
5.00	$7.0 \cdot 10^{-11}$
10.00	$3.0 \cdot 10^{-10}$
20.00	$1.5 \cdot 10^{-9}$

Table 4-4 is derived from Fig 3-9

Pore water and particle properties

ρ_w =1000 kg/m^3
B_w =$2.1 \cdot 10^6$ kPa
α_w =$3.8 \cdot 10^{-4}$ 1/K
ρ_s =2790 kg/m^3

Thermal flux

The following values can be used for the interval $0.7<e<0.9$:

λ =1.25 W/m,K
c =1500 Ws/kg,K

Creep

See chapters 3.2.7 and 4.4.2

Contact properties

The following values can be used for contact surfaces between bentonite and smooth copper or smooth rock in the interval $0.7<e<1.1$:

c_c =80 kPa
ϕ_c =5.5°

At the contact zone with concrete or a rough surface of rock the slip between the materials will take place in the bentonite and the boundary can thus be defined either without contact elements or with the following values for the contact element (corresponding to Mohr-Coloumb parameters of the bentonite):

c_c =140 kPa
ϕ_c =8°

Initial conditions

The reference model refers to the buffer material after saturation and swelling in the deposition hole, which yields the following initial conditions:

e_0 =0.75
p_0 =8000 kPa
u_0 =5000 kPa

4.4.4 Influence of different factors on the parameters in the model

The CLAYTECH/S reference model refers to a specified material that has been compacted to a certain void ratio and is exposed to a well defined environment. However, the model is very general and valid also for other materials under other circumstances, although the parameters are different. The laboratory tests and the description of the tentative material model allows for changes in input parameters that can take the influence of different conditions into account.

Influence of stress history and initial conditions

The influence of the stress history on the void ratio of the blocks and their swelling in the deposition hole, will above all affect the location of the cap (p_b) and the initial conditions (e_0, p_0, and u_0). If the void ratio differs very much from that of the reference case it may be outside the range of validity for the parameters κ, λ, c_c, and ϕ_c, which thus have to be changed.

Influence of temperature

The only recorded influence of temperature refers to the properties of the pore water. The hydraulic conductivity will increase with increasing temperature according to Eqn 3-28. At a temperature of 90°C the hydraulic conductivity will be higher than that at the reference temperature 20°C by a factor of 3.7. The bulk modulus of water is only slightly influenced. It is reduced by 4% at an increased temperature from 20°C to 90°C. The change in density will be changed automatically by the coefficient of thermal expansion.

Influence of buffer material composition

Several parameters are influenced by the bentonite type especially the montmorillonite content and the exchangeable cation. E.g. a change from Na-bentonite to Ca-bentonite will influence the values of the following parameters: a, c, *cap hardening relation*, κ, k, c_c, and ϕ_c. All these parameters can be evaluated from the results shown in this report except the cap hardening function.

Influence of pore water composition

The same parameters that were affected by the bentonite type, i.e. a, c, *cap hardening relation*, κ, k, c_c, and ϕ_c will be affected by a change in pore water composition. If pore water with 3.5% NaCl is absorbed by the bentonite the change in these parameters can be evaluated from the data in this report with the exception of the cap hardening relation.

5 VERIFICATION EXAMPLES

5.1 GENERAL

The CLAYTECH/S/A model has been checked by simulating four different laboratory tests. The following tests were calculated:

- Swelling/compression test in an oedometer
- Compression/swelling test in an oedometer
- Drained triaxial test
- Undrained triaxial test

Two types of calculations have been made for each test. Primarily, the calculations were made with idealised one-element tests. In these calculations the tested samples have been assumed to exert no friction on the walls or filter stones, and to be characterised by completely homogeneous stress fields and void ratios in the entire sample during the test. In order to see if friction has any effect on the recorded data, more complicated multiple element models with simulated friction on the boundaries have also been used.

The parameters used for the calculations differ slightly from the parameters of the "reference model" since some new tests have been made after these calculations. However, the difference is so small that the influence on the results can be neglected.

5.2 TEST 1. SWELLING-COMPRESSION IN AN OEDOMETER

5.2.1 One element calculation

In this sort of test, a radially confined sample with cylindrical shape was allowed to swell axially from a low void ratio and then be compressed back to its original void ratio. No modelling of pore pressure or pore water flow with pore pressure elements was made for this test type. The following input parameters were applied:

Cap plasticity

a = 2.58
c = 2.40
b = 0.77
γ = 0.1
R = 0.1

K = 1.0
p_b = 17000 kPa
p_f = -25000 kPa

Cap hardening

p	$^e\log(1+\varepsilon^v_{pl})$
kPa	
100	0
200	0.103
400	0.192
750	0.264
1200	0.299
2000	0.323
3500	0.379
5500	0.396
8500	0.415
17000	0.444
30000	0.490

Porous elasticity

κ=0.22
ν= variable with
ν_0 =0
ν_{max} =0.49
η =0

Initial conditions

e_0 =0.65
p_0 =9000 kPa

The input parameters thus define that the cap intersects the p-axis at p=17000 kPa while the starting pressure is p=9000 kPa. This means that the buffer material is overconsolidated to the pressure p=17000 kPa, which is justified by the observed elastic swelling after compaction in a series of compaction tests on MX-80.

The sample was unloaded to e=1.25 and then reloaded to e=0.65. The unloading and reloading was assumed to be continuous and slow enough to yield no pore pressure.

Results

The results of the one-element calculation is illustrated in three diagrams. Fig 5-1 shows the calculated stress-path in a *q-p* diagram. The stress path proceeds up to the failure surface and follows the failure surface at unloading. At reloading the principal stresses change sign but the stress path is still along the failure line. However, the location seems to be different, which may be explained by different stress paths. Thus, at unloading, the clay is overconsolidated and the stress path follows line 1 $q=ap^b$ (see Fig 3-7). However, this process is associated with dilatancy, which makes the cap shrink (see Fig 3-8) so that when the sample is reloaded the stress path will instead hit the critical state line $q=cp^b$.

The change in size of the cap is also shown in Fig 5-1, where the location of the cap p_b is plotted as a function of the void ratio. The figure shows that p_b decreases from the initial value 17000 kPa at e=0.65 to p_b=5500 kPa at e=1.25 and then starts to increase on reloading when e>0.85.

Fig 5-2 shows the calculated void ratio as a function of the axial and radial stress, which was measured in this test. The calculated behaviour agrees very well with the measured one, which was shown in chapter 2. It has an almost constant ratio of axial stress at reloading and unloading of about 2, and equal values of the radial stress at reloading and unloading. However, the magnitude of the stresses at high void ratio is somewhat overestimated. This will be further discussed in chapter 5.2.2.

5.2.2 Multiple element calculation

The element mesh for the multiple element calculation is shown in Fig 5-3. It is axi-symmetric around the left boundary and has a symmetry-plane at the bottom boundary. The structure consists of 40 solid elements and 10 friction elements. The friction elements are located at the outer radial boundary. The upper boundary, simulating the contact with the filter stone, does not allow radial deformation (infinite friction). The dimensions of the mesh are

Height 11 mm (total sample height h=22 mm)
Radius 17.5 mm

The same data for the input parameters as in the one-element test were used for the multiple element test with the only exception that ν_{max}=0.48 was used instead of 0.49: The friction angle ϕ_c=6° were used for the friction elements. The same initial conditions and the same unloading to e=1.25 followed by reloading to e=0.65 were simulated.

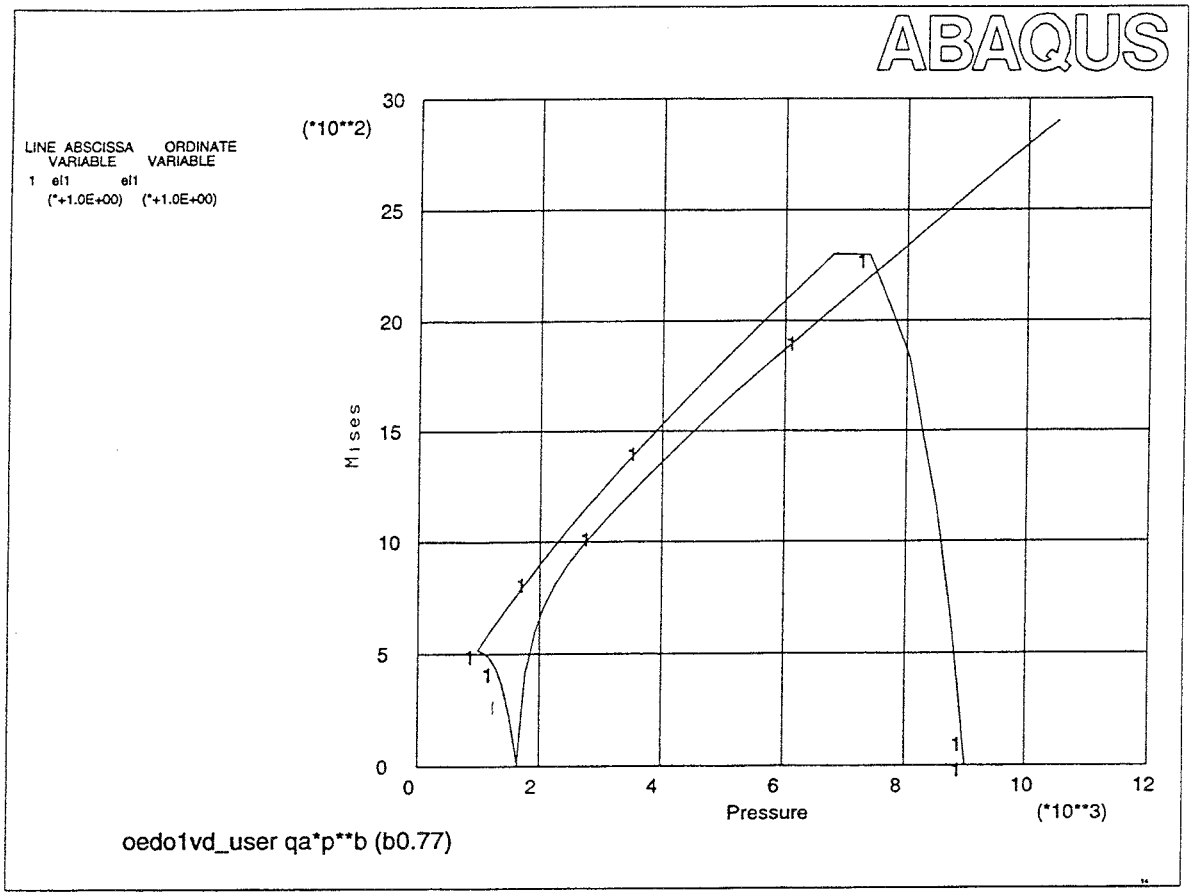

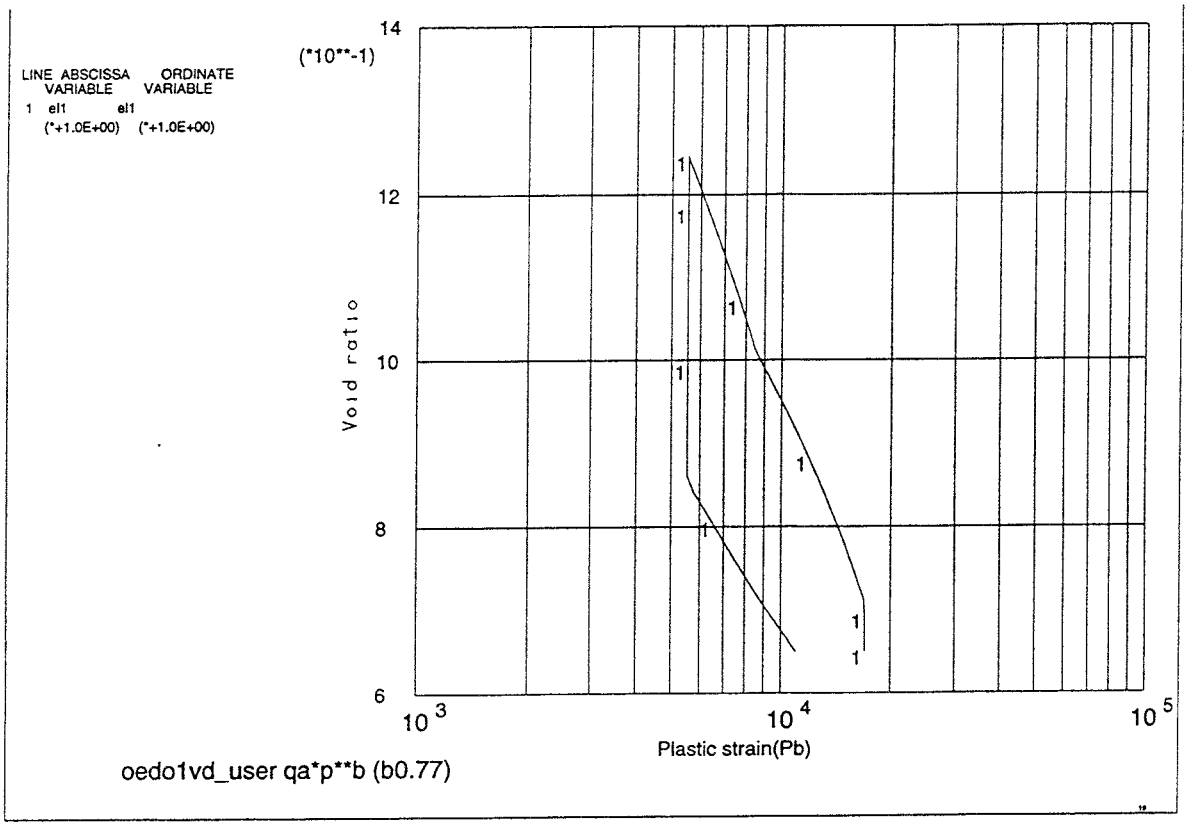

Figure 5-1. *One element calculation of the swelling-compression test.*
Upper: Stress path in a p-q diagram (kPa)
Lower: Location of the cap p_b (kPa) during the test as a function of the void ratio (start: p_b=17000 kPa).

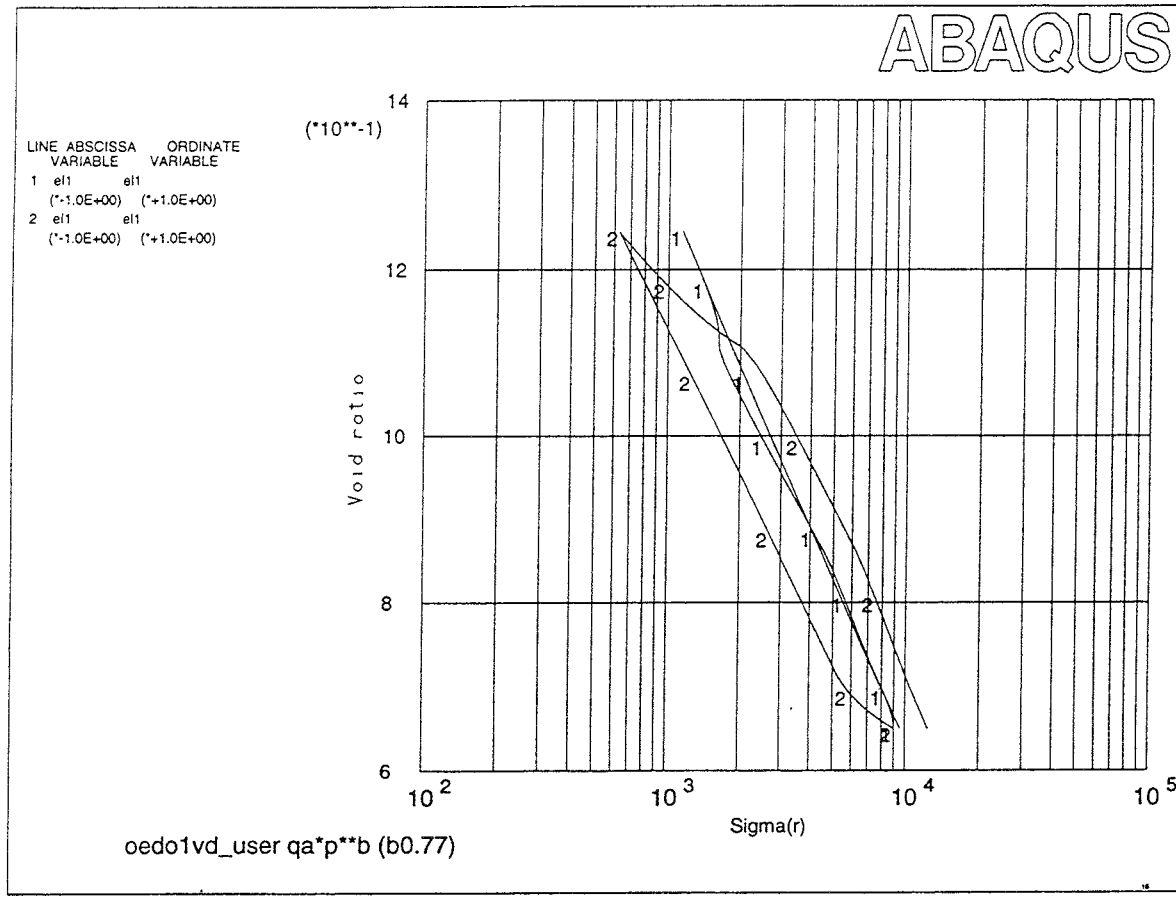

Figure 5-2. One element calculation of the swelling-compression test. σ_r-e (curve 1) and σ_a-e (curve 2). Start at p=9000 kPa and e=0.65.

91	92	93	94	95
81	82	83	84	85
71	72	73	74	75
61	62	63	64	65
51	52	53	54	55
41	42	43	44	45
31	32	33	34	35
21	22	23	24	25
11	12	13	14	15
1	2	3	4	5

Figure 5-3. Element mesh and numbering for the multiple element oedometer calculations. The mesh is axi-symmetric around the left boundary and has a symmetry plane in the bottom.

Results

The results can be specified for the respective element or reported for the entire clay body, simulating a real test. Fig 5-4 shows what can be simulated using the following variables:

- The axial stress σ_a= the applied force divided by the average axial cross section area.
- The radial stress σ_r= the radial pressure on friction element 5 (corresponding to the location of the pressure transducer).
- The void ratio e= the average void ratio in the entire sample

The "deviator stress" is calculated as $D=\sigma_a-\sigma_r$ and plotted as a function of the "average stress" $p=\sigma_a+2\sigma_r$. Fig 5-4 shows that the difference between this calculation and the one-element calculation is not very large (although D can be negative in contrast to q). The effect of the friction on the radial oedometer ring can be seen as a slightly increased ratio of the axial stress at reloading and unloading but the difference is surprisingly small. It thus seems that the measured stronger reduction in pressure at unloading is not caused by the friction but by the choice of parameters. This can be remedied by reducing the swelling. There are two ways of reducing the swelling; one is to decrease κ (makes the material stiffer) and the other one is to reduce the dilatancy (reduces the volume increase during unloading along the failure line).

The resulting stresses, pore pressure and strains in each element have been calculated but cannot be shown here since it will need too much space, but Figs. 5-5 and 5-6 show some examples. Fig 5-5 shows the stress path in a q-p diagram for three elements; one located in the centre of the sample (element 1), one close to the filter stone (element 91), and one close to the oedometer ring (element 4). Fig 5-6 shows contour plots of the void ratio and the Mises' stress after swelling to e=1.25. The effect of the friction is seen as inhomogeneities along the right radial boundary.

5.3 TEST 2. COMPRESSION-SWELLING IN AN OEDOMETER

This test differed from Test 1 by starting with an uncompacted sample at a very low density instead of a very high one. The sample was loaded to a high pressure similar to the starting pressure of the other test. After loading the sample, it was unloaded back to the initial pressure. The process during loading differs very much from the process during loading at Test 1 since the sample in this test was normally consolidated during the entire loading phase and the plastic strain was thus large. The input parameters for the calculation were the following:

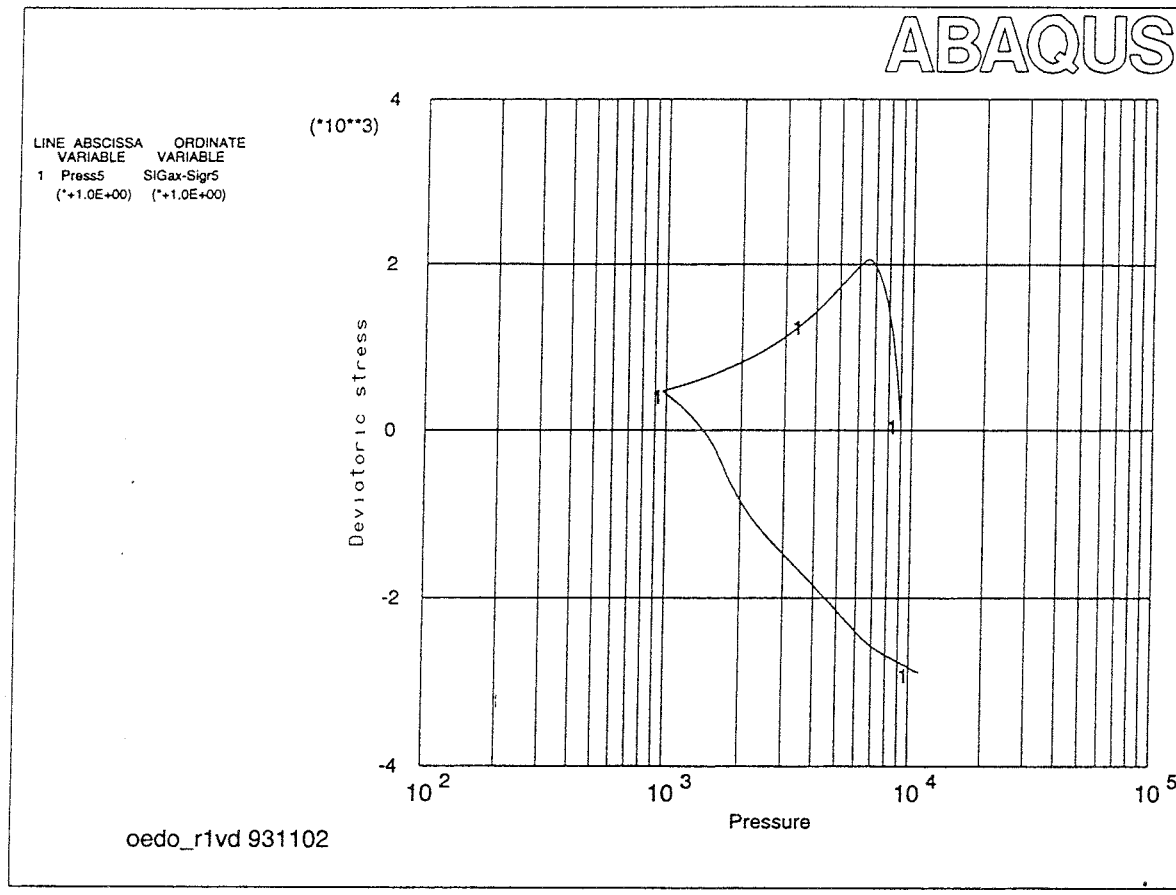

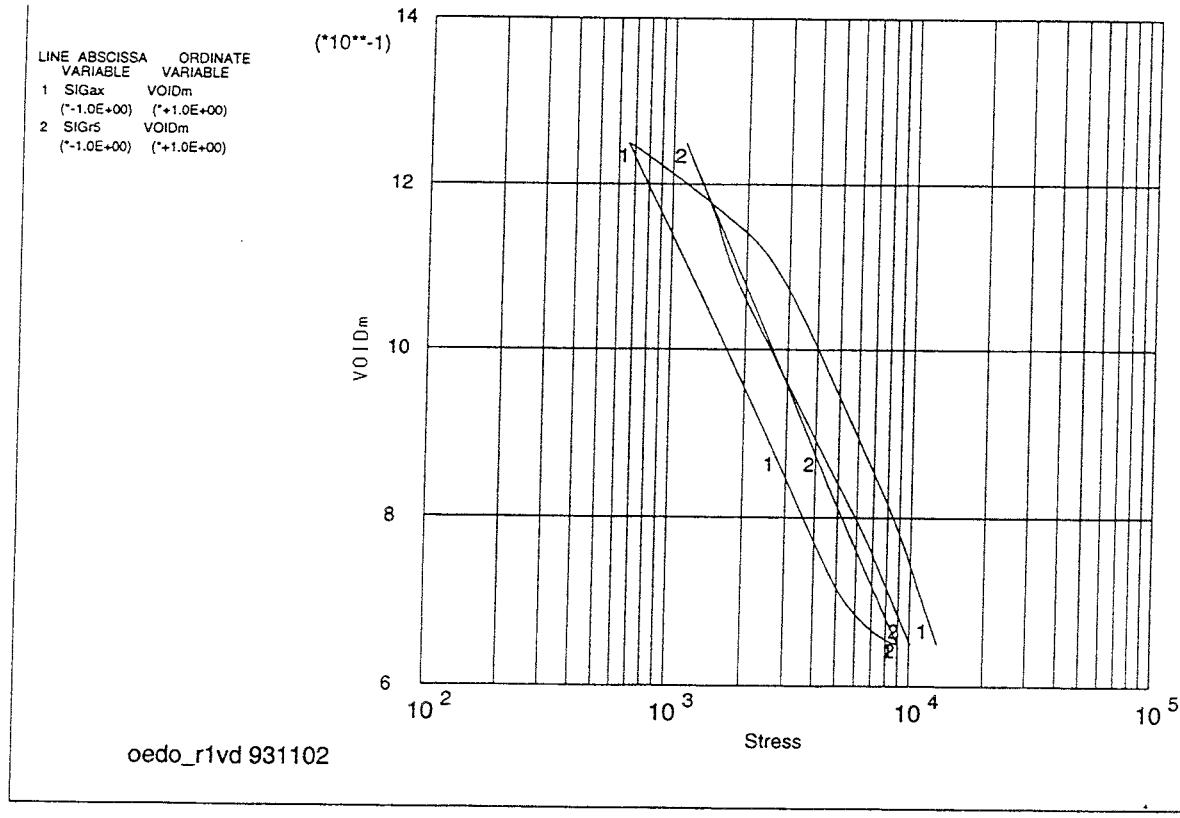

Figure 5-4. *Multiple element calculation of the swelling-compression test. Upper: Deviatoric stress D (kPa) as a function of the average pressure p (kPa).*
Lower: Void ratio e as a function of the axial stress σ_a (kPa; curve 1) and σ_r (kPa; curve 2)

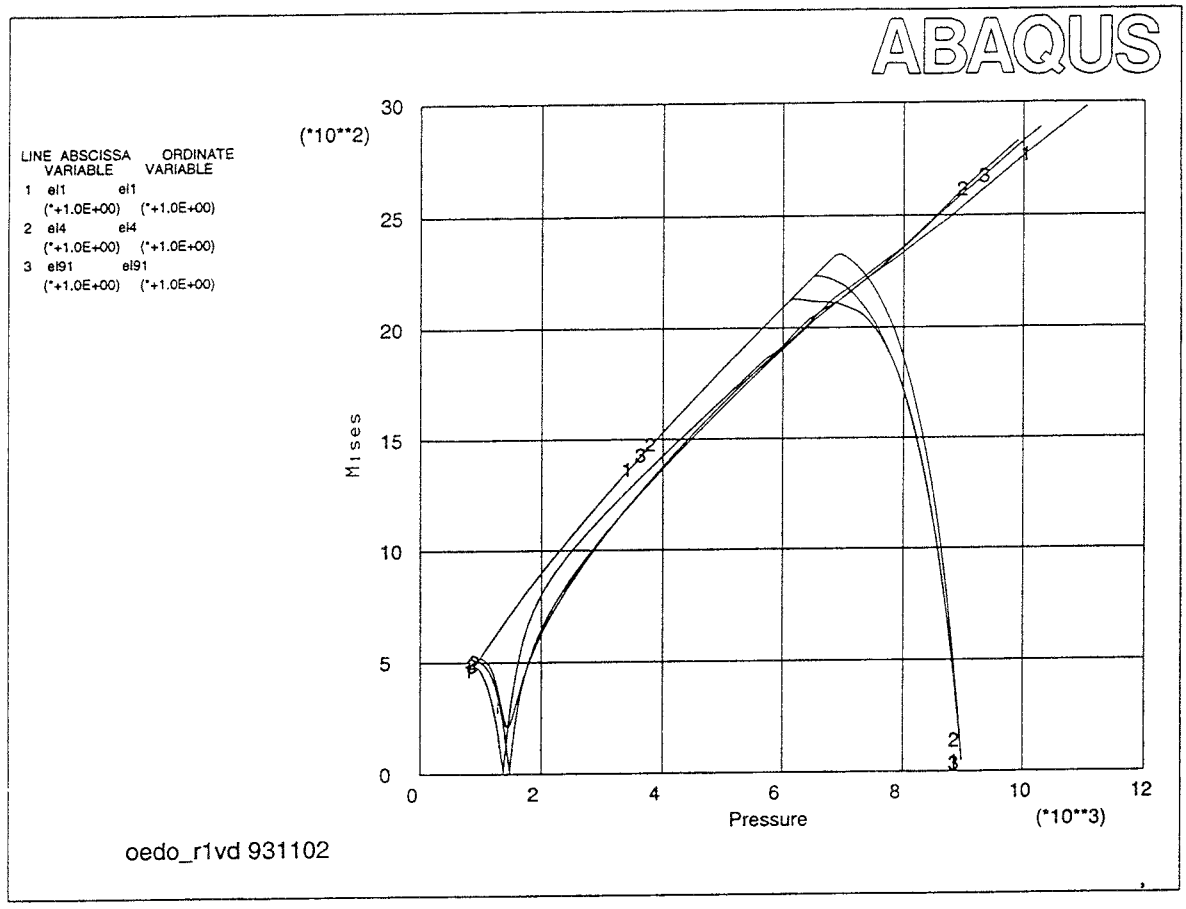

Figure 5-5. *Multiple element calculation of the swelling-compression test. Mises stress q (kPa) as a function of the average stress p (kPa) in three elements.*

Cap plasticity

a	= 2.58
c	= 2.40
b	= 0.77
γ	= 0.1
R	= 0.1
K	= 1.0
p_b	= 100 kPa
p_f	= -25000 kPa

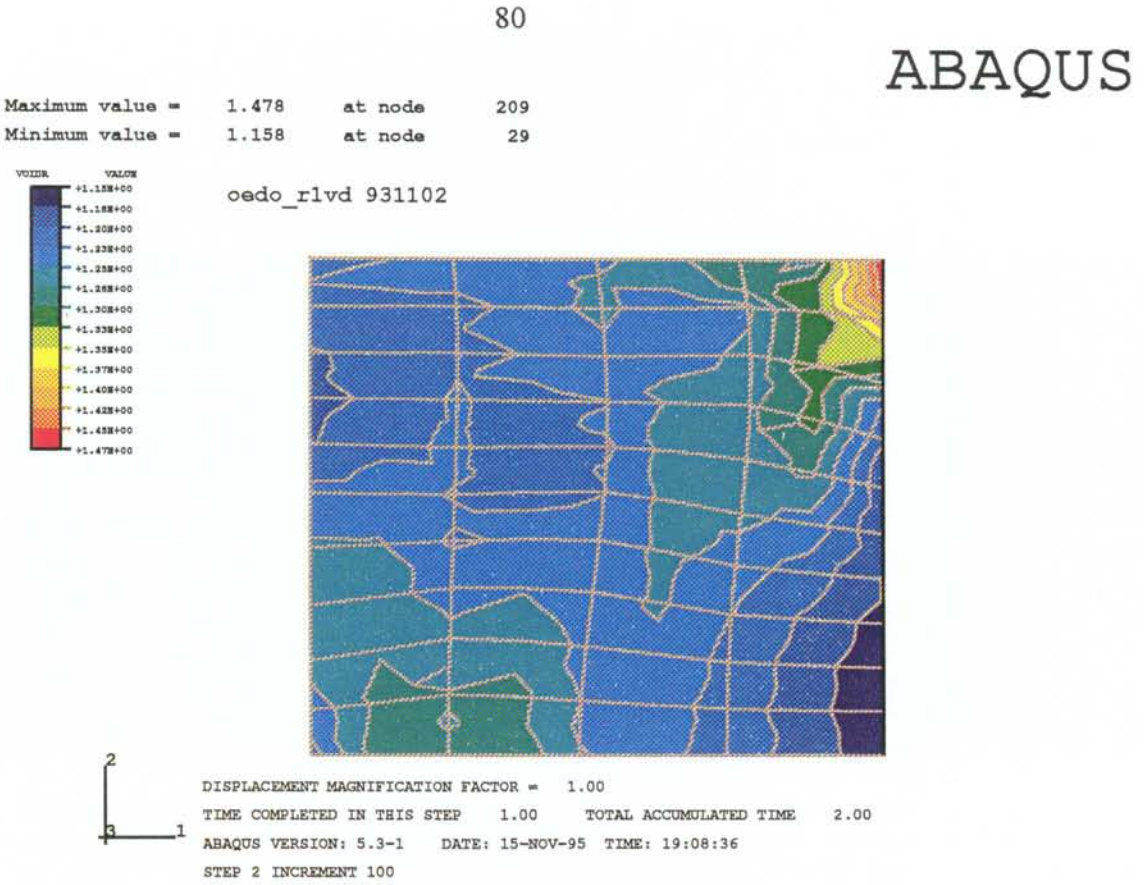

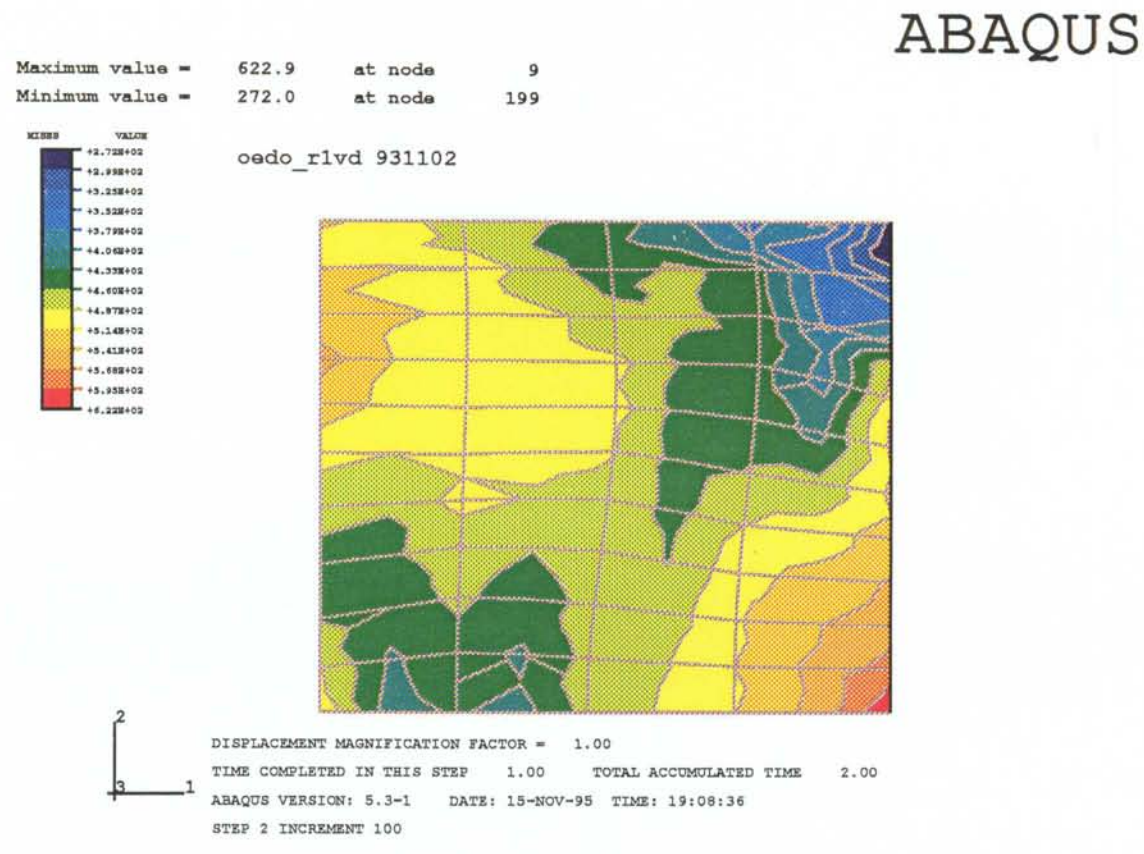

Figure 5-6. *Multiple element calculation of the swelling-compression test. Contour plots of the void ratio (upper) and the Mises' stresses (kPa; lower) after maximum swelling to an average void ratio of e=1.25.*

Cap hardening

p	${}^{e}\log(1+\varepsilon^{v}_{pl})$
kPa	
100	0
200	0.103
400	0.192
750	0.264
1200	0.299
2000	0.323
3500	0.379
5500	0.396
8500	0.415
17000	0.444
30000	0.490

Porous elasticity

κ=0.22
ν= variable with
ν_0 =0
ν_{max} =0.49
η =0

Initial conditions

e_0 =2.7
p_0 =100 kPa

The only difference in input parameters from test 1 was the location of the cap p_b and the initial conditions. In the present case p_b was equal to the start stress p=100 kPa. The sample was loaded and deformed from e=2.7 to e=0.8 and then unloaded to e=1.6.

Results

The results are illustrated in the same way as test 1. Fig 5-7 shows the stress path and the location of the cap p_b. These diagrams show that the stress path follows the critical state line $q=cp^b$ and moves the cap in front of the path during the entire loading phase until p=8.4 MPa and p_b=8.8 MPa. At unloading, the stress path goes "backwards" in the elastic domain, the principal stresses change sign, and the stress path hits the failure line $q=ap^b$. Here, the material starts to dilate and the cap begins to shrink at the same time as the path follows the failure line to very low stresses.

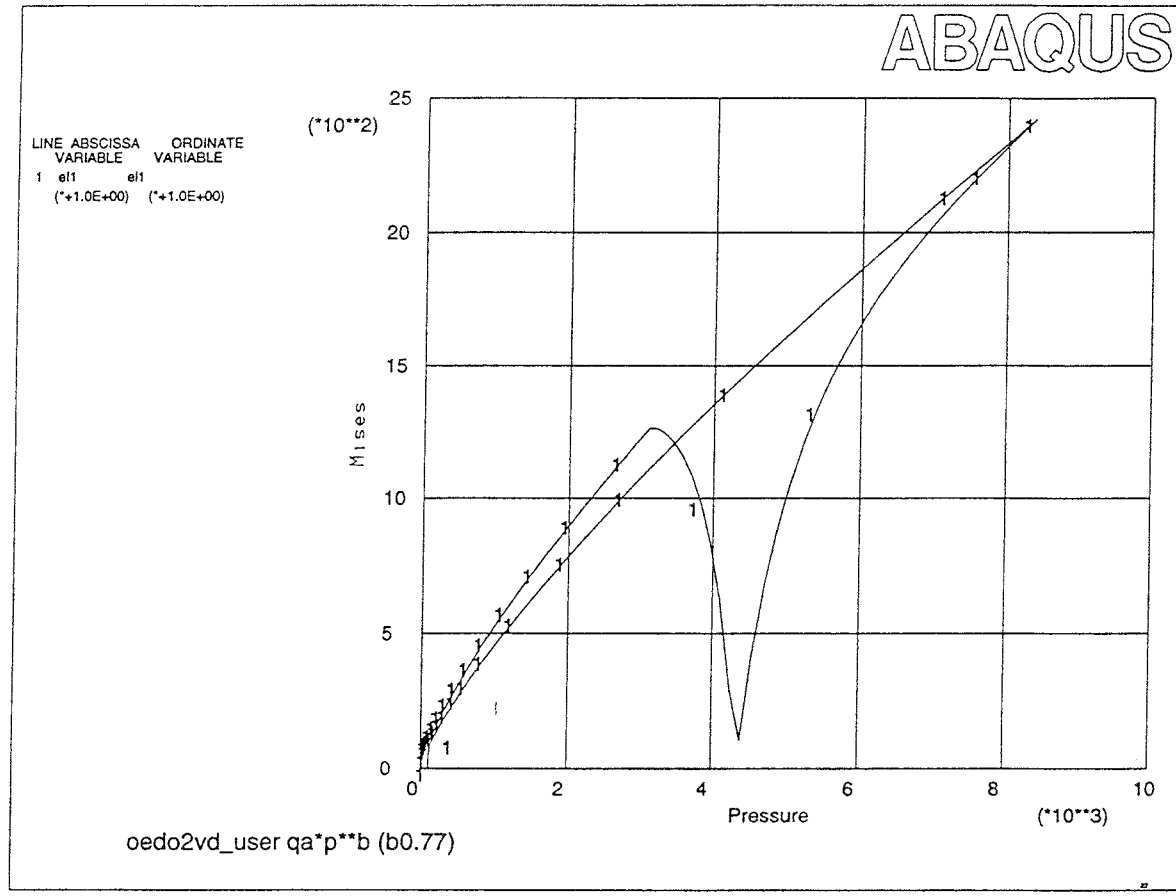

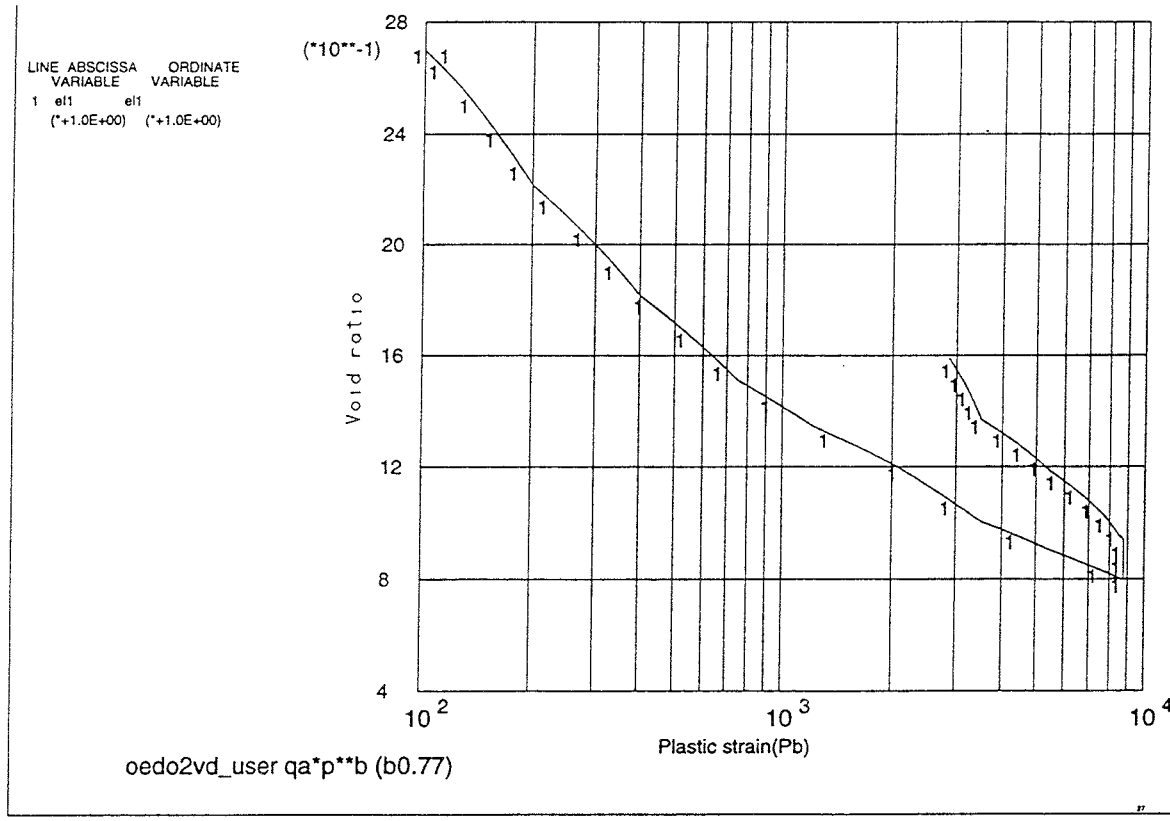

Figure 5-7. *One element calculation of the compression-swelling test. Upper: Mises' stress q (kPa) as a function of the average stress p (kPa). Lower: Relation between the void ratio and athe location of the cap p_b (kPa). The start value of both p and p_b are 100 kPa.*

Fig 5-8 shows the void ratio as a function of the axial and radial stresses. The diagram shows the large influence of the cap yielding much smaller swelling than compression. The void ratio is only e=1.6 at the average stress p=100 kPa, which can be compared to the start condition e=2.7 at p=100 kPa.

This effect was not possible to simulate by use of the earlier model because of the missing cap. The true behaviour of the clay, which is predicted by the model, can be seen in Fig 5-9, which shows the measured relation between the void ratio and the axial (p_a) and radial (p_r) pressures. The e-p_a relation agrees at compression as well as at swelling while the e-p_r relation agrees very well during compression but not at swelling for e>1.2. In fact, the measured very high radial pressure at e>1.2 does not make real sense and some complementary tests should be made to study the behaviour at swelling to high void ratios.

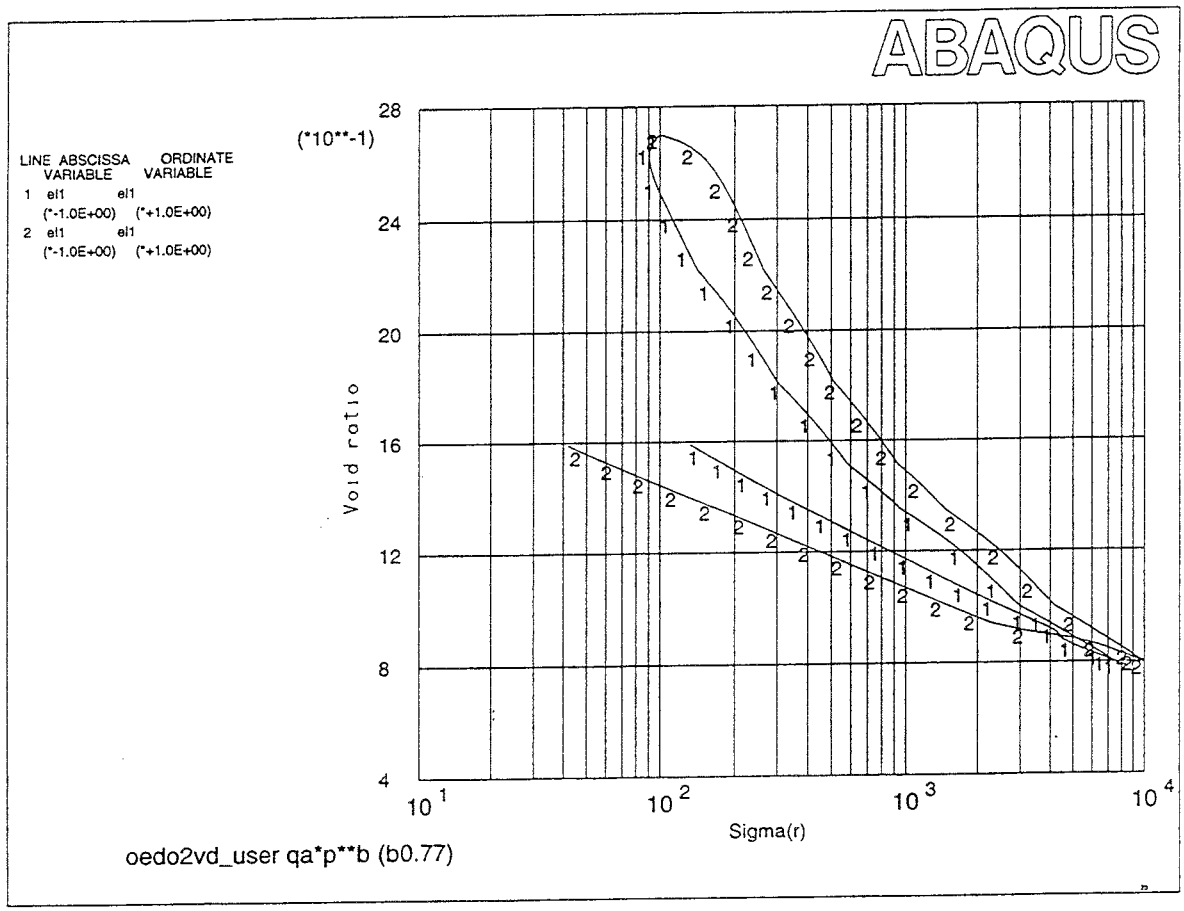

Figure 5-8. *One element calculation of the compression swelling test. The void ratio e as a function of the axial pressure σ_a (curve 2) and the radial pressure σ_r (curve 1)(kPa).*

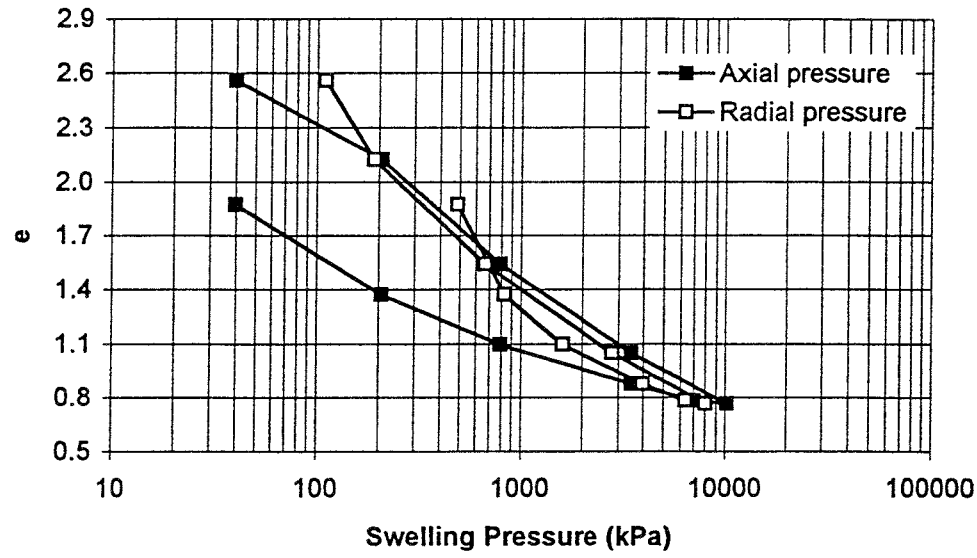

Figure 5-9. Measured pressures at a compression-swelling test on MX-80 made in the laboratory (KMXAR4).

5.4 TEST 3. DRAINED TRIAXIAL TEST

5.4.1 General

Both drained and undrained triaxial tests have been simulated by use of the new model. The idealised case with only one element and no friction, as well as the realistic case with many elements have been considered.

5.4.2 One-element calculation

In the one-element calculation of the drained test, no pore pressure gradients can occur so the pore pressure was not modelled in this calculation. The element was axi-symmetric with 3.5 cm height and 1.75 cm radius. The input parameters were identical to those of the one element calculation of test 1. This means that the sample was overconsolidated with the cap at p_b=17000 kPa and that the start conditions corresponded to a void ratio of e=0.65 and an isotropic pressure of p=9000 kPa. The sample was loaded axially until 10% strain was reached.

Results

The results are illustrated in Fig 5-10 where Mises' stress and the void ratio are plotted as a function of the displacement. The total displacement $3.5 \cdot 10^{-3}$ thus corresponds to 10% strain. The results show the following facts:

- Failure occurs at the correct Mises stress (according to Fig 3-6).
- The stress-strain curve is non-linear in the same way as in the real test.
- The void ratio decreases from 0.65 to at minimum 0.626 and then starts to increase slowly. The corresponding volume decrease is 1.5%, which is in the same range as achieved in the measurements (1%-3%).

5.4.3 Multiple element test

The element mesh for the calculation using many elements and friction between the filter stones and the sample is shown in Fig 5-11. The mesh is similar to that used in Test 1 with axial symmetry around the left boundary and a symmetry plane in the bottom. The friction against the filter stone was simulated by locking the upper nodes in the radial direction. In the real tests filter strips were emplaced along the radial periphery of the sample in order to allow for faster radial drainage. The filter stones at the top and the filter strips were hydraulically simulated by ascribing a pore pressure u=0 to the upper and right boundaries during the entire test. The pore pressure and pore water flow were simulated in this calculation.

The total mesh was given a height of 3.5 cm and a radius of 1.75 cm. The sample was sheared in the same way as in a real triaxial test by displacing all the upper element nodes simultaneously at a constant rate of 10% in 40 days, corresponding to about 0.01% per hour, which is equal to the rate used in the real tests.

Results

The results are accounted for in the same way as for Test 1. Fig 5-12 shows the results recalculated to correspond to the average deviator stress and the average void ratio, which are plotted as functions of the strain. The results do not differ very much from the results of the one-element test but the transition from elastic to plastic behaviour, which can be seen as a discontinuity in the one element curves, has disappeared. Also, the start of the volume increase has been delayed to beyond 8% strain instead of 5%.

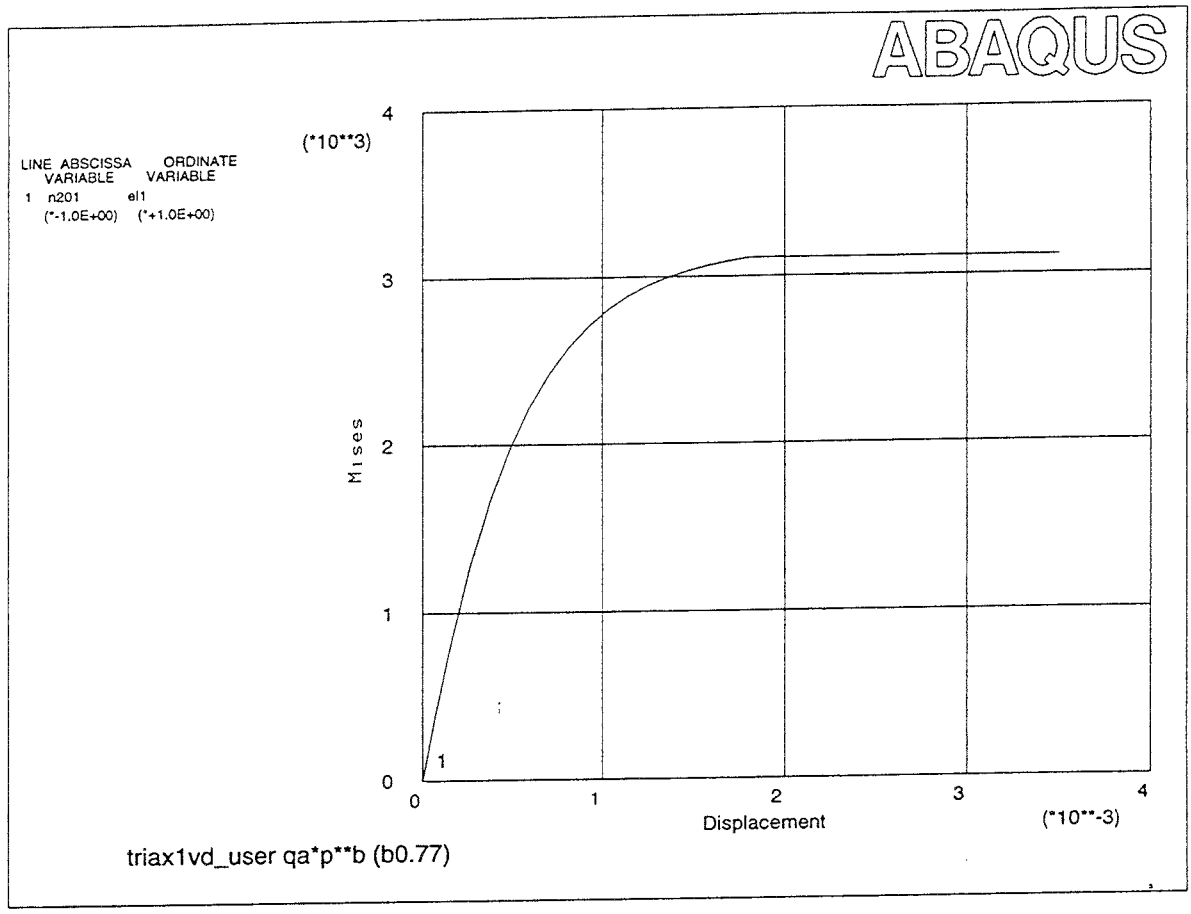

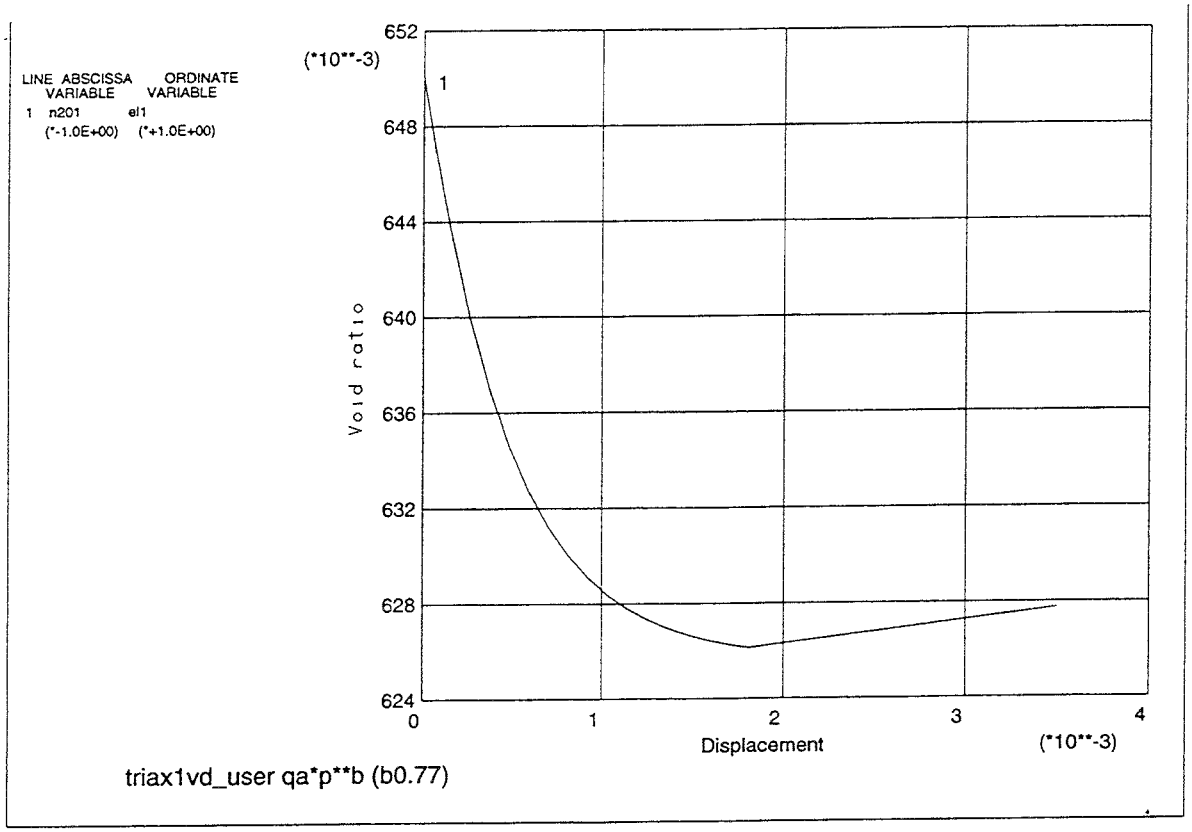

Figure 5-10. *One element calculation of a drained triaxial test. Upper: Mises' stress (kPa) as a function of the axial displacement (m). Lower: Void ratio as a function of the axial displacement (m).*

181	183	185	187
161	163	165	167
141	143	145	147
121	123	125	127
101	103	105	107
81	83	85	87
61	63	65	67
41	43	45	47
21	23	25	27
1	3	5	7

Figure 5-11. *Element mesh and numbering for the multiple element triaxial test calculations. The mesh is axi-symmetric around the left boundary and has a symmetry plane in the bottom bondary.*

The processes in element 1 (centre), element 7 (at the radial boundary), and element 181 (at the filter stone) are shown in 4 diagrams in Figs 5-13 and 5-14. The stress path and stress-strain relation are shown in Fig 5-13. Element 181 is the only one that behaves in a significantly different fashion than the average element. In Fig 5-14 the pore pressure and void ratio development are plotted in two diagrams, showing that the void ratio of element 181 is quite different from that of the central elements. One finds that the pore pressure quite logically is highest for element 1. The pore pressure development is interesting because it shows that despite the drainage and slow displacement, there are quite high pore pressures in the beginning of the test even close to the drained boundaries. However, the pore pressure disappears fairly quickly and at the end of the test it is close to zero. At the failure surface, which is reached after half the test time, the maximum pore pressure is about 200 kPa or 2% of the average stress, which is acceptable for a drained test. However, it is obvious that the strain rate according to this calculation is a bit too high.

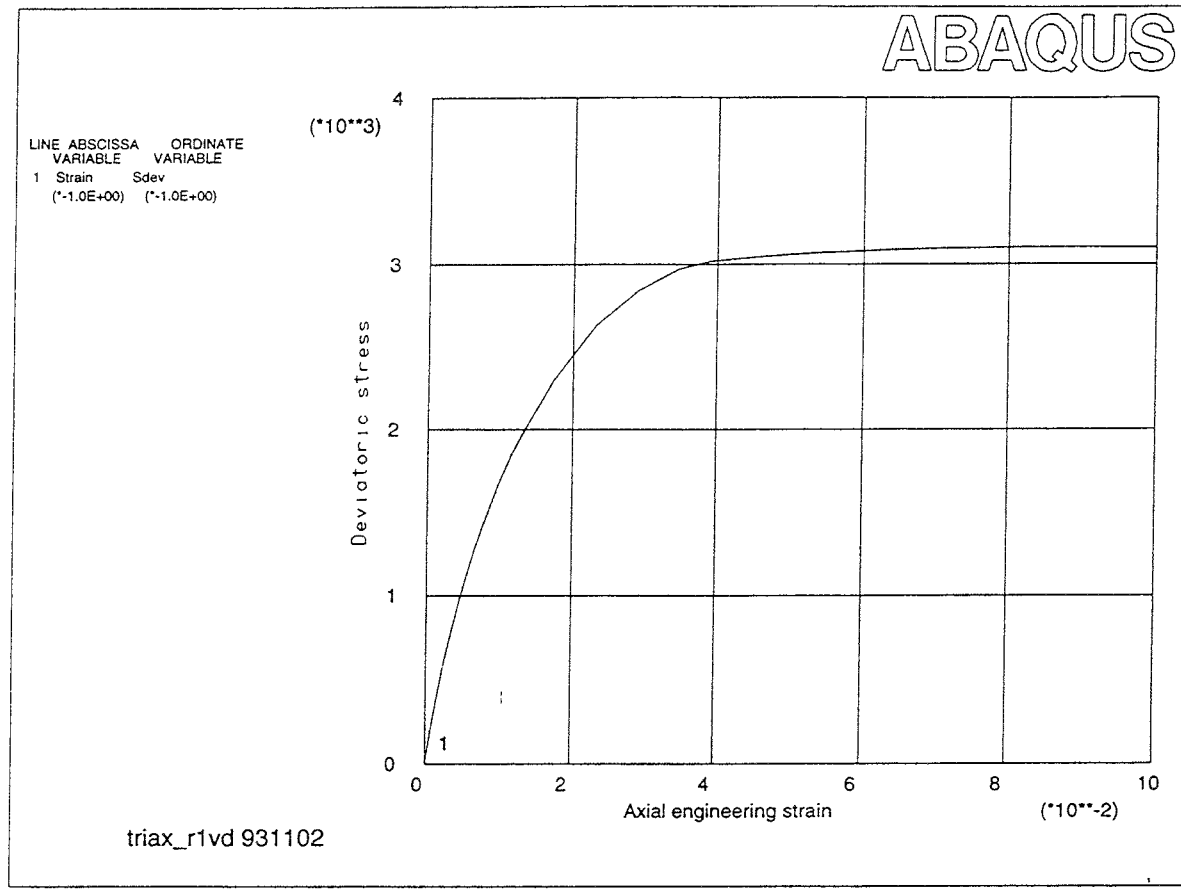

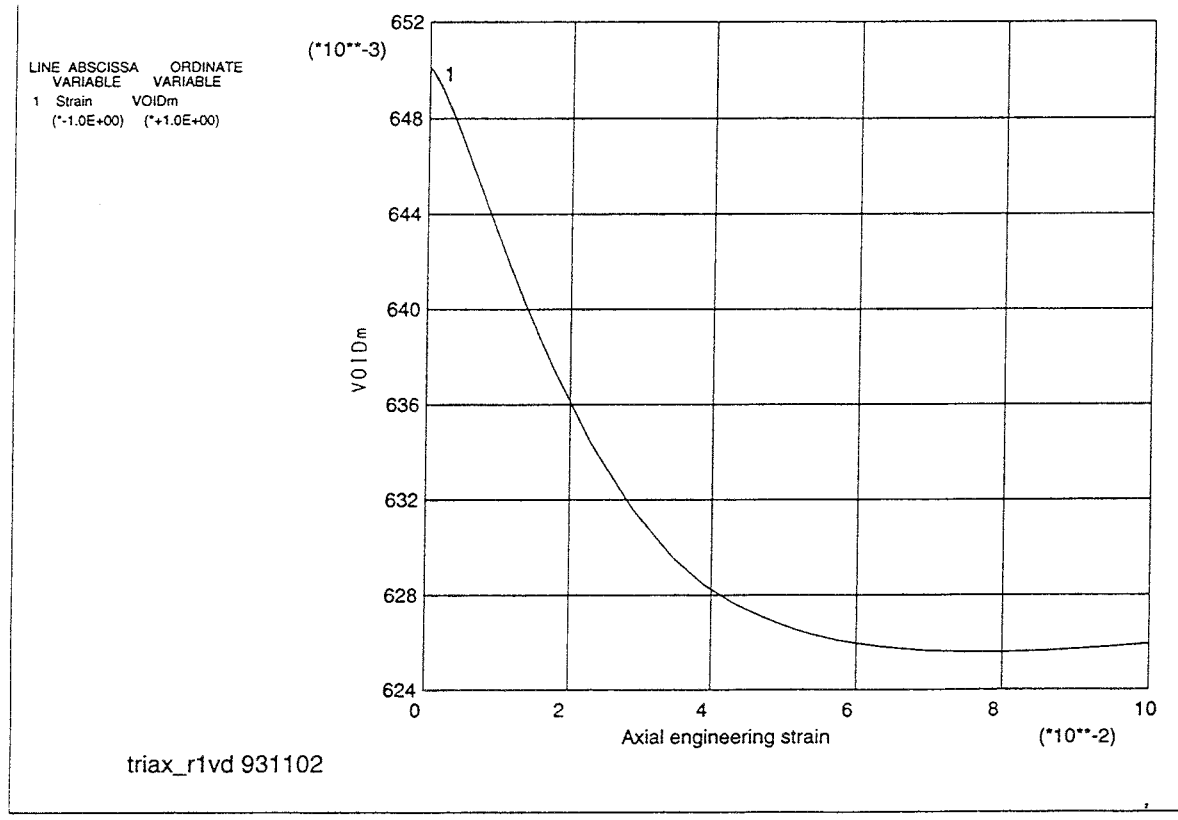

Figure 5-12. *Multiple element calculation of a drained triaxial test. Upper: Deviatoric stress D (kPa) as a function of the axial strain. Lower: Average void ratio e as a function of the axial strain*

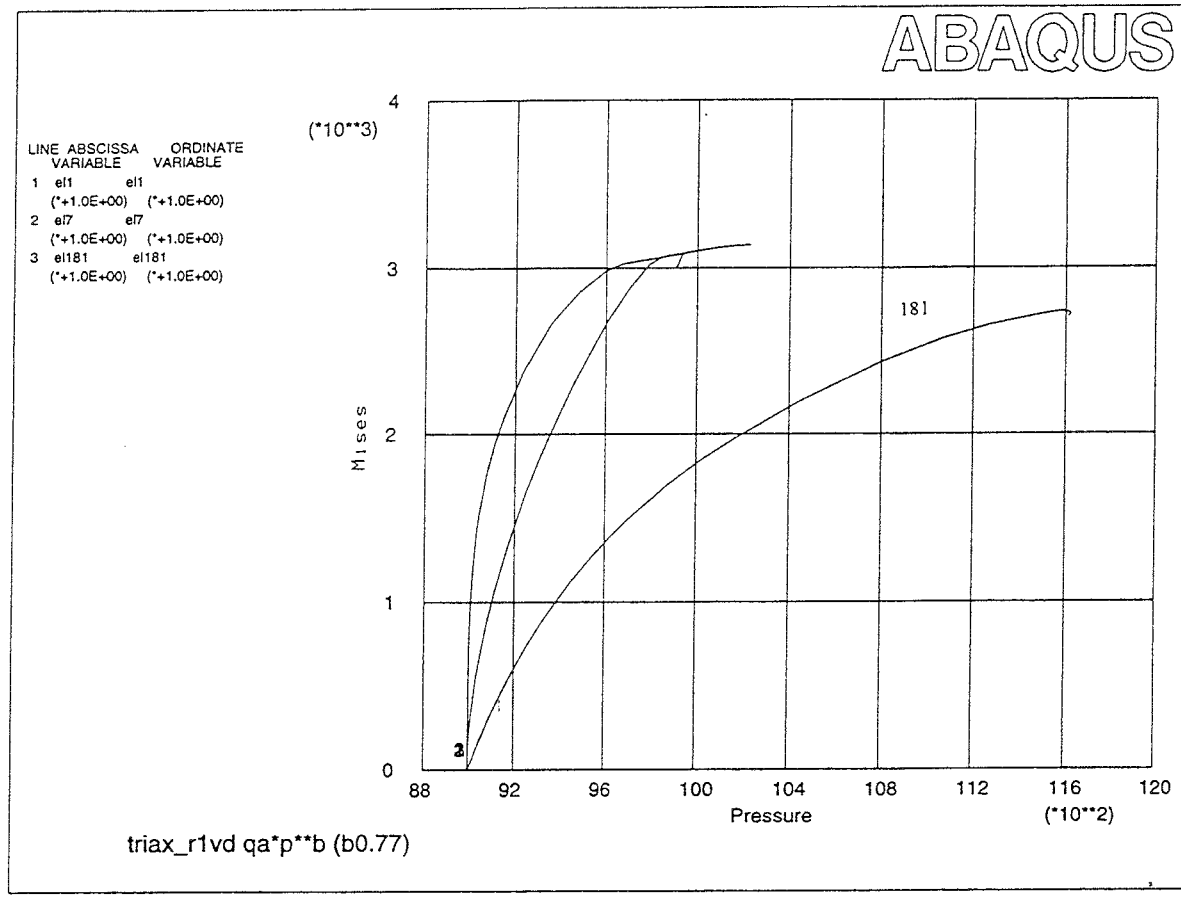

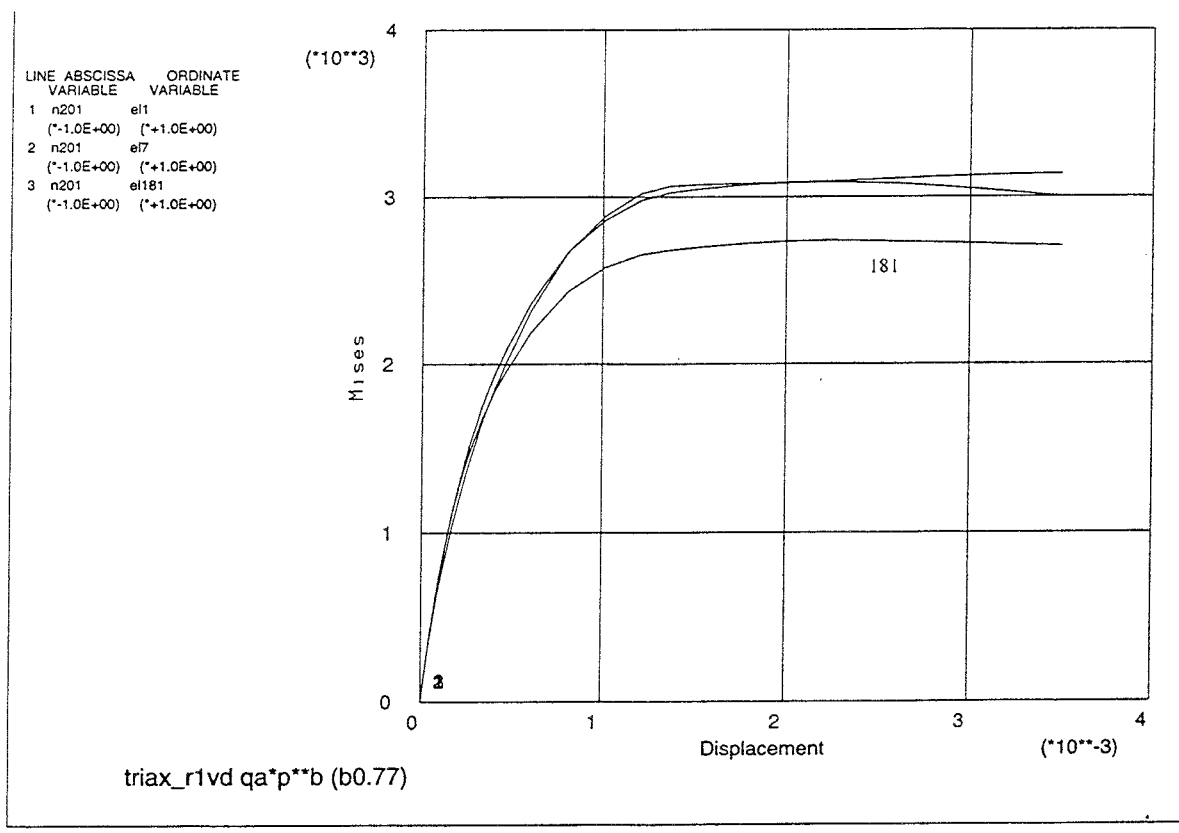

Figure 5-13. *Multiple element calculation of a drained triaxial test. Results for elements 1, 7 and 181.*
Upper: Mises' stress q (kPa) as a function of the average stress p (kPa).
Lower: Mises' stress q (kPa) as a function of the axial displacement (m).

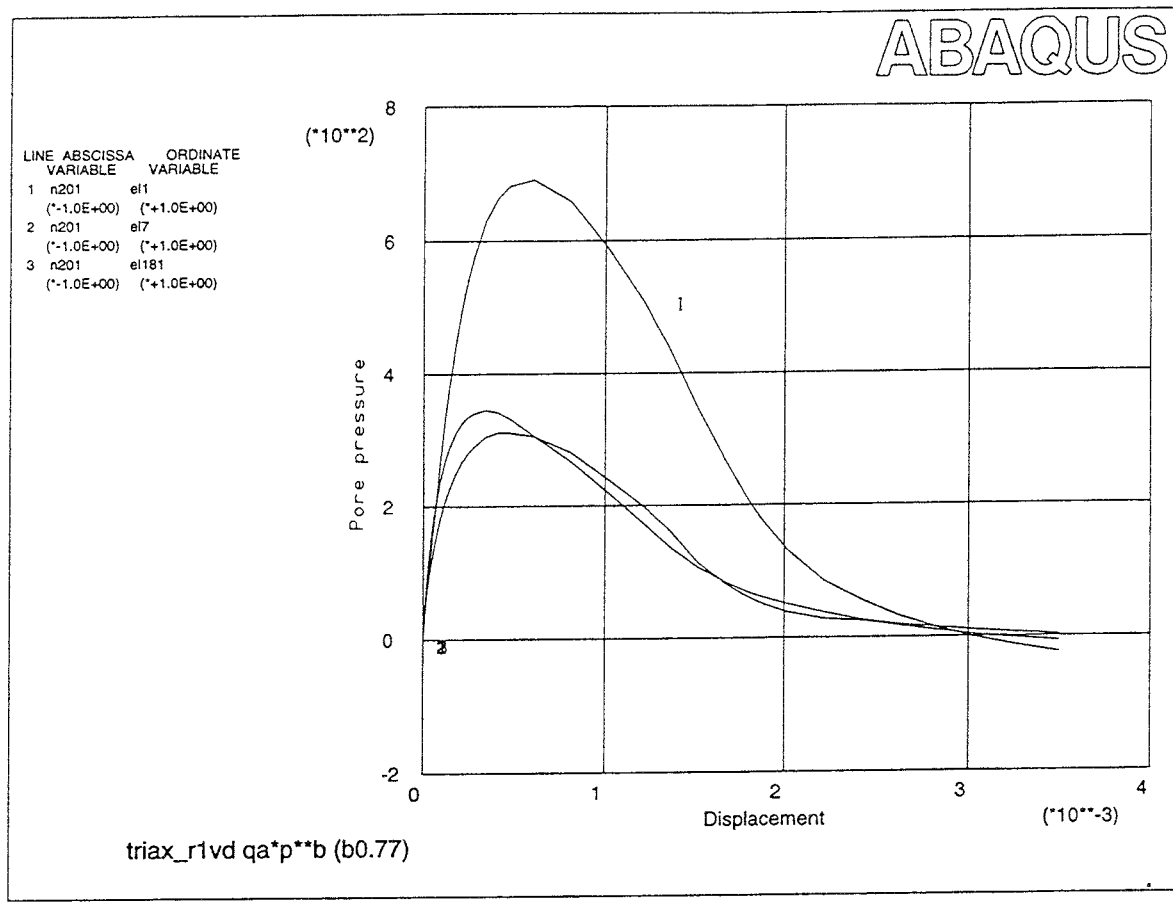

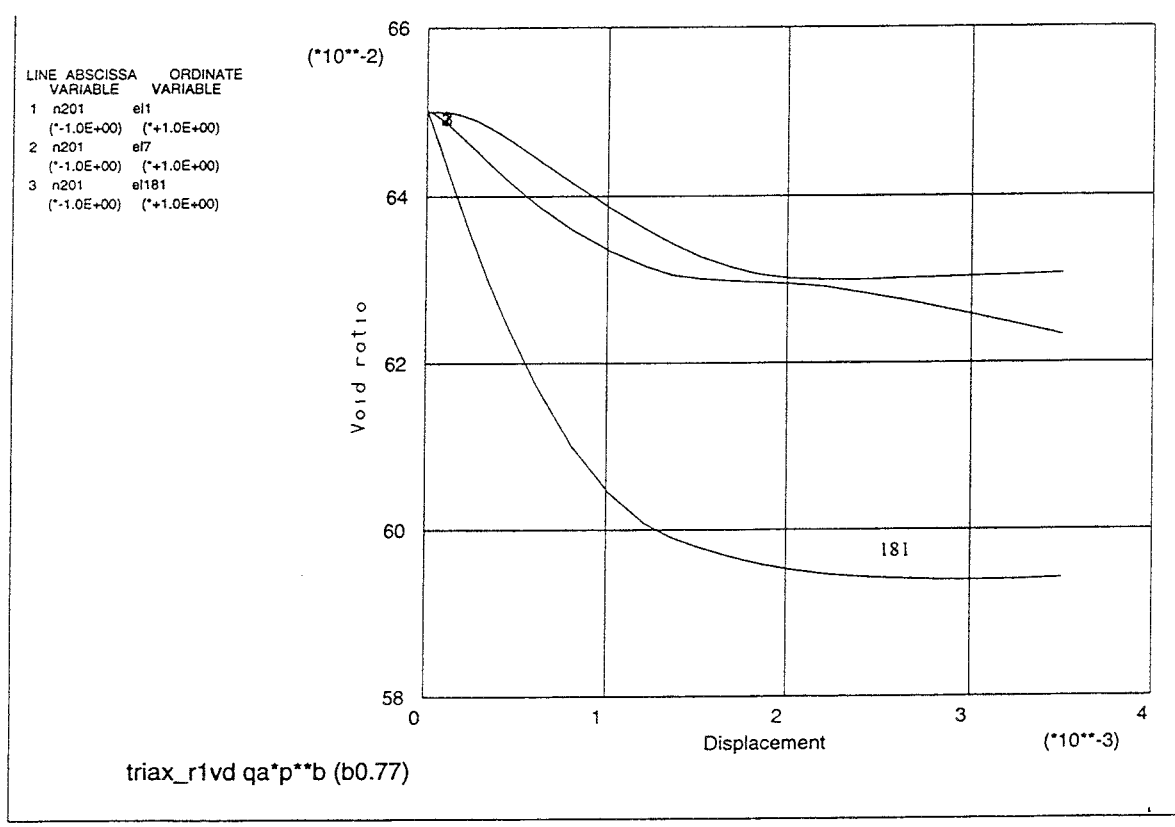

Figure 5-14. *Multiple element calculation of a drained triaxial test. Results for elements 1, 7 and 181.*
Upper: Pore pressure u (kPa) as a function of the axial displacement (m).
Lower: Void ratio as a function of the axial displacement (m).

Fig 5-15 shows the deformed structure after 5% and 10% strain and the void ratio distribution after 5% strain. The figure shows that the sample is rather homogeneous with a variation in void ratio that is smaller than a few per cent except for close to the filter stone. The deformed structure shows two interesting features. At 5% strain the sample is barrel-shaped as in the calculation with the earlier model. However, at 10% strain there is a quite different eccentric bulge at some distance from the symmetry plane. One interpretation of this phenomenon is that the sample is about to fail asymmetrically, which it does in most cases in real tests, resulting in a slip plane at about 45° angle to the axis of the sample. However, since the mesh is axi-symmetric it cannot fail in this way and the result will instead be a bulge. This phenomenon should be investigated by conducting calculations using real 3D element meshes.

5.5 TEST 4. UNDRAINED TRIAXIAL TEST

5.5.1 General

The undrained triaxial test was simulated by performing the same type of calculations as for the drained test.

5.5.2 One-element test

The same element type and boundary conditions were used as in Test 3, the only difference being that the pore pressure was simulated by using a so-called pore pressure element. The undrained condition was simulated by letting the boundaries of the element be free with respect to the pore pressure, implying that no water could leave the element. The input parameters were identical with the ones in Test 3 and the initial pore water pressure was given the value u=0. The sample was deformed axially until 10% strain was reached, corresponding to a displacement of 3.5 mm.

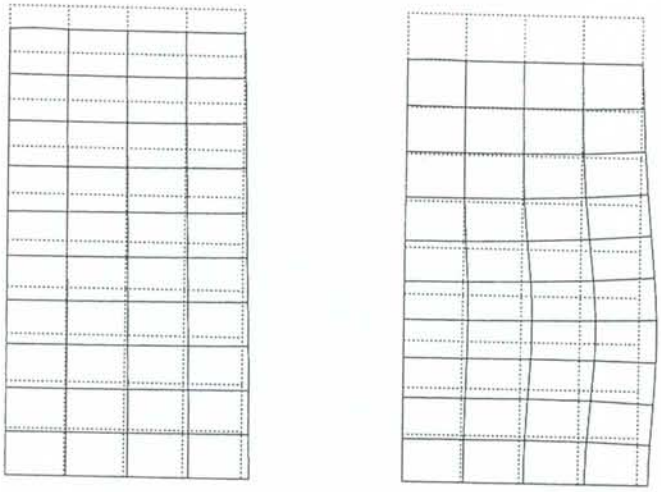

ABAQUS

Maximum value = 0.6473 at node 202
Minimum value = 0.5861 at node 209

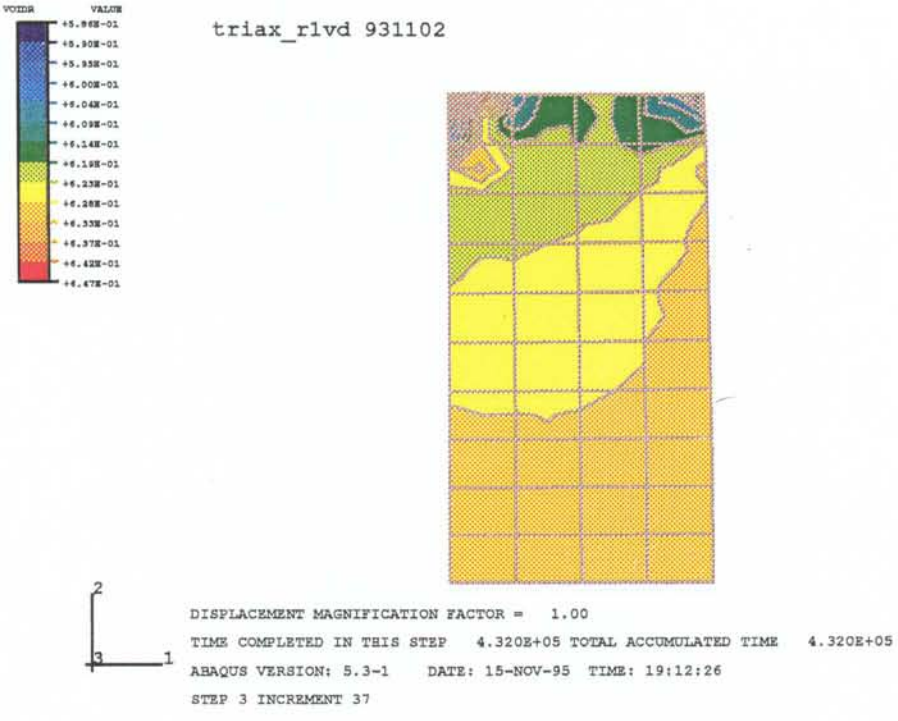

Figure 5-15. *Multiple element calculation of a drained traixial test.*
Upper: Deformed structure after 5 and 10% axial strain.
Lower: Contour plot of the void ratio after 5% axial strain.

Results

The results are illustrated in Figs 5-16 and 5-17. The Mises stress and the pore pressure are shown in Fig 5-16 as a function of the displacement. The results are similar to the results of Test 3 but the maximum Mises stress, corresponding to the shear strength is a little lower and the decrease in void ratio a little higher, corresponding to an increase in pore pressure to 900 kPa. The increase in pore pressure affects the stress path, which is shown in Fig 5-17 together with the change in void ratio. The pore pressure increase balances the increase in average stress almost exactly, which makes the stress path practically vertical in the *p-q* diagram until the failure surface is reached and the sample starts to dilate. The stress path thus shows that the strength in an undrained test is lower than in a drained test since the stress path hits the failure envelope at a lower average stress. The deviation from a perfectly vertical stress path is due to the very small decrease in void ratio that takes place despite the undrained conditions. The decrease is very small, however, as shown in the diagram. It is caused entirely by the compression of the pore water.

5.5.3 Multiple element test

The element mesh in Test 3, which was shown in Fig 5-11, was also used for Test 4. The only difference was the boundary condition for the pore pressure which was defined by an equation that makes the pore pressure in the nodes in the upper and left boundaries (corresponding to the filters) equal. The geometry and all input parameters were the same as in Test 3 except for the rate of strain which was 10% in 10 days (4 times faster than in the drained test).

Results

Figs 5-18 and 5-19 show the results recalculated to yield average parameters that can be measured. The deviator stress (or Mises' stress) and pore pressure differ very little from the results of the one-element test and the stress path in this calculation is also very close to vertical as shown in Fig 5-19 although the average stress decreases a little from the start value p=9000 kPa to p=8900 kPa at the beginning of the yielding.

Figs 5-20 and 5-21 show the specific results for the three elements 1, 7, and 181 (see Fig 5-11). The stress-strain relation and the stress path, shown in Fig 5-20, resemble the results from the drained test. The Mises' stress is lower and the stress path different for element 181, which is located in contact with the filter stone. The pore pressure development and the change in void ratio, accounted for in Fig 5-21, show that there is quite a substantial change in void ratio despite the undrained conditions. The achieved inhomogeniety causes a difference in pore pressure and redistribution of water inside the sample. The pore pressure curves show that there is a difference in pore pressure of about 100 kPa at a certain stage and that this difference has dissipated at the end of the test.

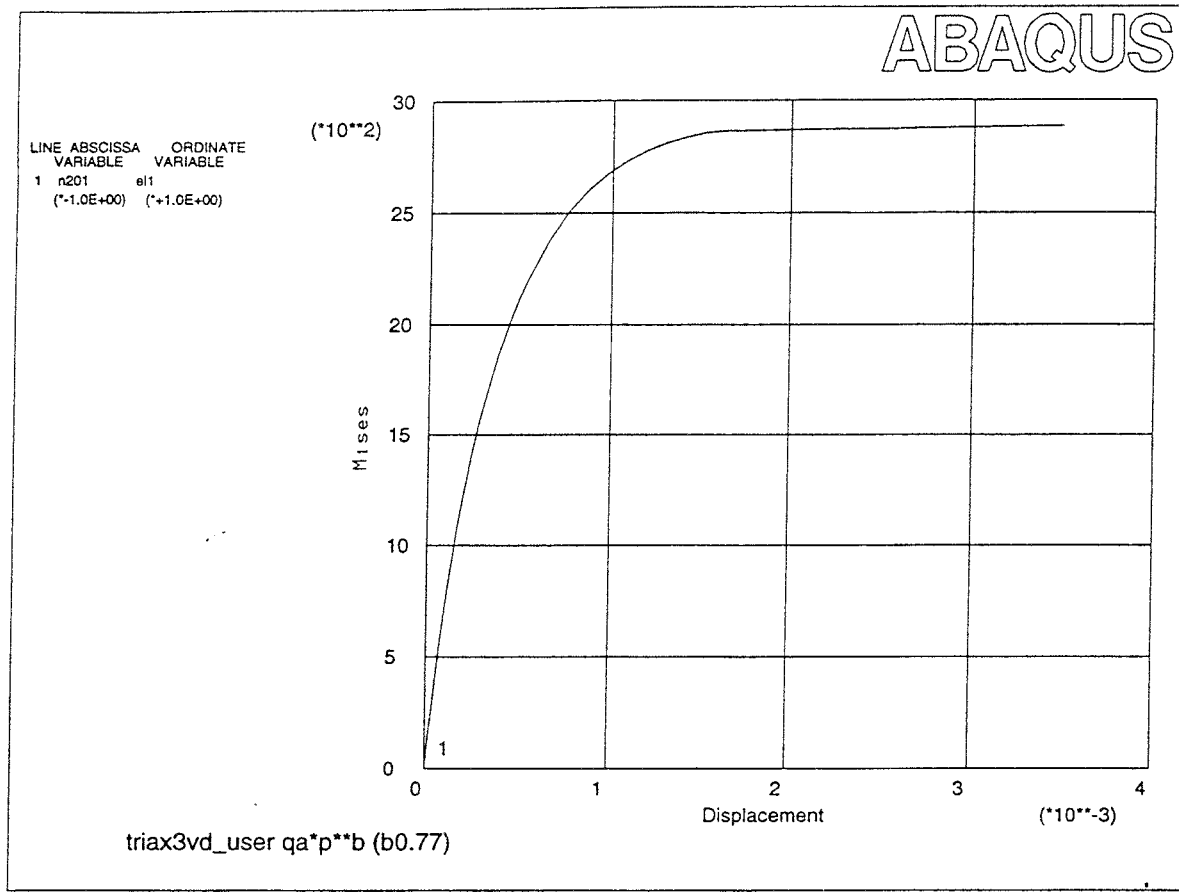

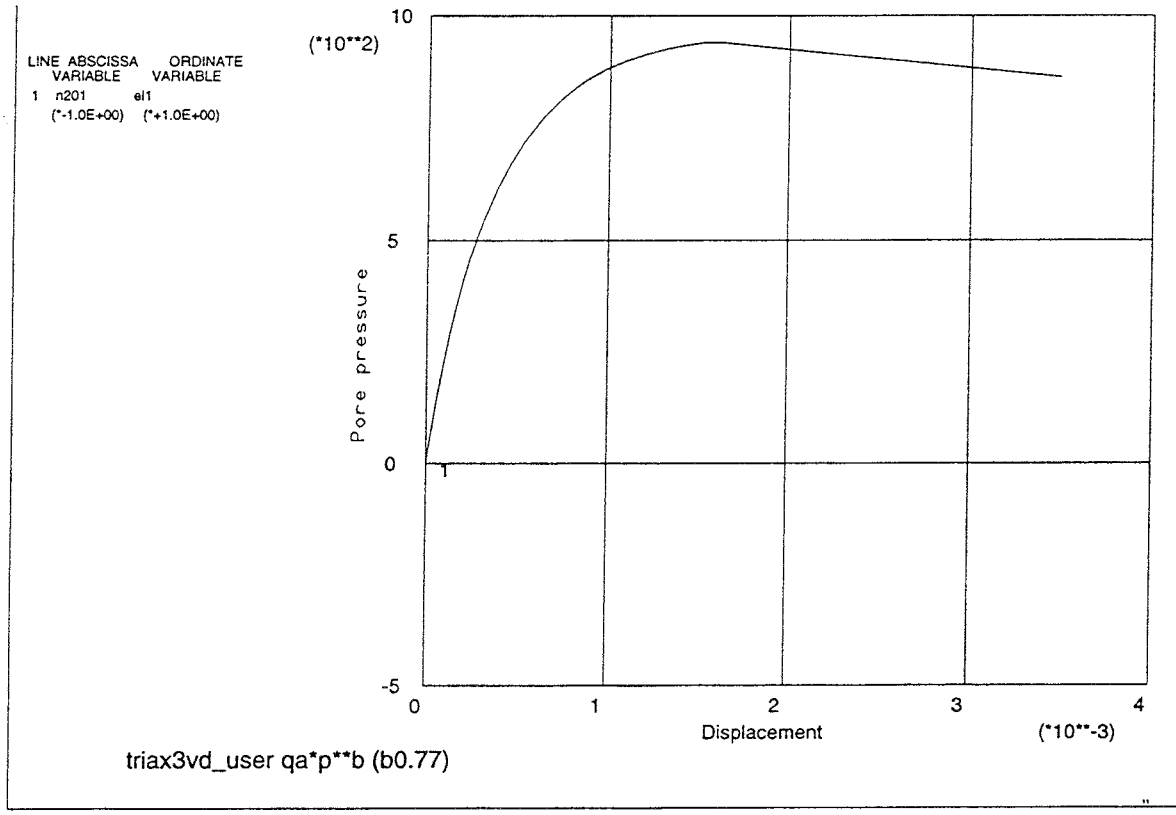

Figure 5-16. *One element calculation of an undrained triaxial test. Upper: Mises' stress (kPa) as a function of the axial displacement (m). Lower: Pore pressure (kPa) as a function of the axial displacement (m).*

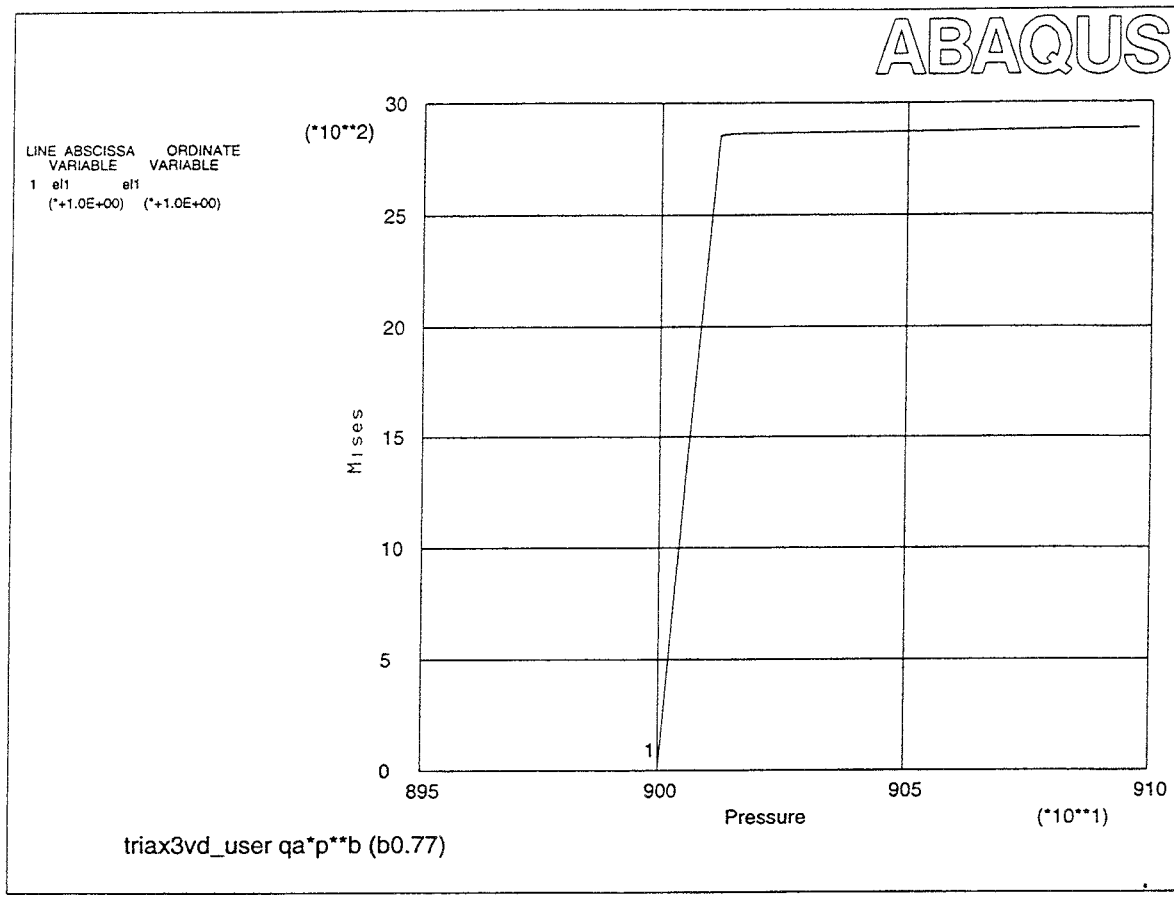

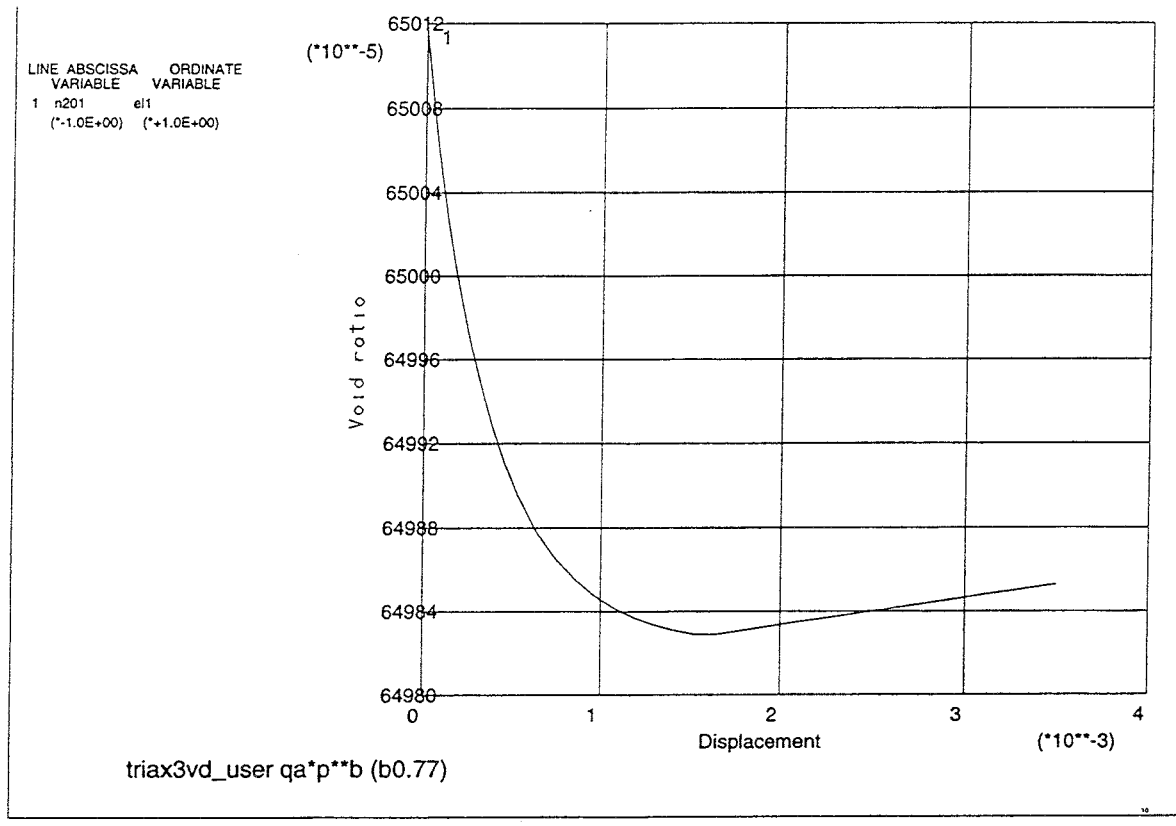

Figure 5-17. *One element calculation of an undrained triaxial test. Upper: Mises' stress q (kPa) as a function of the average stress p (kPa). Lower: Void ratio e as a function of the axial displacement (m).*

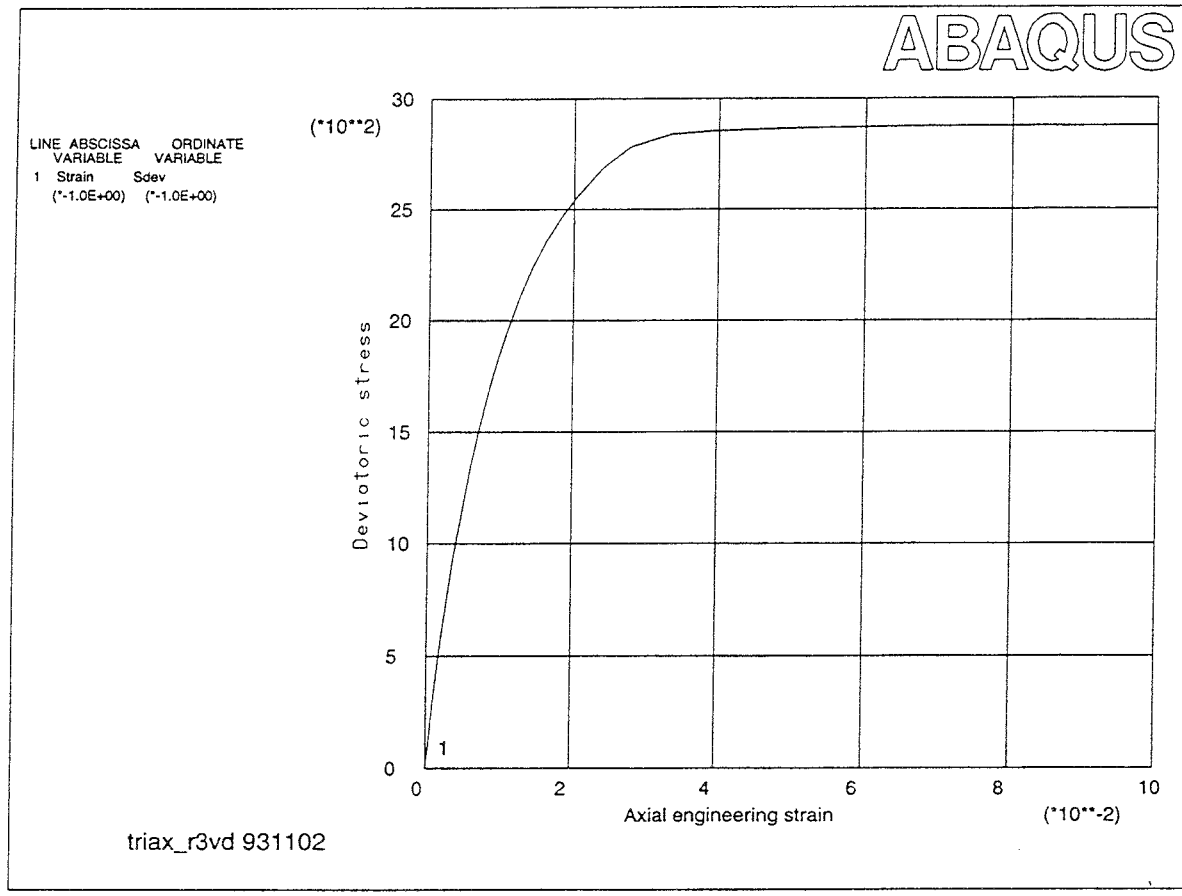

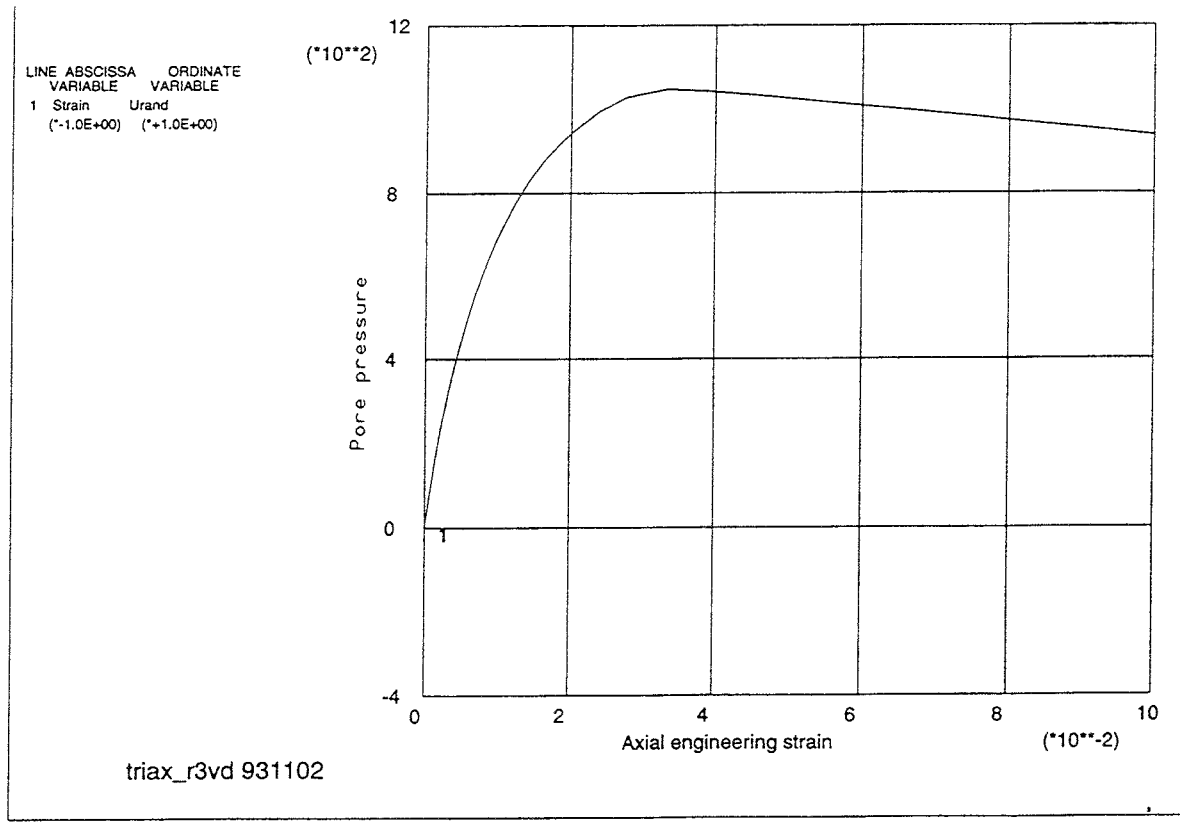

Figure 5-18. *Multiple element calculation of an undrained triaxial test.*
Upper: Deviator stress D (kPa) as a function of the axial strain.
Lower: Pore pressure u (kPa) in the filters as a function of the axial strain.

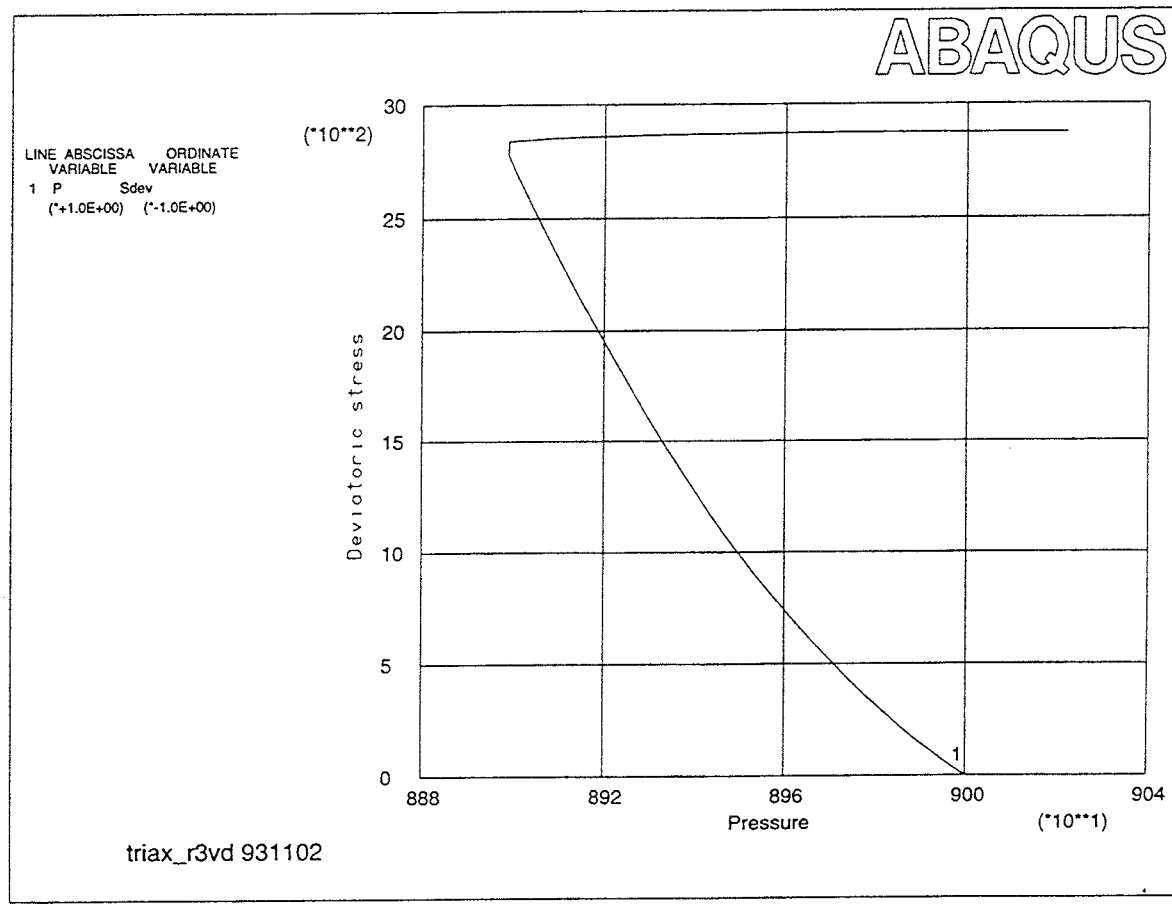

Figure 5-19. *Multiple element calculation of an undrained triaxial test. Deviator stress D (kPa) as a function of the average stress p (kPa)*

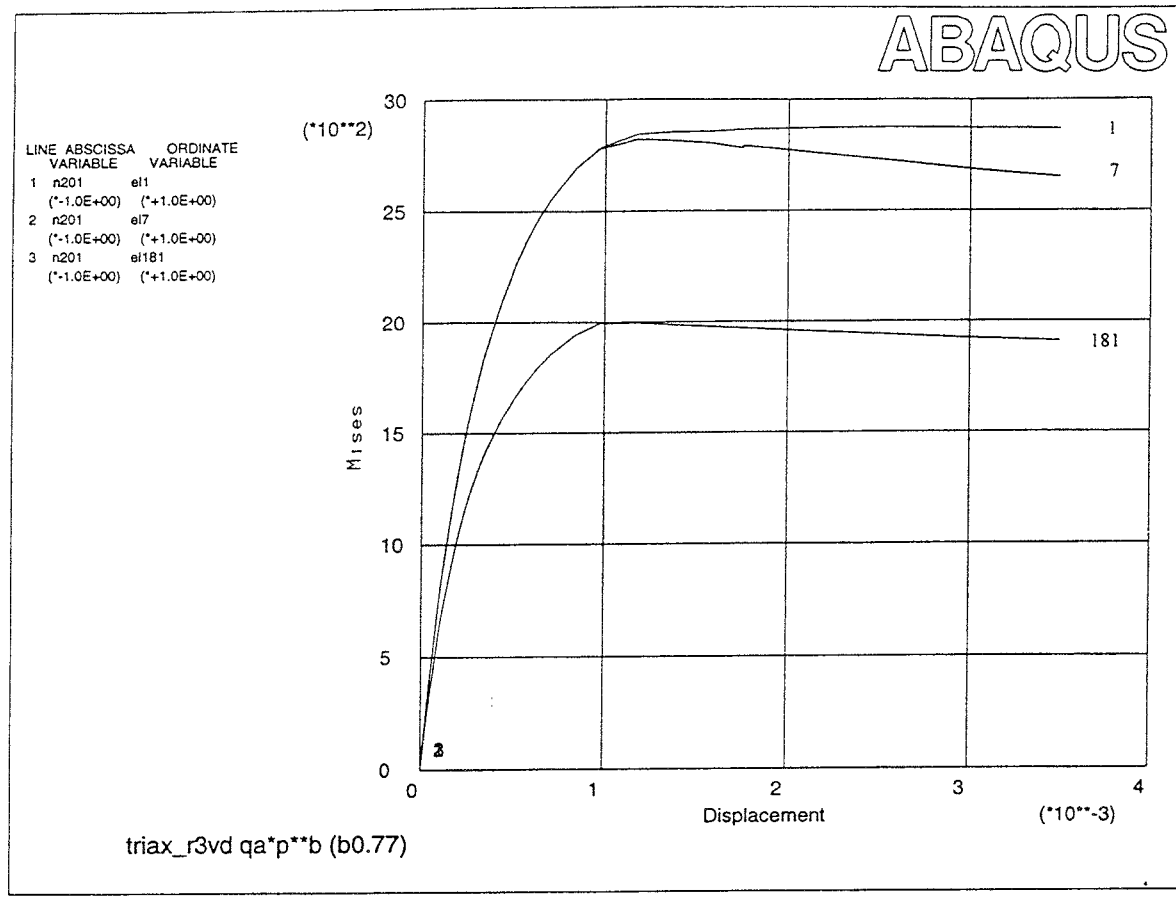

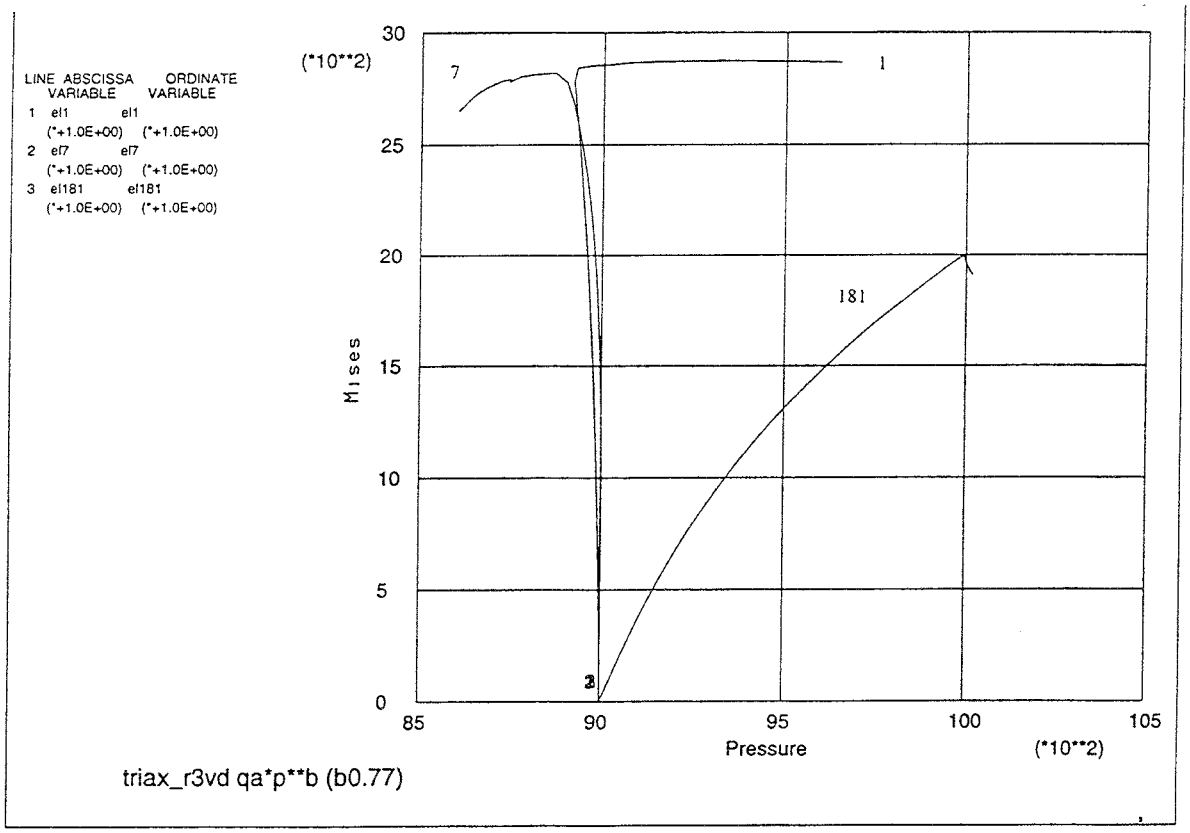

Figure 5-20. *Multiple element calculation of the undrained triaxial test. Results in elements 1, 7 and 181.*
Upper: Mises' stress q (kPa) as a function of the axial displacement (m).
Lower: Mises' stress q (kPa) as a function of the average stress p (kPa).

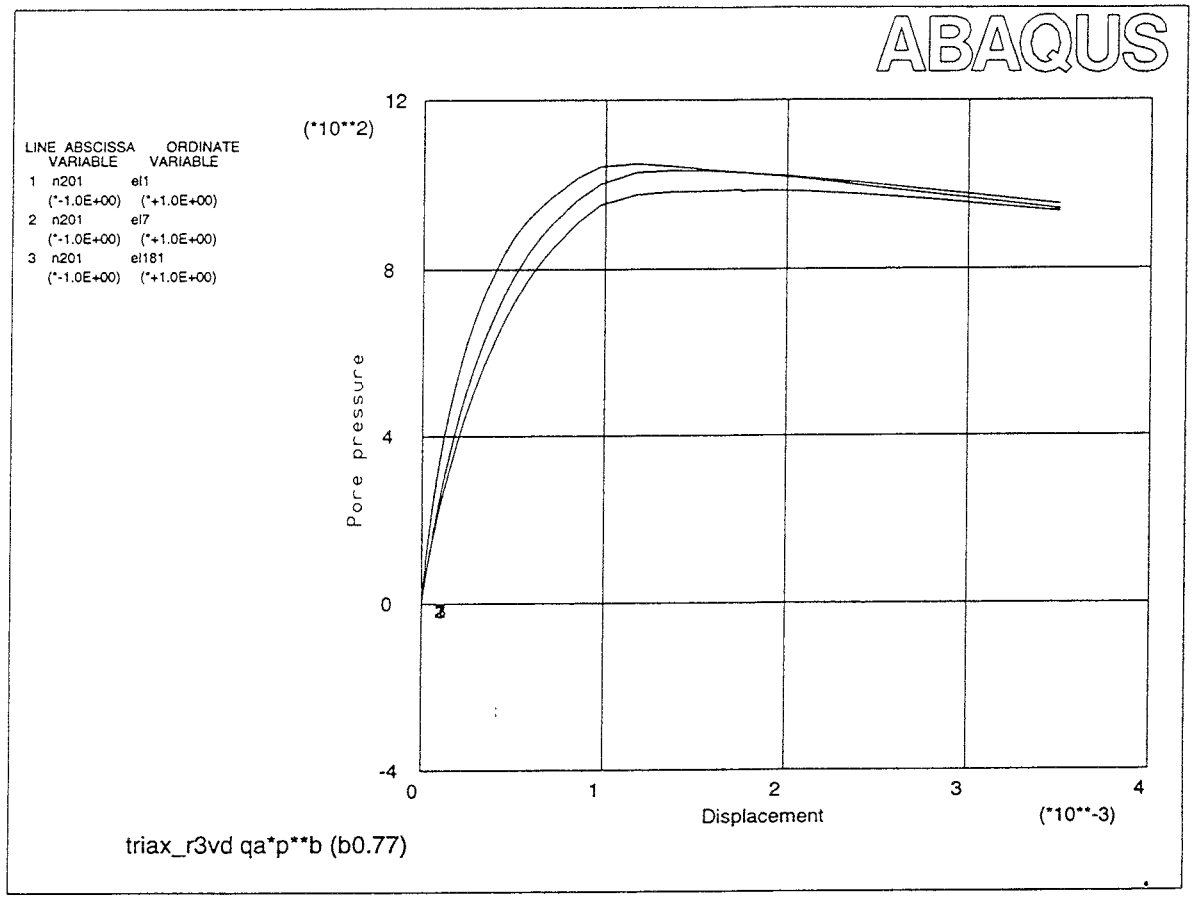

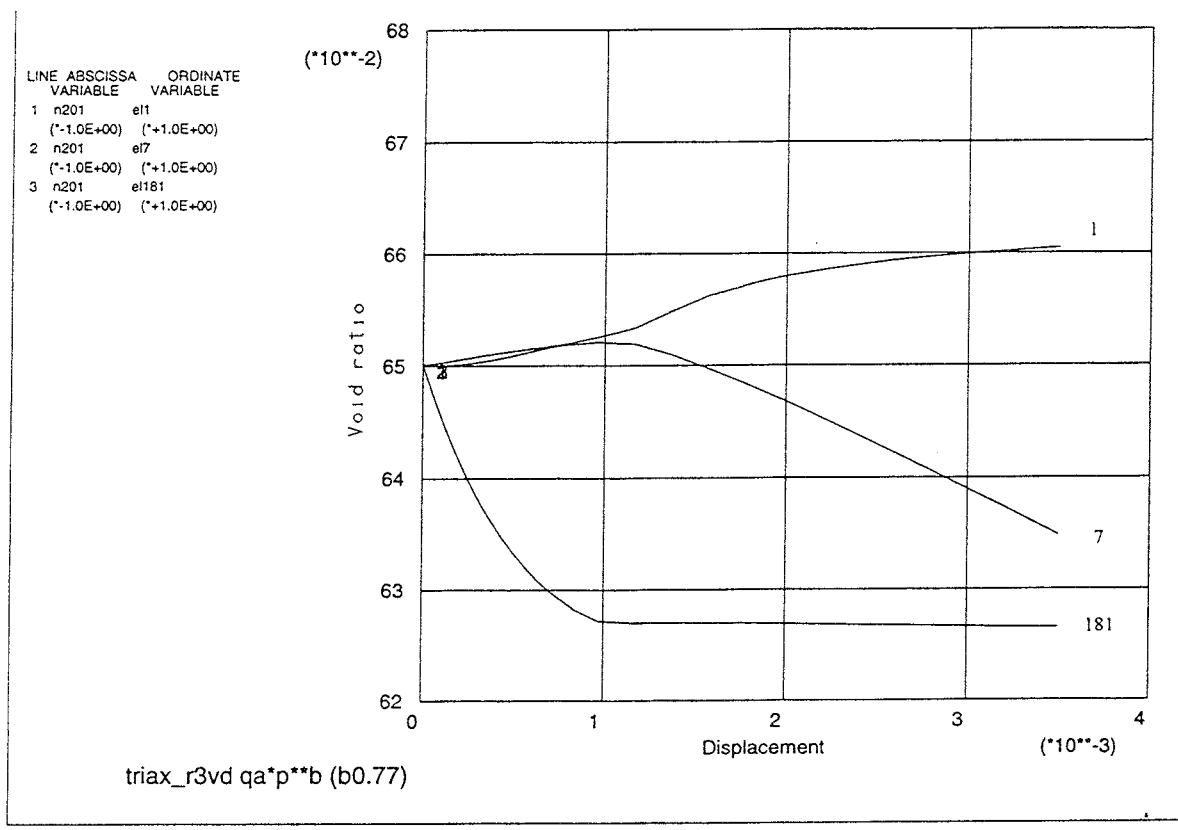

Figure 5-21. *Multiple element calculation of the undrained triaxial test. Results in elements 1, 7 and 181.*
Upper: Pore pressure u (kPa) as a function of the axial displacement (m).
Lower: Void ratio e as a function of the average stress p (kPa).

Fig 5-22 shows the deformed structure after 5% and 10% strain and the pore pressure distribution in the sample after 5% strain. In this calculation the bulge of the sample occurs already after 5% strain, which is much earlier than in the drained case. The reason for this deviation is the difference in plastization, which starts earlier in the undrained test. The plot of the pore pressure distribution shows that the dilation, with decreased pore pressure at the eccentric bulge, had started already at 5% strain.

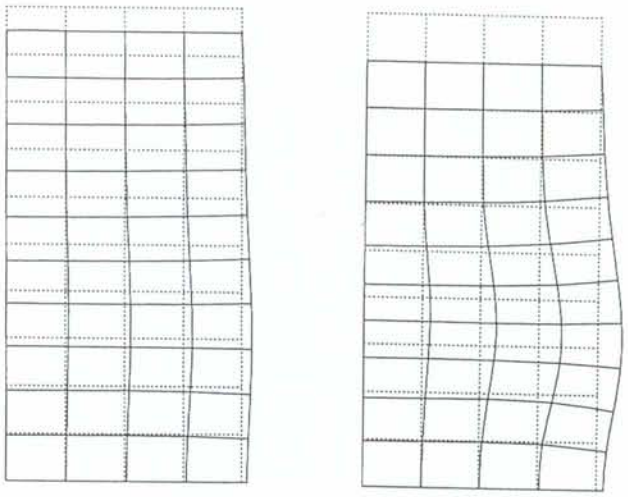

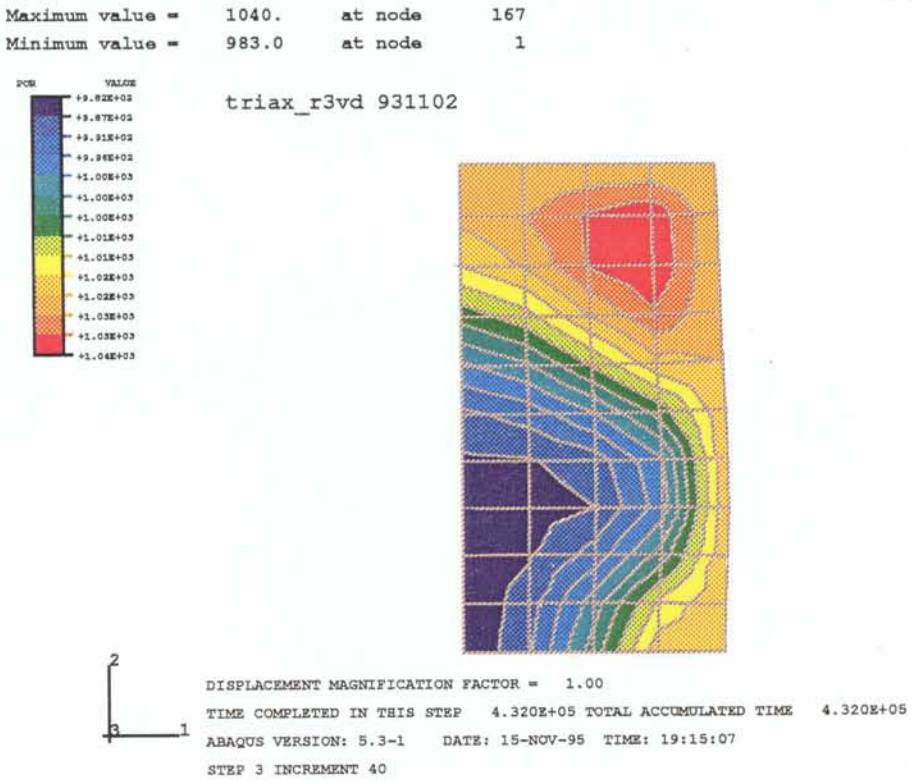

Figure 5-22. *Multiple element calculation of the undrained triaxial test. Upper: Deformed element mesh after 5 and 10% strain. Lower: Contour plot of the pore pressure u (kPa) after 5% strain.*

6 CONCLUSIONS

The tentative model CLAYTECH /S/T covers the entire range of THM behaviour that is required for predicting the function of water saturated buffer materials with a few exceptions, like volumetric creep, for which additional information is desired. Although some more information, especially concerning the plastic hardening, is required for the sake of completeness, it is not required for predicting the performance of buffers in a repository.

The finite element model CLAYECH/S/A is not complete compared to the tentative model and additional coding for taking the missing items into account should be made.

The model verification tests including simulation of four types of laboratory tests, show that a substantial improvement of the model has been achieved and that the new model can be used for a wide range of scenarios. However, they also show that there are still some uncertainties and that some of the new parameters should be determined with an improved experimental base.

The triaxial test calculations with the new model show that the variable Poisson's ratio yields a behaviour that is characterised by non-linear stress, void ratio, and pore pressure functions at shear that agree very well with the recorded behaviour. However, the parameters in the equations for Poisson's ratio obviously need to be different at repeated loading and unloading and must be chosen with care and adjusted to the respective load case.

An interesting new phenomenon that occurred at the calculation of the triaxial tests was that there seems to be a tendency for slip failure which could not take place due to the symmetry conditions. Since such slip failures often appear in real tests, true 3-dimensional calculations of these tests should be made. It has not been possible to model slip failures with other models, which shows the potential of the new one.

The oedometer test calculations (swelling/compression or vice versa) showed that one single material model can well represent the behaviour of initially very dense, highly compacted bentonite samples as well as the behaviour of non-compacted samples at low density with the same set of parameters. However, such a model seems to yield some overestimation of the swelling of highly compacted bentonite and some underestimation of the swelling of bentonite compacted from a soft state. It is not quite clear whether this difference is caused by parameter imperfections or if different parameters are required for different precompaction histories.

The compression of an uncompacted bentonite with combined elastic and plastic volume decrease seems to be well modelled but the problems with the swelling, as previously mentioned, may be caused by difficulties in separating the elastic and plastic volume decrease and in finding the correct location of the yield surface p_b.

Finally it may be concluded that the CLAYTECH /S/A model appears to be very relevant for modelling the behaviour of bentonite-based buffer materials but additional coding for updating it to the level of the tentative model should be done.

REFERENCES

Börgesson L. (1988) - Modelling of buffer material behaviour. Some examples of material models and performance calculations. SKB Technical Report 88-29.

Börgesson L., Hökmark H., and Karnland O. (1988) - Rheological properties of sodium smectite clay. SKB Technical Report 88-30.

Börgesson L. (1990) - Interim report on the laboratory and theoretical work in modelling the drained and undrained behaviour of buffer materials.

Börgesson L. (1992) - Interaction between rock, bentonite buffer, and canister. FEM calculation of some mechanical effects on the canister in different disposal concepts. SKB Technical Report 92-30.

Börgesson L. and Pusch R. (1993) - In situ test on the interaction between rock, buffer, backfill, and canister. 1993 Joint CSCE-ASCE National Conference on Environmental Engineering, Montreal, Canada.

Börgesson L., Karnland O., and Johannesson L-E. (1993) - Modelling of the physical behaviour of clay barriers close to water saturation. International workshop on thermo-mechanics of clays and clay barriers. Bergamo; Italy.

Börgesson L., Fredriksson A., and Johannesson L-E. (1994) - Heat conductivity of buffer materials. SKB Technical Report 94-29.

Chen W. F. and Mizuno E. (1990) - Nonlinear analysis in soil mechanics. Theory and implementation. Developments in geotechnical engineering vol. 53. Elsevier.

Feda J. (1992) - Creep of soils and related phenomena. Elsevier. Developments in geotechnical engineering, 68.

Graham J., Oswell J. M., and Gray M.N. (1992) - The effective stress concept in saturated sand-clay buffer. Canadian Geotechnical Journal, 29: 1033-1043.

Hibbit, Karlsson, and Sorensen. ABAQUS manuals.

Karnland O., Pusch R., Sandén T. (1992) - The importance of electrolyte on the physical properties of MX-80 bentonite. SKB AR 92-35 (In Swedish).

Karnland O, Pusch R and Sandén T. (1994) - Buffer Material Characterization. SKB AR 94-60 (In Swedish).

Pusch R. (1980) - Swelling pressures of highly compacted bentonite. SKB TR 80-13

Pusch R. (1980) - Permeability of highly compacted bentonite. SKB TR 80-16.

Schofield A. and Wroth P. (1968) - Critical state soil mechanics. Mc Graw-Hill, London.

Singh A. and Mitchell J.K. (1968) - General stress-strain-time function for soils. American Society of Civil Engineers, Proceedings, Vol. 94, No SM1.

APPENDIX 1

Implementation of the mechanical model

1. Introduction

The material models contained in the ABAQUS material library have been extensively tested and a lot of exercises have been performed in order to calibrate material parameters against obtained results from measurements. The results have indicated that some changes of the ABAQUS CAP-material routine might improve the calibration. The CAP-model is in detail described in ABAQUS Theory Manual and will not be described within this report but roughly the following changes were proposed based on the performed exercises:

- the linear relation between p (pressure) and q (mises stress) should be changed to a power law, $q=a*p^b$
- the failure curve should be defined by another power law, $q=c*p^b$
- the dilatation angle should be decreased especially at low values of q (this means a modification of the flow potential).

This report contains theoretical background of implementation of a modified CAP-model included in ABAQUS material library.

2. Yield surface

The yield surface consists of three parts, see also Fig 1.:

- Region 1, defined by $q=a*p^b$
- Region 2, the transition surface, an ellipse tangent to region 1 and region 3. The ellipse is defined by the ratio between the two axis by the user defined parameter γ.
- Region 3, an ellipse having one point with horizontal slope going through $a=c*p^b$ and the other point at q = 0. The origin of the ellipse is defined at q=0 and $p=p_a$.

The yield hardening is then defined by a user defined law where p_a is defined as a function of plastic volumetric strain (this is the hardening rule in the ABAQUS CAP-model and it has not been changed).

The transition surface is defined as:

$((q-q_c)/R_3)^2+((p-p_a)/R_1)^2=1$

where $R_3/R_1=\gamma$

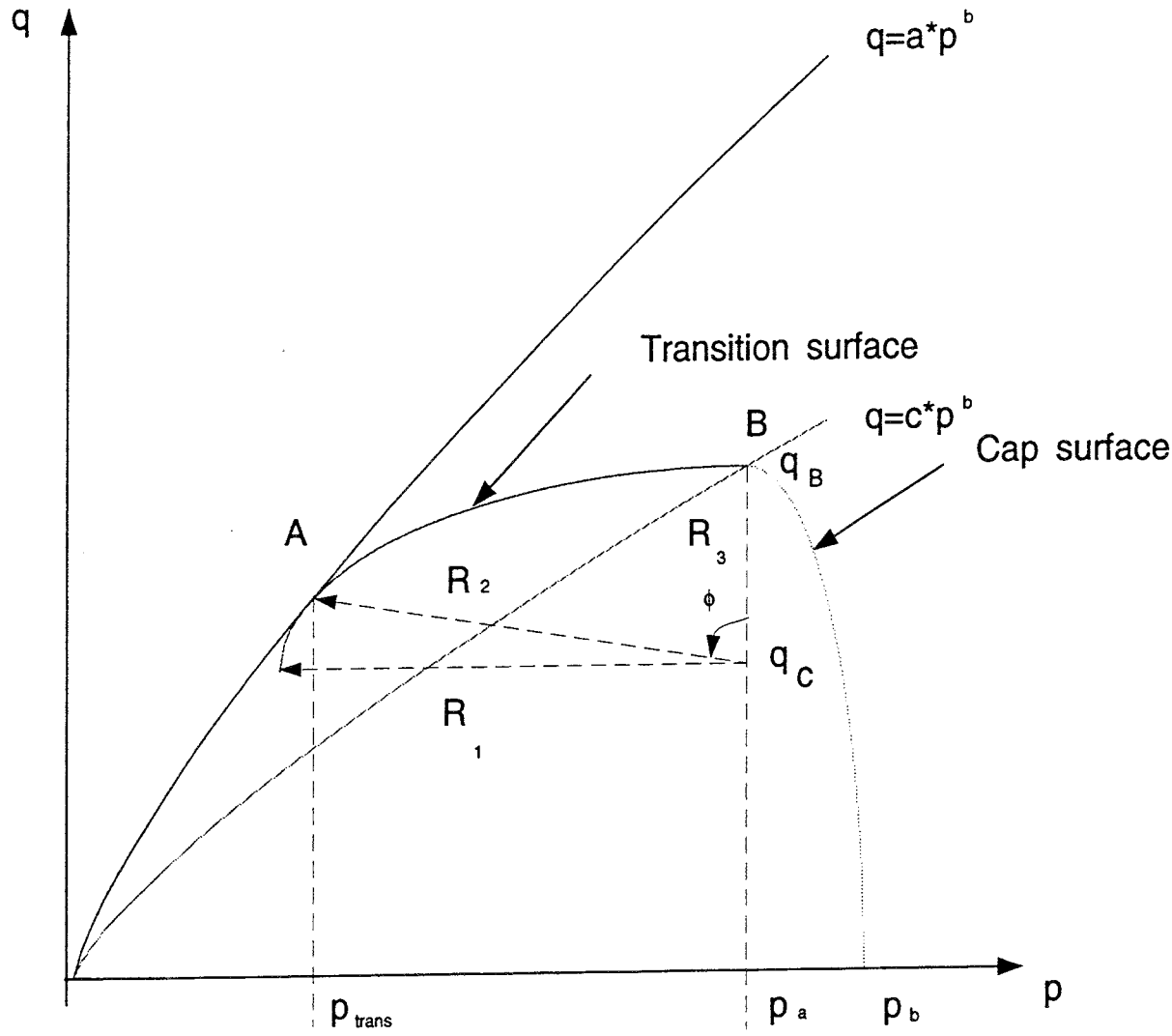

Fig 1. Definition of Yield surface

The cap surface is defined as:

$(q/q_B)^2+((p-p_a)/(p_b-p_a))^2=1$

where $(p_b-p_a)/q_f=\alpha$

$R_2=R_3*(\cos^2\phi+\gamma^2\sin^2\phi)^{-1/2}$

At point A:

$$q=a*p^b$$
$$q=q_c+R_2*\cos(\phi)$$
$$p=p_a-R_2*\sin(\phi)$$
$$R_3=c*p_a^b - q_c$$

$$R_2=\sqrt{(p-p_a)^2 + (q-q_c)^2}$$

$$\Rightarrow q_a=q_c+R_2*\cos(\phi)=a*(p_a-R_2*\sin(\phi))^b$$
$$q'_A=a*b*p^{b-1}=-\gamma^2*(p-p_a)/q_f$$

define:

$$h_1=q_c+R_2*\cos(\phi)-a*p^b = 0$$
$$h_2=a*b*p^{b-1}+\gamma^2*(p-p_a)/q_f = 0$$

then solve using Newton-Raphson's method $\Rightarrow$

$$\delta h_1/\delta q_c = 1+\delta R_2/\delta q_c*\cos(\phi)-a*b*\delta p/\delta qc*p^{b-1}$$
$$\delta h1/\delta\phi = \delta R_2/\delta\phi*\cos(\phi)-R_2*\sin(\phi)-a*b*\delta p/\delta\phi*p^{b-1}$$
$$\delta h_2/\delta q_c = a*b*(b-1)*\delta p/\delta q_c*p^{b-2}+\gamma^2\{\delta p/\delta q_c-(p-p_a)*(\delta q_f/\delta q_c)/q_f\}/q_f$$
$$\delta h_2/\delta\phi = a*b*(b-1)*\delta p/\delta\phi*p^{b-2}+\gamma^2\{\delta p/\delta\phi-(p-p_a)*(\delta q_f/\delta\phi)/q_f\}/q_f$$

where:

$$\delta R_2/\delta q_c = \delta R_3/\delta q_c(\cos^2\phi+\gamma^2\sin^2\phi)^{-1/2}$$
$$\delta R_2/\delta\phi = \delta R_3/\delta\phi(\cos^2\phi+\gamma^2\sin^2\phi)^{-1/2}+R_3*(1-\gamma^2)\cos\phi*\sin\phi*(\cos^2\phi+\gamma^2\sin^2\phi)^{-3/2}$$
$$\delta R_3/\delta\phi = 0$$
$$\delta R_3/\delta q_c =-1$$
$$\delta p/\delta q_c =-\sin\phi*\delta R_2/\delta q_c$$
$$\delta p/\delta\phi =-\sin\phi*\delta R_2/\delta\phi-R_2*\cos(\phi)$$
$$\delta q_f/\delta q_c =-(\delta p/\delta q_c)\gamma^2(p-p_a)/q_f+\delta R_3/\delta q_c*R_3/q_f$$
$$\delta q_f/\delta\phi =-(\delta p/\delta\phi)\gamma^2(p-p_a)/q_f$$

Newton-Raphson implies:

$$(\delta h_1/\delta q_c)\Delta q_c + (\delta h1/\delta\phi)\Delta\phi = -h_1$$
$$(\delta h_2/\delta q_c)\Delta q_c + (\delta h2/\delta\phi)\Delta\phi = -h_2$$

or:

$$\Delta q_c =(1/\text{det})((\delta h_2/\delta\phi)*h_1 - (\delta h_2/\delta q_c)*h_2)$$
$$\Delta\phi =(1/\text{det})(-(\delta h_1/\delta\phi)*h_1 + (\delta h_1/\delta q_c)*h_2)$$

where $\text{det}=(\delta h_1/\delta q_c)*(\delta h_2/\delta\phi)-(\delta h_2/\delta q_c)*(\delta h_1/\delta\phi)$

Initial guess for the Newton iteration:

$q_1 = p_a*(1-(c/a)^{1/b})$
$\phi = \tan^{-1}(a*b*p_a^{b-1})$
$q_c = 0$

20 iterations are performed to solve the non-linear equations.

3. Flow potential

p_f - user defined parameter to control dilation angle
t - is equal to q if K=1

The flow potential is defined from two elliptical surfacees:

- for $p<p_a$

$$g = \sqrt{(\{(p-p_a)/(p_a-p_f)\}^2 + \{\alpha*t/(p_b-p_a)\}^2)}$$

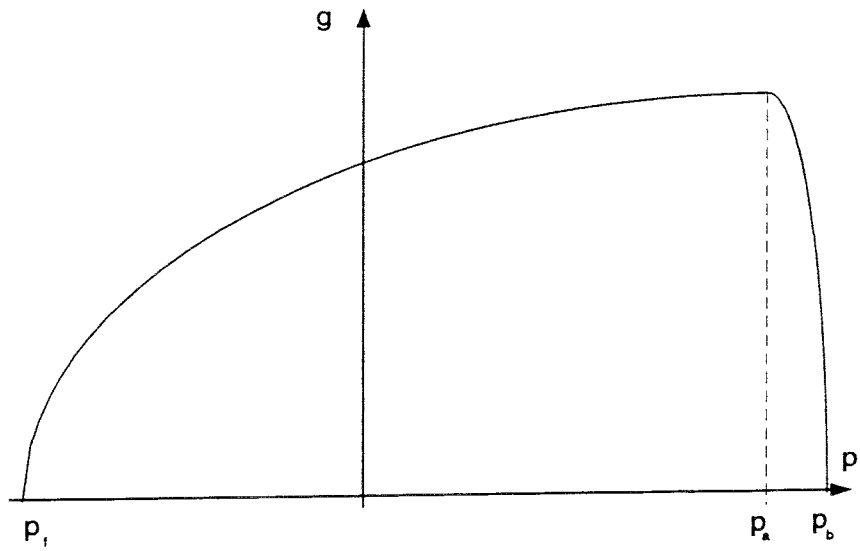

Fig 2. The flow potential

$$\delta g/\delta p = (p-p_a)/((p_a-p_f)^2*g)$$
$$\delta g/\delta t = \{\alpha/(p_b-p_a)\}^2*t/g$$
$$\delta g/\delta p_a = (-(p_a-p_f)^{-3}(p-p_a)^2-(p_a-p_f)^{-2}(p-p_a)-\alpha^2(p_a-p_b)^{-3}\alpha cbp_a^{b-1}t^2)/g$$

$$\delta^2 g/\delta p^2 = ((p_a-p_f)^{-2} - (\delta g/\delta p)^2)/g$$
$$\delta^2 g/\delta p\delta t = -(\delta g/\delta t)*(\delta g/\delta p)/g$$
$$\delta^2 g/\delta p\delta p_a = (-(p_a-p_f)^{-3}(p-p_a)-(p_a-p_f)^{-2}(\delta g/\delta p)(\delta g/\delta p_a))/g$$
$$\delta^2 g/\delta t^2 = (\alpha/(p_b-p_a)\}^2 - (\delta g/\delta t)^2)/g$$
$$\delta^2 g/\delta t\delta p_a = -\delta^2 g/\delta p\delta t$$

- for $p>p_a$

$$g = \sqrt{(\{(p-pa)/\alpha\}^2+t^2)}$$

$$\delta g/\delta p = (1/\alpha^2)*(p-pa)/g$$
$$\delta g/\delta t = t/g$$
$$\delta g/\delta p_a = -\delta g/\delta p$$

$$\delta^2 g/\delta p^2 = (1/\alpha^2 - (\delta g/\delta p)^2)/g$$
$$\delta^2 g/\delta p\delta t = -(\delta g/\delta t)*(\delta g/\delta p)/g$$
$$\delta^2 g/\delta p\delta p_a = -\delta^2 g/\delta p^2$$
$$\delta^2 g/\delta t^2 = (1 - (\delta g/\delta t)^2)/g$$
$$\delta^2 g/\delta t\delta p_a = -\delta^2 g/\delta p\delta t$$

4. Usage

The implementation is made for use with ABAQUS version 5.2/5.3 and requires the normal input parameters as for the CAP-model. The parameters for the modified cap is defined by a user subroutine as:

```
*USER SUBROUTINE
      include '/str0/femtech/sgab/umat/user_2.f'
      subroutine capmat
      implicit real*8(a-h,o-z)
      include '/str0/femtech/sgab/umat/cjh.cmn'
      pf=-5000
      a=2.58
      b=0.77
      c=2.40
      gamma=0.1
      return
      end
```

The convergence rate is affected by decreasing values of γ and α (the shape of the ellipses and the results indicate that values below 0.1 should be avoided).

APPENDIX 2

Triaxial tests

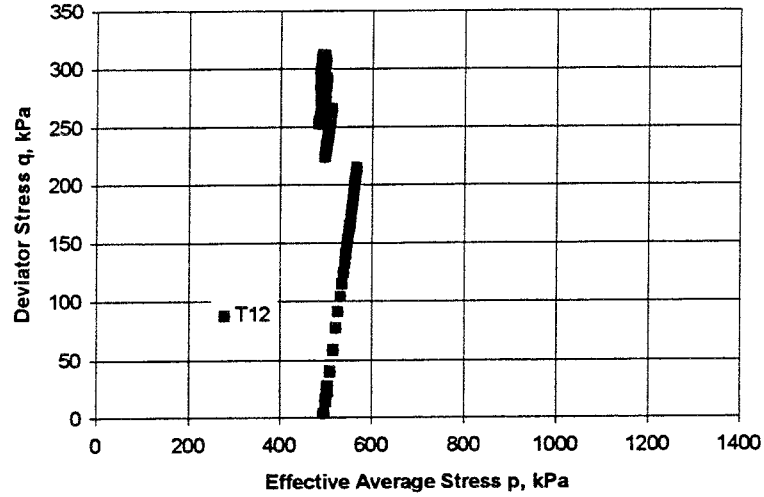

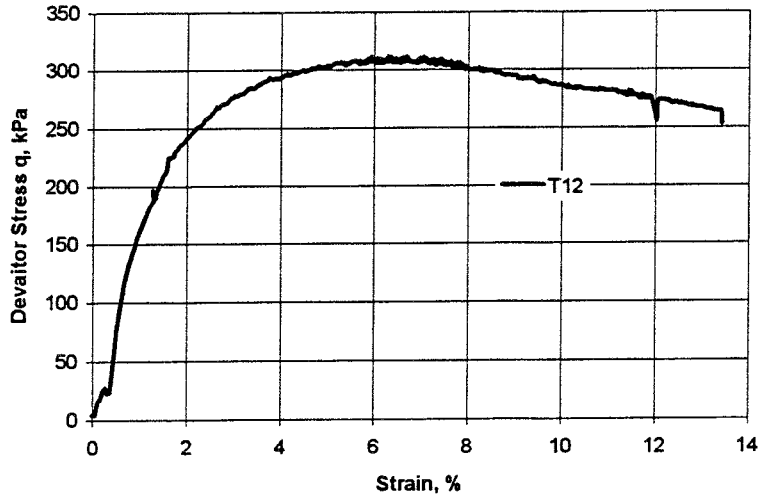

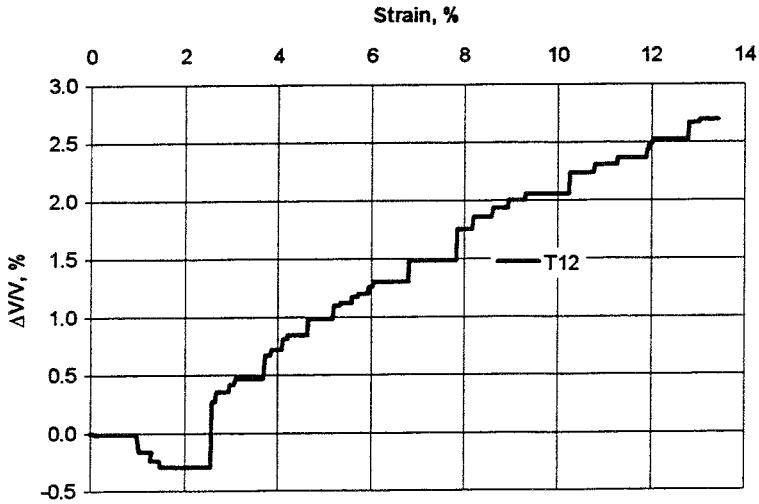

Triaxial test T12

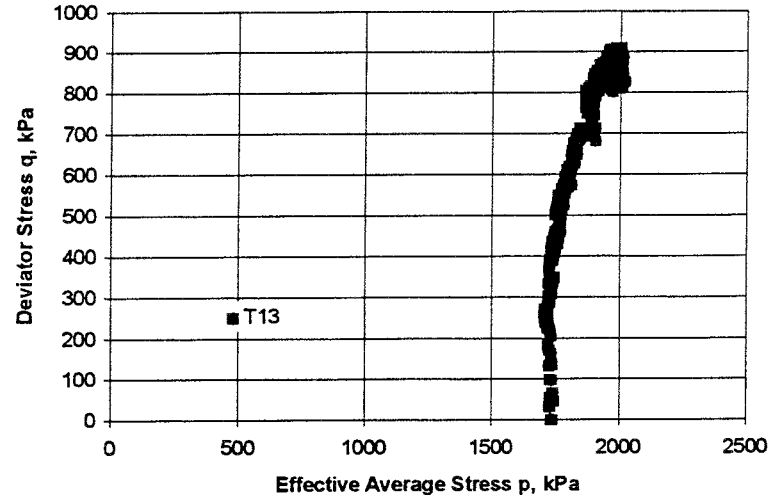

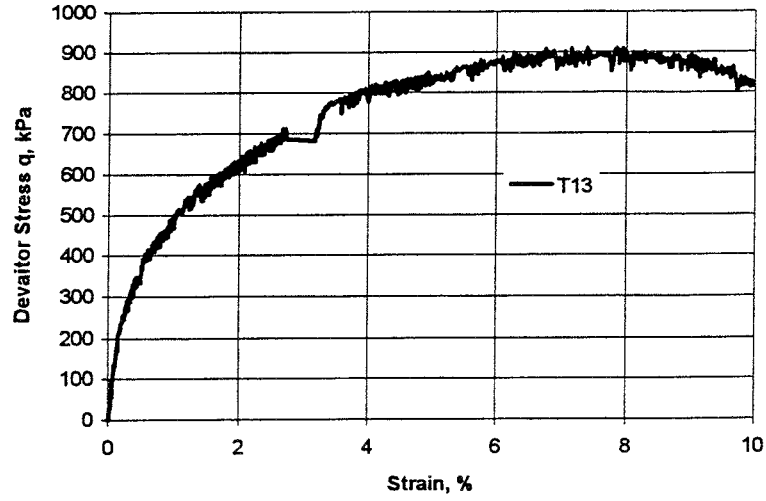

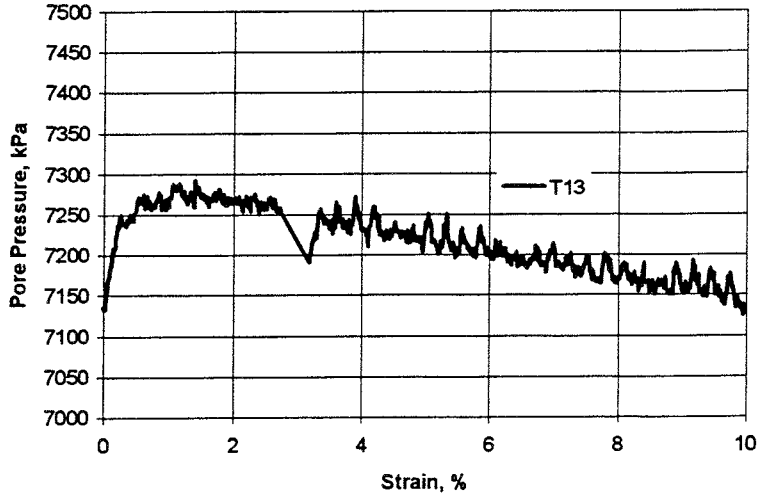

Triaxial test T13

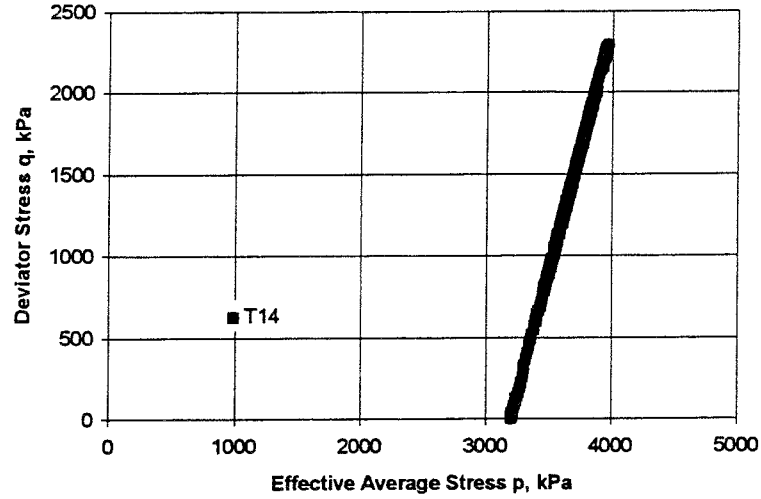

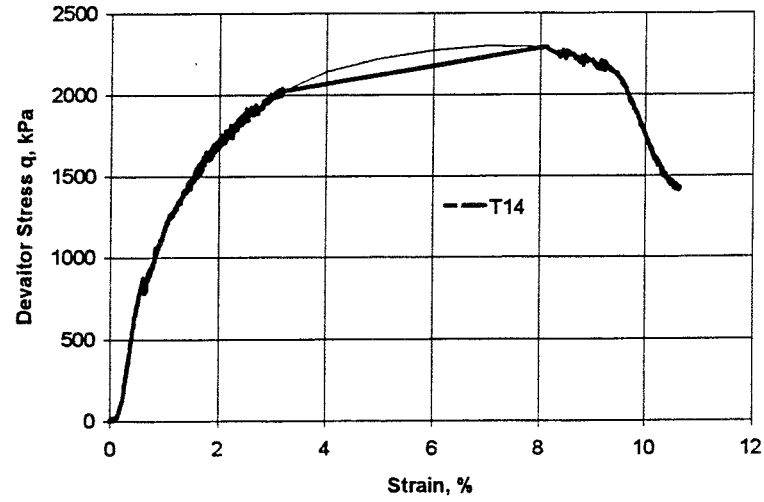

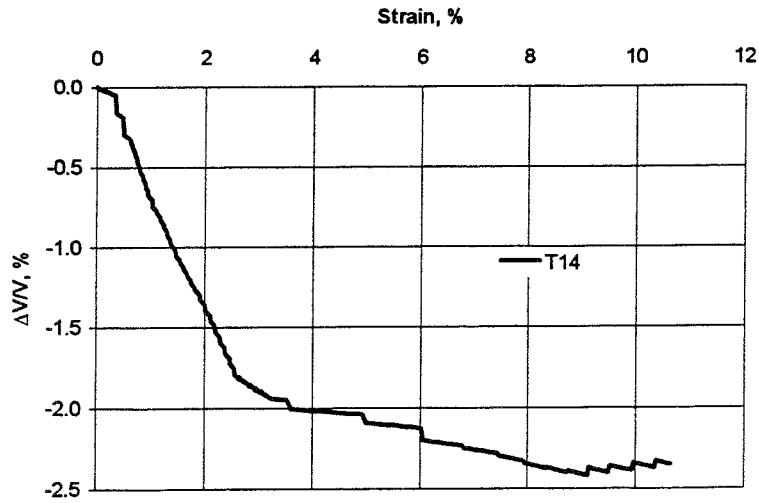

Triaxial test T14

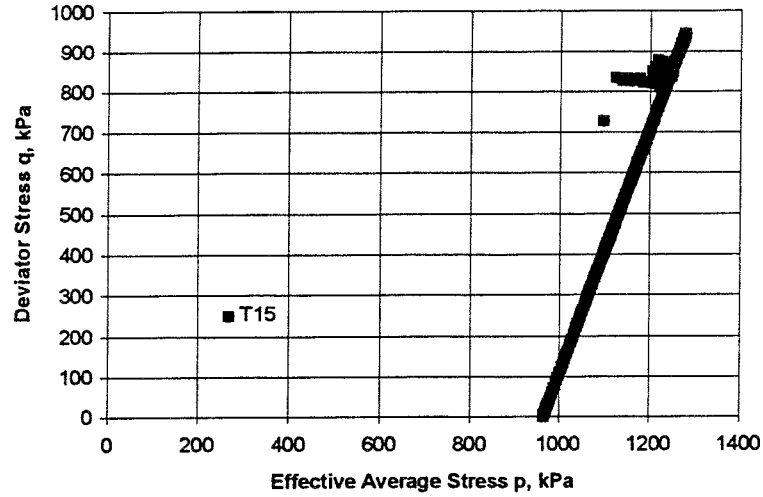

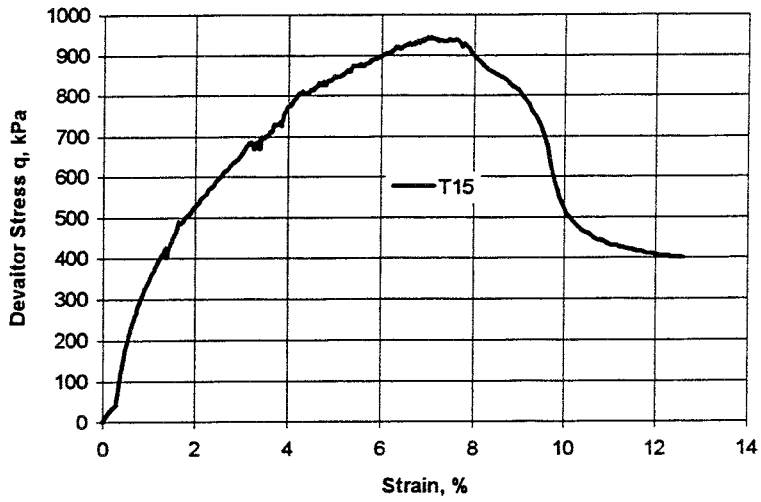

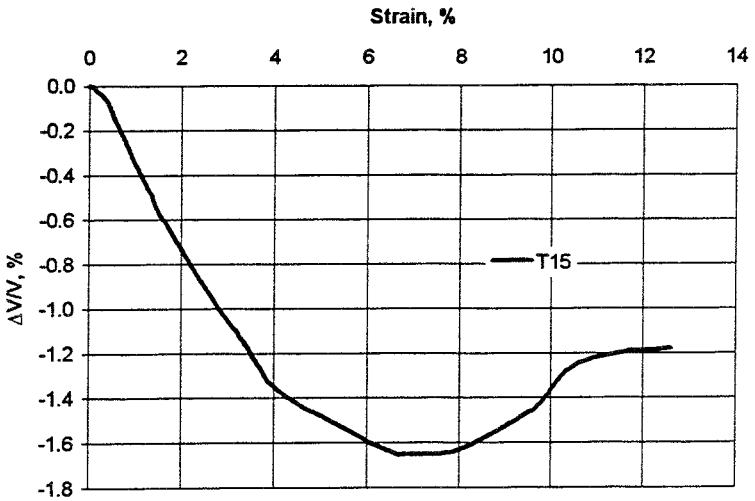

Triaxial test T15

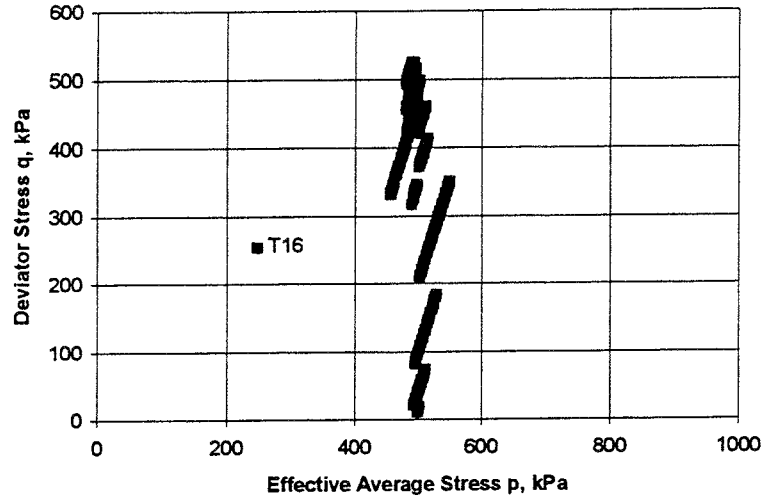

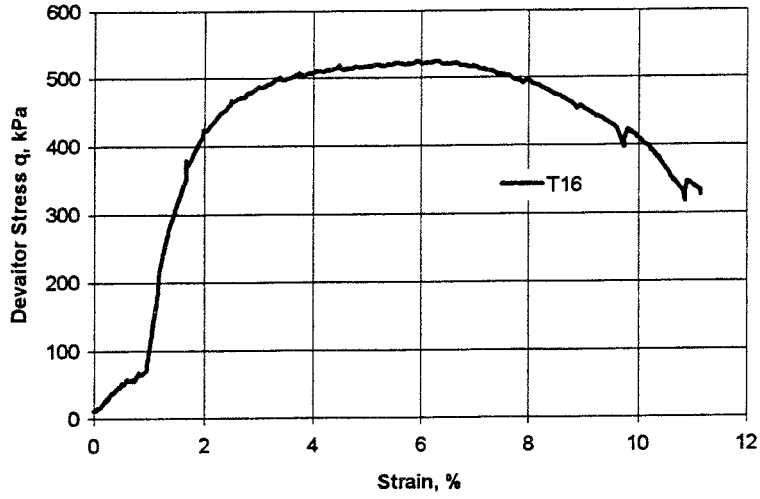

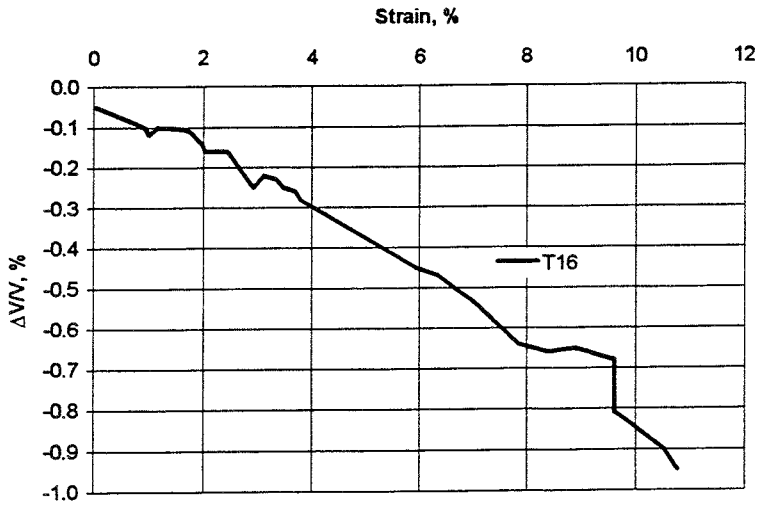

Triaxial test T16

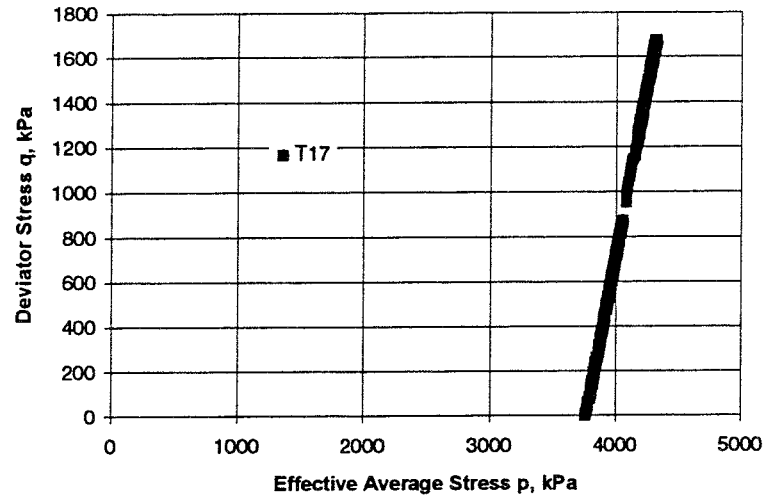

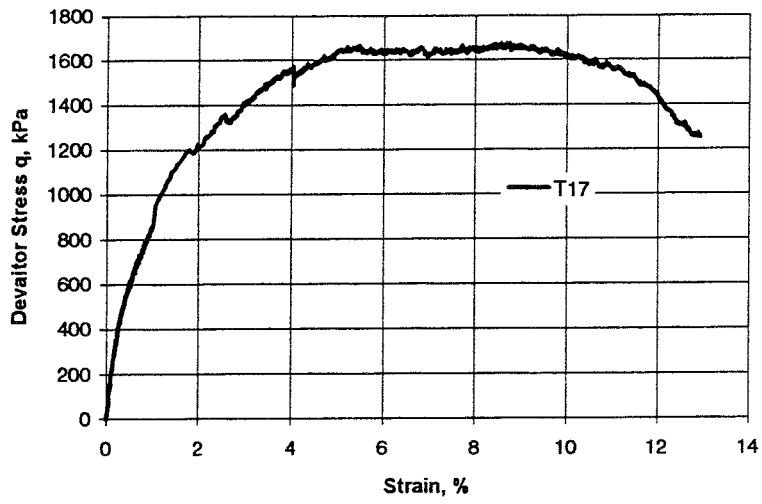

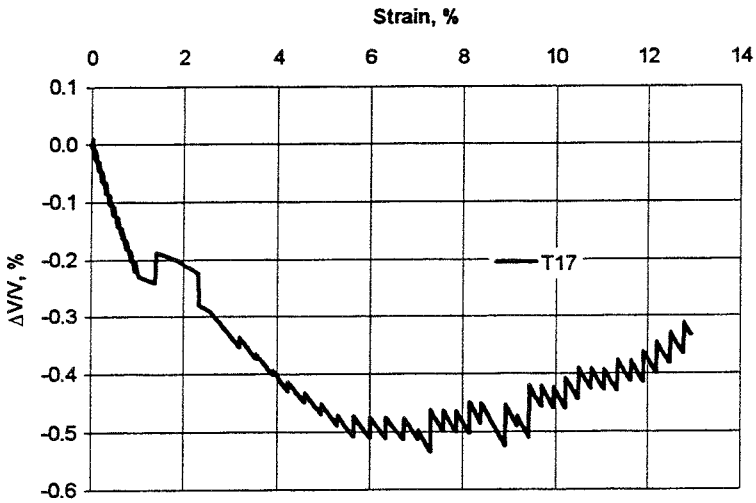

Triaxial test T17

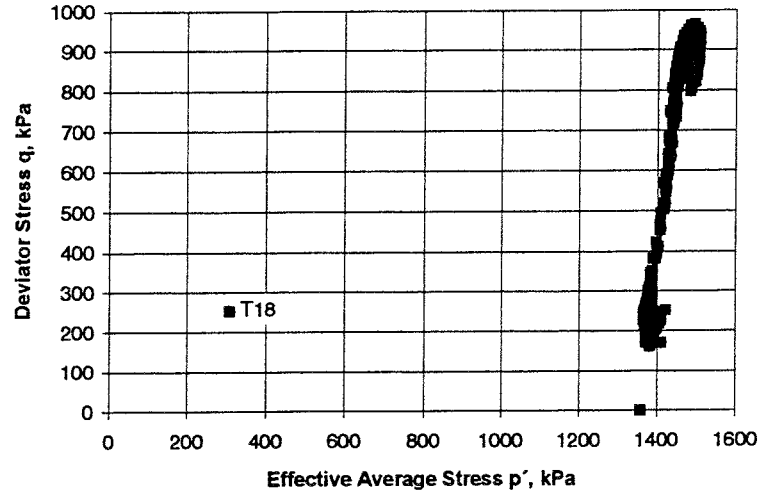

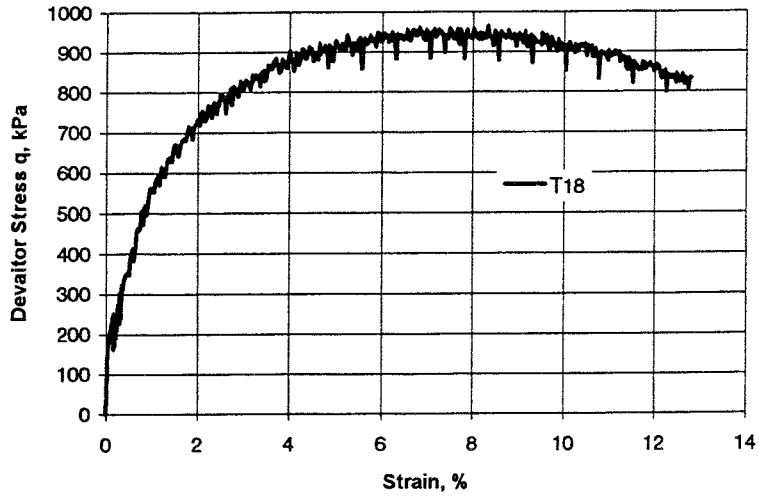

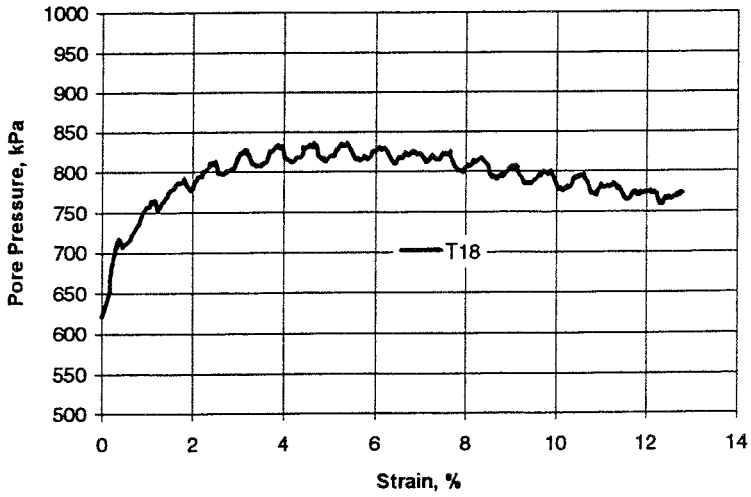

Triaxial test T18

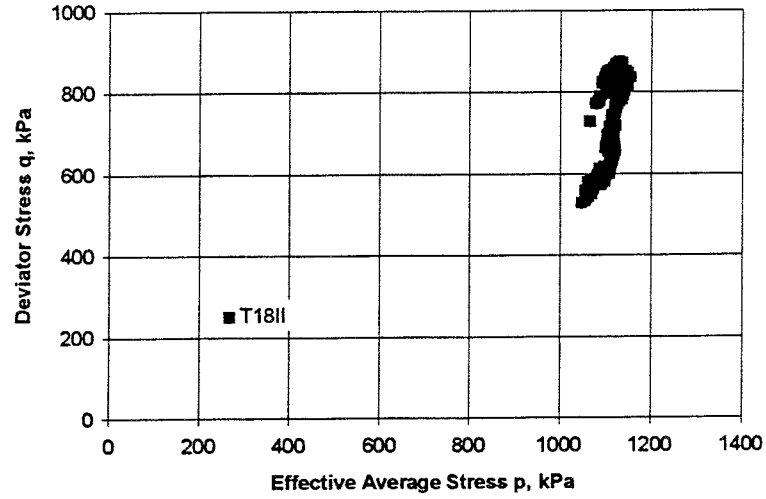

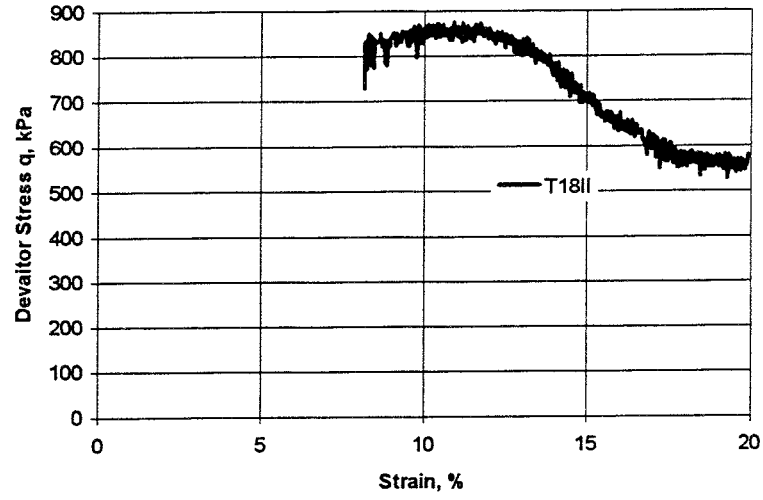

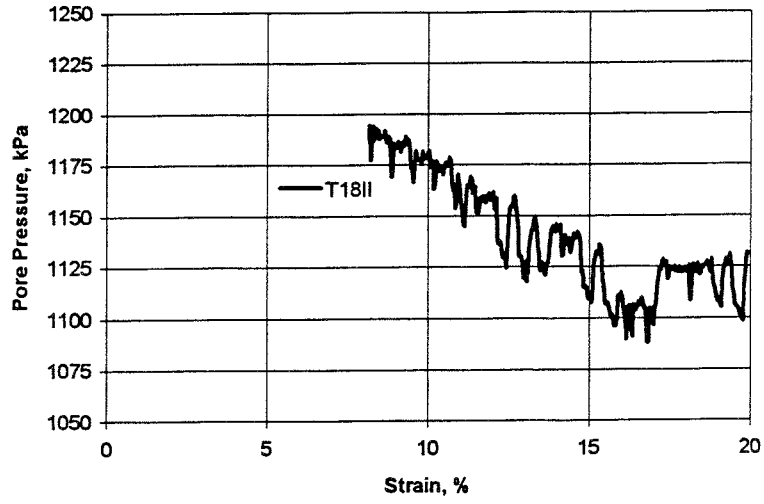

Triaxial test T18II

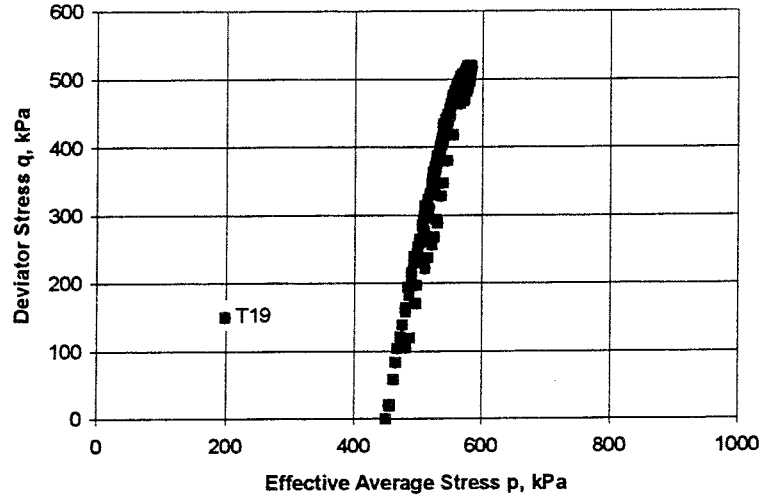

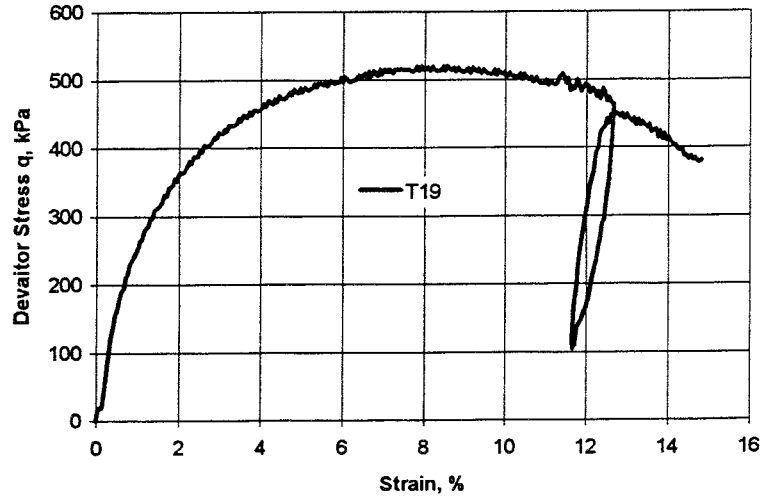

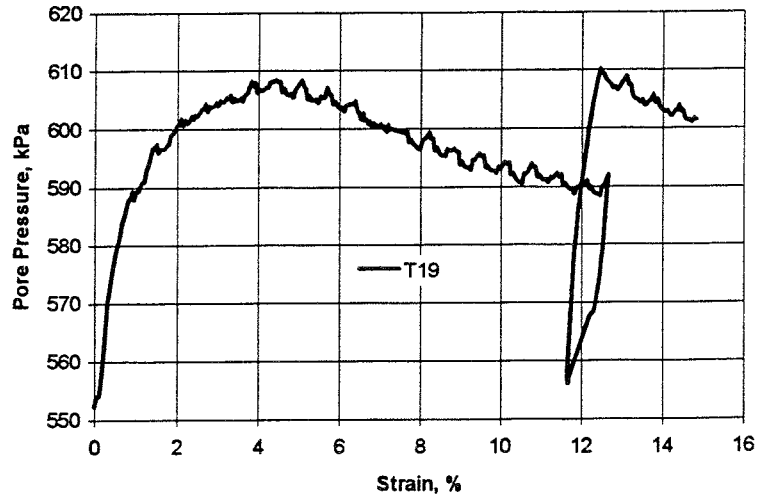

Triaxial test T19

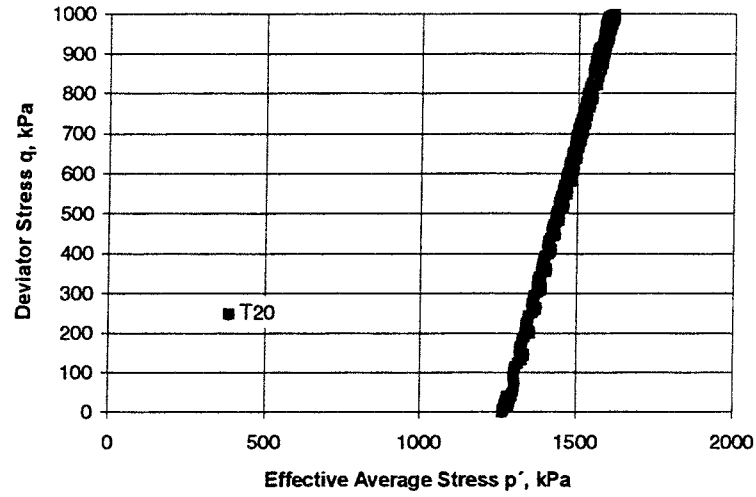

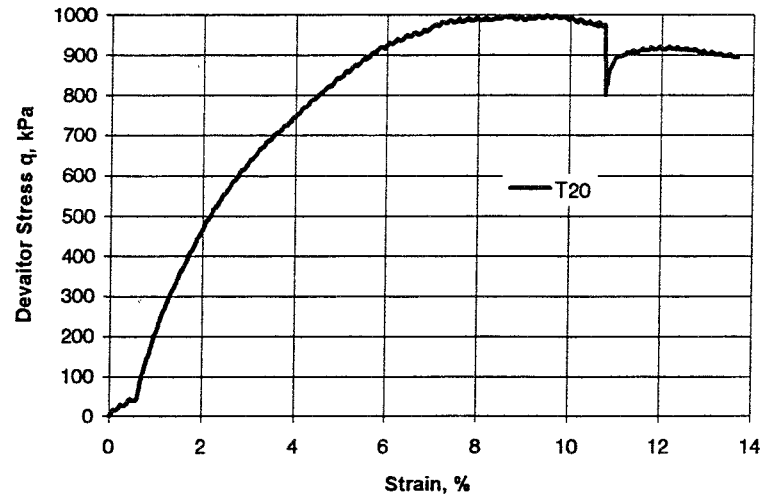

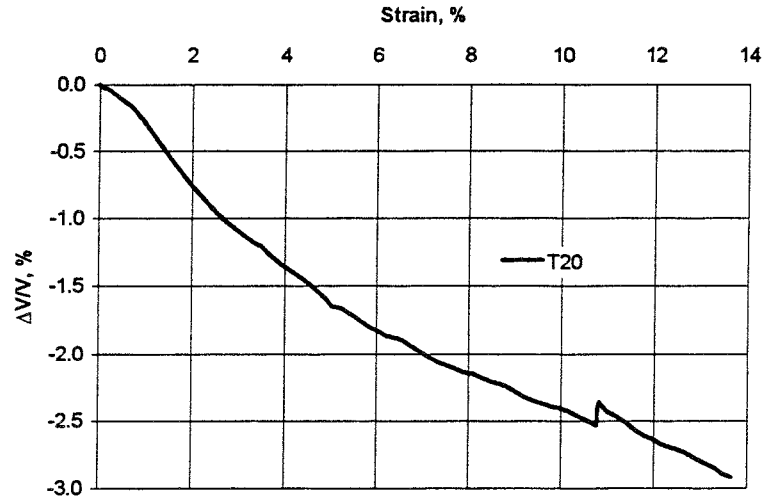

Triaxial test T20

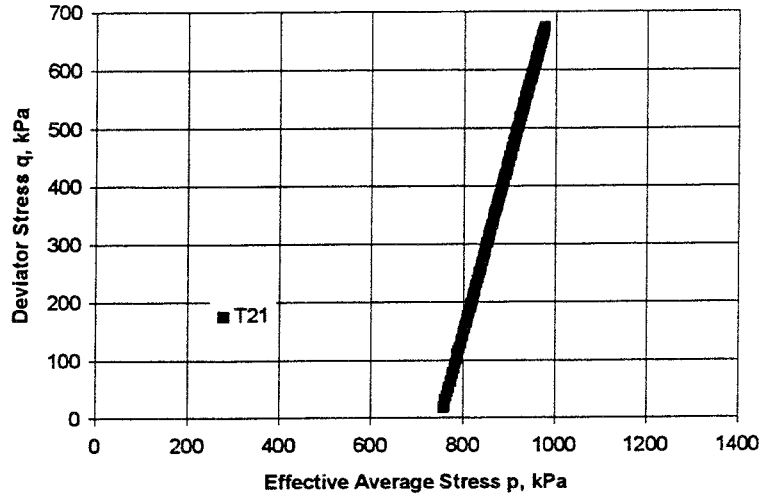

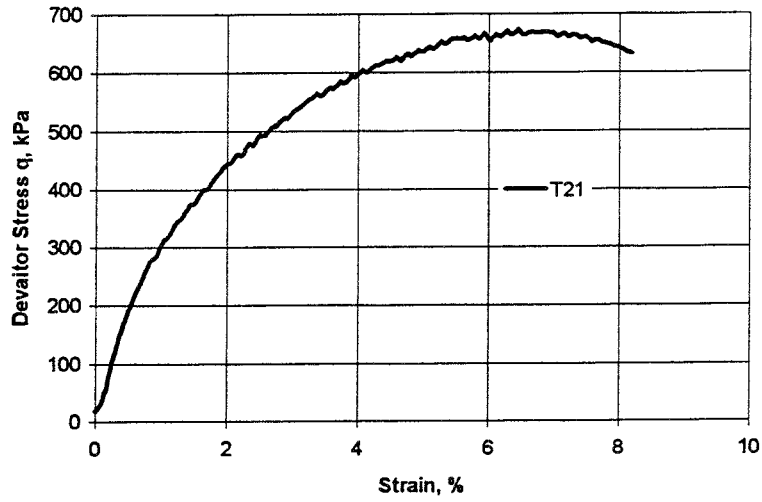

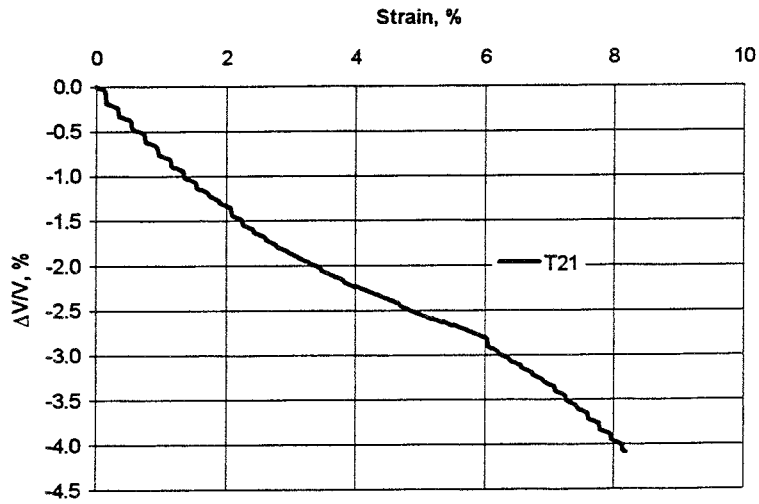

Triaxial test T21

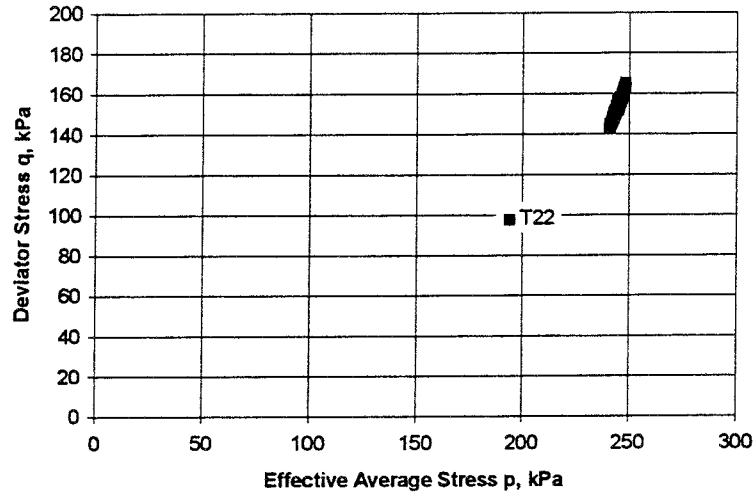

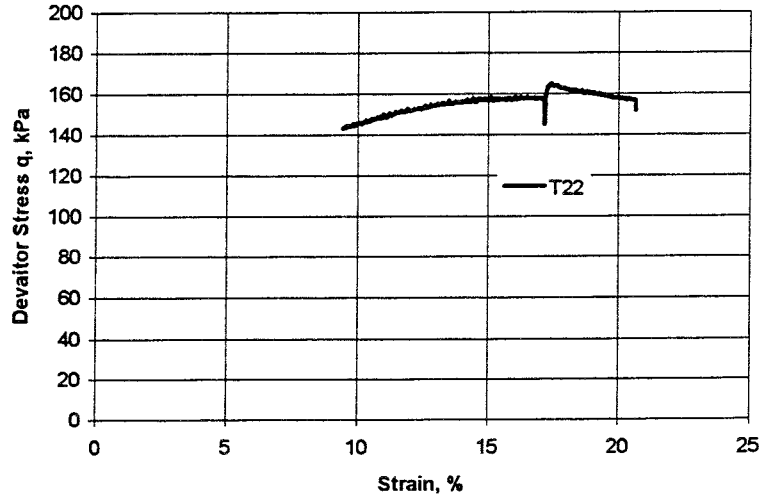

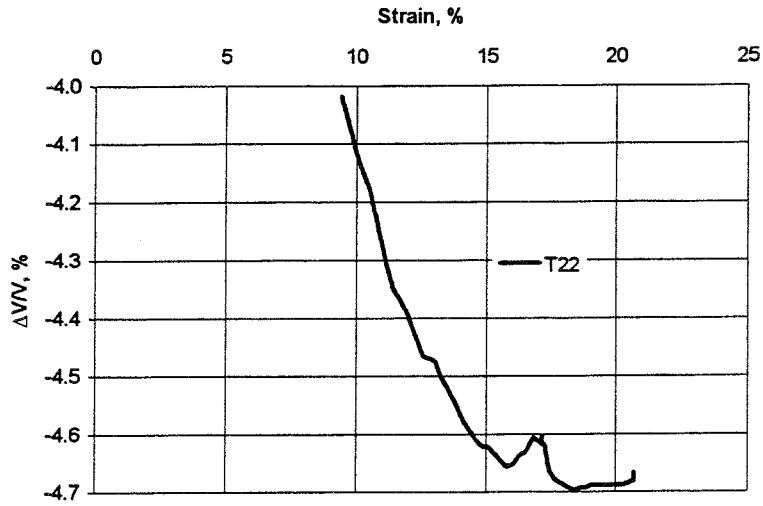

Triaxial test T22

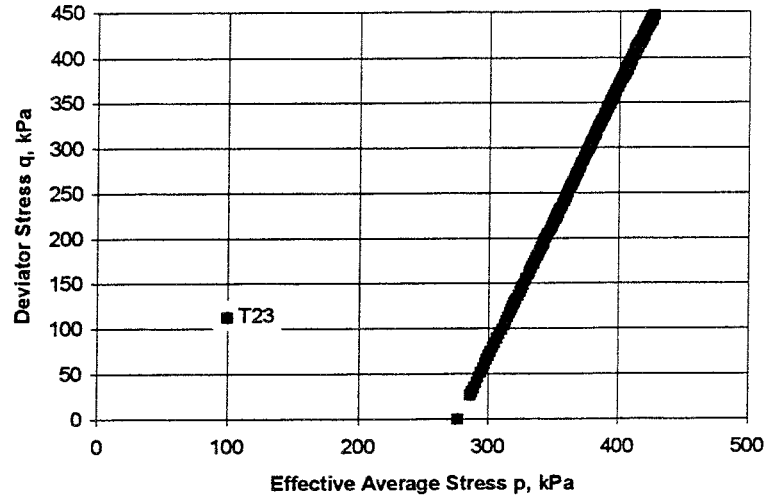

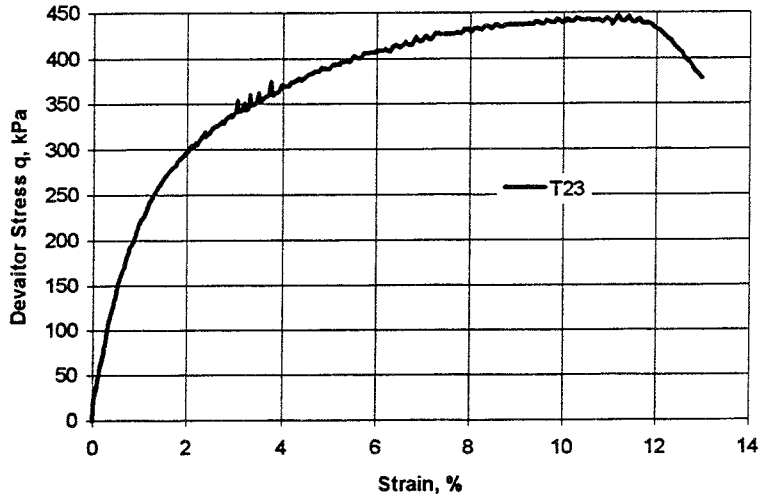

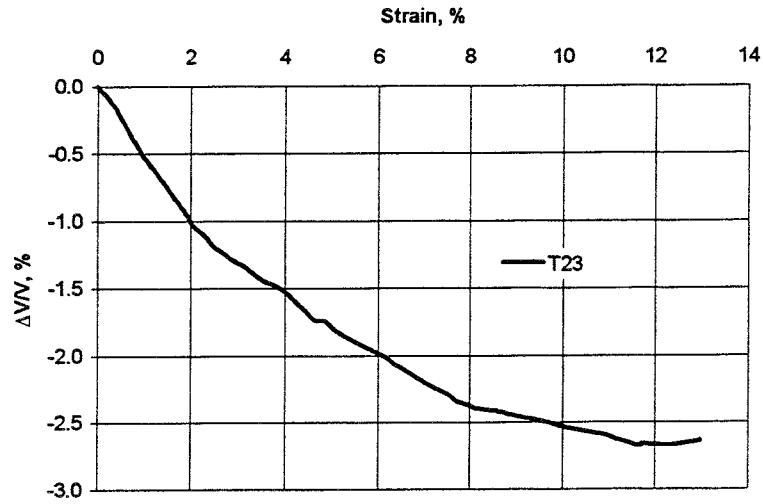

Triaxial test T23

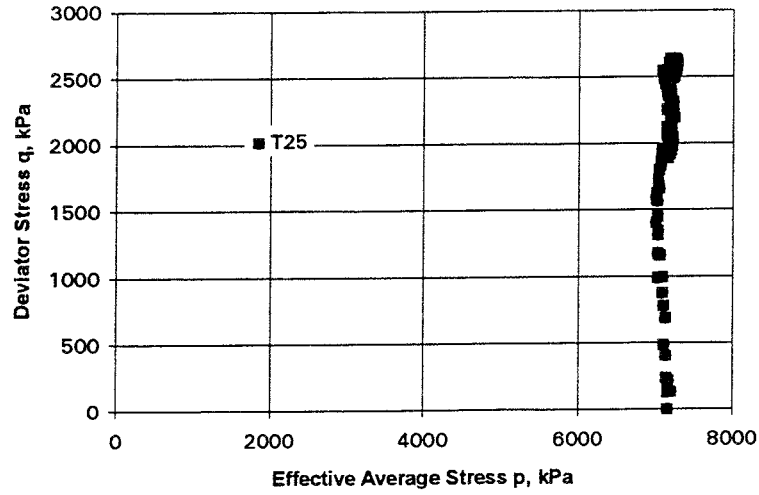

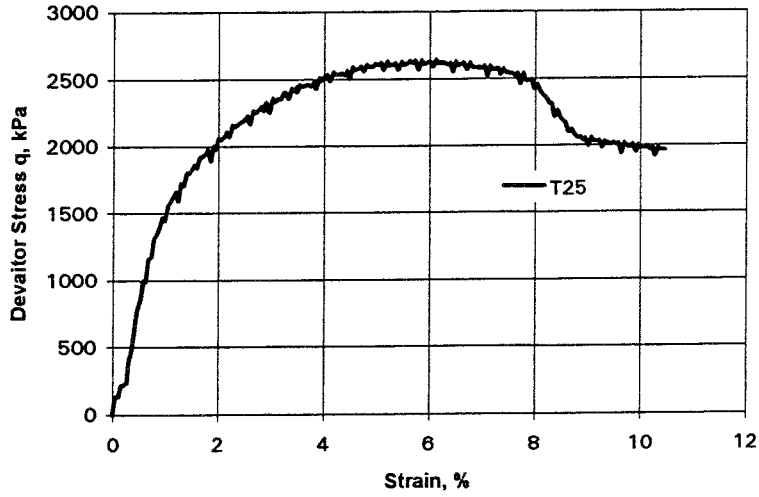

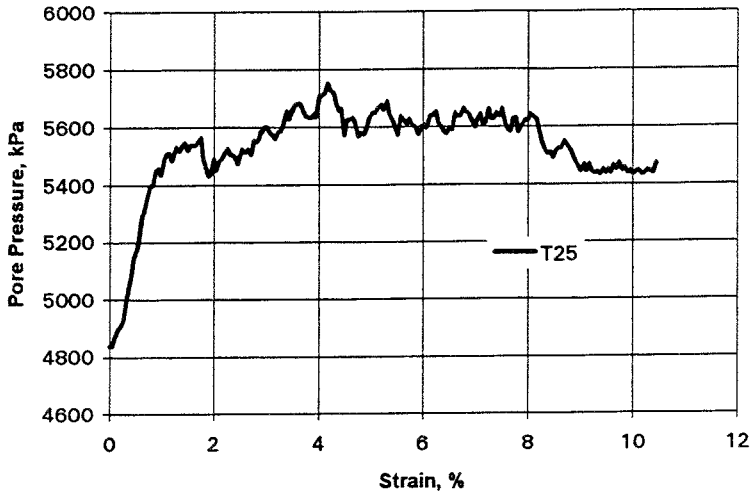

Triaxial test T25

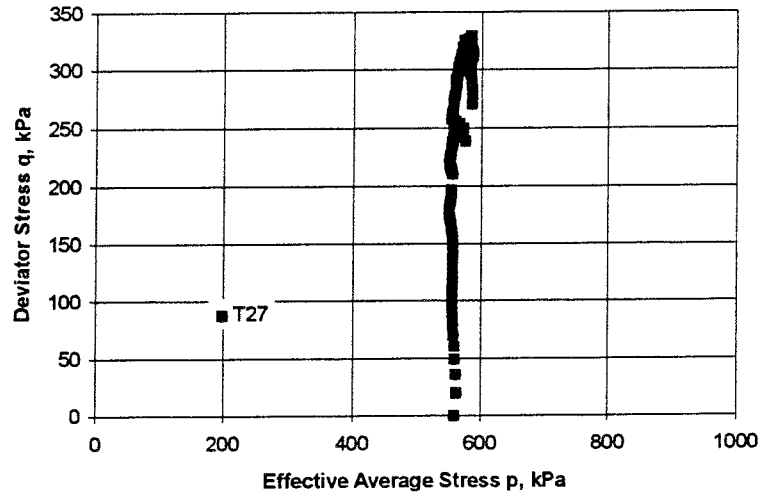

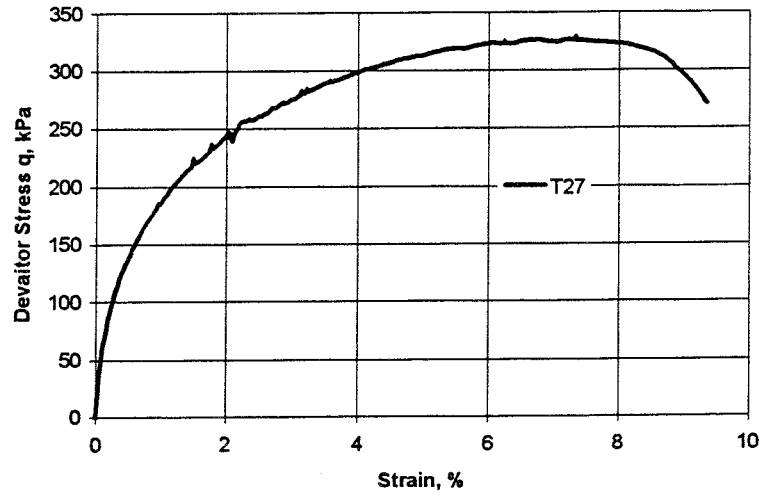

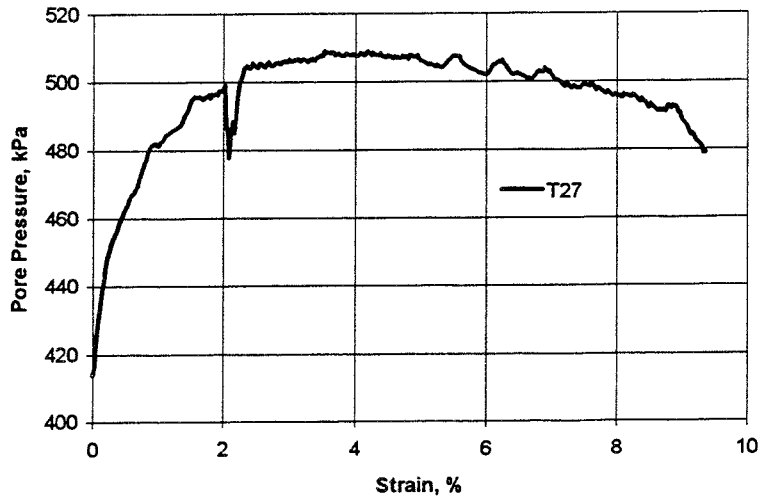

Triaxial test T27

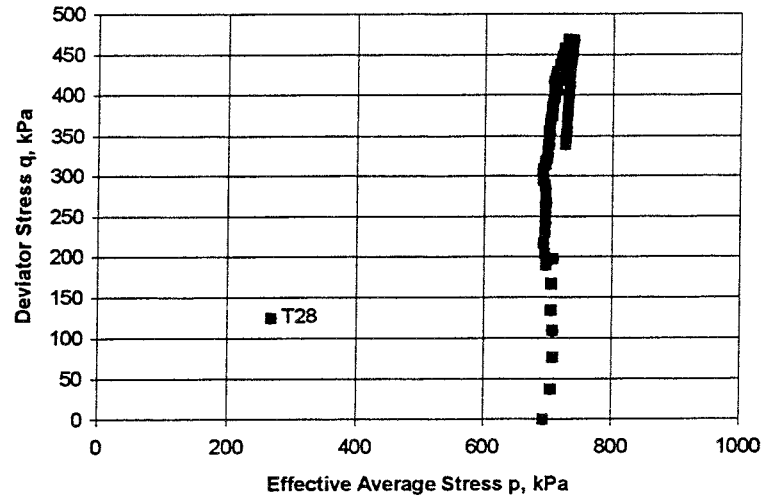

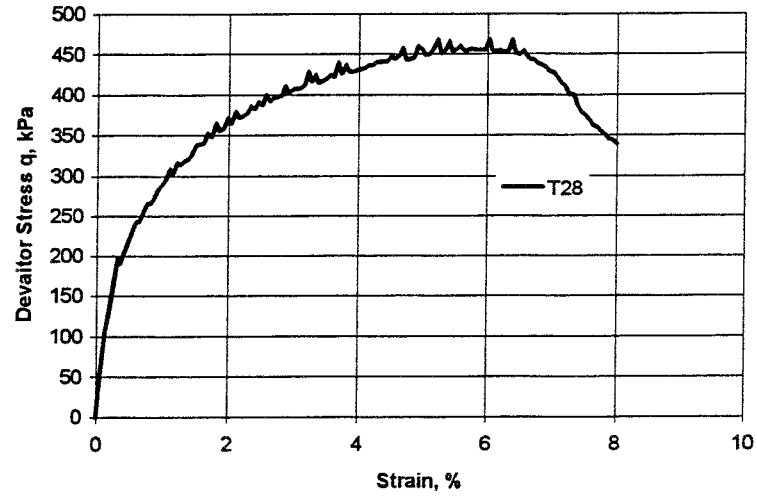

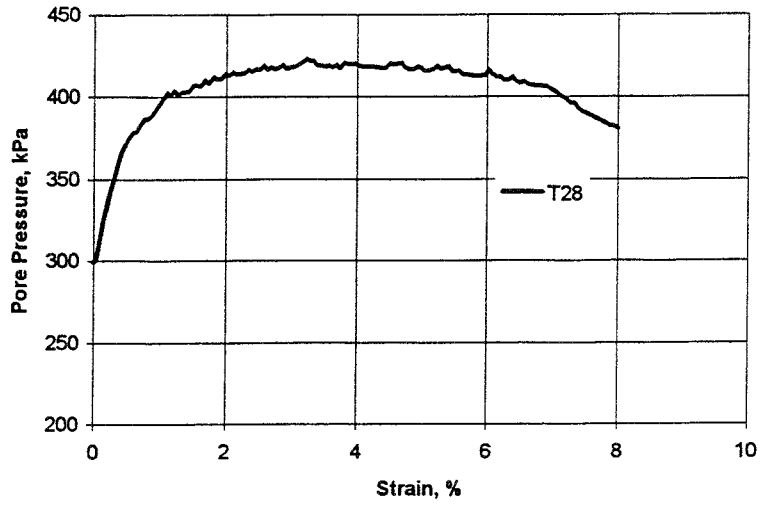

Triaxial test T28

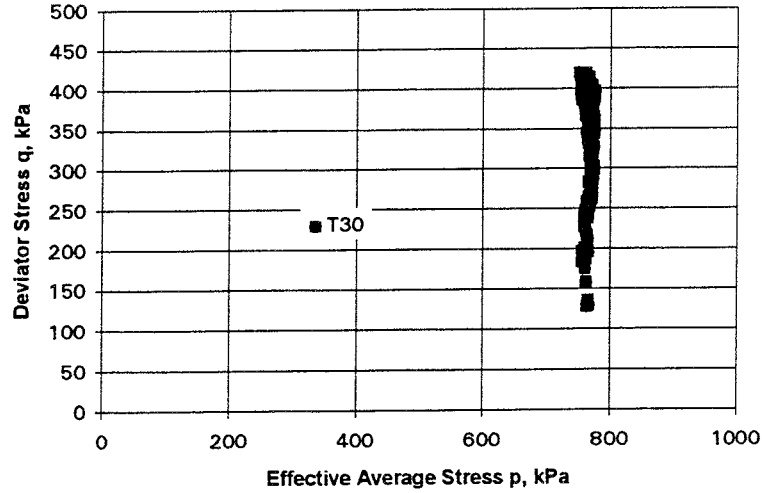

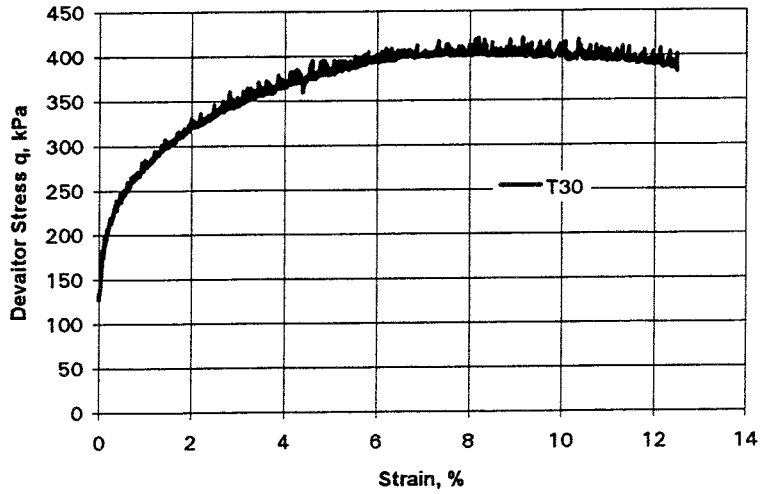

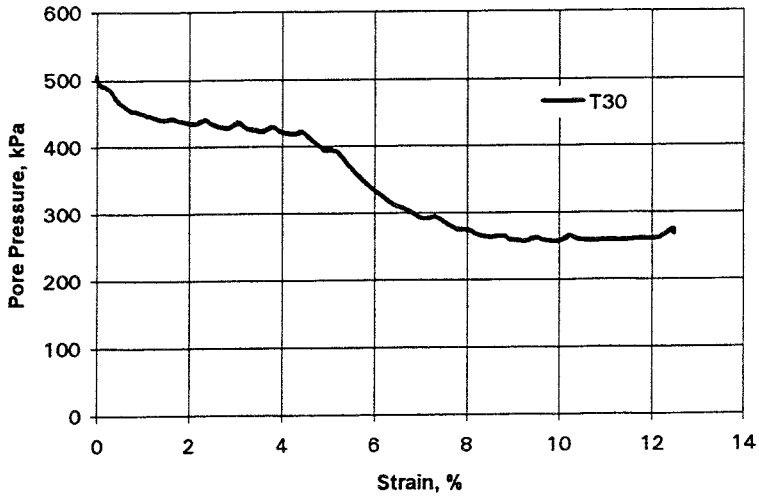

Triaxial test T30

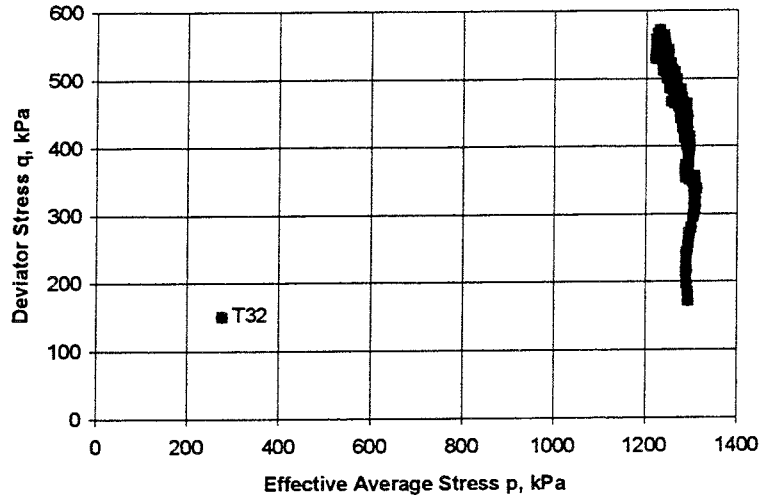

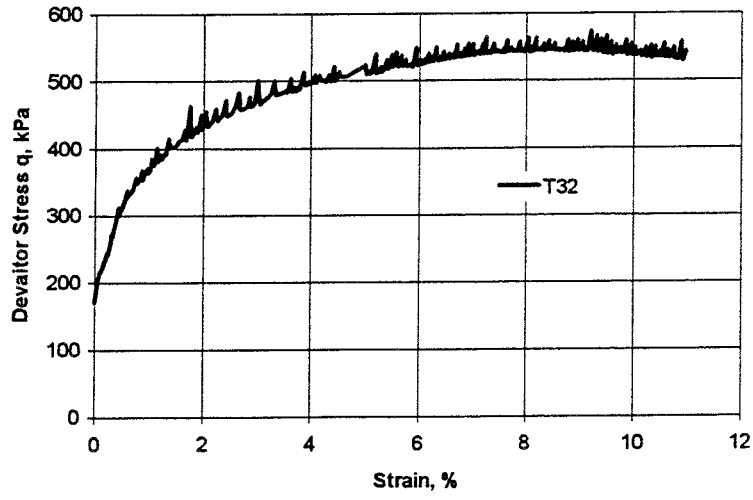

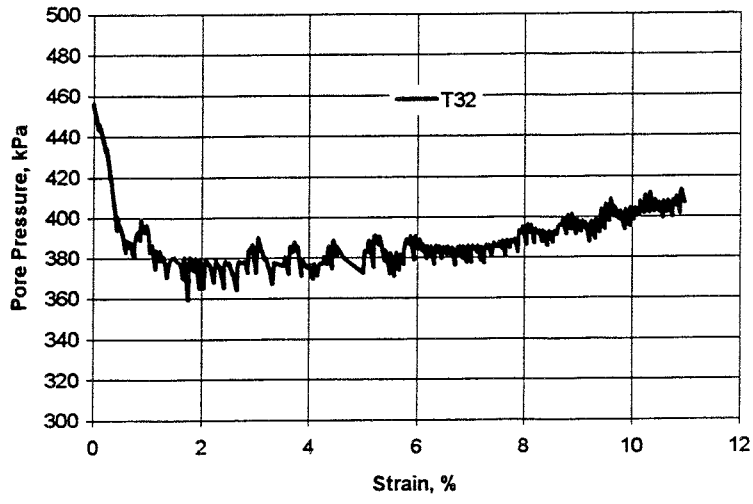

Triaxial test T32

APPENDIX 3

Swelling/compression tests

KMXAR2 Expansion of Mx-80. Sample height at start: 20mm
Normal stress at start: 13 MPa Density at start: 2.07 g/cm³

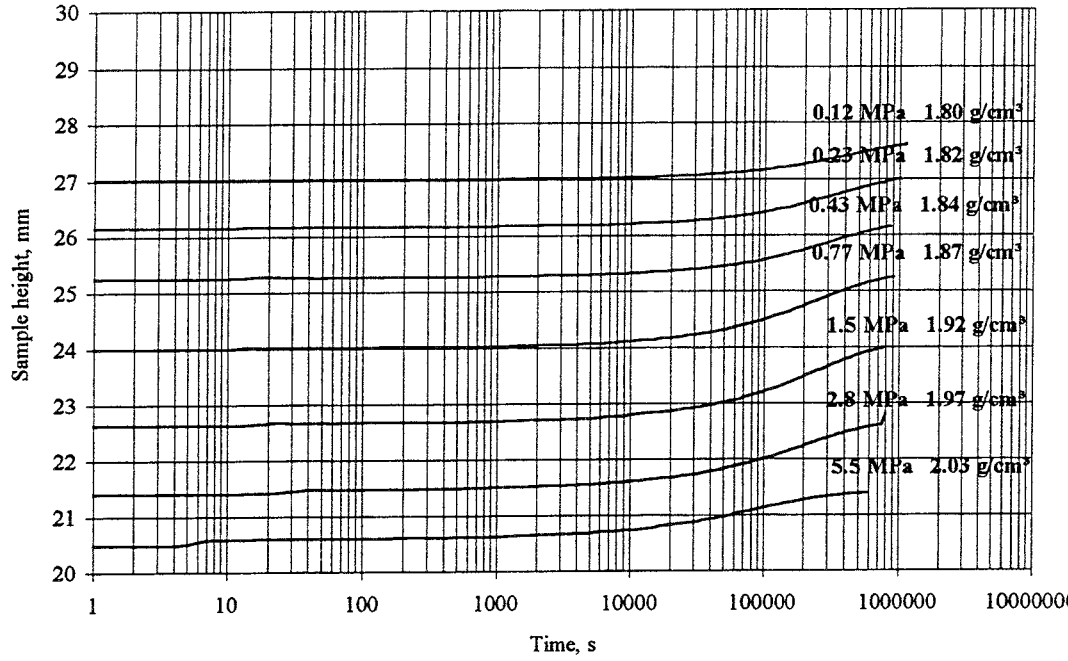

KMXAR2 Consolidation of Mx-80. Normal stress at start: 0.12 MPa

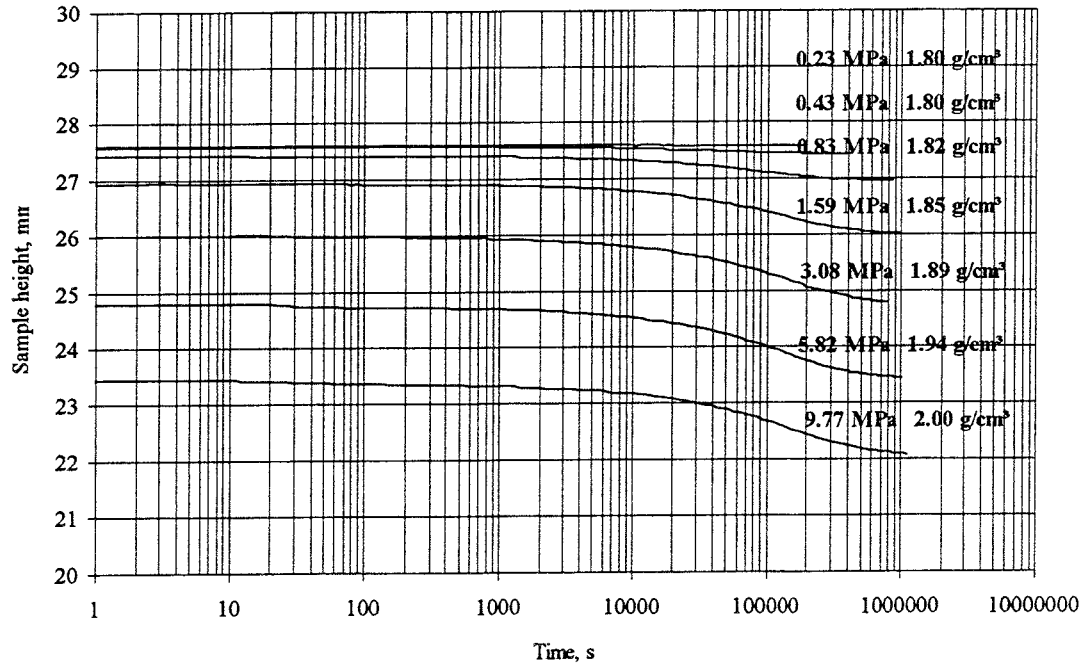

Test KMXAR2

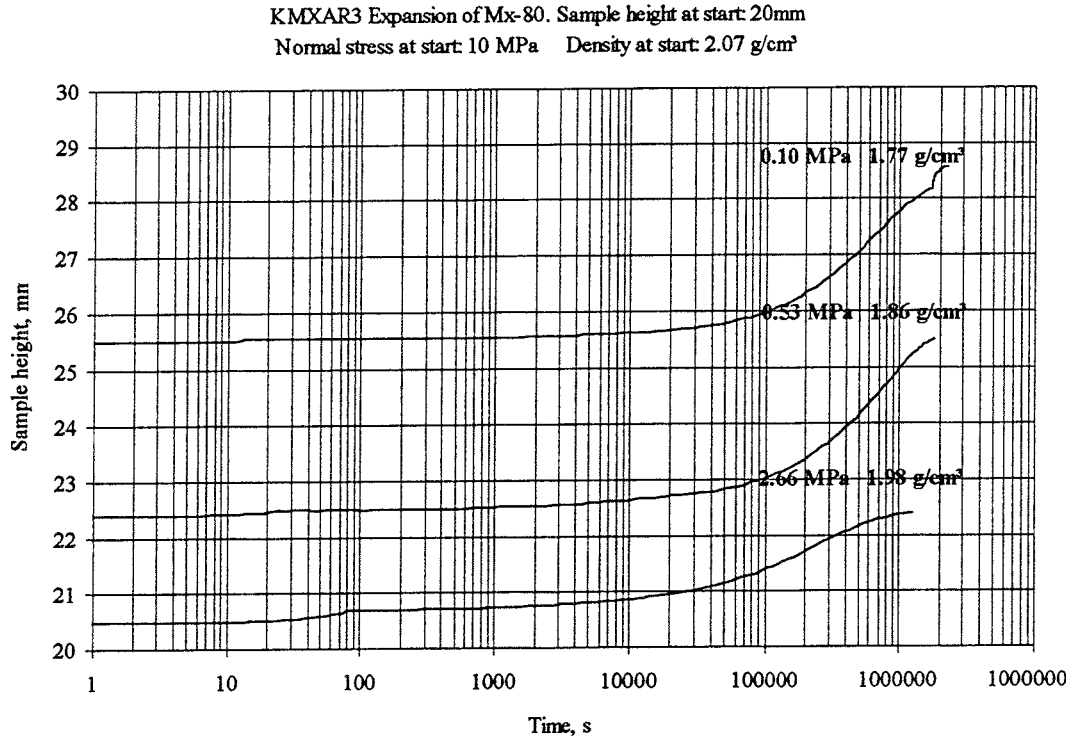
KMXAR3 Expansion of Mx-80. Sample height at start: 20mm
Normal stress at start: 10 MPa Density at start: 2.07 g/cm³
Sample height, mm
30
29
28
27
26
25
24
23
22
21
20
1
10
100
1000
10000
100000
1000000
10000000
Time, s
0.10 MPa 1.77 g/cm³
0.53 MPa 1.86 g/cm³
2.66 MPa 1.98 g/cm³

Test KMXAR3

KMXAR4 Consolidation of Mx-80. Sample height at start: 50mm
Normal stress at start: 40 kPa Density at start: 1.5 g/cm³

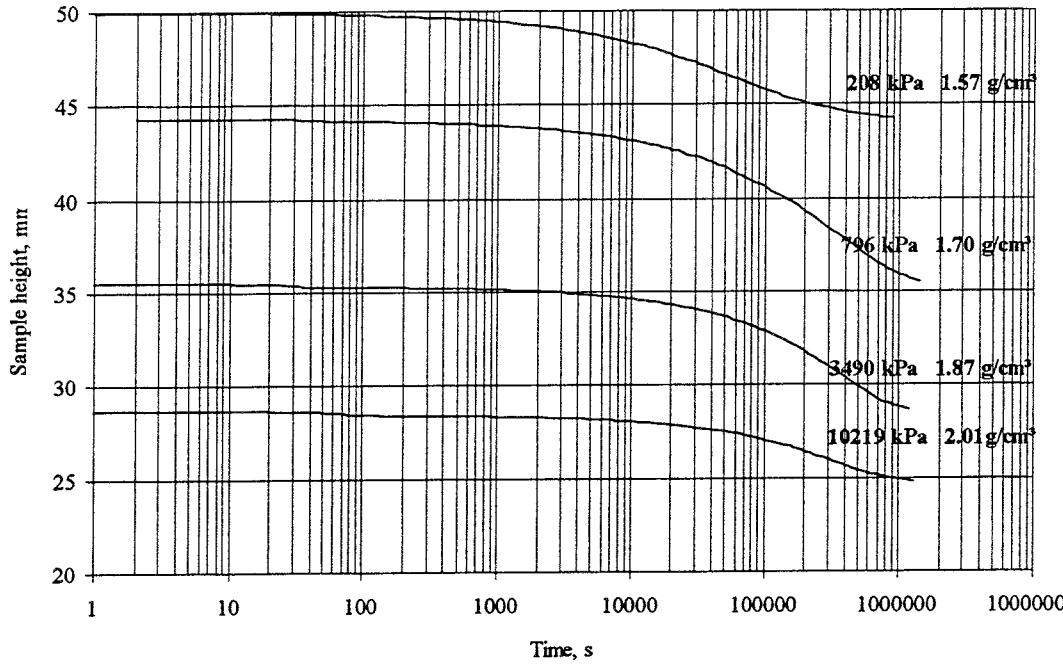

KMXAR4 Expansion of Mx-80. Normal stress at start: 10219 kPa
Density at start: 2.01g/cm³

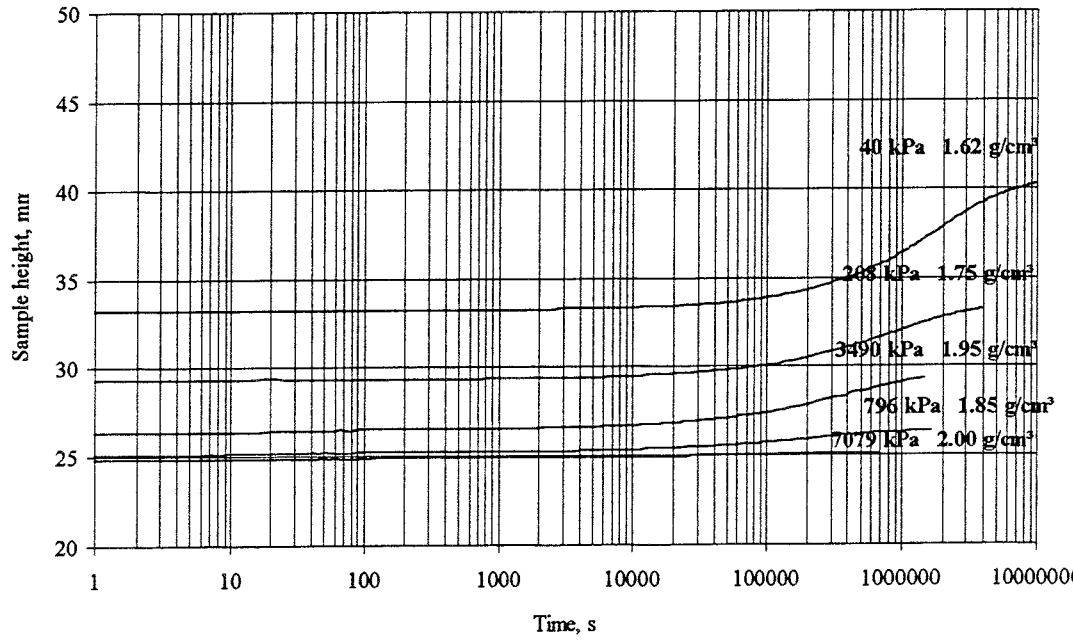

Test KMXAR4

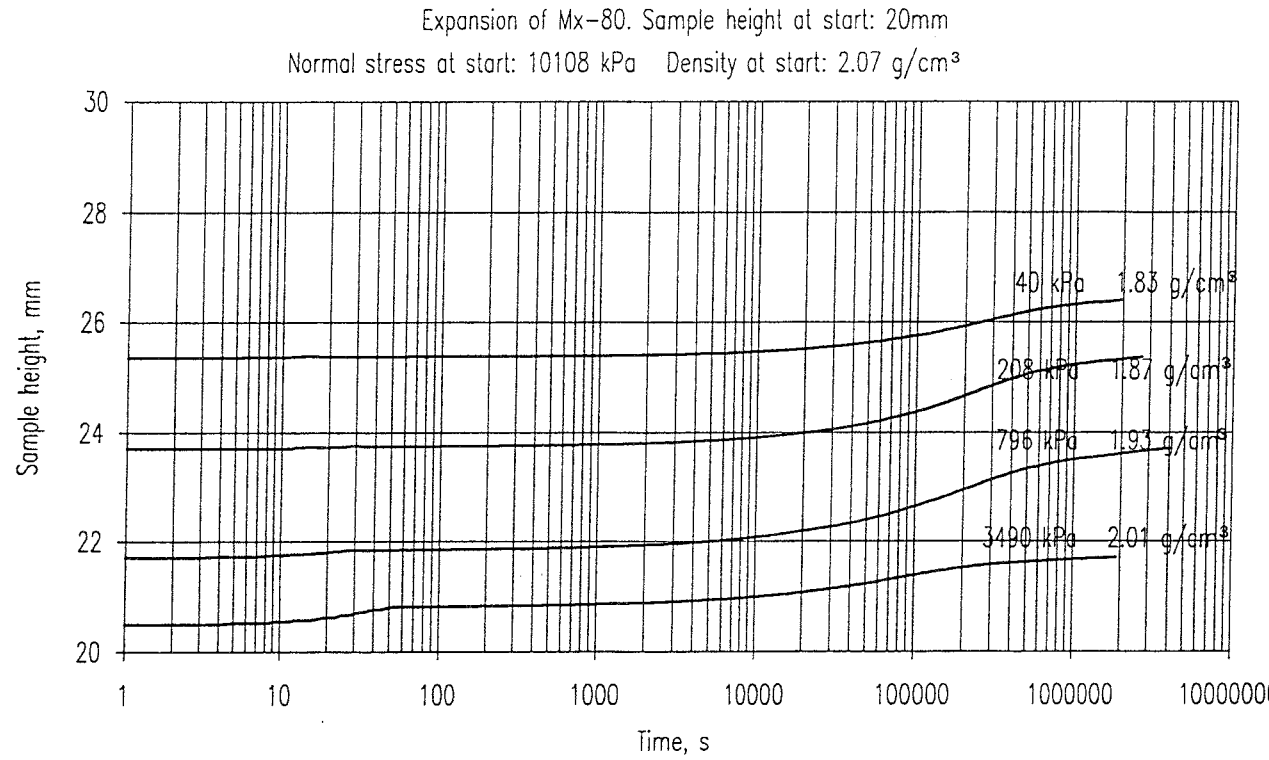
Expansion of Mx-80. Sample height at start: 20mm
Normal stress at start: 10108 kPa Density at start: 2.07 g/cm³
Sample height, mm
30
28
26
24
22
20
1
10
100
1000
10000
100000
1000000
10000000
Time, s
40 kPa 1.83 g/cm³
208 kPa 1.87 g/cm³
796 kPa 1.93 g/cm³
3490 kPa 2.01 g/cm³

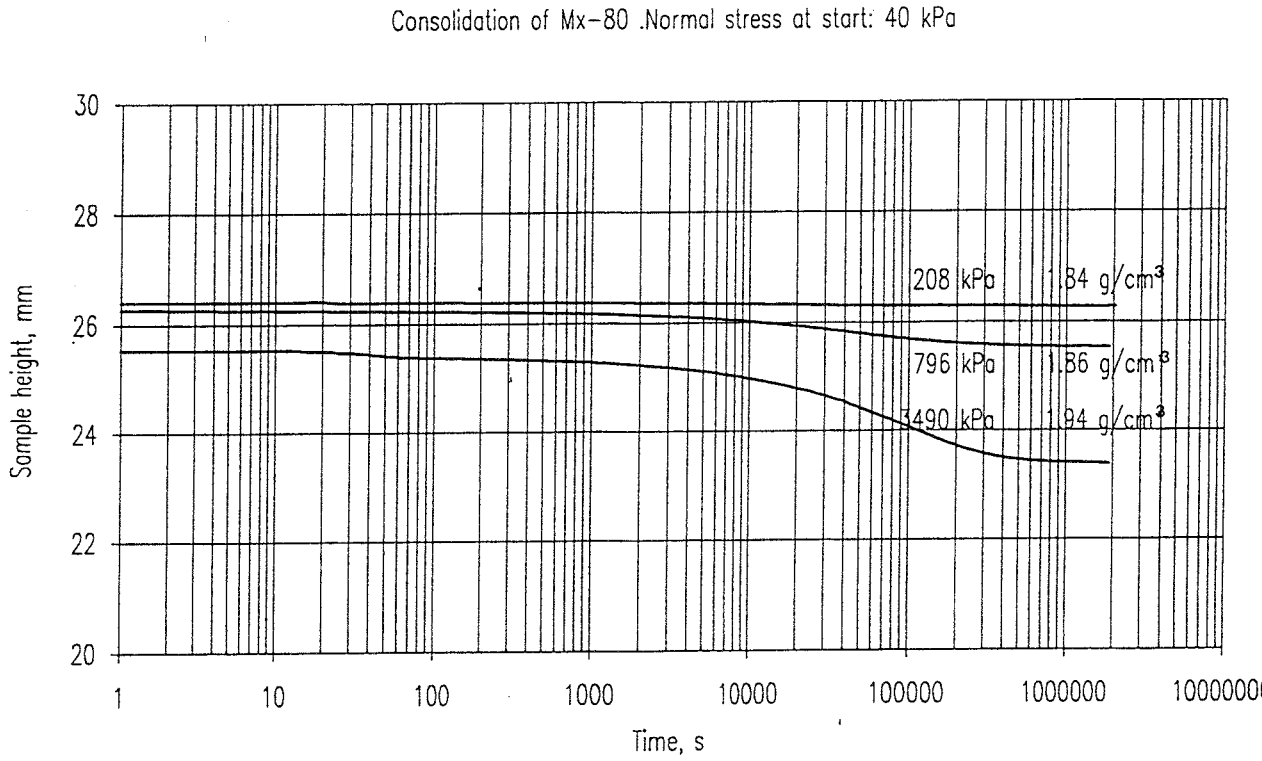
Consolidation of Mx-80 .Normal stress at start: 40 kPa
Sample height, mm
30
28
26
24
22
20
1
10
100
1000
10000
100000
1000000
10000000
Time, s
208 kPa 1.84 g/cm³
796 kPa 1.86 g/cm³
3490 kPa 1.94 g/cm³

Test KMXAR5

KMXAR6 Expansion of Mx-80. Normal stress at start: 10119 kPa

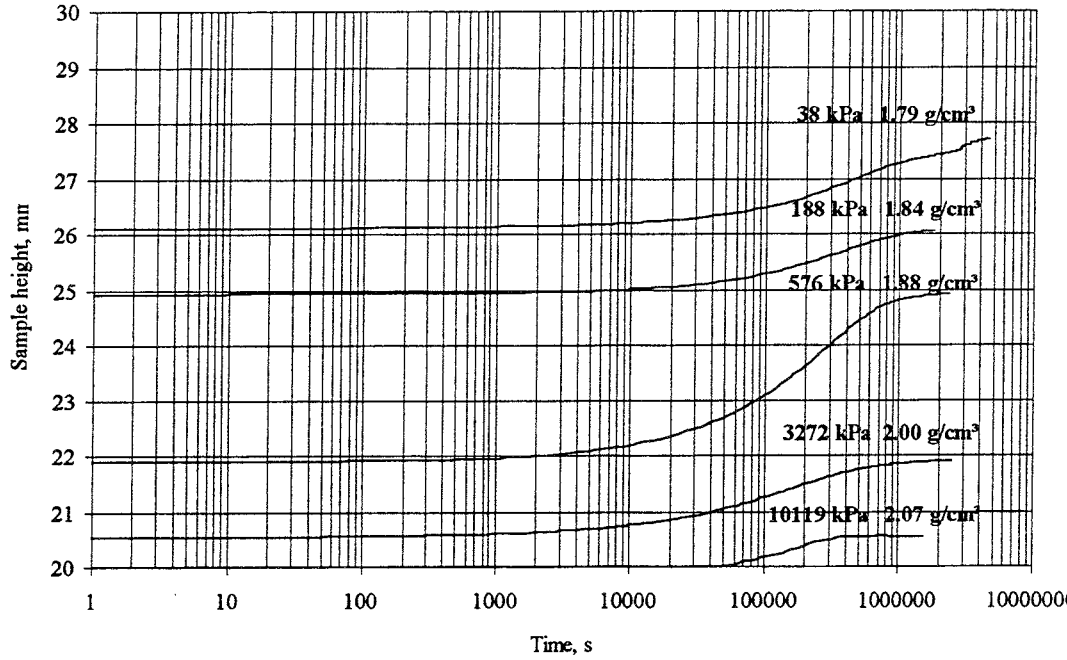

KMXAR6 Consolidation of Mx-80. Normal stress at start: 38 kPa

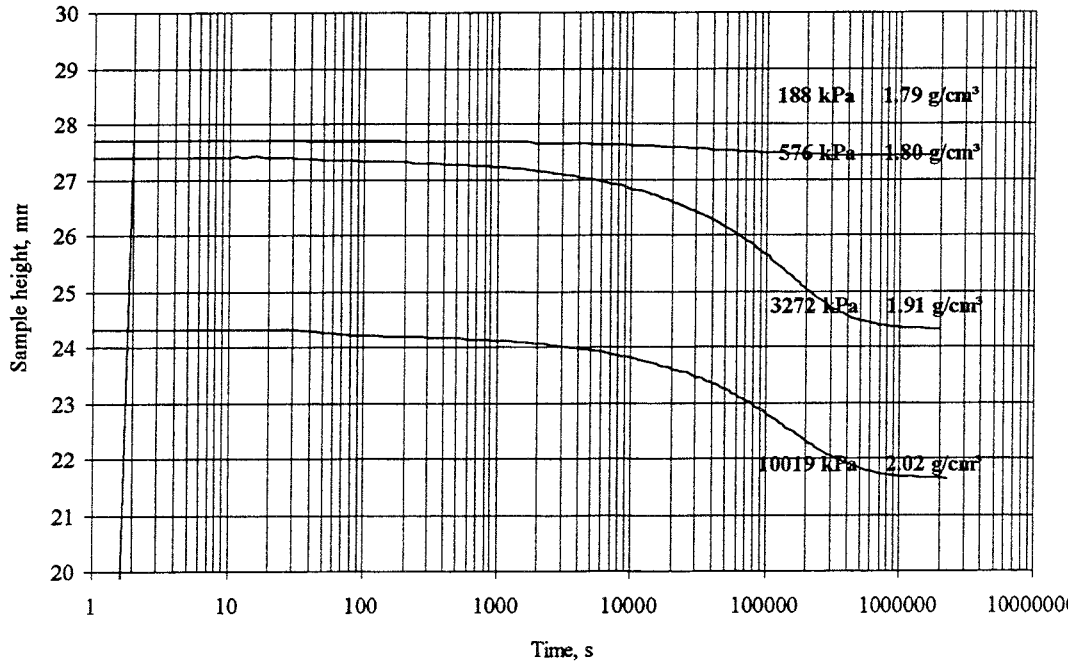

Test KMXAR6

KMXAR7 Expansion of Mx-80 at high temperature(T=90°C).
Normal stress at start=9929 kPa

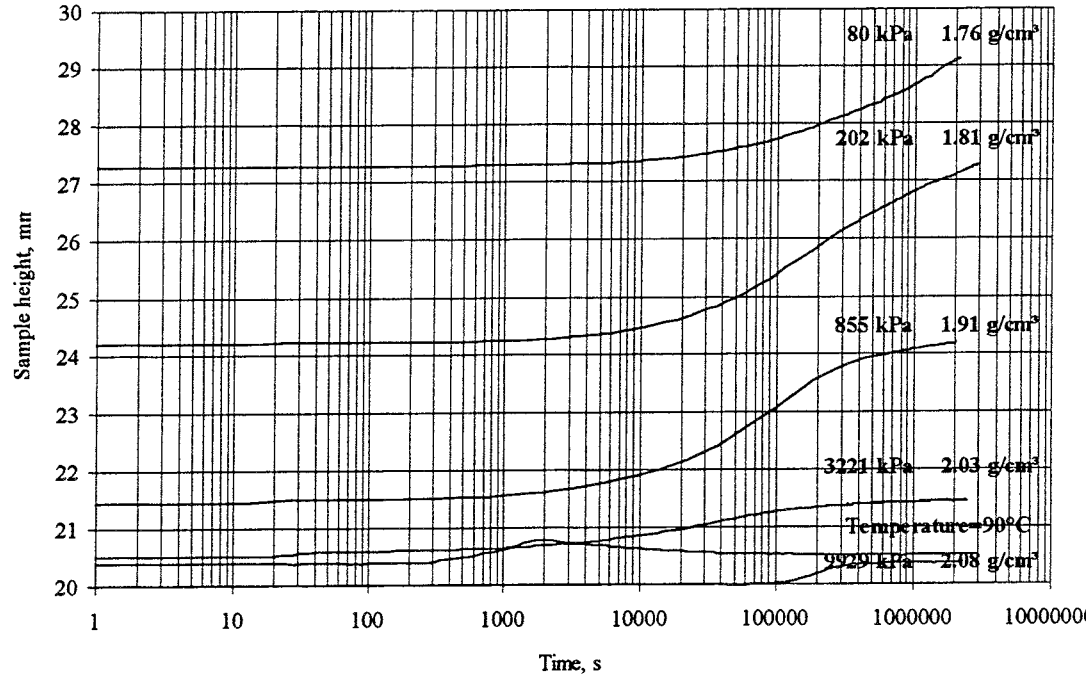

KMXAR7 Consolidation of Mx-80 at high temperature(T=90°C).

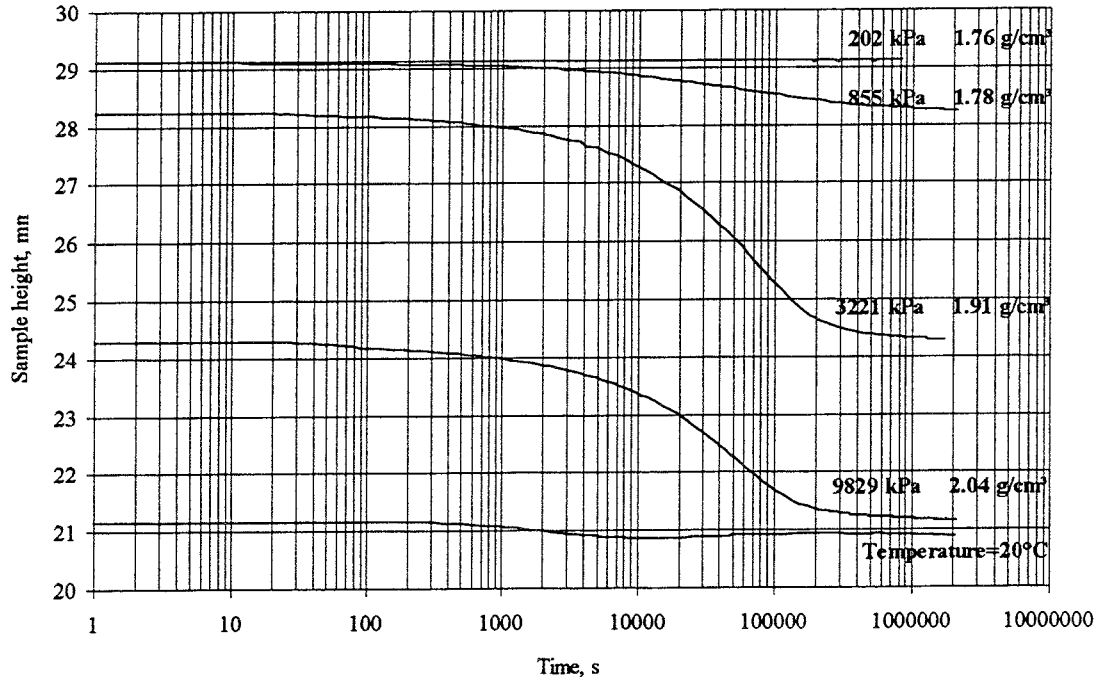

Test KMXAR7

KMoos1 Expansion of Moosburg. Sample height at start: 20mm
Normal stress at start: 10 MPa. Density at start: 2.09 g/cm³

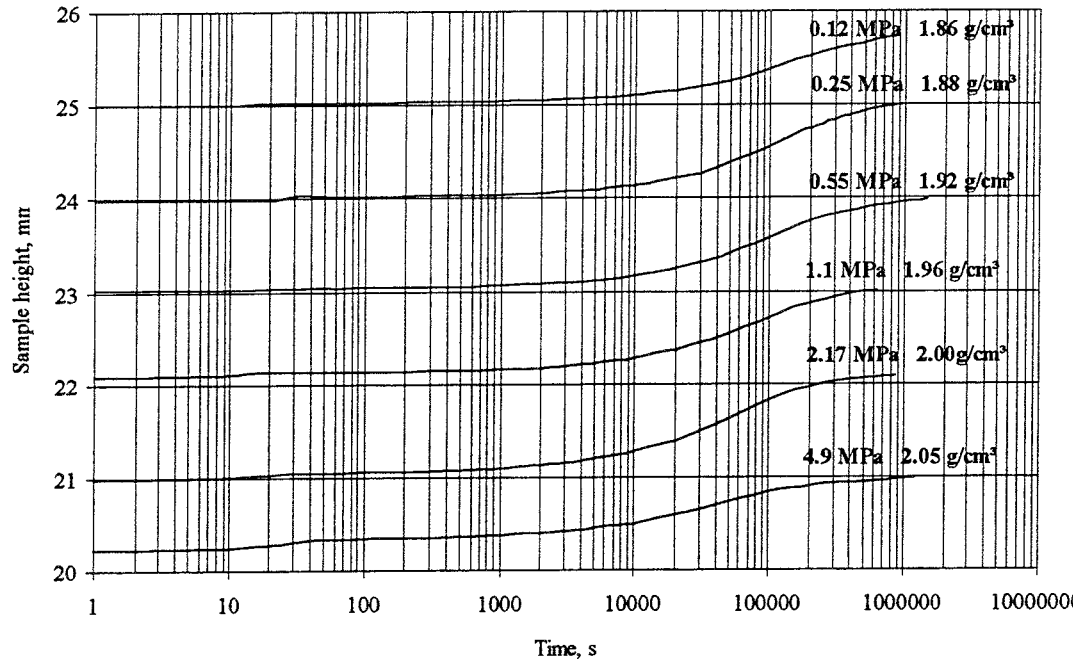

KMoos1 Consolidation of Moosburg. Normal stress at start: 0.12 MPa

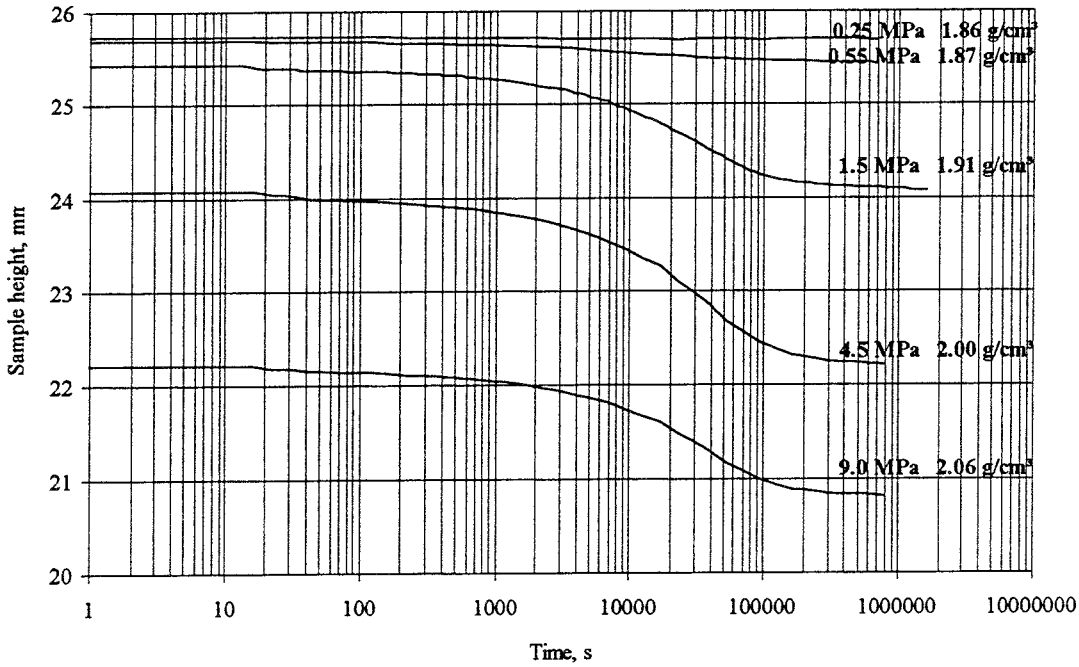

Test KMoos1

List of SKB reports

Annual Reports

1977-78
TR 121
KBS Technical Reports 1 – 120
Summaries
Stockholm, May 1979

1979
TR 79-28
The KBS Annual Report 1979
KBS Technical Reports 79-01 – 79-27
Summaries
Stockholm, March 1980

1980
TR 80-26
The KBS Annual Report 1980
KBS Technical Reports 80-01 – 80-25
Summaries
Stockholm, March 1981

1981
TR 81-17
The KBS Annual Report 1981
KBS Technical Reports 81-01 – 81-16
Summaries
Stockholm, April 1982

1982
TR 82-28
The KBS Annual Report 1982
KBS Technical Reports 82-01 – 82-27
Summaries
Stockholm, July 1983

1983
TR 83-77
The KBS Annual Report 1983
KBS Technical Reports 83-01 – 83-76
Summaries
Stockholm, June 1984

1984
TR 85-01
Annual Research and Development Report 1984
Including Summaries of Technical Reports Issued during 1984. (Technical Reports 84-01 – 84-19)
Stockholm, June 1985

1985
TR 85-20
Annual Research and Development Report 1985
Including Summaries of Technical Reports Issued during 1985. (Technical Reports 85-01 – 85-19)
Stockholm, May 1986

1986
TR 86-31
SKB Annual Report 1986
Including Summaries of Technical Reports Issued during 1986
Stockholm, May 1987

1987
TR 87-33
SKB Annual Report 1987
Including Summaries of Technical Reports Issued during 1987
Stockholm, May 1988

1988
TR 88-32
SKB Annual Report 1988
Including Summaries of Technical Reports Issued during 1988
Stockholm, May 1989

1989
TR 89-40
SKB Annual Report 1989
Including Summaries of Technical Reports Issued during 1989
Stockholm, May 1990

1990
TR 90-46
SKB Annual Report 1990
Including Summaries of Technical Reports Issued during 1990
Stockholm, May 1991

1991
TR 91-64
SKB Annual Report 1991
Including Summaries of Technical Reports Issued during 1991
Stockholm, April 1992

1992
TR 92-46
SKB Annual Report 1992
Including Summaries of Technical Reports Issued during 1992
Stockholm, May 1993

1993
TR 93-34
SKB Annual Report 1993
Including Summaries of Technical Reports Issued during 1993
Stockholm, May 1994

1994

TR 94-33

SKB Annual Report 1994

Including Summaries of Technical Reports Issued during 1994.
Stockholm, May 1995

List of SKB Technical Reports 1995

TR 95-01

Biotite and chlorite weathering at 25°C. The dependence of pH and (bi) carbonate on weathering kinetics, dissolution stoichiometry, and solubility; and the relation to redox conditions in granitic aquifers

Maria Malmström[1], Steven Banwart[1], Lara Duro[2], Paul Wersin[3], Jordi Bruno[3]
[1] Royal Institute of Technology, Department of Inorganic Chemistry, Stockholm, Sweden
[2] Universidad Politécnica de Cataluña, Departmento de Inginería Química, Barcelona, Spain
[3] MBT Tecnología Ambiental, Cerdanyola, Spain
January 1995

TR 95-02

Copper canister with cast inner component. Amendment to project on Alternative Systems Study (PASS), SKB TR 93-04

Lars Werme, Joachim Eriksson
Swedish Nuclear Fuel and Waste Management Co, Stockholm, Sweden
March 1995

TR 95-03

Prestudy of final disposal of long-lived low and intermediate level waste

Marie Wiborgh (ed.)
Kemakta Konsult AB, Stockholm, Sweden
January 1995

TR 95-04

Spent nuclear fuel corrosion: The application of ICP-MS to direct actinide analysis

R S Forsyth[1], U-B Eklund[2]
[1] Caledon-Consult AB, Nyköping, Sweden
[2] Studsvik Nuclear AB, Nyköping, Sweden
March 1995

TR 95-06

Palaeohydrological implications in the Baltic area and its relation to the groundwater at Äspö, south-eastern Sweden – A literature study

Bill Wallin
Geokema AB, Lidingö, Sweden
March, 1995

TR 95-07

Äspö Hard Rock Laboratory Annual Report 1994

SKB
April 1995

TR 95-08

Feasibility study for siting of a deep repository within the Storuman municipality

Swedish Nuclear Fuel and Waste Management Co., Stockholm
January 1995

TR 95-09

A thermodynamic data base for Tc to calculate equilibrium solubilities at temperatures up to 300°C

Ignasi Puigdomènech[1], Jordi Bruno[2]
[1] Studsvik AB, Nyköping, Sweden
[2] Intera Information Technologies SL, Cerdanyola, Spain
April 1995

TR 95-10

Investigations of subterranean microorganisms. Their importance for performance assessment of radioactive waste disposal

Karsten Pedersen[1], Fred Karlsson[2]
[1] Göteborg University, General and Marine Microbiology, The Lundberg Institute, Göteborg, Sweden
[2] Swedish Nuclear Fuel and Waste Management Co., Stockholm, Sweden
June 1995

TR 95-11

Solute transport in fractured media – The important mechanisms for performance assessment

Luis Moreno, Björn Gylling, Ivars Neretnieks
Department of Chemical Engineering and Technology, Royal Institute of Technology, Stockholm, Sweden
June 1995

TR 95-12

Literature survey of matrix diffusion theory and of experiments and data including natural analogues

Yvonne Ohlsson, Ivars Neretnieks
Department of Chemical Engineering and Technology, Royal Institute of Technology, Stockholm, Sweden
August 1995

TR 95-13

Interactions of trace elements with fracture filling minerals from the Äspö Hard Rock Laboratory

Ove Landström[1], Eva-Lena Tullborg[2]
[1] Studsvik Eco & Safety AB
[2] Terralogica AB
June 1995

TR 95-14

Consequences of using crushed crystalline rock as ballast in KBS-3 tunnels instead of rounded quartz particles

Roland Pusch
Clay Technology AB
February 1995

TR 95-15

Estimation of effective block conductivities based on discrete network analyses using data from the Äspö site

Paul R La Pointe[1], Peter Wallmann[1], Sven Follin[2]
[1] Golder Associates Inc., Seattle, WA, USA
[2] Golder Associates AB, Lund, Sweden
September 1995

TR 95-16

Temperature conditions in the SKB study sites

Kaj Ahlbom[1], Olle Olsson[1], Stefan Sehlstedt[2]
[1] Conterra AB
[2] MRM Konsult AB
June 1995

TR 95-17

Measurements of colloid concentrations in the fracture zone, Äspö Hard Rock Laboratory, Sweden

Anna Ledin, Anders Düker, Stefan Karlsson, Bert Allard
Department of Water and Environmental Studies,Linköping University, Linköping, Sweden
June 1995

TR 95-18

Thermal evidence of caledonide foreland, molasse sedimentation in Fennoscandia

Eva-Lena Tullborg[1], Sven Åke Larsson[1], Lennart Björklund[1], Lennart Samuelsson[2], Jimmy Stigh[1]
[1] Department of Geology, Earth Sciences Centre, Göteborg University, Göteborg, Sweden
[2] Geological Survey of Sweden, Earth Sciences Centre, Göteborg, Sweden
November 1995

TR 95-19

Compaction of bentonite blocks. Development of technique for industrial production of blocks which are manageable by man

Lars-Erik Johannesson, Lennart Börgesson, Torbjörn Sandén
Clay Technology AB, Lund, Sweden
April 1995